Impacts of Cascadia Subduction Zone M9 Earthquakes on Bridges in Washington State: SDOF Idealized Bridges

Zachary Kortum

A thesis
submitted in partial fulfillment of the
requirements for the degree of

Master of Science in Civil Engineering

University of Washington

2021

Committee:
Jeffrey W. Berman
Marc O. Eberhard
Brett Maurer
Nasser Marafi

Program Authorized to Offer Degree:
Civil and Environmental Engineering

University of Washington

Abstract

Impacts of Cascadia Subduction Zone M9 Earthquakes on Bridges in Washington State: SDOF Idealized Bridges

Zachary Kortum

Chair of the Supervisory Committee:
Jeffrey Berman and Marc Eberhard
Civil and Environmental Engineering

The Cascadia Subduction Zone has the potential to generate Magnitude 9 earthquakes that could have large impacts on bridges throughout western Washington State. The likelihoods of damage to bridges during an M9 event at various locations in Western Washington were estimated by the following process:

1. Ten locations in Washington State were selected to reflect a wide variety of fault distances and sedimentary basin depths. At each location, the ground motions for an M9 event were simulated for 30 earthquake scenarios by a United States Geological Survey (USGS) and University of Washington (UW) team, with the support of the National Science Foundation (Frankel et al. 2018). The baseline motions were modified to account for four sets of 30 site profiles, corresponding to four subcategories of the NEHRP site classes.
2. WSDOT, UW, and Washington State University engineers compiled a detailed database of key properties of 609 WSDOT bridges along key lifelines in the Puget Sound region. About three quarters of these bridges were constructed before 1976.

Nearly 70% of the bridges documented in this database were supported by at least one reinforced concrete column at intermediate supports.

3. The bridges with reinforced concrete columns were idealized as single-degree-of-freedom systems in which the effective stiffness and lateral strength were derived from the column properties, and the resistance provided by the abutments was neglected. The cyclic force-deformation responses of the columns were modeled with an Ibarra-Medina-Krawinkler deterioration model that was calibrated using force-deformation histories from the UW-PEER Column Performance Database (UW-PEER 2020).
4. The deformation demands for pre-1976 and 1976-present bridges were estimated for 30 M9 scenarios, the 10 locations, N-S and E-W directions, 120 site profiles (sorted into four site categories) and 18 periods. Both the response of systems with mean strengths and reduced strengths were simulated.

The researchers found that the lateral strengths of most of the lifeline bridges exceeded the strengths expected from design procedures, even after accounting for material overstrength and strain hardening. As a result, many of the bridges, even older bridges designed before the mid-1970s, performed better than expected. In particular:

- Bridges located along the west coast of the Olympic Peninsula (e.g., Ocean Shores, Forks) had median displacement ductility demands in the range of 2 to 4. Collapse probabilities above 15-20% were only predicted for older pre-1976 bridges with periods below 0.3s. Averaged over many events, the likelihood of column concrete spalling range from 40-60% for a wide range of periods, and the likelihood of buckling for most periods was in the range of 5% to 25%.

- The likely performance of bridges located on sedimentary basins in the Puget Sound region (e.g., Seattle, Tacoma, Everett) depended strongly on the bridge's effective period.
    - Bridges with periods below 0.5s had median displacement ductilities below or near 2.
    - Between periods of 0.5s and 3s, the displacement ductilities were larger than at lower or higher periods, and they reached values of 5 for older bridges located on soil profiles corresponding to the softer end of Site Class D (Subclass D3).
    - New bridges had negligible likelihoods of collapse, and the likelihood of bridge collapse for older bridges only exceeded 20% for soil subclass D3.
- Bridges located at similar distances from the coast as Seattle, but located outside of sedimentary basins (e.g., the Seattle basin), had median displacement demands below 2, and negligible collapse probabilities and likelihoods of bar buckling. Some spalling might be experienced in bridges located on softer soils.

From the ductility demand data, fragility curves were constructed using both S_a and $S_{a,eff}$ for various levels of ductility demand. The fragility curves produced using S_a showed significant regional variation, whereas those produced using $S_{a,eff}$ were highly consistent across the 10 locations. In addition, the fragility curves produced using $S_{a,eff}$ were much steeper and showed less scatter than those produced using spectral acceleration alone.

The results of these analyses come with several caveats. Namely, the analyses conducted as part of this study:

- Neglected the resistance provided by abutments

- Did not consider the behavior of very soft soils (e.g., site classes E and F). The interaction between the site profiles with long periods might exacerbate the amplification of long-period components of motions observed in sedimentary basins.
- Neglected the likelihood of span unseating, under the assumption that previous WSDOT retrofit efforts have precluded this failure mode
- Neglected the likely correlation between ductility demand and performance levels for a given M9 event. In other words, some events might lead to much larger (or smaller) demands and damage that others, leading to much larger (or smaller) damage levels for a particular event.
- Most importantly, shear or foundation failure were not considered. Both of these failure modes might be critical in older bridges.

Table of Contents

Figures

Tables

Chapter 1: Research Motivation

The Cascadia Subduction Zone is a 600-mile long tectonic plate boundary that separates the Juan de Fuca Plate from the North American Plate. It stretches from Vancouver, B.C., to Northern California (Figure 1.1). Subduction zones generate some of the largest magnitude earthquakes in the world (PNSN 2021). The last known megathrust earthquake in the Cascadia Subduction Zone occurred in 1700, and geologic evidence indicates that at least 7 such earthquakes have occurred in the last 3500 years, with a return period of approximately 400 - 600 years (PNSN 2021).

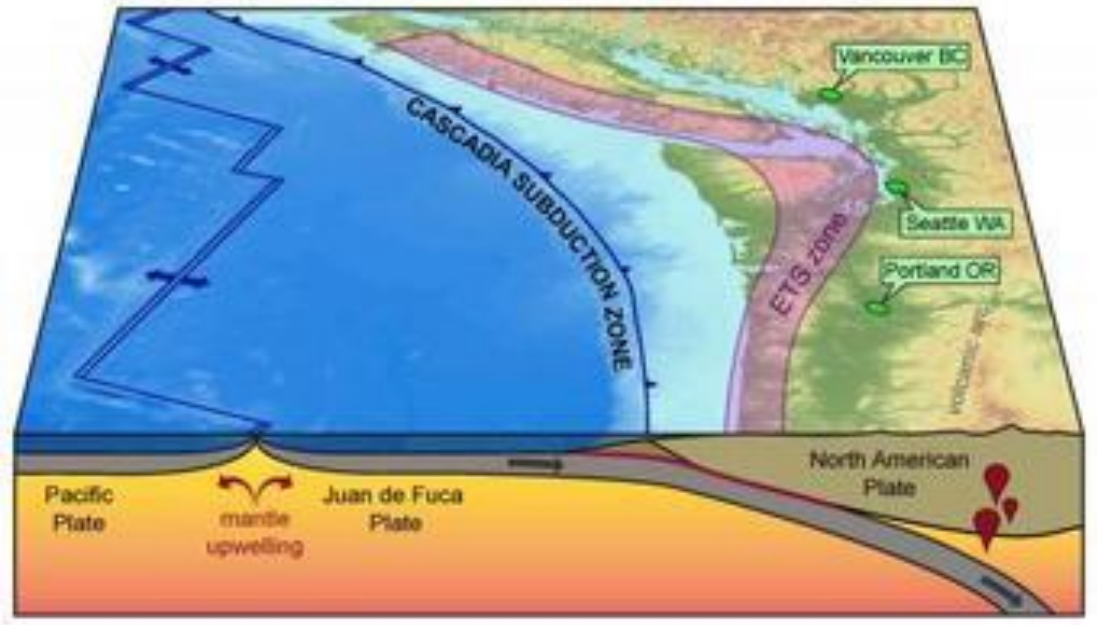

Figure 1.1. Cascadia Subduction Zone. (USGS 2020)

Records from previous subduction zone earthquakes around the world indicate that these earthquakes can have large spectral accelerations, long durations, and will be amplified by deep sedimentary basins (Marafi 2017). Current seismic hazard design maps for bridges in the US do

not consider the effects of ground-motion amplification due to sedimentary basins (Marafi 2017). The Pacific Northwest Puget Sound Region, including the city of Seattle, is located near the Cascadia Subduction Zone and is underlaid by a deep sedimentary basin. As a result, subduction zone earthquakes are likely to be especially damaging to structures in and around the Puget Sound region.

This report presents an investigation of the effects of simulated, soil-adjusted M9 ground motions from the Cascadia Subduction Zone on idealized single-degree-of-freedom oscillators in 10 locations in Western Washington State. The following sections describe the development of models of the Cascadia Subduction Zone by the United State Geological Survey, as well as previous research efforts to understand the hazards posed to structures due to M9 Cascadia Subduction Zone earthquakes.

1.1 CASCADIA SUBDUCTION ZONE MODELS

Researchers at the United States Geological Survey (USGS) and the University of Washington (UW) collaborated to produce 30 sets of synthetic seismograms of magnitude 9 Cascadia Subduction Zone earthquakes. These ground motion simulations were produced by combining synthetic seismograms derived from 3D finite- difference simulations with finite-source, stochastic synthetics (Frankel et al. 2018). The 30 synthetic seismograms included a range of rupture parameters to capture a wide range of possible M9 events (Frankel et al. 2018). Rupture parameters varied included the hypocenter of the motion, the rupture velocity, and the magnitude and location of subevents (Wirth et al. 2018). The ground motions were produced using a two-component model: first, high stress-drop magnitude 8 subevents, and second, large slip motions with long durations (Frankel et al. 2018). These two components were superimposed on each other to produce the final simulated M9 motions.

The generated M9 motions had long significant durations, ranging from 70 seconds along the Pacific Coast to 120 seconds further inland (Frankel et al. 2018). In addition, the motions had large spectral accelerations near the coast (Figure 1.2), and spectral accelerations at longer periods were significantly amplified by the presence of sedimentary basins (Figure 1.3). Amplification factors in the sedimentary basins ranged from 2 to 5 for periods between 1 and 10 seconds (Frankel et al. 2018).

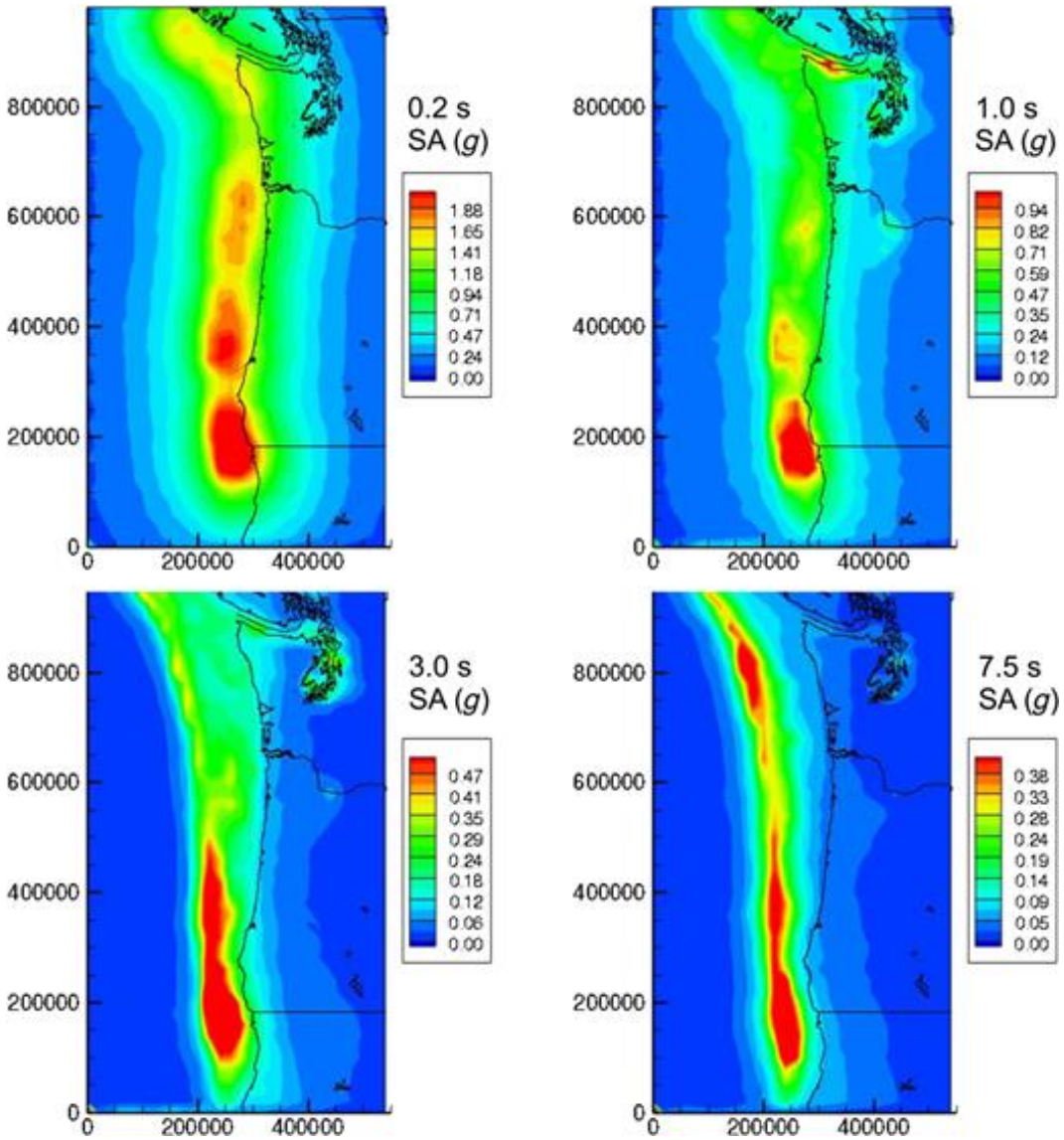

Figure 1.2. Log-averaged Spectral accelerations for the 30 M9 ground motions. (Frankel et al. 2018)

Figure 1.2 shows the log-averaged spectral accelerations for the suite of 30 baseline M9 ground motions. In general, spectral accelerations are high at locations close to the Pacific Coast, as well as in the Puget Sound region. Figure 1.3 shows a magnified view of the Puget Sound region, with the boundary of the Seattle sedimentary basin outlined in black. It can be seen that spectral accelerations are magnified inside the basin at periods of both 2 and 5 seconds. The Tacoma sedimentary basin (labelled but not outlined) shows similarly amplified spectral accelerations.

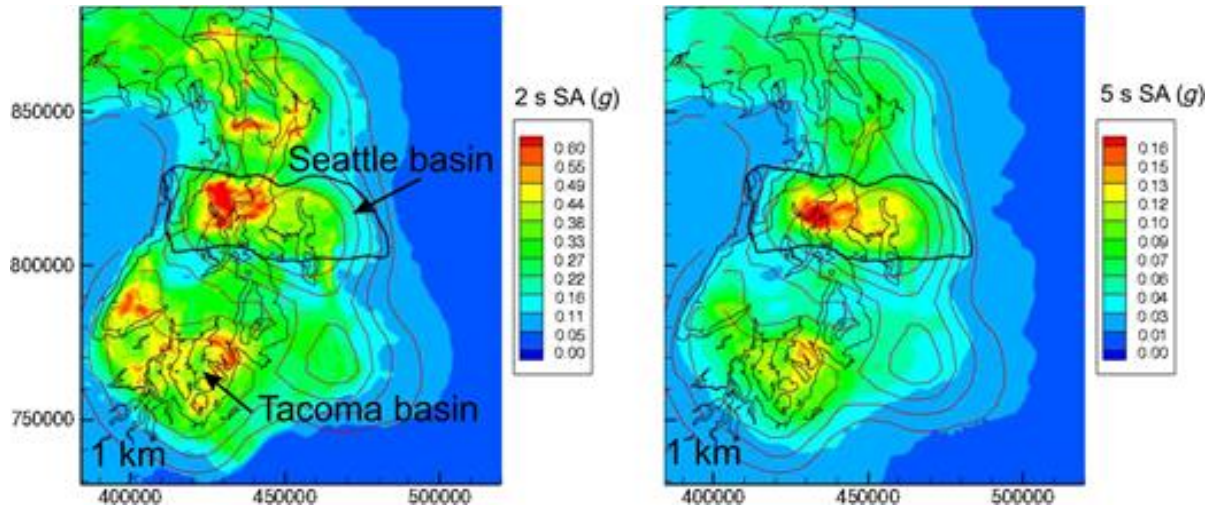

Figure 1.3. Log averaged spectral accelerations for the Puget Sound region for the 30 M9 ground motions. The boundary of the Seattle sedimentary basin is outlined in black. (Frankel et al. 2018)

1.2 PRIOR RESEARCH

Marafi et al. (2020) investigated the effects of simulated M9 ground motions on tall reinforced concrete core wall buildings. The study found that, for buildings located in Seattle, the M9 motions produced larger spectral accelerations, more damaging spectral shapes, and longer significant durations than typical motions corresponding to the maximum considered earthquake (MCE). In addition, the collapse probability (conditioned on the occurrence of an M9

earthquake) for buildings designed to code minimum standards averaged 27%, while building archetypes reflecting code-enhanced design averaged a collapse probability of 11%.

M9 motions in the Pacific Northwest are expected to have long durations because of the large magnitude of the earthquakes. Chandramohan et al (2019) investigated the effect of ground motion duration on collapse of reinforced concrete bridge piers. They found that when comparing sets of "spectrally equivalent" long- and short-duration ground motions, the collapse capacity for reinforced concrete bridge piers was 17% lower for the long-duration motions. Chandramohan also found that structures with high deformation capacities (like those expected to be found in new designs of highway bridges) were most sensitive to the effects of long duration.

De Zamacona (2019) investigated the effects of simulated, soil-adjusted M9 ground motions on several types of single-degree-of-freedom oscillators in ten locations in Western Washington. The oscillators were assumed to have strengths that were 50% higher than the 2019 WSDOT code-minimum values for bridges. She found that short-period structures suffered severe damage in cities close to the fault, while longer period structures were more heavily damaged in cities located on sedimentary basins.

1.3 RESEARCH GOALS

Previous research by de Zamacona (2019) investigated the effects of soil-adjusted M9 ground motions on idealized single-degree-of-freedom systems. However, the strengths and cyclic deterioration properties of the SDOF oscillators in that study were derived from code-based minimum design strengths for bridges, which might not accurately reflect the strengths of bridges in the field. In addition, that study examined oscillators with only a limited number of periods, and only M9 motions in the North-South direction were considered.

The primary goal of the work presented in this report is to more accurately model the risk to Washington state bridges in the event of an M9 earthquake by taking into account the properties of the bridge inventory in Western Washington, and by examining a comprehensive range of oscillator periods. Engineers at the Washington State Department of Transportation (WSDOT) compiled a database containing information on key parameters for 609 highway bridges in Western Washington. From the information in this database, estimates are made for the strength, stiffness, mass, and period of bridges in the inventory. These estimates are used to inform the properties of single-degree-of-freedom oscillators subjected to M9 ground motions. Oscillators were modeled over a wide range of periods, locations, strengths, and soil types to ensure a comprehensive understanding of the effects of an M9 event on Washington bridges. Additionally, the cyclic force-displacement behavior of the SDOF oscillators are calibrated to accurately capture the complex, nonlinear, cyclic behavior of reinforced concrete columns.

1.4 SCOPE OF WORK

Chapter 2 and presents the development of the baseline and soil-adjusted M9 ground motions. The differences in spectral acceleration obtained from bridge design codes and the M9 motions are presented. The chapter also discusses the effects of location, sedimentary basin, and soil conditions on the spectral accelerations from the M9 motions.

Chapter 3 summarizes the contents of a WSDOT-compiled bridge database which contains information on key parameters for bridges in the Puget Sound region. In Chapter 4, the contents of this database are used to estimate the strength, stiffness, mass, and period of the database bridges in order to characterize single-degree-of-freedom systems to be used in a parametric study.

Chapter 5 presents the calibration of a cyclic material model in OpenSEES, the modified Ibarra-Medina-Krawinkler (IMK) model, using cyclic column test data from the UW-PEER Structural Performance Database. Key parameters for the IMK model are calibrated, and simple relationships are proposed between these parameters and properties of reinforced concrete columns. The fully calibrated material model was used to represent the force-displacement behavior for the SDOF systems analyzed in the parametric study.

Chapter 6 outlines the parameters varied, and presents the modeling methodology used for the parametric study. Chapter 7 discusses the results of the parametric study, presented in terms of spectral accelerations, median displacement ductility demands, and likelihood of exceeding various ductility demand thresholds and damage states (e.g., onset of bar buckling).

Chapter 8 presents the development of fragility curves using the results of the parametric study. Fragility curves were developed using two measures of ground motion intensity: S_a, and $S_{a,eff}$, an intensity measure that takes into account spectral acceleration, ground motion duration, and spectral shape.

Finally, Chapter 9 presents conclusions from the research study, identifies limitations of this study, and highlights opportunities for future research.

Chapter 2: Development of M9 Ground Motions

This chapter presents an overview of the baseline and soil-adjusted M9 ground motions developed by researchers at the United States Geological Survey (USGS) and the University of Washington. The set of baseline M9 ground motions represent a range of 30 scenarios that consider various rupture and rupture propagation parameters (Frankel et. al 2018). The 30 simulated motions (referred to as the "baseline" motions), were generated for a site with a soil profile having a soil shear-wave velocity in top 30 meters, V_{S30} of 1968 ft/s (600 m/s). These motions were then adjusted to take into account the effects of a variety of soil profiles.

Section 2.1 provides the details of the 10 locations selected for detailed analyses, Section 2.2 describes the characteristics of these baseline motions, while Section 2.3 discusses the procedure used for adjusting the motions for different site classes.

2.1 LOCATIONS OF GROUND-MOTION SIMULATIONS

Ten representative locations across Western Washington were selected for study for this research. The locations of the 10 cities are shown in Figure 2.1. The cities were selected to encompass a range of distances to the fault and a range of site conditions (e.g., areas atop, and outside of, deep sedimentary basins). For each selected location, Table 2.1 gives the chosen city names, coordinates, and values of $Z_{2.5}$, which is defined as the depth to a shear-wave velocity of 2500 m/s (8200 ft/s). The parameter $Z_{2.5}$ has previously been used by ground motion modellers to characterize the presence or absence of a sedimentary basin, since basins have thick sediment deposits with lower shear-wave velocities, resulting in higher values of $Z_{2.5}$. The cities were categorized into four groups based on distance to the fault and values of $Z_{2.5}$ (as a proxy for the presence of a basin).

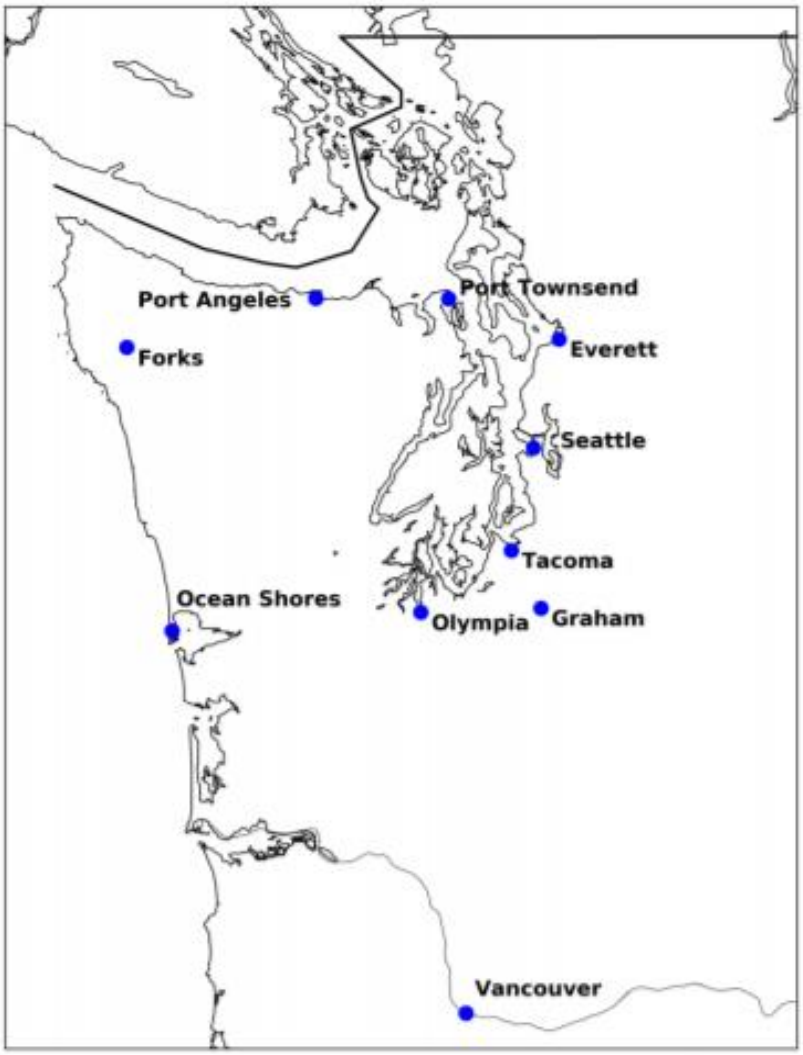

Figure 2.1. Location of the 10 cities chosen for study. (de Zamacona 2019)

City Name	Latitude	Longitude	$Z_{2.5}$ (km)	Category
Forks	47.9504	-124.3855	0.76	Coastal Outside of Basin
Ocean Shores	46.9737	-124.1563	0.98	Coastal Outside of Basin
Port Angeles	48.1181	-123.431	2.29	Inland Shallow Basin
Olympia	47.0379	-122.901	1.96	Inland Outside of Basin
Port Townsend	48.117	-122.76	2.84	Inland Shallow Basin
Vancouver	45.6272	-122.673	1.76	Inland Outside of Basin
Tacoma	47.2529	-122.444	2.86	Inland Shallow Basin
Seattle	47.6062	-122.332	6.7	Inland Deep Basin
Graham	47.0529	-122.294	0.2	Inland Outside of Basin
Everett	47.979	-122.202	3.42	Inland Deep Basin

Table 2.1. 10 selected cities. (de Zamacona 2019).

Cities were categorized according to distance from fault and $Z_{2.5}$ values. Cities with a $Z_{2.5}$ of less than 2.0 km were classified as having no basin. Cities with $Z_{2.5}$ between 2.0 and 3.0 km were classified as having a shallow basin, and cities with $Z_{2.5}$ greater than 3 were classified as having a deep basin. The basin depths used to classify each location are consistent with those of Marafi et al. (2017) where the impacts of basin depth on ground motion characteristics were studied for ground motions recorded in Japan. Using these designations, cities were grouped into four categories:

- Coastal cities (closer to fault) outside of the basin (Forks and Ocean Shores),
- Inland cities (further from fault) outside of basin (Olympia, Vancouver, and Graham),
- Inland cities on a shallow basin (Port Townsend, Port Angeles and Tacoma), and
- Inland cities on a deep basin (Seattle and Everett).

These categories are consistent with those used by de Zamacona (2019).

The Cascadia Subduction Zone model used to create the M9 ground motions made ground motion records available at 169 locations (referred to as stations below) across Washington. For each of the 10 selected cities above, ground motion records were obtained from the station closest to the city. Table 2.2 lists the stations used for each city, as well as the coordinates of each station. Ground motions from these simulations for all stations may be found at the online data repository, DesignSafe, under the citation Frankel et al. (2018).

City Location			**Nearest Station Location**		
City	**Latitude**	**Longitude**	**Station ID**	**Latitude**	**Longitude**
Forks	47.9504	-124.386	Z0FORK	47.9456	-124.566
Ocean Shores	46.9737	-124.156	Z0XOCS	46.9778	-124.154
Port Angeles	48.1181	-123.431	Z0XANG	48.1191	-123.431
Olympia	47.0379	-122.901	Z00CPW	46.9717	-123.138
Port Townsend	48.117	-122.76	Z0XTWN	48.1146	-122.756
Vancouver	45.6272	-122.673	Z0HUBA	45.6287	-122.653
Tacoma	47.2529	-122.444	Z0TBPA	47.2559	-122.368
Seattle	47.6062	-122.332	Z0XWLK	47.612	-122.338
Graham	47.0529	-122.294	Z00GHW	47.0395	-122.274
Everett	47.979	-122.202	Z0EVCC	48.0056	-122.204

Table 2.2. Selected cities and location of the nearest station (de Zamacona 2019).

2.2 BASELINE M9 GROUND MOTIONS

Figure 2.2 shows response spectra for each of the 10 cities. Spectral accelerations were calculated using the geometric mean of the 30 ground motions, and for each ground motion using the geometric mean of the two directions (North-South and East-West). The impacts of distance to the fault and presence of a basin can be clearly seen. The coastal cities, located close to the fault, have high spectral accelerations at low periods, with S_a quickly declining at higher periods. Cities located on shallow and deep basins show ground motion amplification for periods above 1 second, while inland cities without a basin have relatively low spectral accelerations.

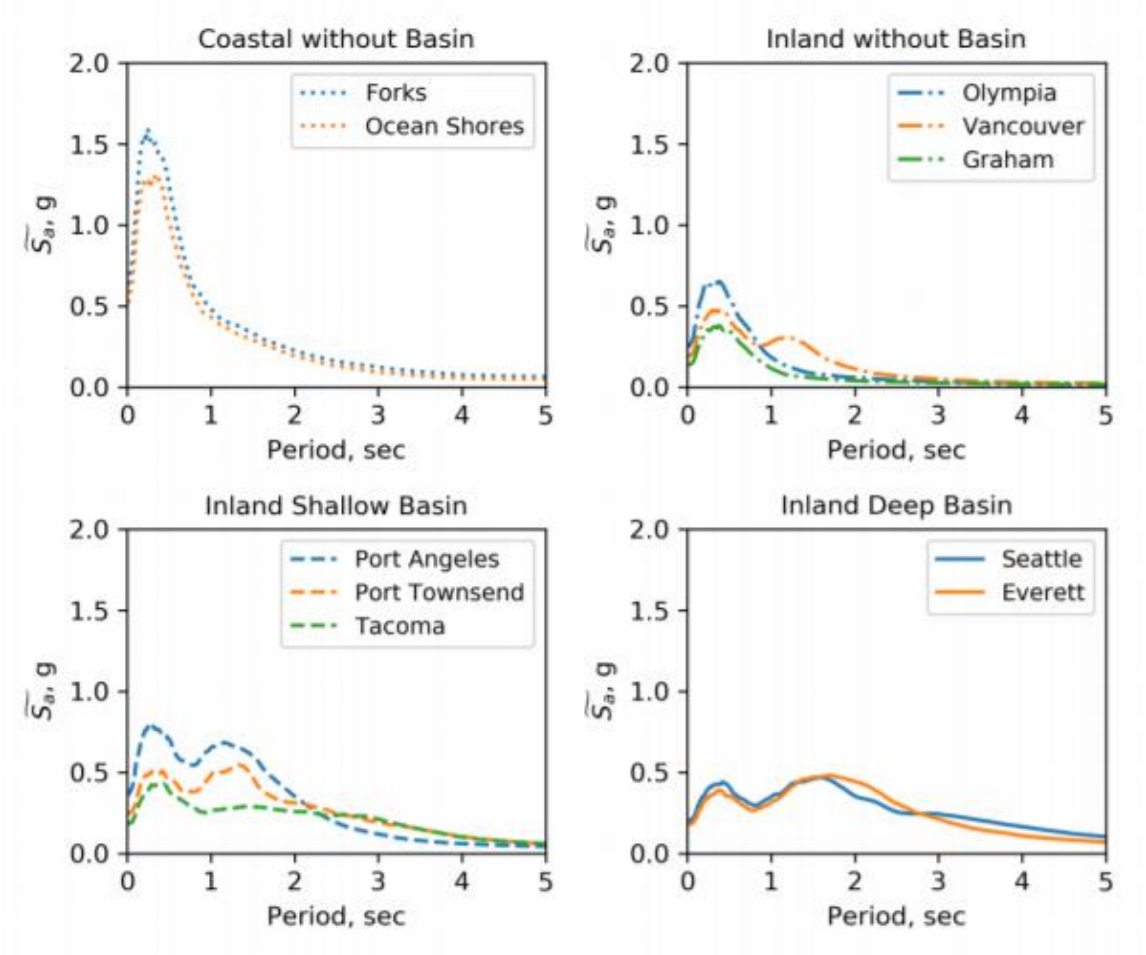

Figure 2.2. Response spectra for selected cities (de Zamacona 2019).

Figure 2.3 shows a comparison of the M9 spectral accelerations to design values obtained using AASHTO 2017 and WSDOT 2018 (calculations for design values were performed by de Zamacona 2019). Comparisons are shown for three periods: 0.2, 1.0 and 2.0 seconds. At a period of 0.2 seconds, Forks and Ocean Shores are the only cities for which the M9 spectral accelerations exceed at least one of the design values, due to these cities' close proximity to the fault. At a period of 2.0 seconds, however, all of the cities located on either deep or shallow basins (Port Angeles, Port Townsend, Tacoma, Seattle, and Everett) exceed both the AASHTO and WSDOT design accelerations due to basin effects. Seattle and Everett, located on deep basins, show especially large gaps between the design accelerations and the M9 accelerations. The five basin cities have M9 accelerations ranging from 12% to 100% higher than the AASHTO accelerations, and up to 138% higher than the WSDOT accelerations.

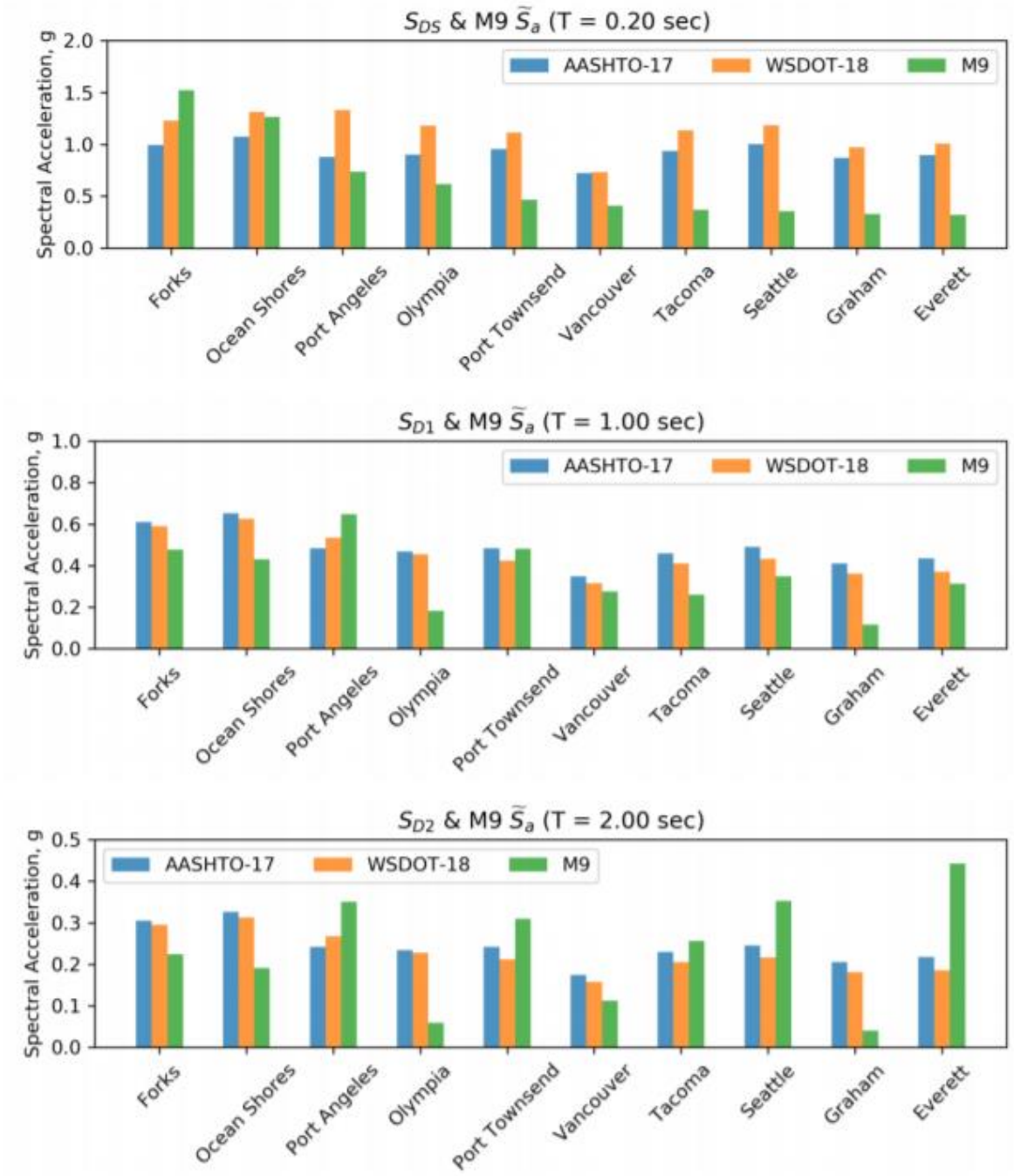

Figure 2.3. Comparison of M9 spectral accelerations to values of design S_a (de Zamacona 2019).

2.3 SOIL-ADJUSTED M9 GROUND MOTIONS

This section describes the adjustment of the baseline M9 ground motions to account for the effects of various site conditions. This process was carried out by alex grant of the United

States Geological Survey (USGS). The baseline M9 ground motions were developed for a site with a soil profile having a V_{S30} of 1968 ft/s, corresponding to NEHRP Site Class C. Figure 2.4 shows the distribution of seismic site classes for King County (the county which contains Seattle). Long portions of major highways in King County (I-5, I-90, and I-405) are located on Site Class C, D, E and F profiles. It was therefore necessary to adjust the baseline M9 motions to more accurately reflect local soil conditions in and around the Puget Sound region.

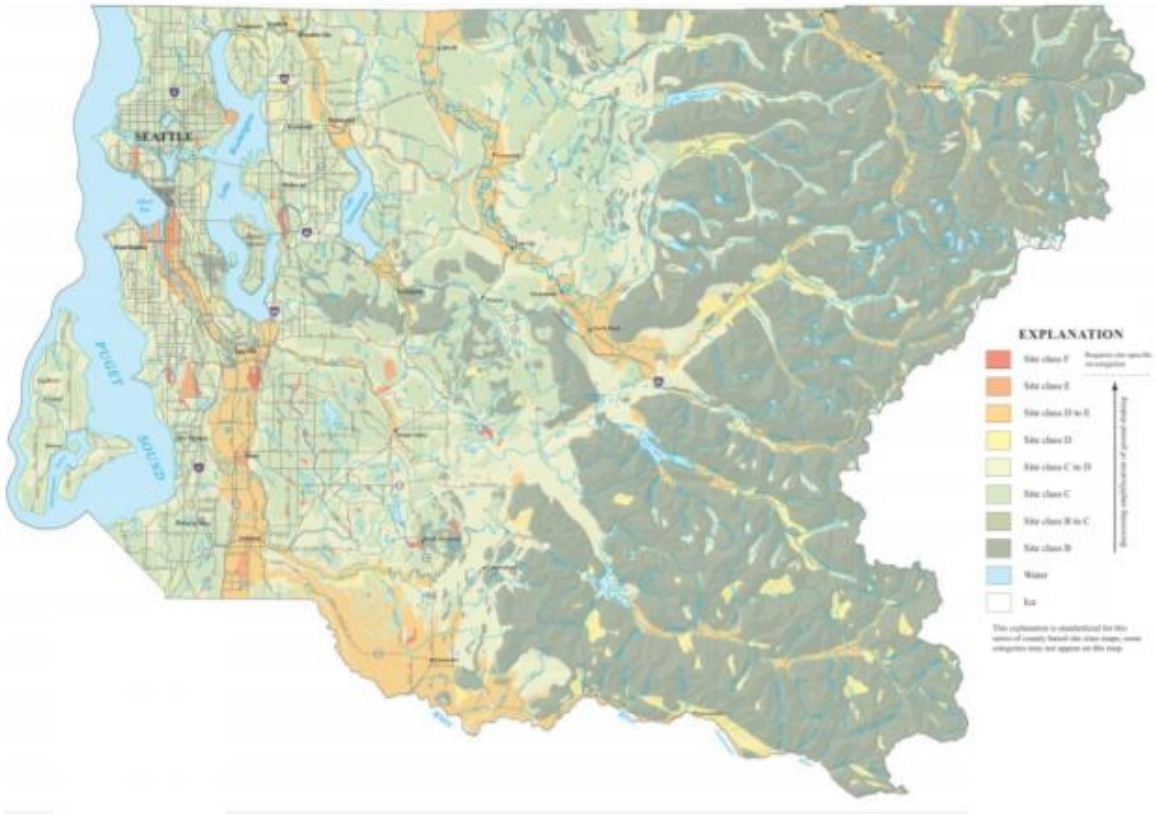

Figure 2.4. Site Class Map of King County, Washington (Palmer et al. 2007)

Using Pacific Northwest shear-wave velocity profiles from Adhi et al. (2017), soil-adjusted ground motions were produced using equivalent linear site response analysis (de Zamacona 2019). Profiles shallower than 32.8 feet or deeper than 3281 feet were removed from the dataset because of insufficient data or insufficient resolution (de Zamacona 2019). Figure 2.5 shows the soil classes and corresponding values of V_{S30} for which soil-adjusted motions were

produced. Also listed are the number of soil profiles within each site class before and after the dataset was reduced. Soil-adjusted motions were produced for both horizontal components of motion using the reduced set of profiles in the 10 cities listed in Table 2.1.

For each profile in the reduced set, the baseline M9 motions were applied to the base of the profile from a stiff linear layer with 1% damping and a V_{S30} of 1968 ft./s (de Zamacona 2019). For profiles with V_{S30} greater than 2362 ft/s, the entire profile was used and appended with a rock input base (de Zamacona 2019). The cutoff was set as 2362 ft/s in order to prevent large velocity inversions over the 1968 ft./s V_{S30} used for the baseline motions. Predicted maximum shear strains within the profiles were generally below proposed limits for judging the credibility of equivalent linear site-response analyses (e.g., Kaklamanos et al. 2013). Nonetheless, the possibility persists, for select motions at select sites, that the equivalent-linear treatment of nonlinear soil behavior could result in differences between the motions predicted by de Zamacona (2019) and studied herein, and those that might be produced using other treatments of nonlinear behavior.

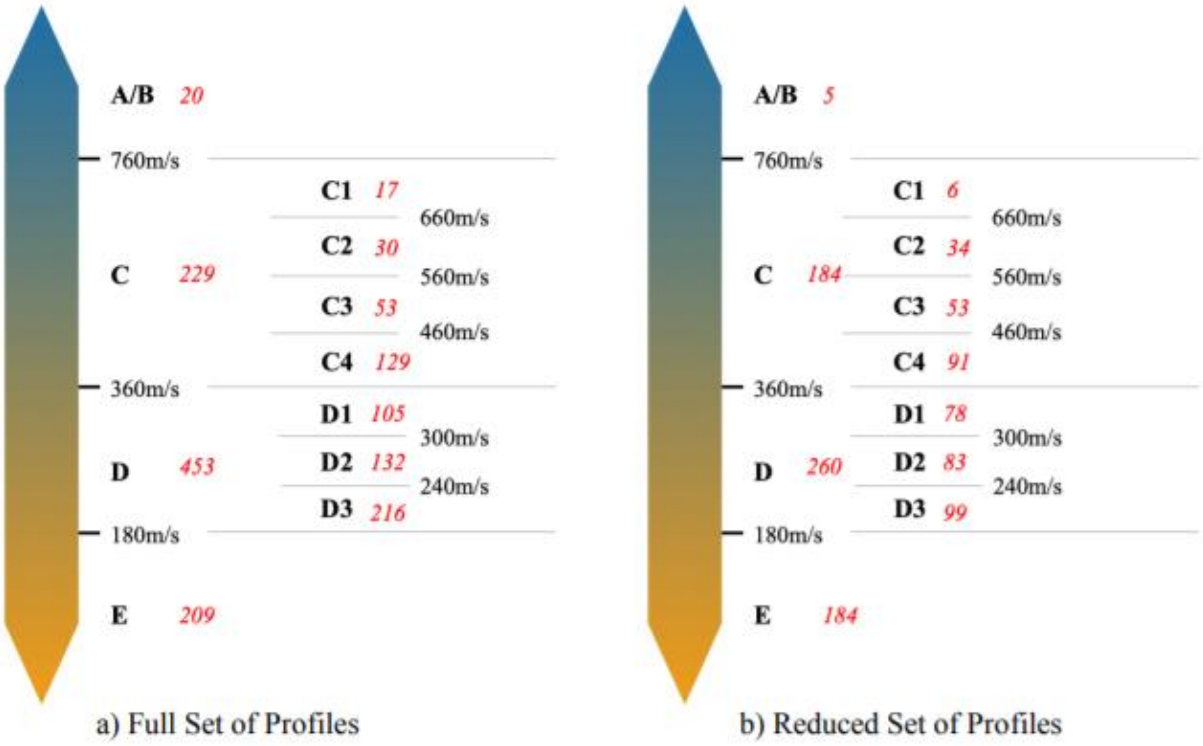

Figure 2.5 Data Available from Ahdi et al. for PNW Velocity Profiles (Figure by A. Grant)

From the site classes above, four were selected to be used in the parametric study described in Chapter 6. The four selected site classes were C2, C4, D1, and D3, chosen because the V_{S30} for these soil classes are representative of soils commonly found in the Puget Sound region. From the soil profiles available in Ahdi et al. (2017) representing each site class, 30 were randomly selected in each class for use in the parametric study. The 30 profiles chosen are listed in Table 2.3.

Soil Type			
C2	**C4**	**D1**	**D3**
WA-DNR-08_87	7026	WA-DNR-08_210	DOGAMI-13_196
WA-DNR-08_90	WA-DNR-08_69	WA-DNR-08_24	WA-DNR-08_196
WA-DNR-08_41	KIMB-1	WA-DNR-08_68	DOGAMI-13_179
SFER	WA-DNR-08_91	DOGAMI-13_255	SCPT94-1
WA-DNR-08_57	WA-DNR-08_14	DOGAMI-13_74	DOGAMI-13_233
WA-DNR-08_164	PCFR	WA-DNR-08_39	FD86-4
WA-DNR-08_161	DOGAMI-13_132	WA-DNR-08_171	DOGAMI-13_131
ALKI	WA-DNR-08_20	7041	DOGAMI-13_223
GL2	WISH	DOGAMI-13_89	SCP95-24
WA-DNR-08_85	WA-DNR-08_73	LAWT	DOGAMI-13_123
BUCK	DOGAMI-13_79	WA-DNR-08_97	WA-DNR-08_225
HAO	DOGAMI-13_146	7043	DOGAMI-13_180
LTY	WA-DNR-08_12	WA-DNR-08_172	DOGAMI-13_141
DOGAMI-13_102	WA-DNR-08_45	WA-DNR-08_165	WA-DNR-08_190
WA-DNR-08_21	WA-DNR-08_217	ROSS	FD97-5
WA-DNR-08_77	LANE	DOGAMI-13_187	WA-DNR-08_143
WA-DNR-08_231	WA-DNR-08_28	WA-DNR-08_123	WA-DNR-08_5
WA-DNR-08_3	WA-DNR-08_75	DOGAMI-13_106	DOGAMI-13_20
WA-DNR-08_26	WA-DNR-08_187	DOGAMI-13_78	DOGAMI-13_38
BEVT	MRIN	WA-DNR-08_121	WA-DNR-08_232
WA-DNR-08_62	DOGAMI-13_76	WA-DNR-08_65	DOGAMI-13_181
WA-DNR-08_128	WA-DNR-08_175	WA-DNR-08_129	DOGAMI-13_98
WA-DNR-08_176	WA-DNR-08_219	WA-DNR-08_33	DOGAMI-13_31
WA-DNR-08_44	WA-DNR-08_81	WA-DNR-08_208	DOGAMI-13_28
WA-DNR-08_36	DOGAMI-13_114	7027-A	WA-DNR-08_46
WA-DNR-08_6	WA-DNR-08_83	DOGAMI-13_164	WA-DNR-08_199
LYNC	7034	DOGAMI-13_150	WA-DNR-08_115
WA-DNR-08_18	QKTN	2172	WA-DNR-08_234
ERW	WA-DNR-08_151	WA-DNR-08_169	DOGAMI-13_64
BH_DEEPBH	SEW	WA-DNR-08_48	KNEL

Table 2.3. List of selected soil profiles within each soil class.

Figure 2.6 shows the median spectral accelerations for the 30 baseline and soil-adjusted M9 ground motions in both horizontal directions, using the 30 selected soil profiles within each soil subclass (C4, C4, D1, D3). Results are shown for one city from each of the categories described above. Complete results for all cities can be found in Appendix A. Figure 2.6 also shows the ratio of the spectral accelerations for each site class to the spectral acceleration of the baseline ground motions.

For all of the cities, Site Class C2 had spectral accelerations closest to the baseline ground motions, because the V_{S30} value used to develop the baseline motions was close to the V_{S30} value for site class C2. Site class D3, the softest soil considered, had the largest spectral accelerations at high periods, but tended to deamplify the motions at periods less than about 0.5 seconds. At very long periods, motions for all four site classes begin to converge to the same spectral accelerations as the baseline motions. This occurs because the soils trend toward rigid-body behavior at long periods, regardless of the stiffness of the soil.

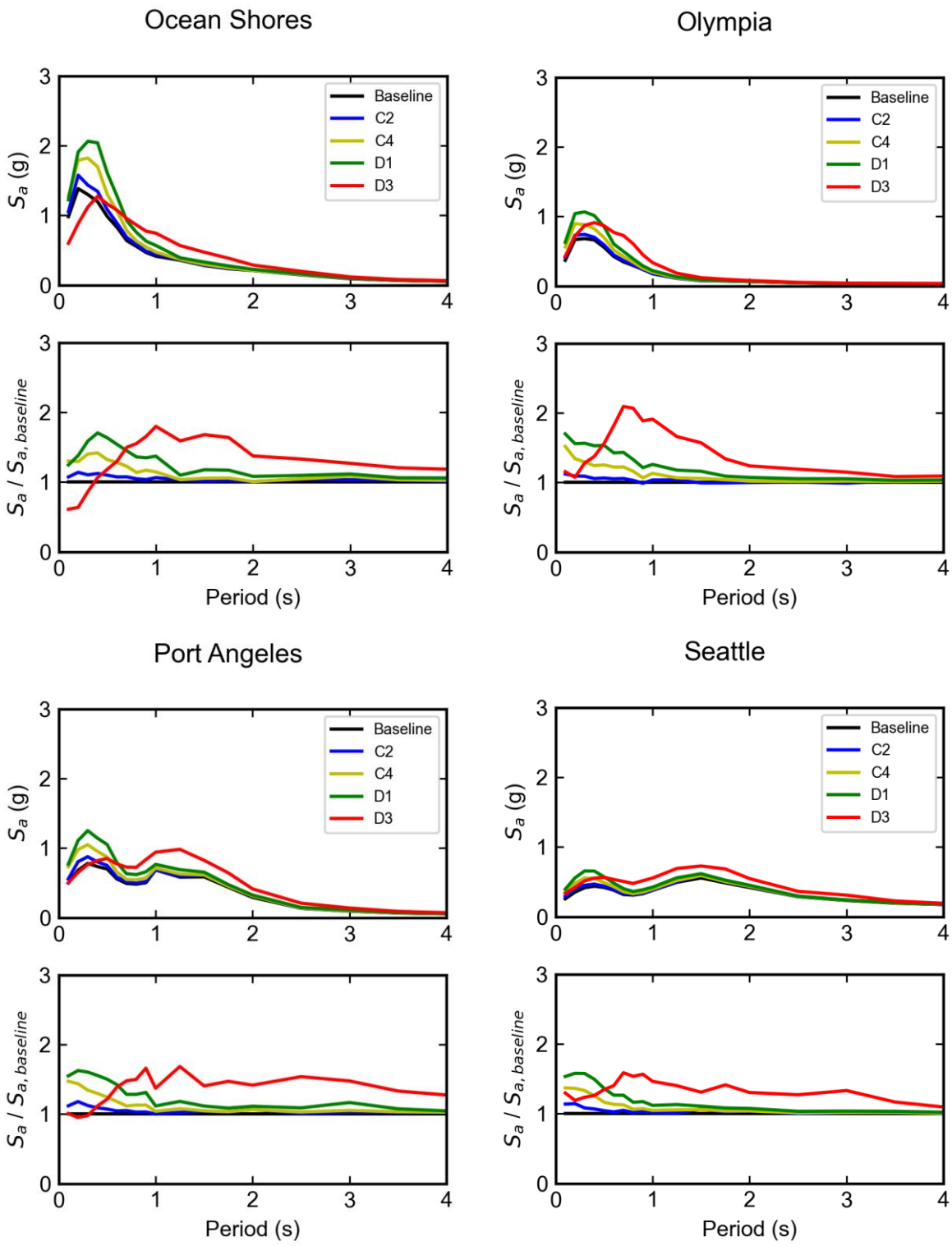

Figure 2.6. Median spectral accelerations for the baseline and soil-adjusted M9 motions.

Chapter 3: WSDOT Bridge Database

Engineers at the Washington Department of Transportation (WSDOT) identified several "lifeline" routes that could be used to carry supplies and emergency personnel into Seattle in the event of an M9 earthquake. These lifeline routes include: I-90 between Seattle and Snoqualmie Pass, I-5 between Tacoma and Everett, I-405, State Route 512, and State Route 167 (Fig 3.1). For each bridge on the lifelines, WSDOT then compiled detailed structural information from the structural plans.

This chapter presents a summary of the bridge properties in this database. The extrapolation of this data to the properties (i.e., mass and stiffness) of single-degree-of-freedom systems is discussed in Chapter 4. The goal of analyzing the compiled data is to understand the key characteristics of the bridges along the lifeline routes to inform the modeling described in subsequent chapters.

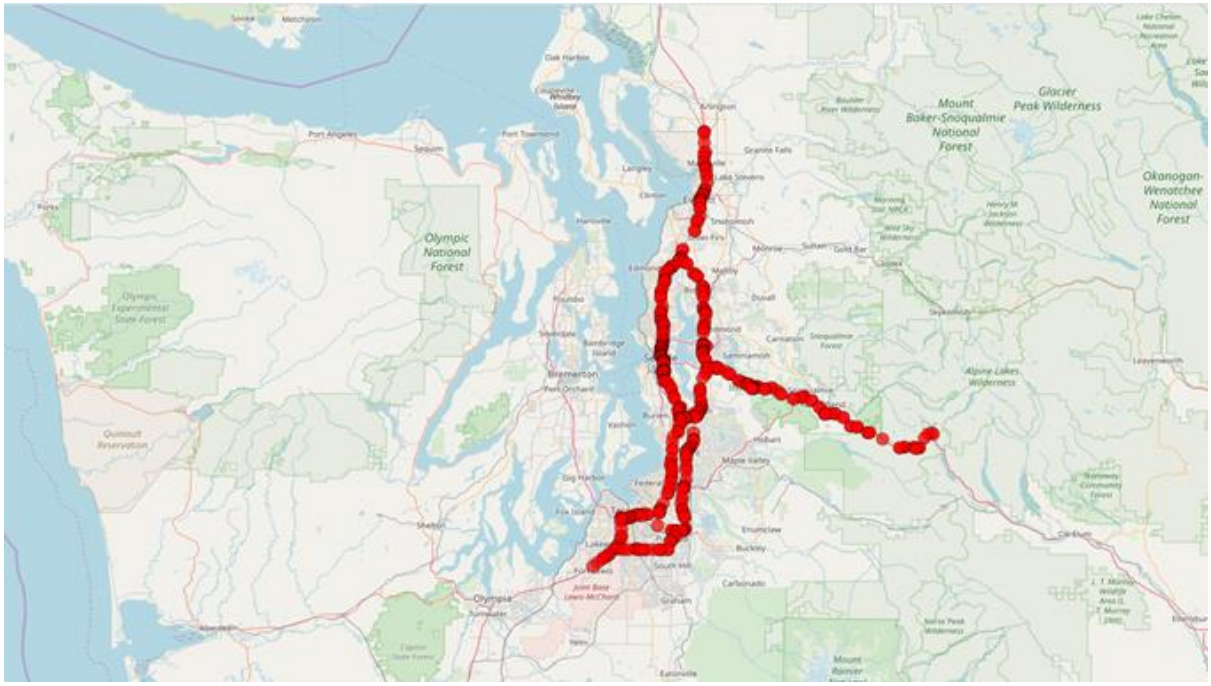

Fig. 3.1. Locations of lifeline bridges

The WSDOT bridge database contains detailed structural information for 609 highway bridges along the identified lifelines. For each bridge in the database, WSDOT compiled information including year of construction, superstructure type, column dimensions, transverse and longitudinal reinforcement, span lengths, and a variety of other characteristics. The database did not include any information on bridge abutments, and contained only limited information on bridge foundations. For bridges supported by columns, column properties were provided for only the tallest and shortest column on the bridge. Summary statistics for a number of important bridge parameters are discussed in the following sections.

3.1 YEAR OF CONSTRUCTION

Bridges in the database ranged in year of construction from 1900 to 2018, with the largest number (410, 67%) of bridges having been built between 1960 and 1975 (Fig 3.2). Earthquake design codes for bridges changed significantly in Washington State in about 1976 following the 1971 San Fernando earthquake. About three quarters of the documented lifeline bridges (480) were constructed before 1976. Only 69 bridges (11%) in the database were built after 2000.

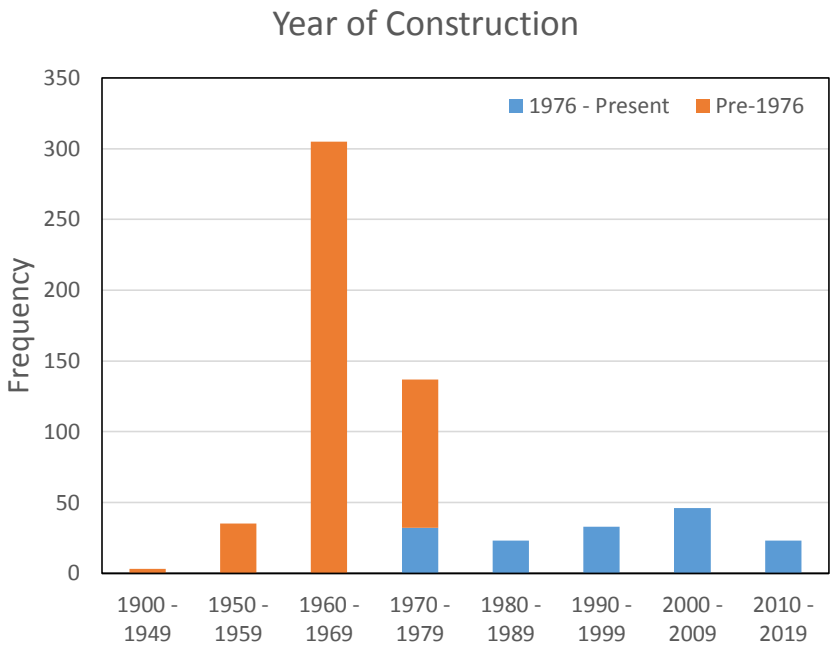

Fig. 3.2. Bridge Year of Construction.

3.2 BRIDGE SUBSTRUCTURE PROPERTIES

3.2.1 Substructure Type

Substructure type is an important parameter for understanding the seismic safety of bridges. If deck unseating has been mitigated, column damage is the next most important consideration in addressing bridge seismic safety. Of the 609 bridges, 415 (~70%) are supported by at least one column, with 101 bridges supported by single-column bents and 314 bridges supported by multi-column bents (Fig. 3.3). Small numbers of bridges are supported by pier walls (48 bridges), piles (40 bridges), or consist of a single span (74 bridges).

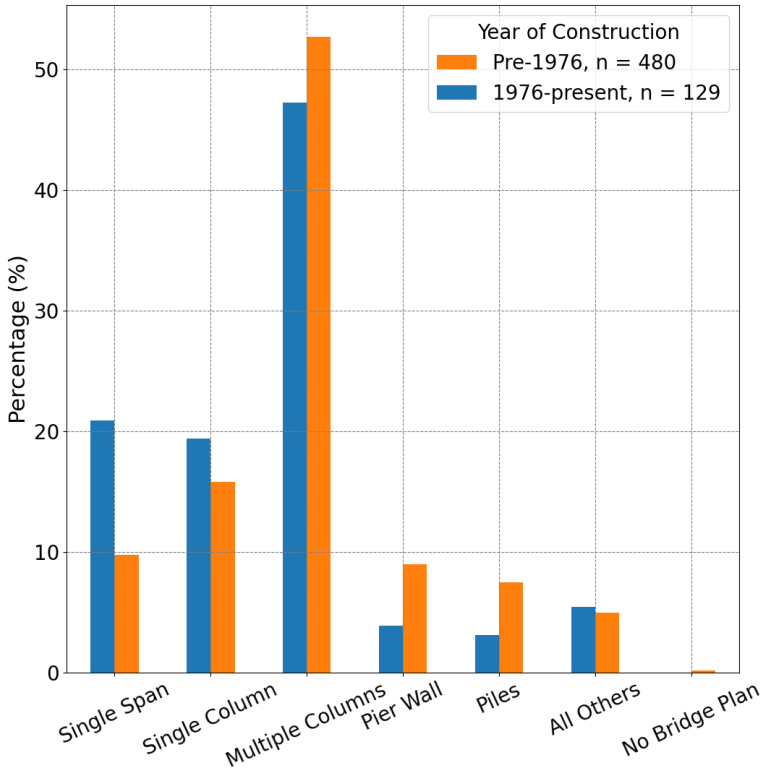

Fig. 3.3. Bridge Substructure Types. Credit: Kan-Jen Liu.

3.2.2 Column Lengths

The WSDOT lifeline database provided column heights for only the shortest and tallest column on each bridge. This data is summarized below (Fig. 3.4). Shortest column heights generally ranged from 15 to 25 feet for both new and old bridges, with 70% of the shortest columns falling in this range. The tallest columns varied in height more but are generally less than 35 feet, with only 25% of the tallest columns exceeding this height.

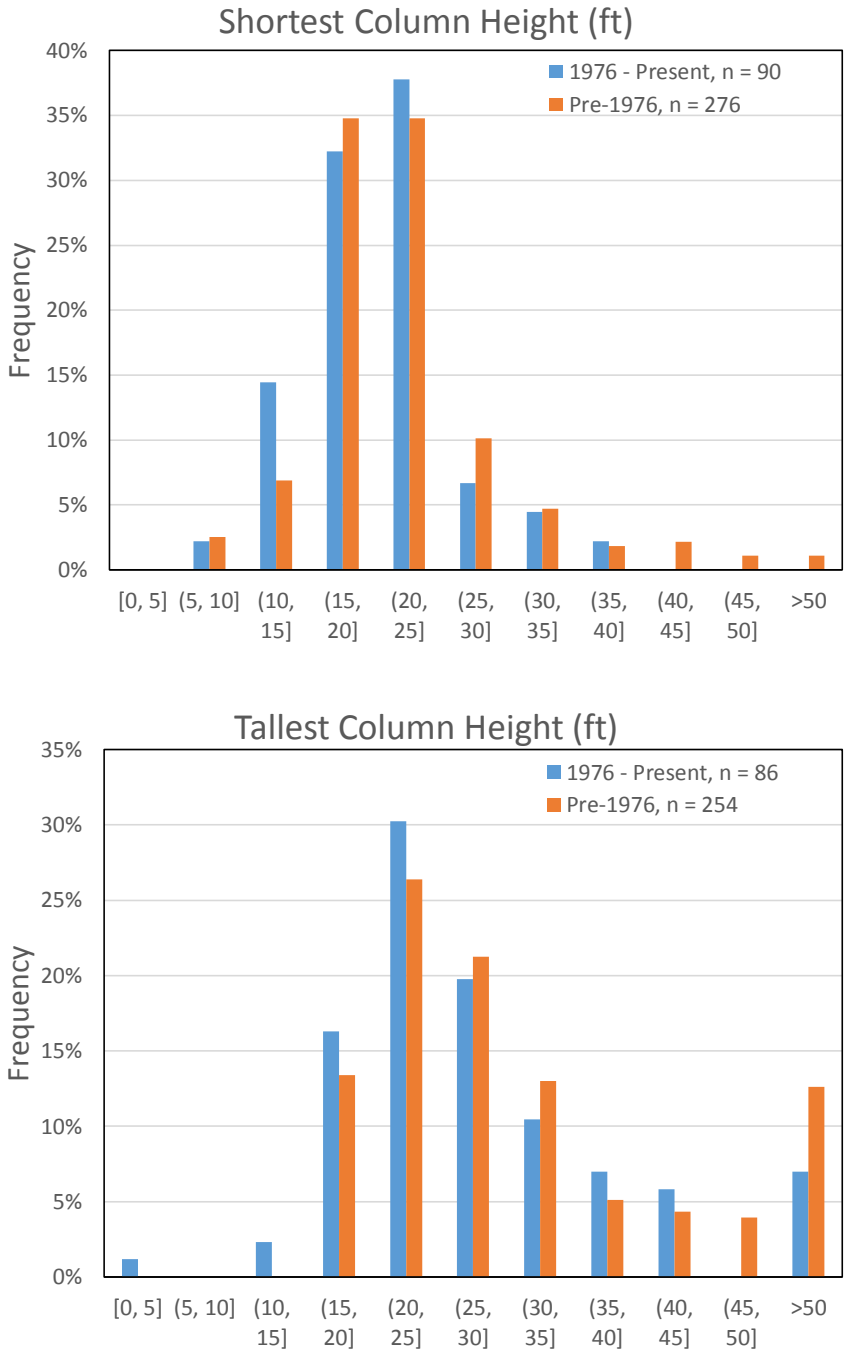

Fig. 3.4. Bridge Column Lengths.

3.2.3 Column Longitudinal Reinforcement Ratio

For each bridge in the database, WSDOT reported reinforcement information for only the shortest and tallest columns on the bridge. Longitudinal reinforcement ratios are reported below

for the shortest column (Fig 3.5). The longitudinal reinforcement ratio was computed as the total area of longitudinal reinforcement, normalized by the gross-section area of the column. Though reinforcement ratios vary widely, the majority (70%) of the ratios for the bridge columns fall between 1% and 2.5% longitudinal reinforcement for both new and old bridges. Further, it does not appear that longitudinal reinforcement ratio varies significantly between old (pre 1976) and new (1976 to present) bridge columns.

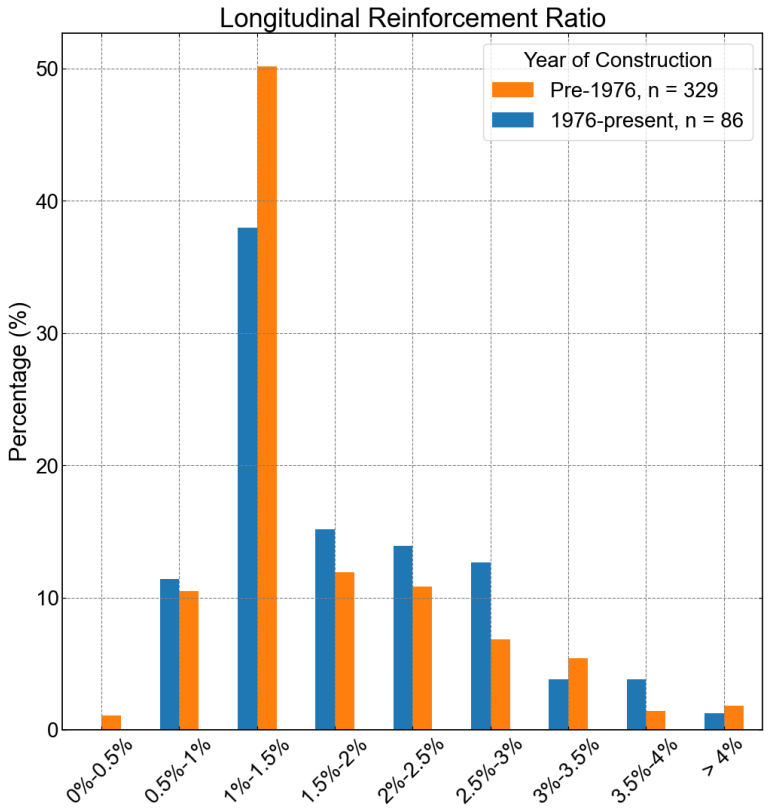

Fig. 3.5. Longitudinal reinforcement ratios for shortest bridge columns. Credit: Kan-Jen Liu.

3.2.4 Column Transverse Reinforcement Ratios

Transverse reinforcement ratios are reported below for the shortest column, separated by "old" (pre-1976) and "new" (1976-present) column categories (Fig 3.6). Transverse reinforcement ratio was calculated as the ratio of the volume of the transverse bars to the volume of the confined concrete core, with the confined core extending to the centerline of the transverse

reinforcement bars. In general, older bridges tend to have significantly lower transverse reinforcement ratios than newer bridges, with 79% of old bridges falling below 0.5% transverse reinforcement, compared to only 9% of new bridges. New bridges have a wide range of transverse reinforcement ratios, but peak around 1.5 - 2.0%.

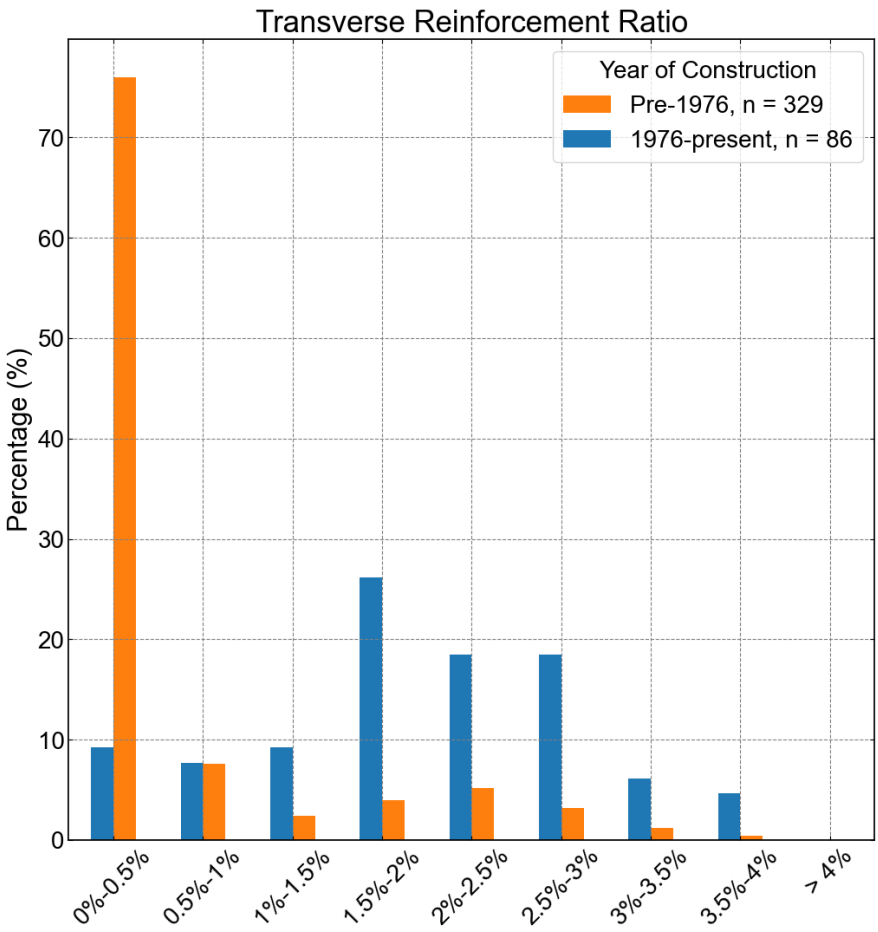

Fig. 3.6. Transverse reinforcement ratios for shortest bridge columns. Credit: Kan-Jen Liu.

3.2.5 Axial-Load Ratios

For 32 bridges in the database, WSDOT provided axial-load ratios for either the tallest column, the shortest column, or both, for a total of 45 columns. Although data is limited, the calculated axial load ratios are generally close to 5% for most of the bridges for which information is provided (Fig 3.7).

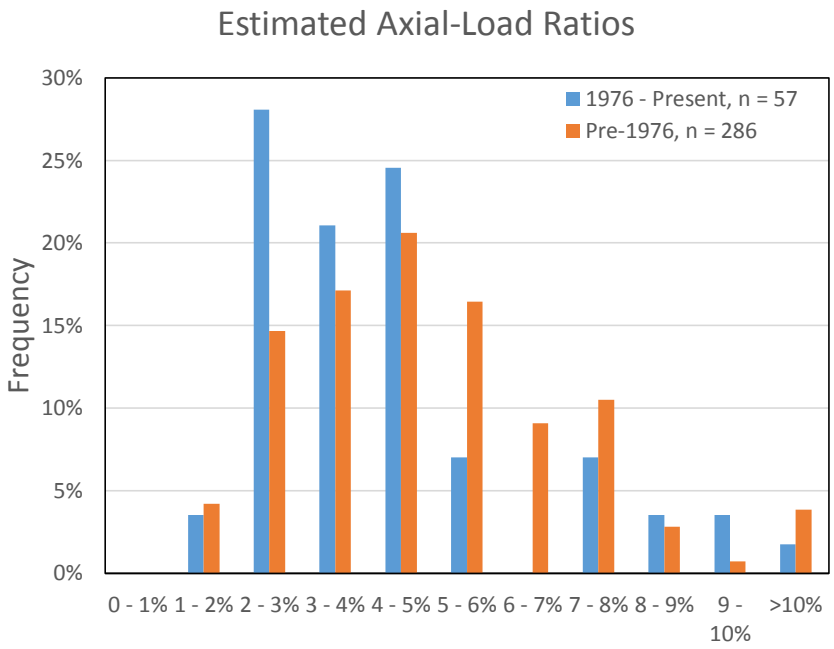

Fig. 3.7. Axial-load ratios for bridge columns

3.3 BRIDGE SUPERSTRUCTURE PROPERTIES

3.3.1 Superstructure Type

Bridges in the database had a diverse array of superstructure types. The three most common by far, however, were prestressed girders (277), box girders (132), and slabs (73). Non-prestressed girders (26) and a variety of miscellaneous types (101) accounted for the remainder of the bridge superstructures (Fig. 3.8).

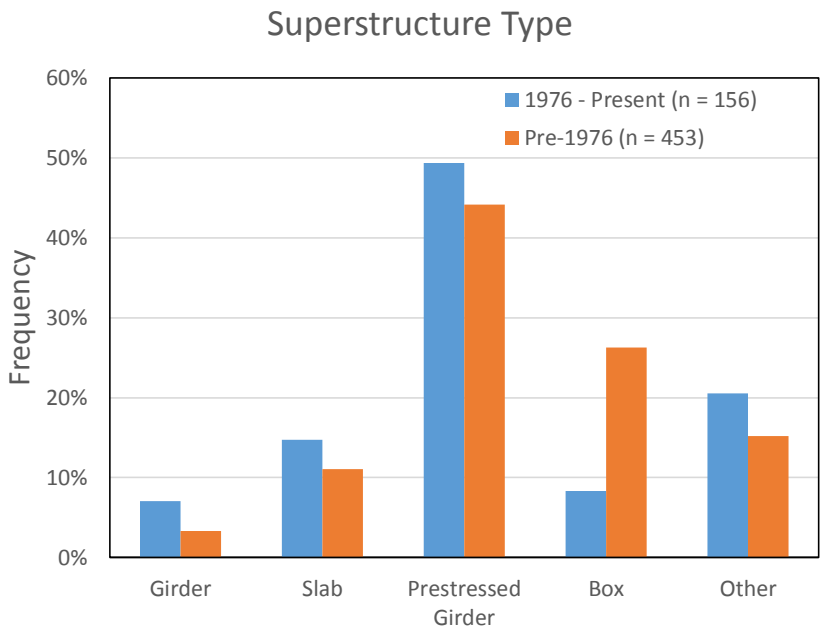

Fig 3.8. Bridge Superstructure Types

3.3.2 Span Lengths

Span lengths in the database were reported for the shortest span and longest span for each bridge (Fig. 3.9). 60% of shortest spans fall between 25 and 50 feet, with only 19% of shortest spans exceeding 100 feet. The longest span on new bridges tends to be slightly longer than on older bridges, with a mean longest span of 113 feet for new bridges vs 96 feet for old.

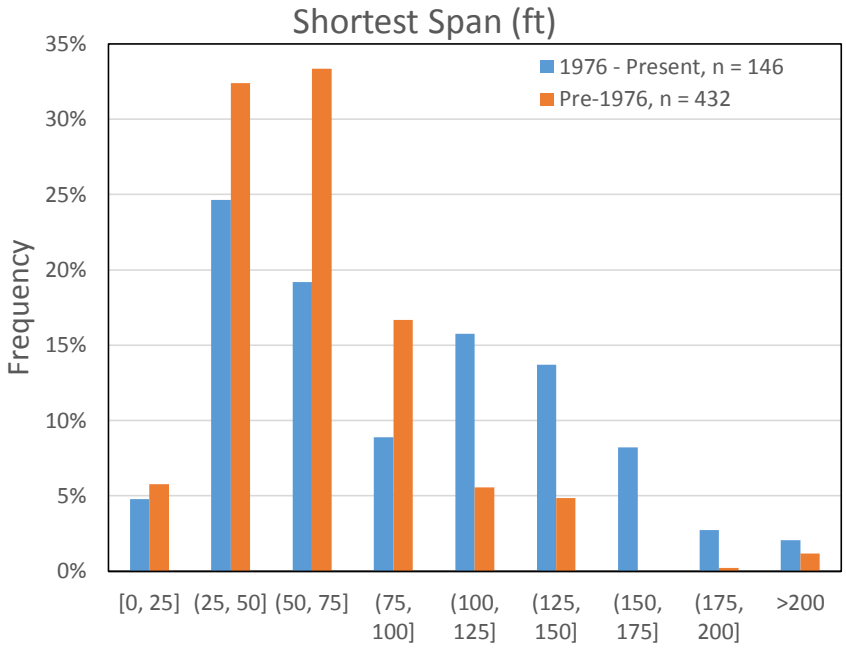

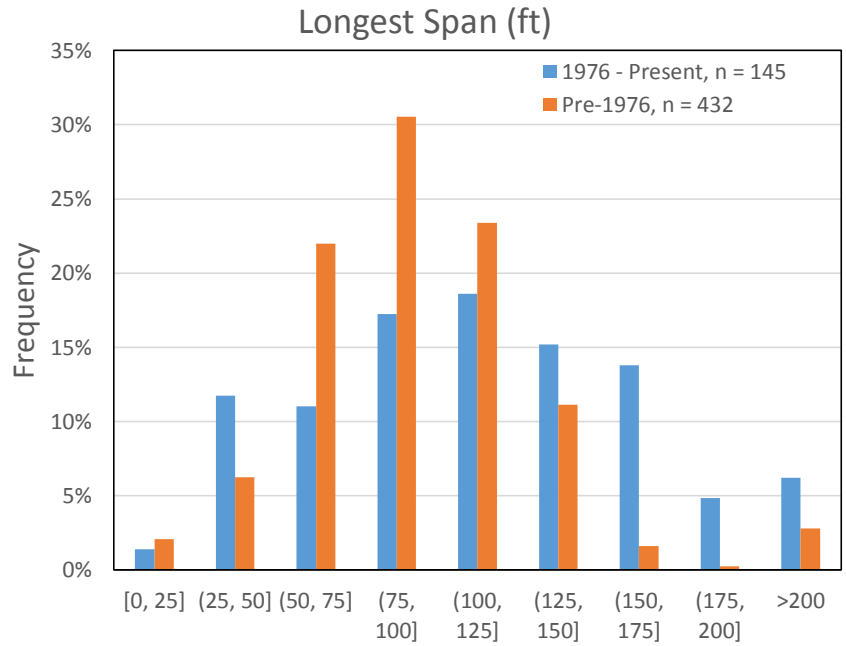

Fig. 3.9 Bridge Shortest and Longest Span Lengths

3.3.3 Number of Spans

Nearly 40% of the bridges in the lifeline database have 3 spans, making this the most common bridge configuration by far (Fig. 3.10). Few bridges exceed 5 spans (17%). Newer

bridges are somewhat more likely to be single span than older bridges (29% vs 8%) but the distributions are otherwise similar.

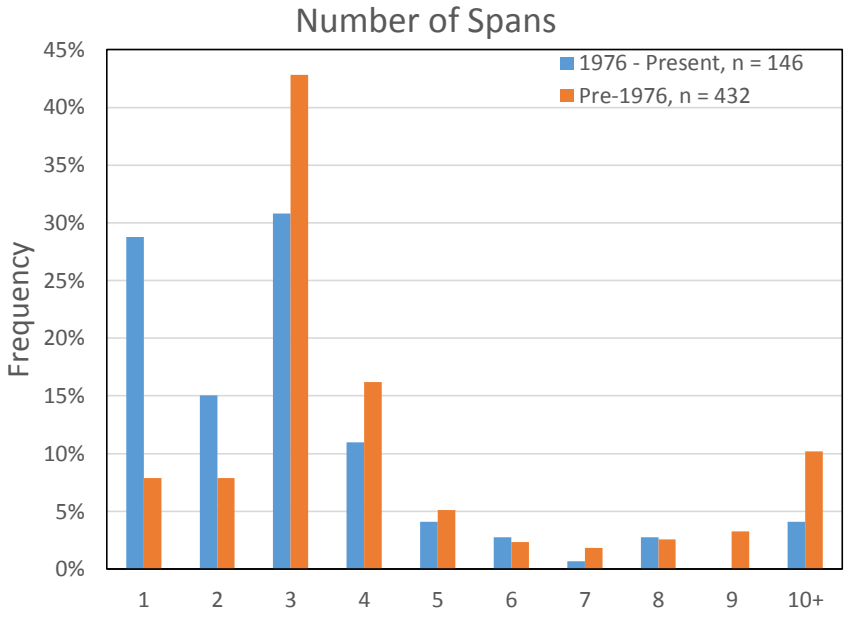

Fig. 3.10. Number of Spans

Chapter 4: Periods and Strengths of SDOF Bridge Models

This chapter discusses the use of the WSDOT bridge database (Chapter 3) to develop the periods and strengths of the single-degree-of-freedom (SDOF) bridge models used to conduct the parametric study (Chapter 6). The SDOF models were developed to account for the resistance of the bridge columns, neglecting the contributions of the abutments. Detailed review of drawings of representative bridges were used to develop relationships between the database properties and the bridge mass (Section 4.1), equivalent column length (Section 4.2) and lateral stiffness (Section 4.3). These properties were then used to estimate the effective period and yield strength, while neglecting the contribution of abutments. This data was used to characterize equations for bridge strength as a function of period, and the resulting strength curves were used to characterize the SDOF oscillators.

4.1 BRIDGE WEIGHT

For each of the three most common bridge superstructure types in the database (prestressed girder, slab, and box), five representative bridges were selected from the database (Fig. 3.8). The selected bridges encompass a range of ages and span lengths to account for possible variations in bridge design. For each of these five bridges, detailed bridge structural plans (obtained from the WSDOT Bridge Engineering Information System (BEISt)) were used to calculate the total bridge weight (excluding the columns), assuming a unit weight of 150 lb/ft^3 for the concrete. This bridge weight calculation accounted for the weight of the deck, sidewalks, traffic barriers, girders, cap beams and cross beams, but did not include the weight of the columns. The weights of the columns were excluded from this estimate, because the bridge

database contains column dimensions, so column weights can be computed separately for each bridge and added to the estimated superstructure mass (See Table 4.1 for the selected bridges).

Bridge Number	Superstructure Type	Longest Span (ft)	Estimated Weight (kip)	Weight/ Deck Area (kip/ft^2)
5/421	Box	136	3142	0.36
5/461	Box	112	4441	0.35
405/10S-N	Box	91	1591	0.31
5/544	Box	96	7781	0.31
5/547	Box	116	5259	0.32
5/426A	Slab	54	1810	0.38
512/11	Slab	67	1370	0.36
5/462E	Slab	30	1236	0.20
5/536N-E	Slab	49	6181	0.28
5/538E-N	Slab	42	2990	0.29
5/421A	PG	64	378	0.13
5/519E	PG	104	8532	0.22
405/10A	PG	108	4697	0.25
5/520E-S	PG	140	2028	0.29
5/437NCD	PG	85	4130	0.24

Table 4.1. Selected bridges and calculated weights.

Total superstructure mass for each bridge was normalized by deck area and plotted against the bridge's longest span. Longest span was chosen because longer spans will, in general, require deeper and therefore heavier superstructures. For the three superstructure types chosen, a

line was fit to the normalized weight vs longest span (Fig. 4.1). As expected, for each superstructure type, the normalized mass increased with increasing span length for all three superstructure types. As expected, the slab bridges were most common for short spans (e.g., < 60 ft), and this superstructure type had the highest normalized weight. The girder and box superstructure bridges predominated for longer spans and had similar normalized weights.

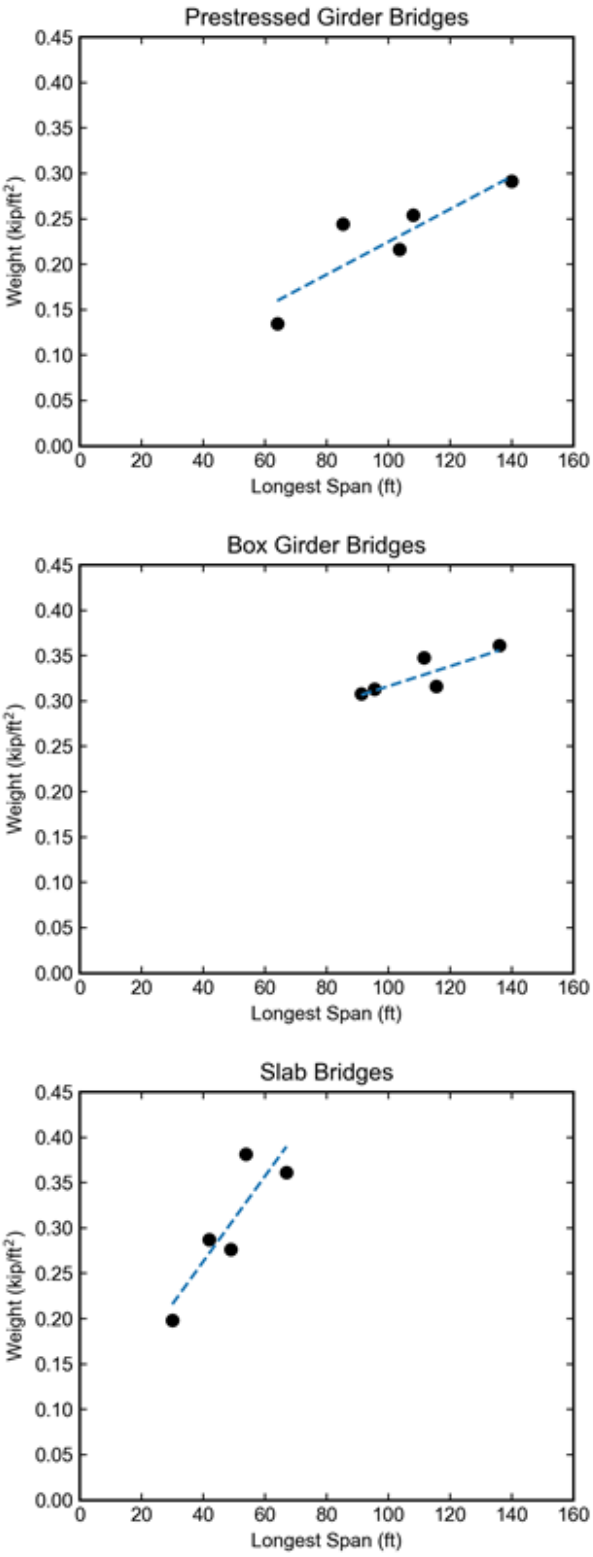

Fig. 4.1. Calculated bridge superstructure mass for the three most common superstructure types in the WSDOT database

The equations for the calculated trendlines are:

$$\text{Box: } W_{norm} = 0.0011 \cdot L_{span} + 0.21 \quad \text{(eq. 4-1)}$$

$$\text{Slab: } W_{norm} = 0.0047 \cdot L_{span} + 0.07 \quad \text{(eq. 4-2)}$$

$$\text{Prestressed Girder: } W_{norm} = 0.0018 \cdot \text{Span} + 0.04 \quad \text{(eq. 4-3)}$$

W_{norm} is the total weight of the superstructure normalized by the deck area, and L_{span} is the length of the longest span on the bridge. The weights for the remaining bridges in the database were estimated using the trendlines shown above, which made it possible to rapidly estimate the weights for the hundreds of bridges in the database without reviewing their structural drawings. Bridges not using the three superstructure types above were not included in weight calculations. For each bridge, axial load ratios were then calculated for the shortest and tallest column. Axial-load ratio was calculated as:

$$ALR = P / (A_g \cdot f'_c \cdot 1.5) \quad \text{(eq. 4-4)}$$

P is the axial load, A_g is the column gross cross-sectional area, and f'_c is the specified concrete compressive strength, multiplied by a factor of 1.5 to account for increased concrete strength with age. To calculate axial load ratios, it was assumed that a portion of the mass (corresponding to half the mass of the shortest span plus half the mass of the longest span for 2 span bridges, or the full mass of the shortest span for bridges with more than 2 spans) was supported by the abutments and the remaining mass was evenly distributed among the columns.

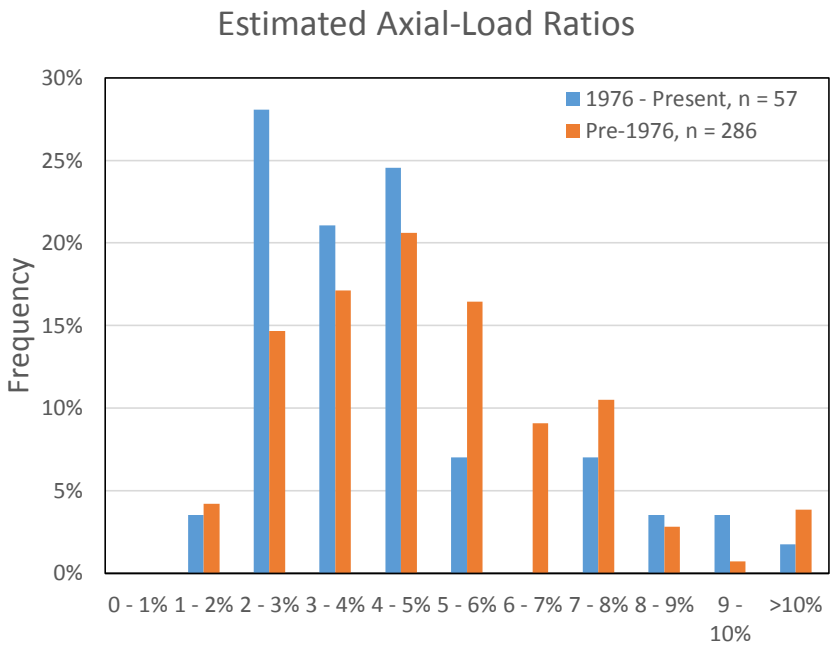

Fig. 4.2. Estimated axial-load ratios for the bridge database

The estimated axial-load ratios range from 1% to as high as 17% (Fig. 4.2), with a median value of 4.5%. The subset of 32 bridges for which WSDOT provided axial load ratios had ratios that ranged from 1% to around 15% (see Figure 3.7), with a median value of 4.7%. The consistency of these two calculations suggests that the algorithm used to estimate axial-load ratios provides a reasonable approximation of the actual axial loads for the bridges in the database.

4.2 COLUMN WEIGHTING FACTOR AND EFFECTIVE COLUMN LENGTH

In order to calculate the total lateral stiffness and strength provided by the columns of a bridge, it is necessary to estimate column properties that represent the contribution of every column on the bridge. However, the WSDOT database contains reinforcement information and column sizes for only the tallest and shortest columns on each bridge, as well as the total number of columns. It was therefore necessary to estimate the lateral stiffness and strength of the bridge

using only the shortest and tallest column properties. This section presents the development of two factors that were used to make these estimates: a column weighting factor, alpha (□), and effective length (L_{eff}).

4.2.1 Column Weighting Factor

To estimate a representative column length for a bridge, it was necessary to estimate the extent to which the bridge columns were more similar to the short columns or the long columns. The column weighting factor, alpha (□), is defined as the proportion of columns on the bridge that will be treated as having properties of the shortest bridge column, where $0 < \square < 1$. In other words, if □ = 0.5, then half the columns will be treated as "short" columns, and half will be treated as "tall" columns, using the reinforcement ratios and column sizes given in the database for a bridge's shortest and tallest columns. Using the □ factor, the total lateral strength and stiffness of a given bridge can be calculated as:

$$F_{y,bridge} = numCols \cdot [\square \cdot F_{y,short} + (1 - \square) \cdot F_{y,tall}] \quad \text{(eq. 4-5)}$$

$$K_{bridge} = numCols \cdot [\square \cdot K_{short} + (1 - \square) \cdot K_{tall}] \quad \text{(eq. 4-6)}$$

$F_{y,short}$ and K_{short} are the calculated strength and stiffness of the shortest column on the bridge, and numCols is the total number of columns on the bridge. The □ factor was calibrated for each bridge using the concept of effective column length.

4.2.2 Effective Column Length

Consider a bridge that has several columns with identical cross-sections but varying lengths along the length of the bridge. Now consider a bridge with the same number of columns, but all of equal length. The effective column length, L_{eff}, is defined as the column length for the

second bridge that would result in the second bridge having the same lateral stiffness as the first. L_{eff} can be expressed as:

$$1 / L^3_{eff} = \Sigma\ 1/ L_i^3 \qquad \text{(eq. 4-7)}$$

L_i is the length of the i-th column on a given bridge. For a subset of 202 bridges in the bridge database, WSDOT provided column lengths for every column on the bridge. For each bridge in this subset, L_{eff} was calculated according to Equation 4-7. It was then possible to calculate a "predicted L_{eff}" using the shortest and tallest columns and the column weighting factor □:

$$1 / L^3_{eff,predicted} = □ / L^3_{short} + (1 - □) / L^3_{tall} \qquad \text{(eq. 4-8)}$$

For a simple case, a bridge with two piers that have one column each, □ = 0.5 will give an exact match between L_{eff} and $L_{eff,predicted}$. Indeed, for the entire subset of bridges, it can be seen that for the bridges with two piers, □ = 0.5 gives an extremely good fit (Fig. 4.3). In this case the algorithm essentially assumes that the column heights are the same within each pier.

Values of □ were calibrated for 83 bridges with 2 piers, 37 bridges with 3 piers, and 65 bridges with 4 or more piers (this is less than the 202 bridges for which all column lengths were provided, because a small number of bridges were missing span lengths in the database). As the number of piers increases the relative contribution to stiffness provided by the shorter columns (usually near the end of the bridges) decreases, so □ decreases. For larger numbers of intermediate piers, the scatter increases, but the calibrated values of □ still provide an excellent fit between calculated and predicted values of L_{eff}. Using the calculated L_{eff} values for each bridge in the subset, □ is calibrated for bridges with 2, 3, and 4+ intermediate piers. Alpha was calculated as 0.5, 0.4, and 0.33 for bridges with 2, 3, and 4+ piers, respectively. These values of □ were subsequently used to calculate total lateral stiffness and strength as in equations 4-5 and 4-6.

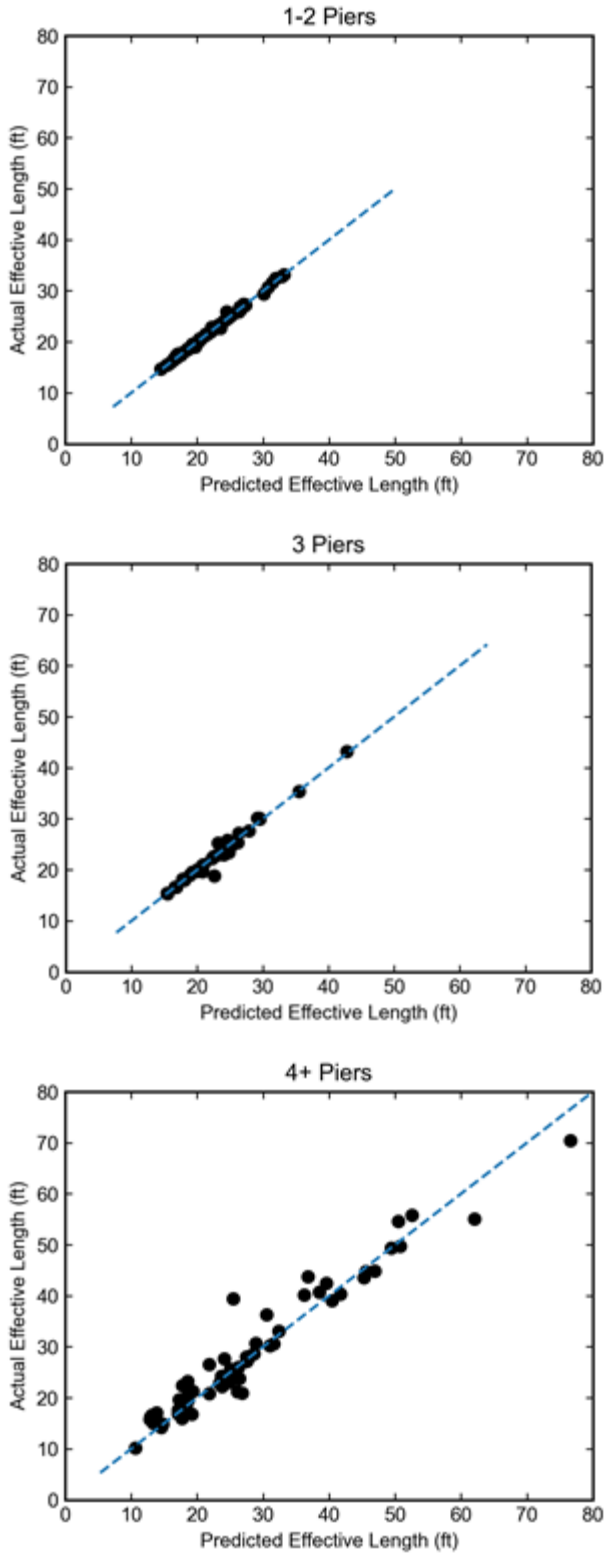

Fig. 4.3. Actual effective length vs. predicted effective length using calibrated values of α for various numbers of piers.

4.3 STIFFNESS ESTIMATES

Individual column stiffnesses were calculated using the effective column stiffness at yield described by Elwood and Eberhard (2009). This effective column stiffness was derived from a three-component model that takes into account the column flexural, shear, and bond slip flexibilities. The effective stiffness was calculated using the following equation from Elwood and Eberhard:

$$\frac{EI_{eff,calc}}{EI_g} = \frac{0.45 + 2.5P/A_g f_c'}{1+110(\frac{d_b}{D})(\frac{D}{a})} \leq 1.0 \; and \; \geq 0.2 \qquad \text{(Eq. 4-9)}$$

P is the column axial load, A_g is the column gross cross-sectional area, f'_c is the nominal concrete compressive strength, d_b is the nominal diameter of longitudinal bars, *D* is the column diameter, and a is the shear span.

The effective column stiffness at yield was calculated using the properties in the bridge database for the shortest and tallest columns on each bridge. Column stiffness was calculated first assuming fixed-fixed boundary conditions, and then assuming fixed-pinned conditions in order to bound the effects of bridge shaking in the transverse vs. longitudinal direction. Corresponding boundary conditions were assumed when computing strength. The total lateral stiffness for each bridge in the database was then calculated using the □ factors and the individual column stiffnesses as described in Equation 4-6.

4.4 PERIOD ESTIMATES

From the above estimates for stiffness and weight, the natural period was calculated for bridges with columns in the lifeline database. Periods were calculated using both fixed-fixed and fixed-pinned boundary conditions. For the fixed-fixed condition, most bridges (70%) fall between a period of 0.25 seconds and 0.75 seconds, and only 12% exceed a period of 1.0

seconds (Fig. 4.4). The fixed-pinned condition had higher periods, with the largest number (51%) falling between 0.75 seconds and 1.25 seconds.

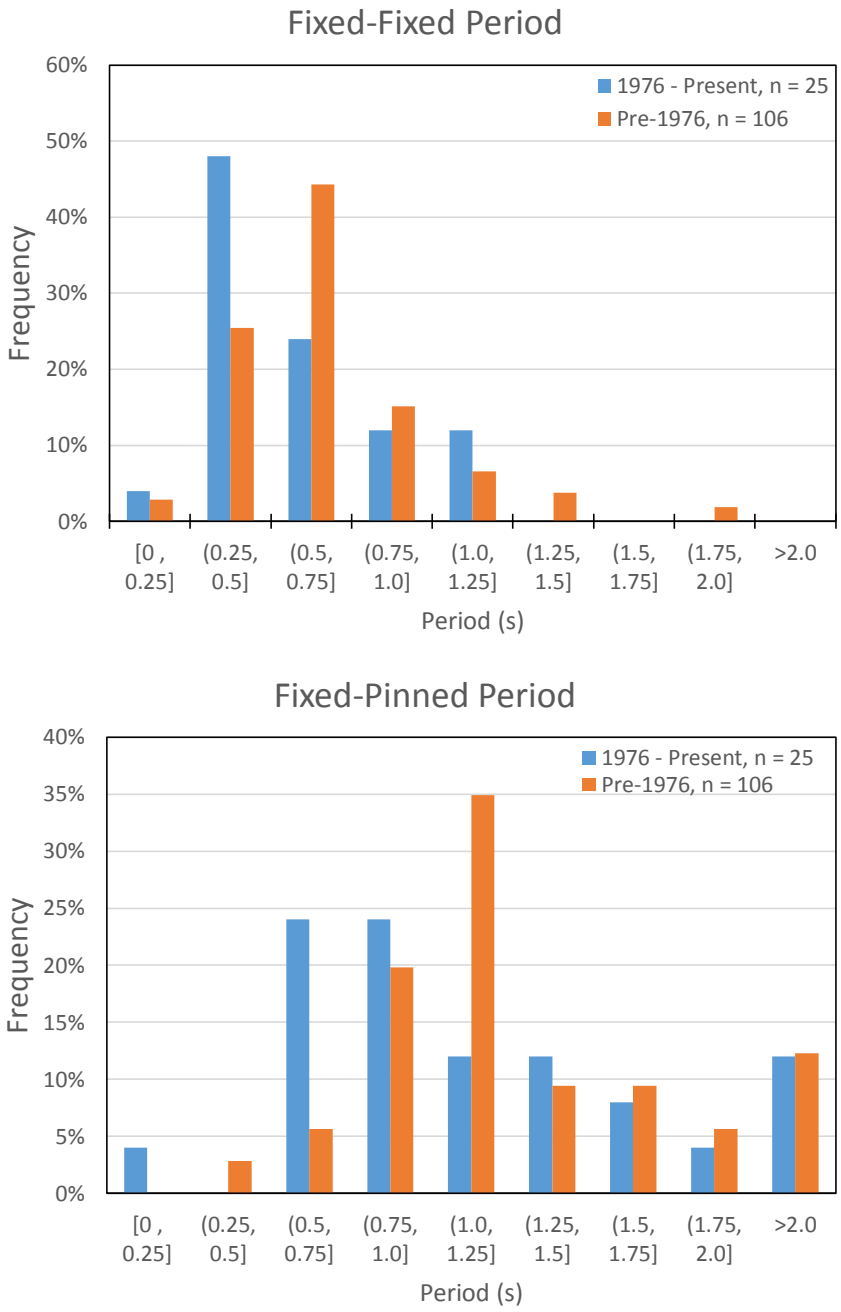

Fig. 4.4. Estimated Bridge Periods

These estimates for period can be related to properties of the bridges in the bridge database. Figures 4.5 and 4.6 present relationships between estimated period and L_{eff} and L/D for

each bridge in the database for which enough information was available to calculate period. Results are shown for both fixed-fixed column conditions and fixed-pin conditions.

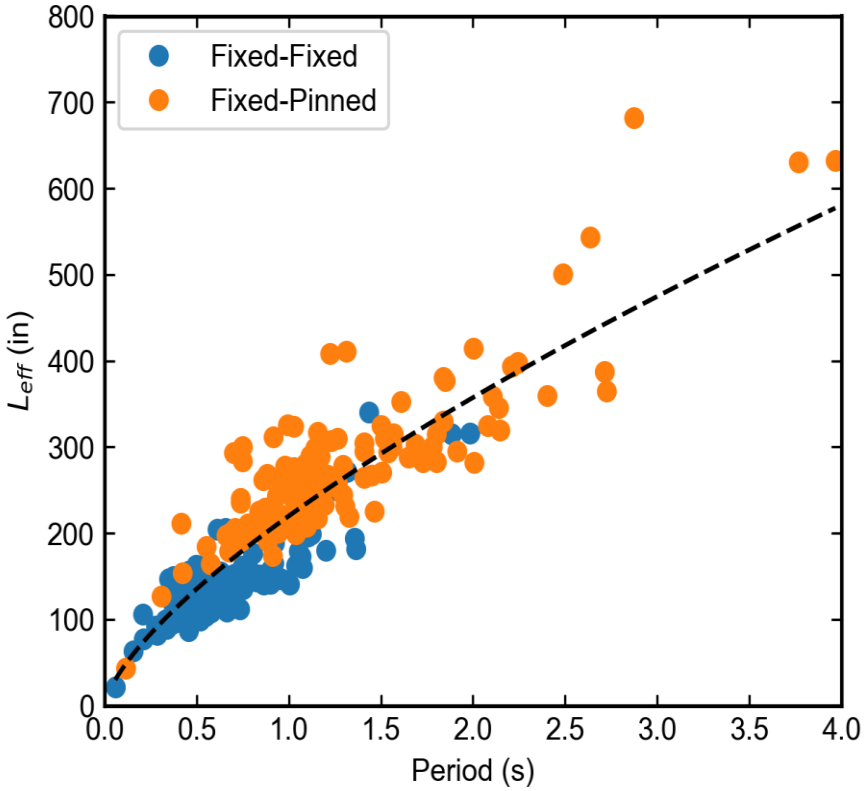

Figure 4.5. Relationship between L_{eff} and estimated period for bridges in the database.

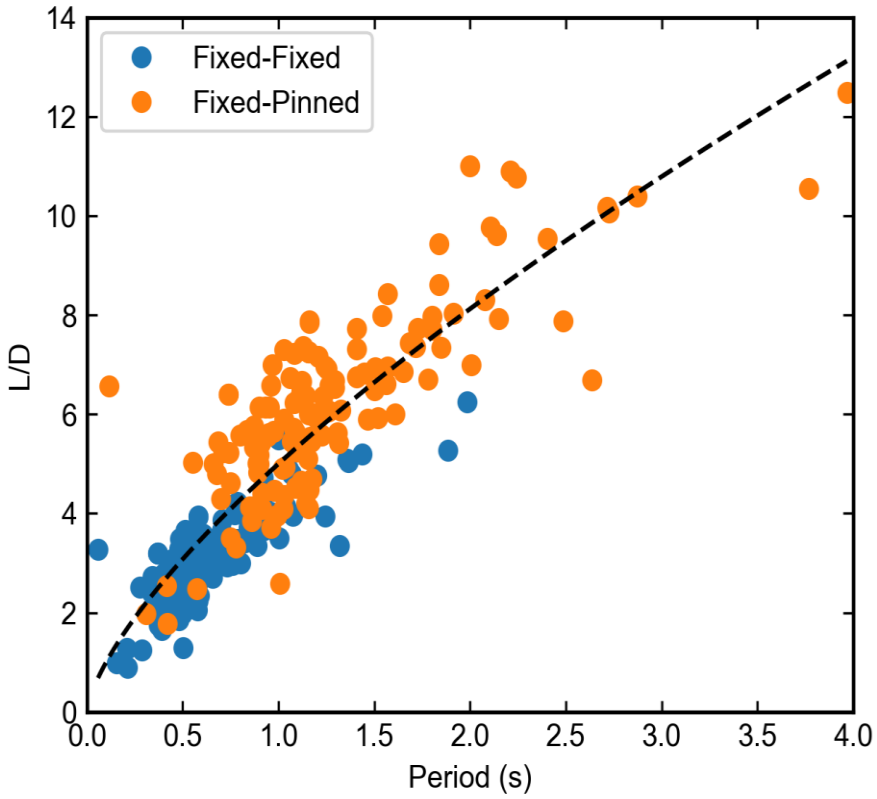

Figure 4.6. Relationship between L/D of the shortest bridge column and estimated period for bridges in the database.

The relationships for both L_{eff} and L/D were described with the following equations:

$$L_{eff} = 220 \cdot T^{0.7} \quad \text{(Eq. 4-10)}$$

$$L/D = 5 \cdot T^{0.7} \quad \text{(Eq. 4-11)}$$

4.5 STRENGTH ESTIMATES

Column moment capacities were calculated by moment-curvature analysis using the OpenSEES modeling software. Column sizes, reinforcement patterns and material strengths were found in the WSDOT bridge database for the tallest and shortest column on each bridge. Column cross sections were modeled using a bilinear steel model with a strain hardening ratio of 1% and the Mander et. al (1988) concrete constitutive relationship. Cross sections were discretized

according to the recommendations of Berry and Eberhard (2007), using circular column cross sections radially discretized with 200 “core” fibers representing confined concrete and 20 fibers representing unconfined concrete.

The effective yield moment for a column was defined as the moment at which the extreme concrete fiber first reaches a compressive strain of 0.004. Effective yield moments were calculated using the properties in the bridge database for the shortest and tallest column on each bridge. Base shear strength at column effective yield moment was calculated first assuming fixed-fixed boundary conditions, and then assuming fixed-pinned conditions. Corresponding boundary conditions were assumed when computing stiffness. The total base shear strength for each bridge in the database was then calculated using the □ factors and the individual column strengths as described in equation 4-5.

4.6 NORMALIZED BASE SHEAR STRENGTH

From the above estimates for weight, period, and strength, it was possible to plot the strength ratio (strength normalized by weight) versus estimated period (Fig. 4.7). For each bridge, stiffness and strength were calculated using two assumed boundary conditions: columns fixed at both ends, and columns fixed at one end and pinned at the other. The bridges were then divided between new (1976-present) and old (pre-1976), and curves were fit to the data.

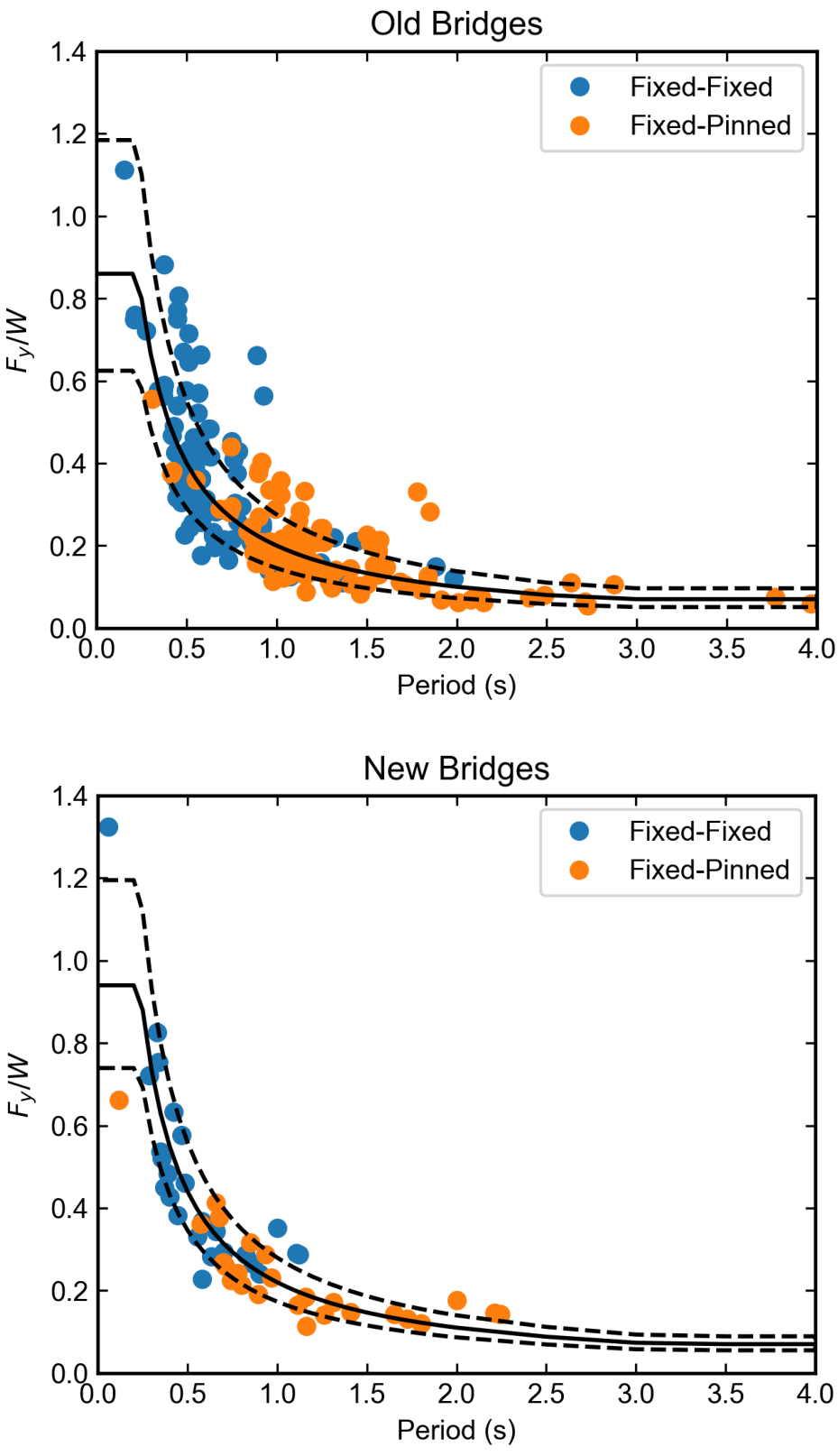

Fig. 4.7. Normalized base shear strength for new and old bridges.

The calculated equations for mean strength were:

$$\text{Old: } F_y/W = \max(0.07, \min(0.20 / T, 0.86)) \quad \text{(eq. 4-12)}$$

$$\text{New: } F_y/W = \max(0.07, \min(0.22 / T, 0.94)) \quad \text{(eq 4-13)}$$

The standard error (in log scale) is 0.32 for old bridges and 0.24 for new bridges. For much of the period range, the strengths of the new and old bridges were similar. New bridges in the database tended to be much stronger at low periods and slightly stronger at high periods than older bridges. Old bridges also show more variability in strength for a given period.

4.6.1 Comparison with Design Strengths for New Bridges

The normalized base shear strengths in Figure 4.7 can be compared with minimum bridge design strengths for new bridges in Seattle. Figure 4.8 shows the mean normalized base shear strength for new and old bridges plotted alongside the minimum design strengths for bridges in Seattle located on Site Class C soils, multiplied by a factor of 1.5 to account for expected overstrength. Minimum design strengths for Seattle were calculated by de Zamacona Cervantes (2019) using the provisions of WSDOT Bridge Design Manual 2018 and AASHTO 2017 LRFD Bridge Design Specifications as:

$$F_y = \Omega \cdot m \cdot g \cdot S_{a,DBE} = \Omega \cdot m \cdot g \cdot C_{sm} / R \quad \text{(eq. 4-14)}$$

Ω is the material overstrength factor, taken as 1.5, g is the gravitational constant, C_{sm} is the elastic seismic response coefficient, and R is the force reduction factor, taken as 5. It can be seen that the lateral strength of most of the bridges in the database exceeds the expected design strength, even after accounting for material overstrength. That the actual bridge strengths greatly exceed minimum design strengths suggests that previous research which derived bridge strengths from code minimum values may have been overly conservative, and that actual bridge ductility demands may be significantly lower than previous studies indicated.

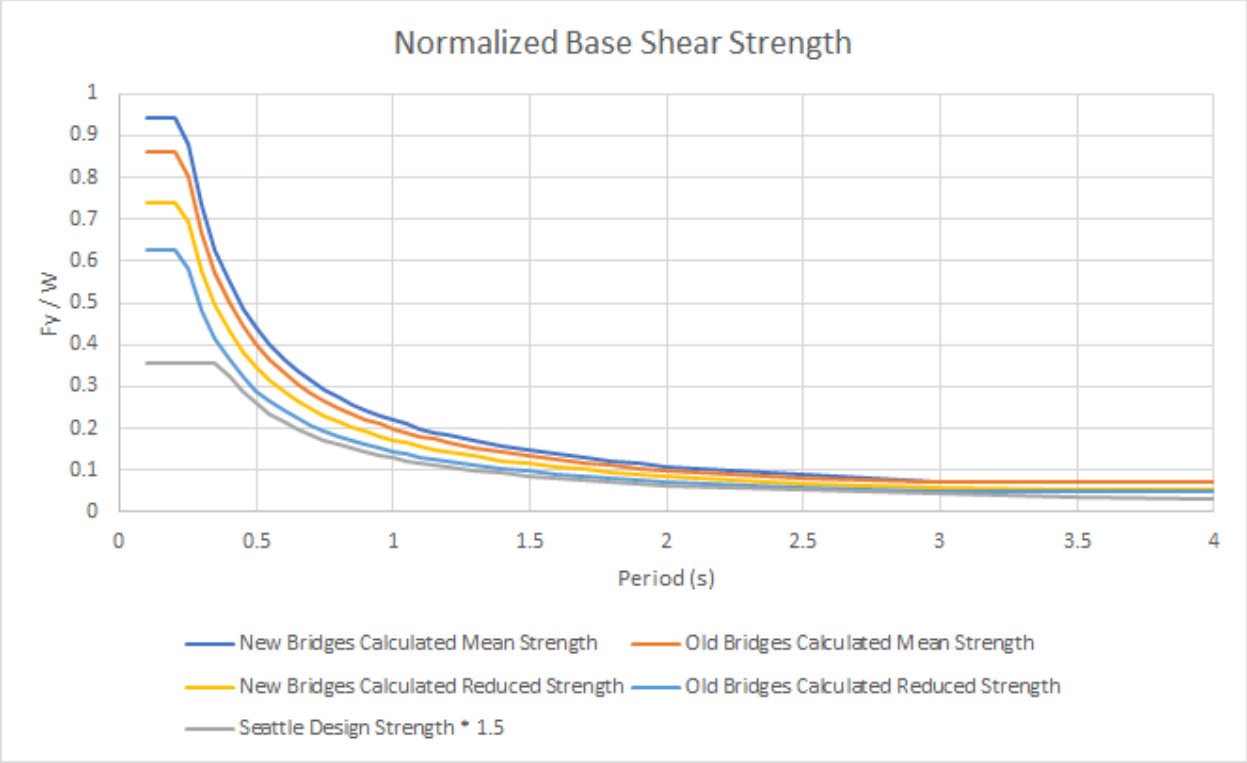

Fig. 4.8. Calculated base shear strengths compared to design strengths for Seattle, including an overstrength factor of 1.5

Chapter 5: Calibration of IMK Parameters

The single-degree-of-freedom oscillators used to conduct the parametric study (Chapter 6) were modeled in OpenSEES using the Modified Ibarra-Medina-Krawinkler (IMK) Deterioration Model with Peak-Oriented Hysteretic Response material. The IMK model has several input parameters that control the backbone force-displacement relationship and hysteretic behavior. A number of these parameters were calibrated to match the measured cyclic, force-displacement response of reinforced concrete column tests documented in the UW-PEER Structural Performance Database. Only circular columns from the database were used to calibrate the IMK model.

Section 5.1 of this chapter introduces the UW-PEER database and describes how columns representative of the lifeline bridges were selected for calibration. Section 5.2 describes the IMK model, and Section 5.3 describes the use of this column test data to calibrate several parameters of the IMK model.

5.1 UW-PEER STRUCTURAL PERFORMANCE DATABASE

The UW-PEER Structural Performance Database (PEER 2020) contains the results of cyclic lateral loading tests of reinforced concrete columns. The database contains information on tests of 165 spiral reinforced columns and 253 rectangular reinforced columns. For each column, the database provides the column geometry, material properties, reinforcing details, test configuration, axial load, and force-displacement history at the top of the column (e.g., Fig. 5.1).

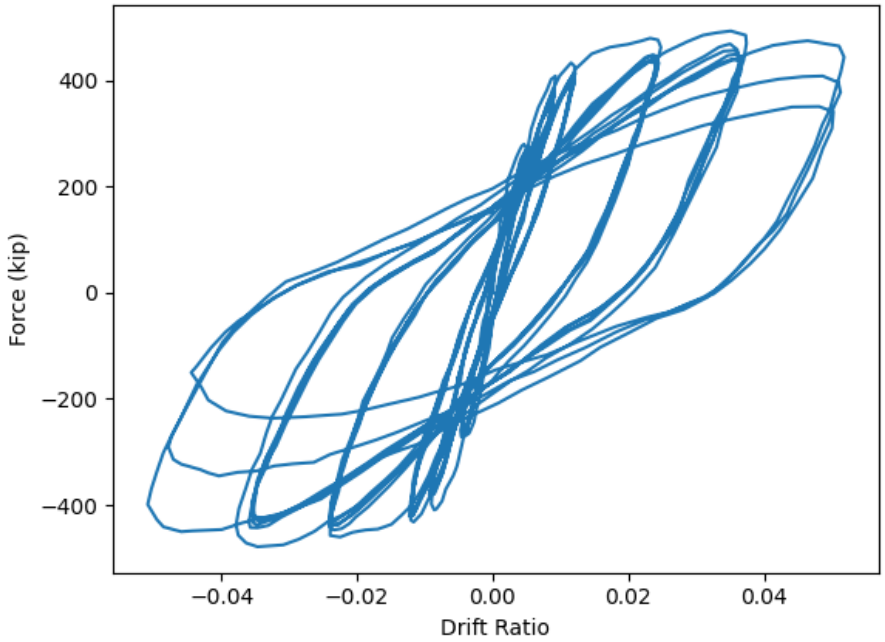

Fig. 5.1. Sample force-displacement history for a representative column in the UW-PEER column performance database

The selected columns were intended to be representative of columns on bridges in the WSDOT lifeline database. For the purposes of calibrating the IMK model for bridge columns, only circular columns from the database were considered, as those are most common in the WSDOT bridges. In addition, a number of restrictions were imposed to select the columns to be used for calibration. Axial-load ratios were limited to a maximum of 30%, longitudinal reinforcement ratios were limited to a minimum of 0.01% and a maximum of 5%, and columns that failed in flexure-shear or shear were excluded from the model calibration. A total of 83 circular columns met these criteria and were used to calibrate parameters for the IMK model.

5.2 IMK MODEL

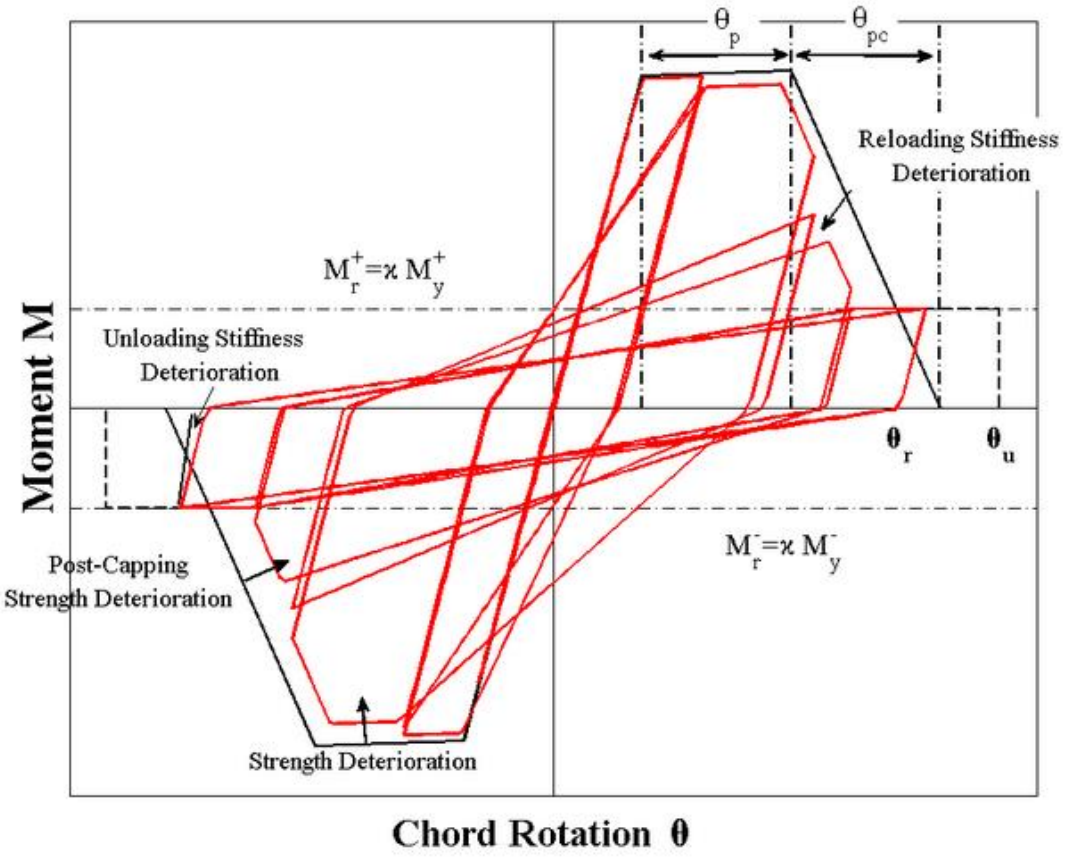

Figure 5.2. IMK model behavior (Lignos and Krawinkler 2012)

Figure 5.2 shows a sample IMK backbone curve and key parameters of the IMK model. The material is initially linear elastic, with an elastic stiffness k and yield strength M_y. Consider monotonic loading first. After rotations exceed $\theta_y = M_y / k$, the material enters a post-yield plateau (the region labeled θ_p above), where the tangent stiffness is reduced. Once the material reaches the end of the yield plateau, it enters the post-capping region (the region labeled θ_{pc} above). In this region, the material resistance reduces. Beyond the post-capping region, the material eventually reaches its residual strength, M_r, and does not show further strength degradation with increasing deformations.

The cyclic behavior of the IMK model is particularly important when evaluating response to earthquakes. As the IMK material is cycled, both the stiffness and strength deteriorate. Four modes of deterioration are present in the IMK model: strength deterioration, post-capping strength deterioration, unloading stiffness deterioration, and reloading stiffness deterioration. The rate of deterioration for each mode is controlled by a cyclic deterioration parameter lambda, and an exponent c. Following the recommendations of Haselton et al. (2008), lambda was assumed to be the same for each mode, and c was taken as 1.0 for all modes. Figure 5.3 shows three identical IMK models with varying lambda values subjected to the same displacement history. The effect of lambda on the cyclic response of the model can be seen, with a higher lambda resulting in less deterioration of strength and stiffness per cycle.

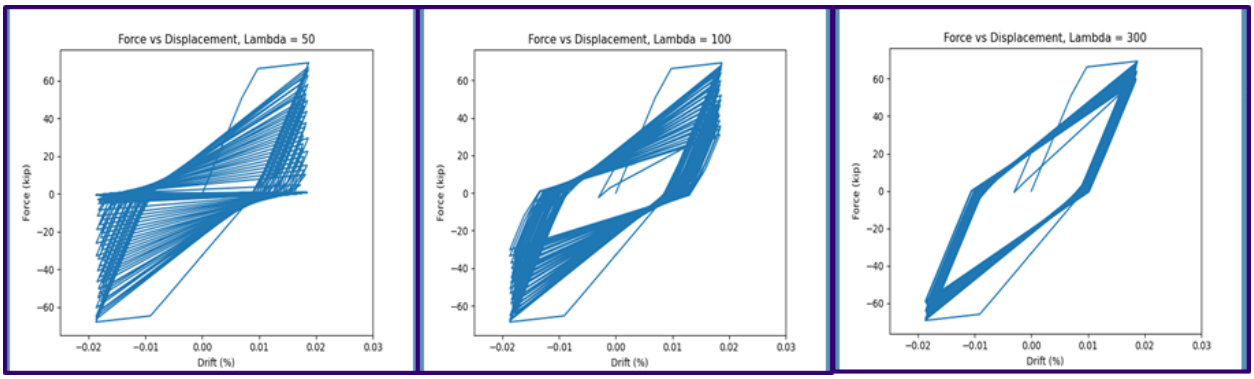

Figure 5.3. Effect of Lambda on IMK hysteretic behavior for small values of lambda (left), moderate lambda (center), and high lambda (right)

5.3 CALIBRATION OF IMK PARAMETERS

To calibrate the IMK model to simulate the behavior of RC columns, a symmetric hysteretic response was assumed, in which the force-displacement parameters for positive and negative deformations are the same. Eight parameters are necessary to completely define the symmetric IMK model:

- Yield Strength. The yield strength for each column was calculated by moment-curvature analysis in OpenSEES using the same procedure for the lifeline bridge database described in Chapter 4.
- Elastic Stiffness. The elastic stiffness was calculated using the Elwood-Eberhard (2009) effective stiffness approximation described in Chapter 4.
- Post-yield stiffness. The post-yield stiffness was assumed to be a constant 5% of the initial elastic stiffness.
- The post capping negative tangent stiffness was assumed to be 10% of the elastic stiffness, and this was used to calculate θ_{pc}.
- θ_u was taken as 100 times the sum of θ_y, θ_p, and θ_{pc}.
- The residual strength was taken as 1% of the yield strength.

The two remaining parameters, lambda and θ_p were calibrated independently for each of the 83 columns selected from the UW-PEER database. The calibration procedures for lambda and θ_p are described in detail below.

5.3.1 Calibration of Lambda

For the calibration of lambda, θ_p was first fixed. Using a post-yield slope of 5% of the elastic stiffness, θ_p was calculated such that the maximum force on the IMK backbone was equal to 110% of the measured maximum moment for a given column test, with a minimum θ_p of 0.04 and a maximum of 0.07. The value of 110% of the maximum measured moment was chosen as the target, because the column tests in the UW-PEER database are cyclic tests in which the strength generally degrades with each cycle, so the maximum moment on the backbone curve needs to be higher than the maximum observed moment for a cyclic test. Once θ_p was fixed for

each column test, an IMK model with the appropriate strength and stiffness of a column test was subjected to the same displacement history as that column test as illustrated in Fig. 5.3.

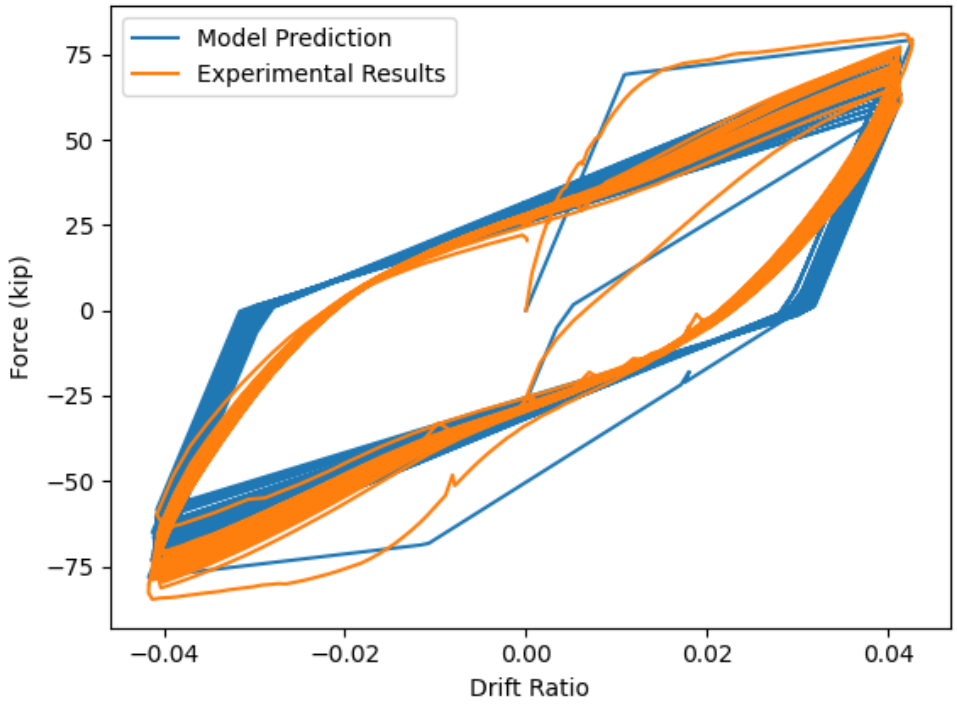

Figure 5.3. Sample Column Test with IMK Model Prediction

The procedure illustrated in Figure 5.3 was repeated for each of the 83 selected column tests and for IMK models with varying values of lambda. Lambda was varied for each column from 25 to 500 in increments of 25, and the error between the IMK model prediction and the experimental results was calculated for each value of lambda. The error was calculated as:

$$\text{Error} = (\Sigma|F_{IMK} - F_{Experiment}|) / (F_{max} \cdot n) \qquad \text{(eq. 5-1)}$$

F_{max} is the maximum force observed in the experiment, n is the number of displacement steps at which the error was calculated, and F_{IMK} and $F_{Experiment}$ are the force at a given displacement step of the IMK model and the experiment, respectively. When calculating the error for different

values of lambda, only the force at the peak displacement of each cycle was considered (Figure 5.4), since the main goal of calibrating lambda was to capture the total amount of strength degradation between each cycle. Fig. 5.4 shows a sample column test and the locations at which the error was calculated for calibration of lambda.

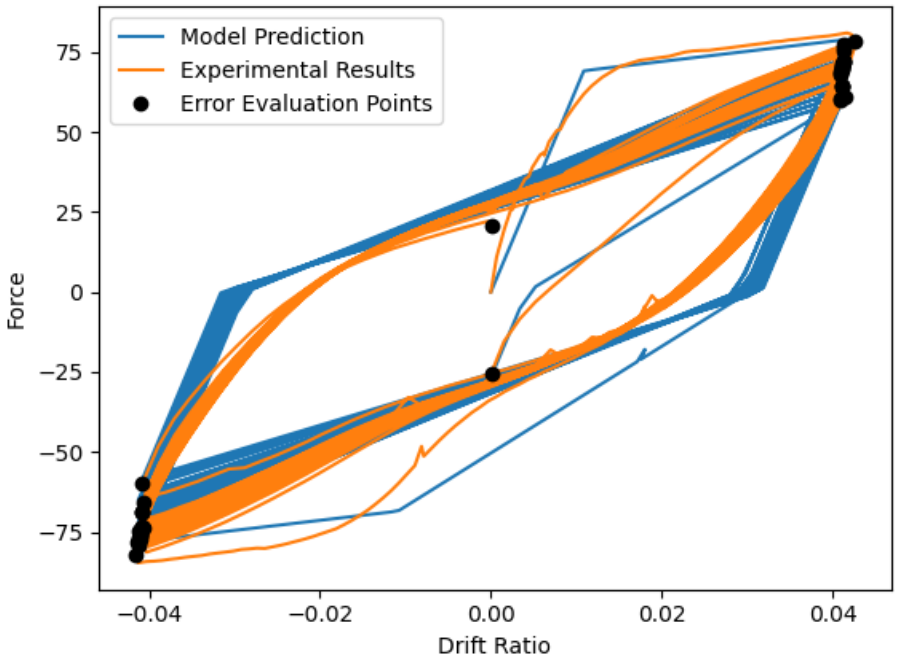

Figure 5.4. Sample column test showing locations at which error was calculated for calibration of lambda

Cyclic deterioration of reinforced concrete columns is governed largely by transverse reinforcement and axial-load ratios. In order to simplify the calibration procedure, and because the axial-load ratios of bridge columns in the WSDOT lifeline database varied over a small range, values for lambda were calibrated against column transverse reinforcement ratios only. Column tests were then binned according to transverse reinforcement ratio. Optimal values of

lambda were found for each bin. Figure 5.5 shows how the error in each bin varied as a function of lambda for several values of the transverse reinforcement ratio.

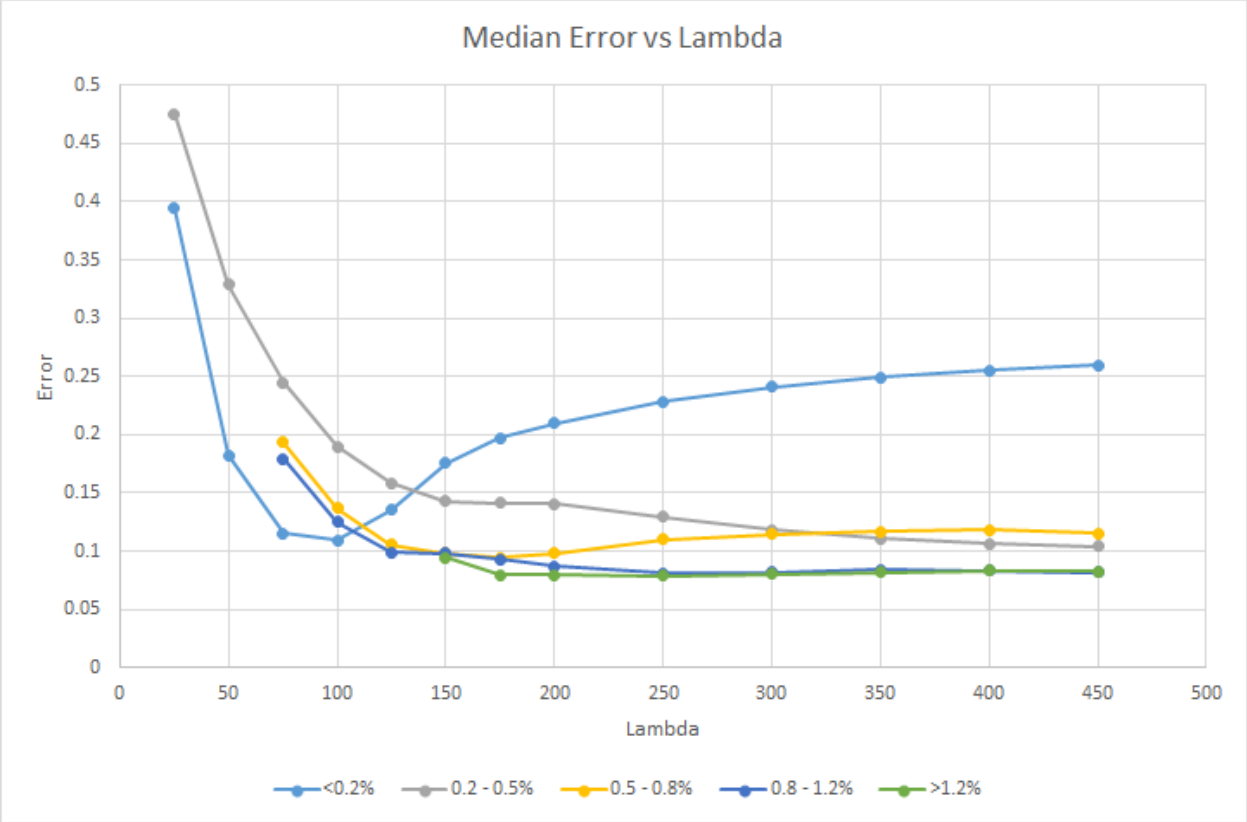

Figure 5.5. Median error vs lambda, with columns binned by transverse reinforcement ratio. Each line represents one bin of transverse reinforcement ratios.

These data were used to characterize a relationship between lambda and transverse reinforcement ratio (Figure 5.6). For the columns considered, optimal values of lambda ranged from a minimum of 100 at a transverse reinforcement ratio of 0%, to a maximum of 300 when transverse reinforcement ratios exceed 0.8%. The value of lambda was assumed to vary linearly between these two points.

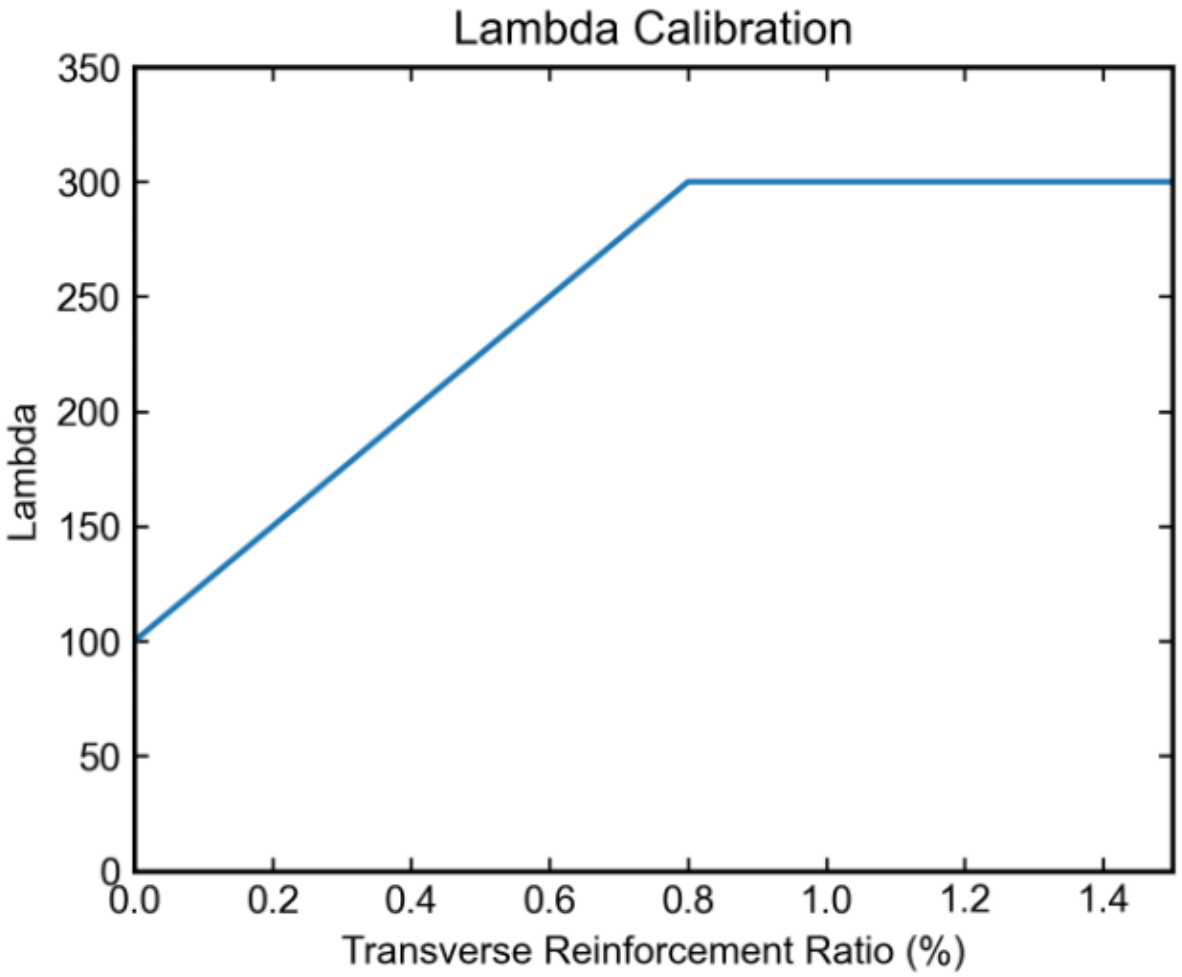

Figure 5.6. Final calibrated values for lambda as a function of column transverse reinforcement ratio.

5.3.2 Calibration of θ_p

Once lambda values were calibrated, the θ_p parameter was also optimized. For each of the 83 columns selected from the UW-PEER database, lambda was assigned according to the relationship given in Figure 5.6. A similar procedure for the calibration of lambda was followed for θ_p. IMK models were created for each column test and subject to the displacement history described in the test. Values of θ_p were varied from 0.04 to 0.12 in increments of 0.02, and the error between the IMK prediction and experimental results was calculated for each θ_p value according to Equation 5-1. Because θ_p affects backbone rather than the cyclic response, error was

calculated at every displacement step, rather than only once per cycle. Columns were then binned according to transverse reinforcement ratio (using the same bins as were used for lambda), and optimal values of θ_p were found for each bin (Figure 5.7).

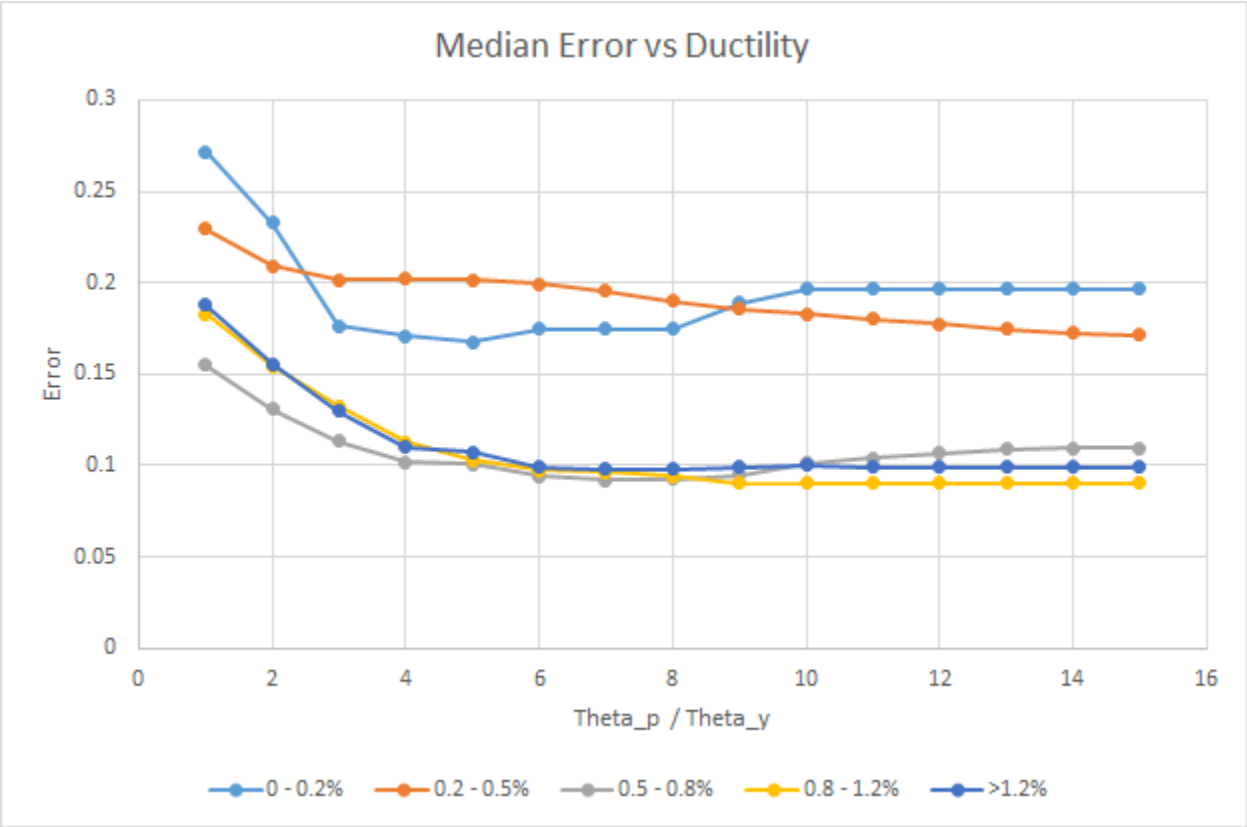

Figure 5.7. Median error vs θ_p, with columns binned by transverse reinforcement ratio. Each line represents one bin of transverse reinforcement ratios.

A relationship was then constructed between optimal θ_p and transverse reinforcement ratio (Figure 5.8).

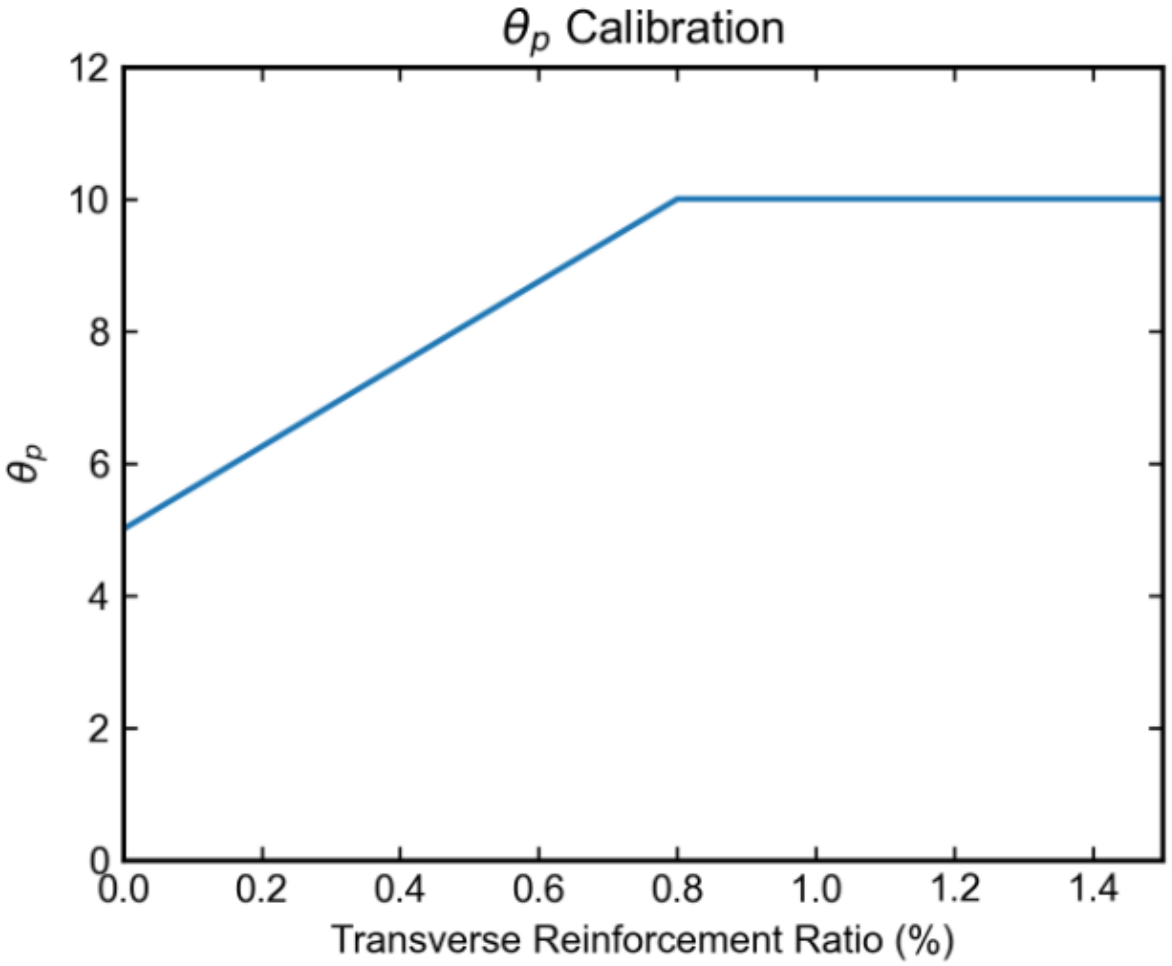

Figure 5.8. Final calibrated values for θ_p / θ_y as a function of column transverse reinforcement ratio.

In the modeling recommendations, the proposed values of θ_p ranged from 5 times the yield displacement at a transverse reinforcement ratio of 0%, up to a maximum of 10 times the yield displacement when transverse reinforcement ratios exceed 0.8%. Values of θ_p vary linearly between these two points.

5.4 APPLICATION OF MODELING RECOMMENDATIONS

Using the calibrated values of lambda and θ_p described in the preceding section, the calculated strength (from moment-curvature analysis) and effective stiffness (from Elwood and Eberhard, 2009), and the assumed values for post-yield stiffness, residual strength, θ_{pc}, and θ_u, a fully calibrated IMK model could be created for each column in the UW-PEER database. Figure 5.9 shows selected results of this model for columns over a wide range of transverse reinforcement ratios.

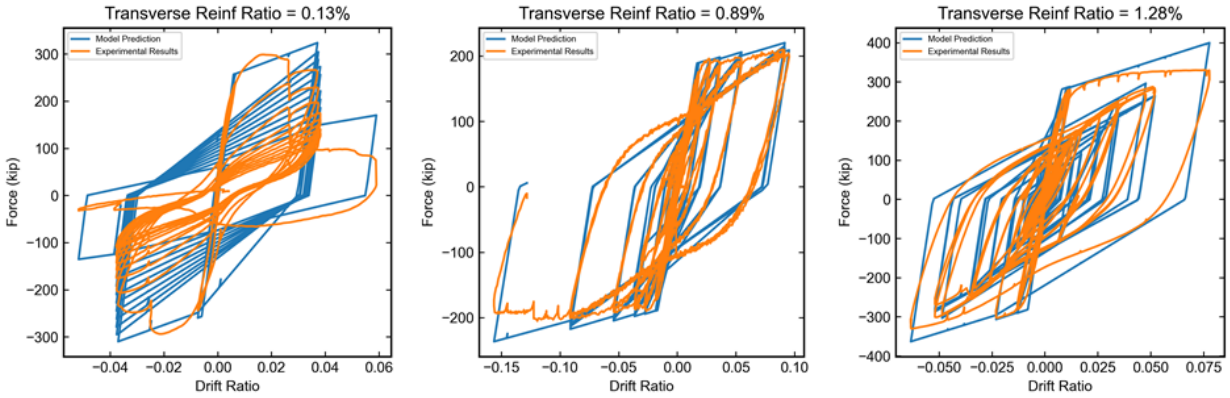

Figure 5.9. Fully calibrated IMK results for a lightly reinforced column (left), moderately reinforced column (center), and heavily reinforced column (right).

In general, the calibrated IMK models accurately capture the lateral cyclic behavior of the reinforced concrete columns. Both strength and stiffness deterioration are well captured by the calibrated lambda values, and the calculated yield strength and effective initial stiffness match well with experimental results. It was found that the calibrated values of lambda performed less well for column tests with large numbers of cycles at low drift levels. In these cases, the calibrated models tended to overestimate the amount of strength deterioration.

Chapter 6: Parametric Study Methodology

This chapter describes the methodology used to conduct the parametric study of single-degree-of-freedom systems. The study was informed by the properties of the WSDOT lifeline bridge database (Chapter 3), the strengths and periods derived from this database (Chapter 4), and the calibrated cyclic material models in OpenSEES to model bridge columns (Chapter 5). The results of the parametric study are described in Chapter 7.

6.1 PARAMETER VARIATION

The following parameters were considered:

- 30 ground motion realizations (see Chapter 2.1)
- 10 locations (Chapter 2.1)
- 4 site classes (Chapter 2.2)
- 30 soil profiles per site class (Chapter 2.2)
- 2 directions (North-South and East-West)
- 18 periods (0.1, 0.2, 0.3, 0.4, 0.5, 0.6, 0.7, 0.8, 0.9, 1.0, 1.25, 1.5, 1.75, 2.0, 2.5, 3.0, 3.5, and 4.0 seconds).
- Oscillator properties representative of new and old bridges (Chapters 4 and 5)
- Mean strength and reduced strength (Chapters 4 and 5)

This combination of parameters resulted in a total of 5.2 million single-degree-of-freedom (SDOF) analyses. The parametric study was conducted using the Stampede2 supercomputer at the Texas Advanced Computing Center (TACC) at the University of Texas at Austin.

6.2 IMK PARAMETERS FOR NEW AND OLD BRIDGE MODELS

Chapter 5 describes the calibration of the IMK model parameters lambda and θ_p as a function of the transverse reinforcement ratio in a column. In line with the division of the WSDOT lifeline database bridges into pre-1976 and 1976-present time ranges based on changing bridge design codes (Chapter 3), the IMK models used for the parametric study were selected to be representative of the properties of new and old bridges. Pre-1976 bridges in the lifeline database averaged transverse reinforcement ratios of less than 0.5%, whereas bridges constructed 1976-present averaged transverse reinforcement ratios above 1% (Figure 3.6). From the relationships derived in Chapter 5 (figures 5.5 and 5.6), lambda was set to be 100 * D_y for SDOFs representing old bridges, and 300 * D_y for new bridges. The post-yield ductility, $\theta_p/\theta_y \cong D_P / D_y$, was set as 5 for old bridges and 10 for new bridges. All other parameters of the IMK model were held constant between new and old bridges (see Chapter 5 for details of other IMK parameters).

6.3 MODELING METHODOLOGY

Each SDOF oscillator was modelled using the OpenSEES software as a zeroLength spring element. The force-displacement behavior for this spring was defined using the Modified Ibarra-Medina-Krawinkler with Peak-Oriented Hysteretic Response material model, using the calibrated input parameters as described in Chapter 5.

Each oscillator was assigned a nominal mass of 1. The elastic stiffness, k, was calculated from the mass and the period as:

$$k = (2\pi / T)^2 / m \qquad \text{(eq. 6-1)}$$

T is the period of the oscillator and m is the mass. The yield strength, F_y, was determined for new and old bridges from the normalized base-shear strength curves developed in Chapter 4 (Figure 4.5). Reduced strength was defined as one standard error below the mean strength for both new and old bridges. The yield displacement for each spring was then defined as:

$$D_y = F_y / k \qquad \text{(eq. 6-2)}$$

For each single-degree-of-freedom analysis, the key results included the maximum displacement ductility, D_{max} / D_y, and whether the system collapsed or not. Collapse was determined by conducting a pushover analysis of the oscillator after it was subjected to the ground motion. If the system was unable to exceed its defined residual strength (taken as 1% of the yield strength F_y) in both the positive and negative loading directions, it was determined to have collapsed.

Chapter 7: Results of SDOF Parametric Study

This chapter presents the results of the parametric study described in Chapter 6. The results are presented in terms of normalized spectral acceleration, median ductility demand, and likelihood of exceeding various ductility demands and damage states. Results are reported in this chapter for four representative cities: Ocean Shores, Port Angeles, Olympia and Seattle. Results for all ten locations can be found in Appendices B and C. The following sections discuss the effect of key parameters on the response of the SDOF systems. Parameters discussed include the location, direction of the ground motion, soil type, bridge age, as well as the mean and reduced strengths.

7.1 LOCATION

Spectral accelerations for the 10 locations considered in the parametric study are shown in Figure 7.1. The locations are grouped into the four categories of cities discussed in Chapter 2: coastal without basin, inland without basin, inland with shallow basin, and inland with deep basin. The normalized spectral accelerations, S_a W / F_y, show the effects of site-to-source distance and sedimentary basins on the ground motions. General observations include:

- The coastal cities, located close to the fault, have high spectral accelerations (up to 2g) at low periods, but the magnitudes quickly drop off as the period increases above approximately 0.3s.
- Inland cities without a basin have generally low spectral accelerations (not exceeding 0.8g) across all periods.
- Inland cities on deep and shallow sedimentary basins show ground-motion amplification at periods above 1 second, with Sa exceeding 0.7g even at periods above 1s.

For the remainder of this chapter, results are discussed for one city from each category (Ocean Shores, Olympia, Port Angeles, and Seattle). Complete results for all 10 cities can be found in Appendices B and C.

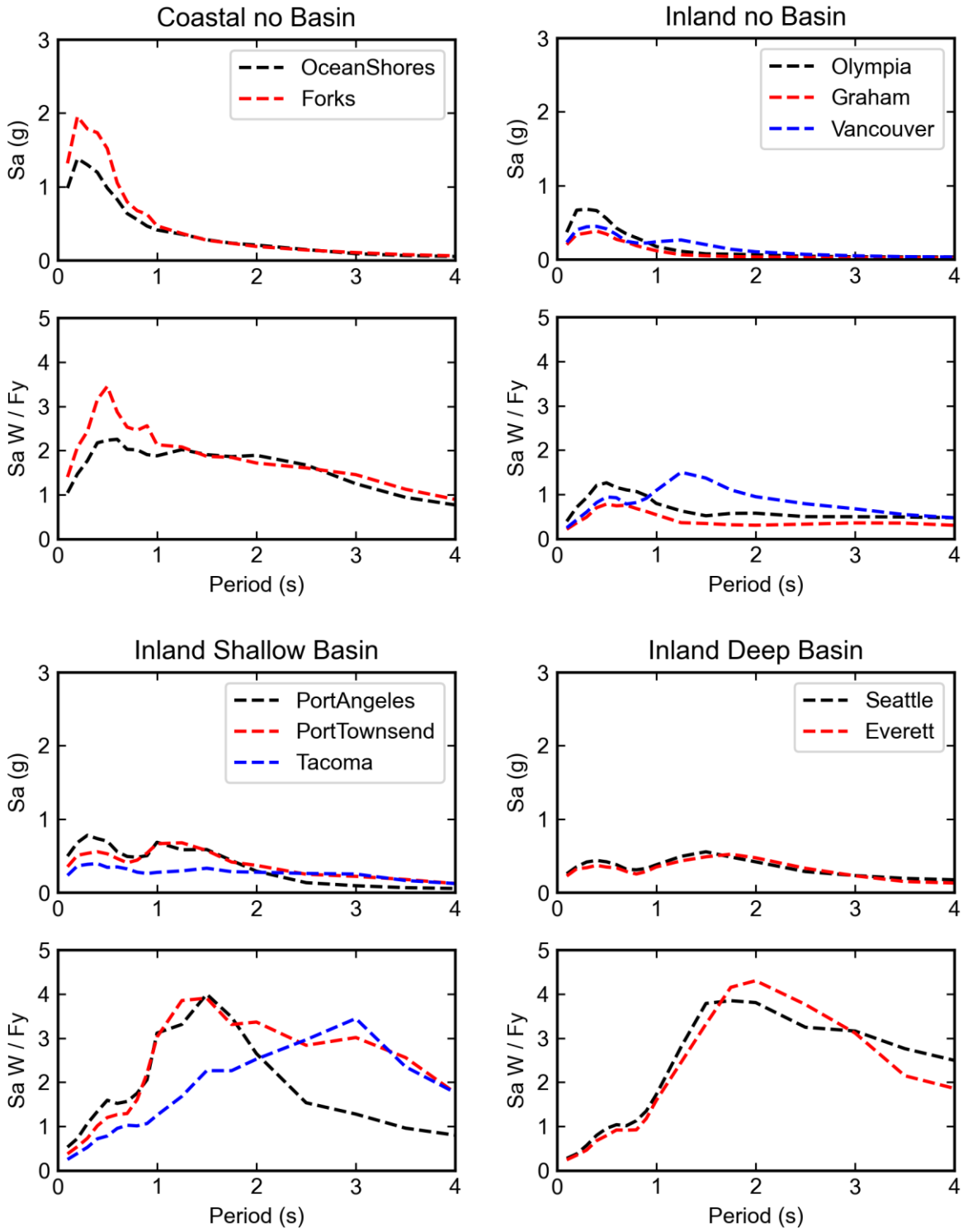

Figure 7.1. Median spectral accelerations for the baseline ground motions in 10 locations, by category. Spectral accelerations are normalized using the mean Fy/W values for new bridges.

7.2 GROUND MOTION DIRECTION

Two ground motion directions were considered in the parametric study: North-South (referred to as the y-direction), and East-West (x-direction). Figure 7.2 shows the median response spectra for four selected cities for all 30 baseline ground motions for the x and y directions.

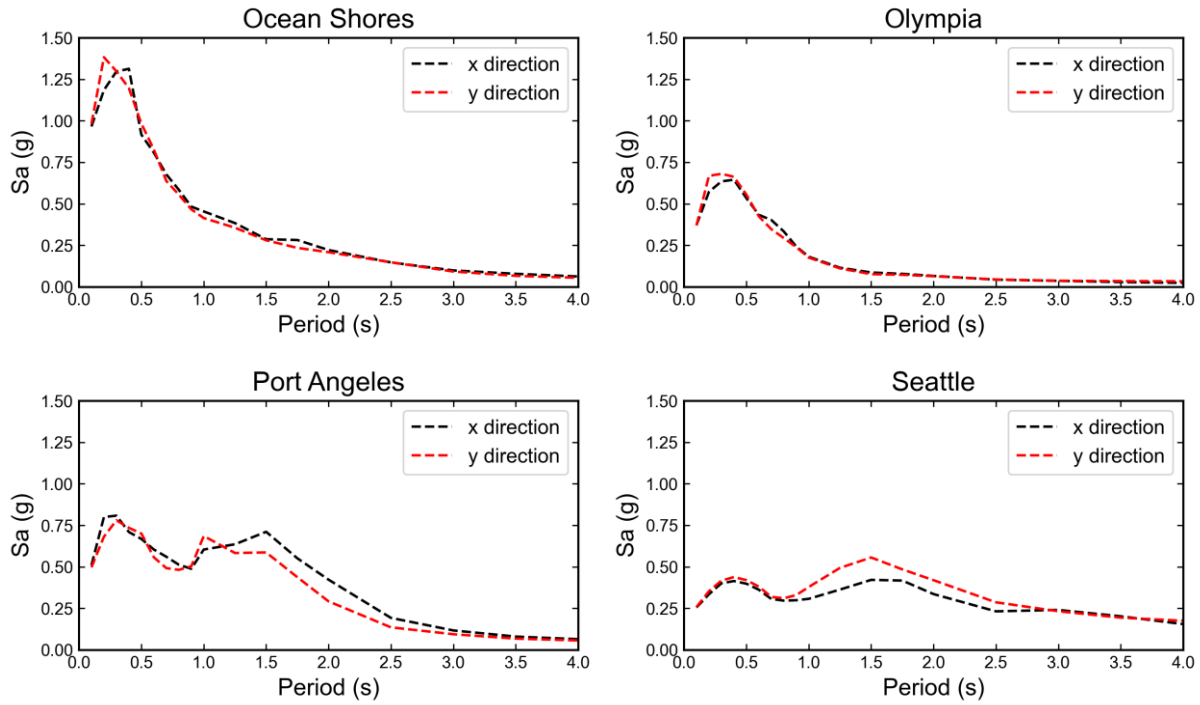

Figure 7.2. Median Spectral accelerations for x and y directions in selected cities.

Figure 7.2 shows that the response spectra are very similar in the x and y directions across a variety of locations. The results are also similar for the six locations not pictured above. Accordingly, in all subsequent discussion, results for ground motions in the x and y directions are combined (i.e., the two components of each ground motion were used in separate analyses and the results are treated equally).

7.3 SITE CLASS

In addition to the baseline non-site-adjusted motions, four site classifications were considered. These sites were designated as C2, C4, D1, and D3 (see Chapter 2 for details), and correspond to four subclasses of the NEHRP Site Class C and D soils (FEMA 2015). Figure 7.3 shows the effect of site type on the median displacement ductility demand for SDOFs representing older bridges in Ocean Shores, Olympia, Port Angeles and Seattle. The displacement ductility results for each site show similar trends as the site-adjusted response spectra presented in Chapter 2 (Figure 2.6)

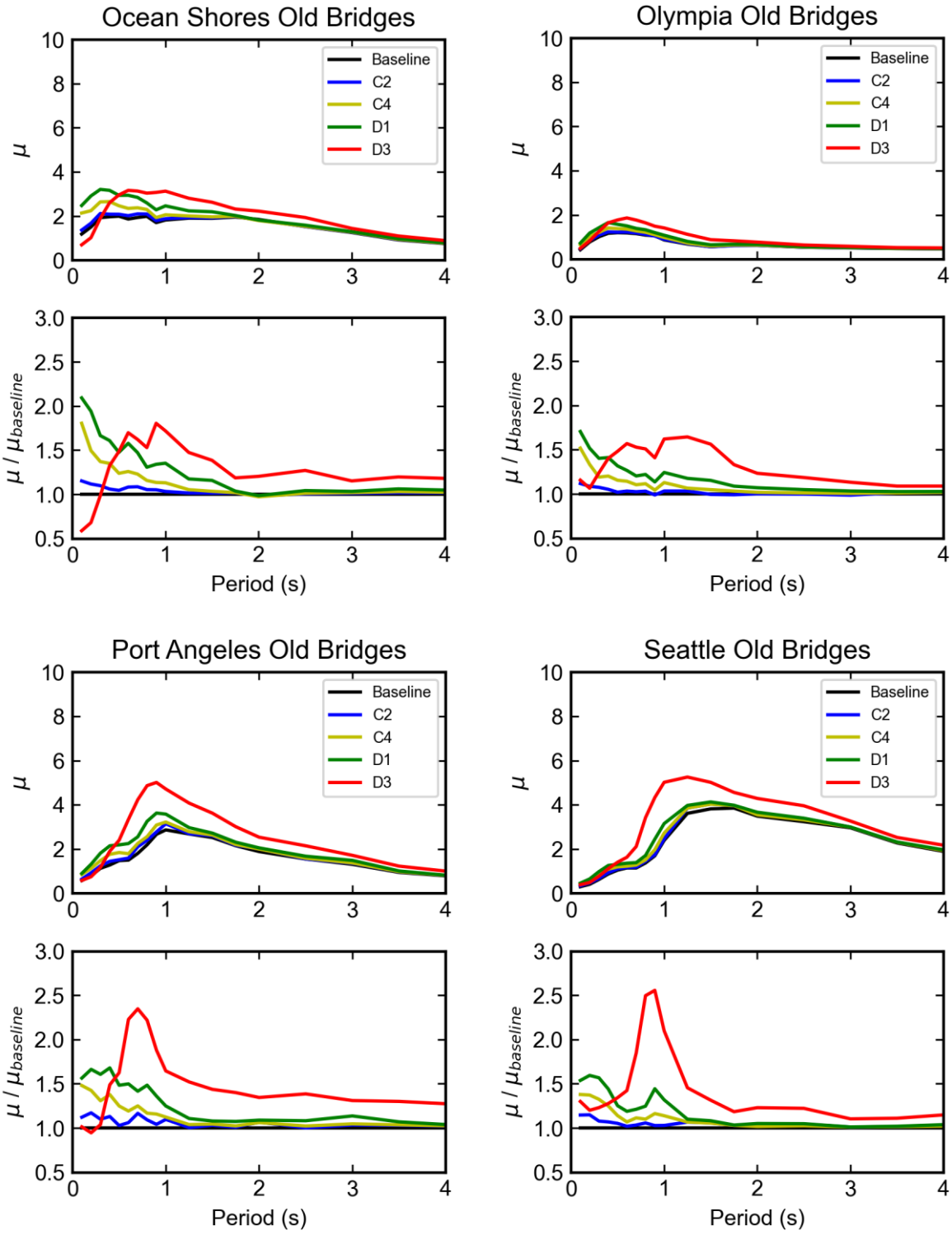

Figure 7.3. Median displacement ductility demands for various soil types.

- At periods below approximately 0.5 seconds, the second-softest soil subclass (D1) had the largest ductility demands with maximum amplification factors (compared to baseline motions) ranging from 1.5 to 2.0. In this period range, the softest soils (D3) had less amplification, and for lowest periods, the displacement demands were even below those of the baseline motions.
- In contrast, at periods longer than about 0.5 seconds, the D3 soil profiles resulted in the largest median displacement ductilities, with the largest amplification factors occurring near a period of 1.0 s. The amplification was largest for the sites within the basin where the median ductility demand found using the D3 soil profiles reached 2.5 times the median from the baseline motions. For all locations, the stiffest soil considered (C2) resulted in little increase in displacement ductilities, with mean displacement ductilities that were nearly equal to the baseline motions (amplification factors near 1).
- At very long periods, the spectral accelerations for all four soil types converged to the same ductility demand as the baseline motions. This occurs because the soils begin to move as rigid bodies at long periods, regardless of the stiffness of the soil.

  Complete results for all cities and soil types can be found in Appendix B.

7.4 NEW AND OLD BRIDGES

Single-degree-of-freedom systems with properties representative of new (1976 - present) and old (pre-1976) bridges were considered as well (see Chapters 5 and 6 for discussion of the properties of new and old bridges). New bridges had slightly higher strengths, more ductility capacity, and less cyclic strength/stiffness deterioration than older bridges. Figure 7.4 shows median displacement ductility demands for new and old bridges in Ocean Shores, Olympia, Port Angeles and Seattle.

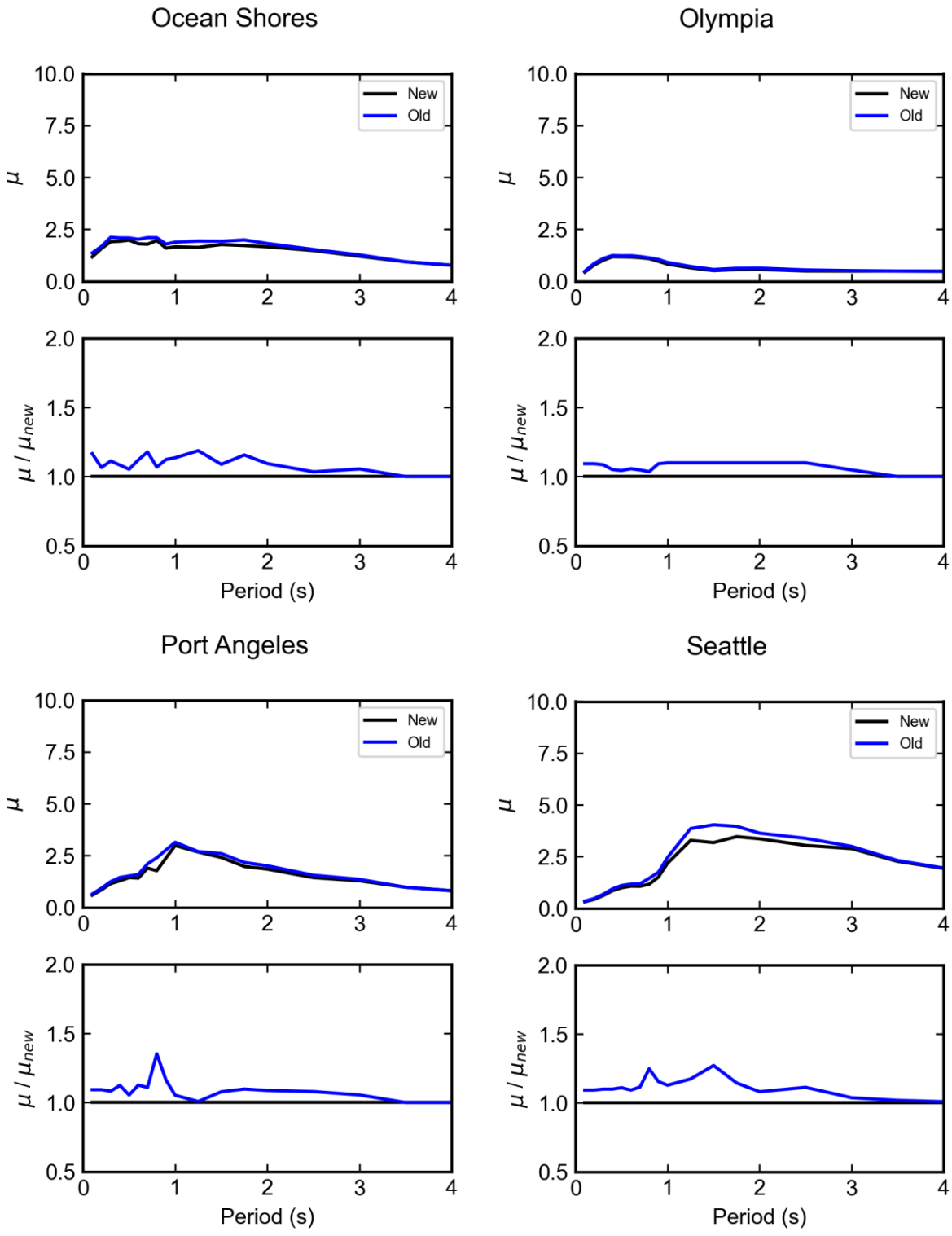

Figure 7.4. Median displacement ductility demand for C2 ground motions for new and old bridges with mean strengths

For all locations, older bridges had slightly higher ductility demands at nearly all periods. For very long periods, greater than about 3 seconds, new and old bridges had nearly identical ductility demands, while for shorter periods, old bridges had demands up to 20% higher in Ocean Shores, 10% higher in Olympia, 30% higher in Seattle, and 35% higher in Port Angeles. Differences between new and old bridges become less significant at longer periods, because long period oscillators will undergo fewer displacement cycles for a given ground motion. With fewer cycles, the difference in cyclic strength/stiffness deterioration between new and old bridges becomes less important, and the responses begin to converge. Sites within the basin, in particular Seattle, had larger differences in ductility demand between new and old bridges at periods between 0.75 and 1.5 seconds. Larger demands at these periods, combined with a spectral shape that is larger at the elongated post-yield period of those bridges, resulted in more deterioration and larger displacement demands.

It is important to note that shear and flexure-shear failures were not considered in this analysis. Older bridges in particular may be more vulnerable to these types of failures at large ductility demands, so the potential for failure of the older bridges may be larger than the results here indicate.

7.5 EFFECT OF REDUCED STRENGTH

SDOFs were also analyzed for systems with strengths representing the mean strength for bridges in the WSDOT lifeline bridge database, and for the mean strength minus one standard deviation (labeled as “reduced strength” below). Figure 7.5 shows the relative strengths as well as the median displacement ductility demand for mean and reduced strength systems.

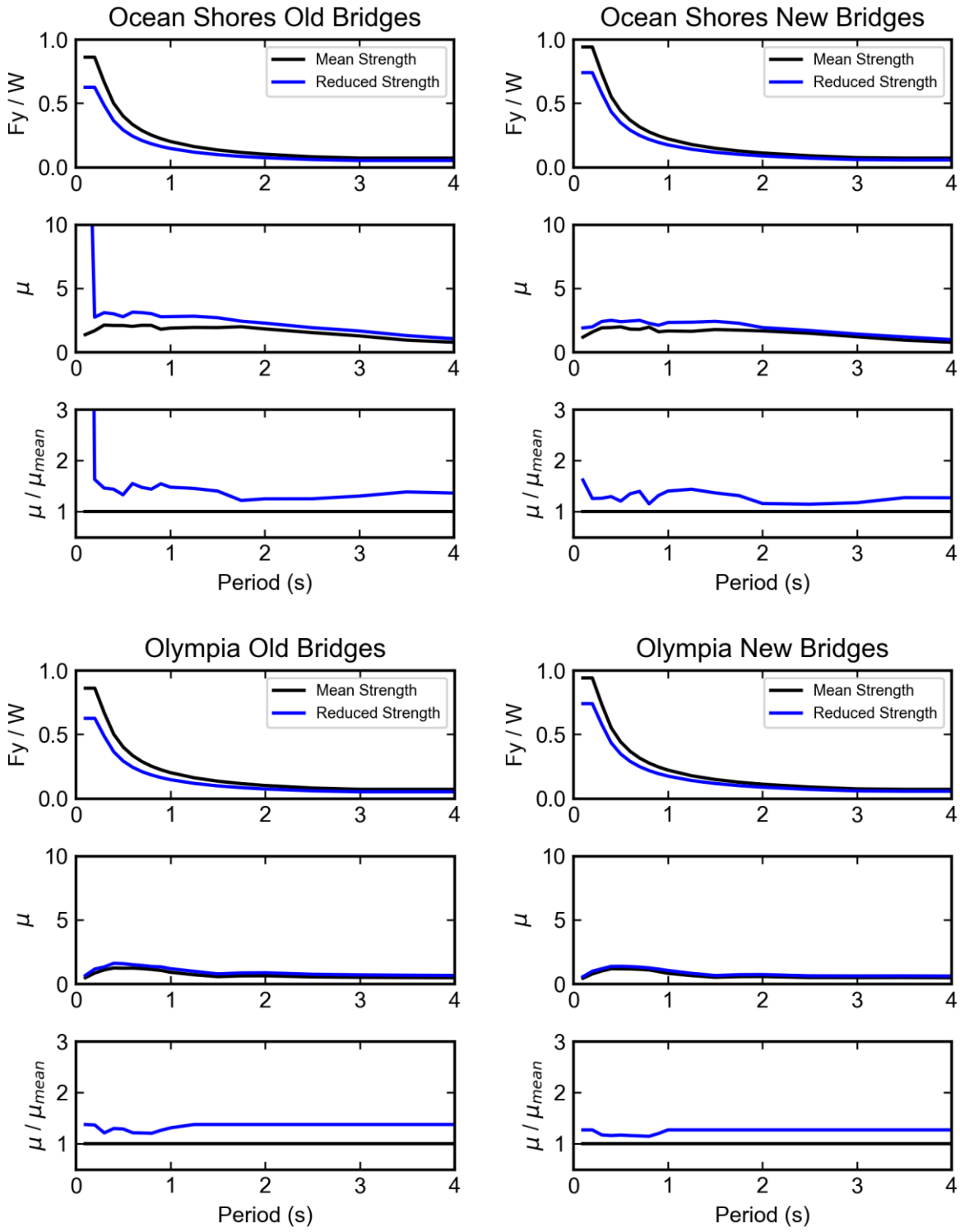

Figure 7.5 Median displacement ductility demand for C2 ground motions for mean strength and reduced strength bridges

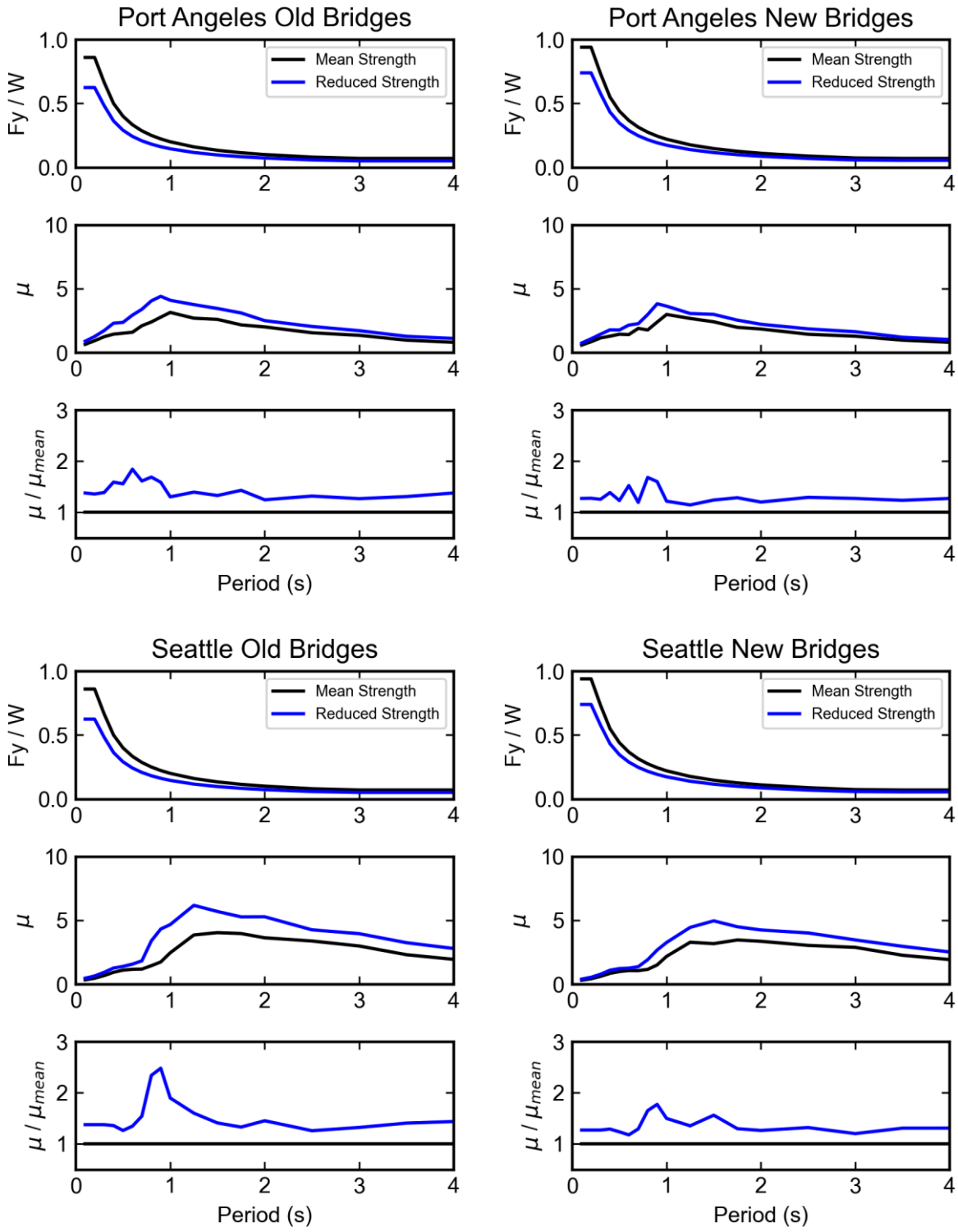

Figure 7.5 Median displacement ductility demand for C2 ground motions for mean strength and reduced strength bridges

In the analysis of the WSDOT lifeline bridges (Chapters 3 and 4), it was found that older bridges had more variability in lateral strength than newer bridges, a trend that was attributed to the less stringent seismic design requirements in older design codes. As a result, old bridges had a much larger increase in ductility demand for reduced strength systems than newer bridges. For new bridges in Seattle, the reduced strength resulted in ductility demands up to 1.75 times higher than mean strength, while old bridges with reduced strength increased ductility demand by a factor of up to 2.5 over the mean strength bridges. In general, Old bridges have median ductility demands only 10 - 25% higher than new bridges, while lower strength bridges have ductility demands up to twice as high as mean strength bridges.

7.6 SPECTRAL ACCELERATIONS AND DUCTILITY DEMANDS FOR MEAN STRENGTH

In this section, the analysis results are presented for each of the four representative locations in terms of spectral acceleration, normalized spectral acceleration, median displacement ductility, and likelihood of exceeding ductilities of 2, 3.5 and 6. In Figures 7.6 to 7.9:

- The plotted spectral accelerations are the median spectral acceleration for the 30 simulated M9 ground motions in both the x and y directions.
- Normalized spectral acceleration, S_a W / F_y, are computed as the ratio of the median spectral acceleration to the normalized base shear strength, F_y / W. Values for the normalized base shear strength at each period were developed in Chapter 4 for both new and old bridges, and for the mean strength and one standard deviation below the mean

(denoted in this chapter as "reduced strength"). The same values of normalized base shear strength were used across all locations.

- Displacement ductility demand, denoted as D / D_y or as μ, is the ratio between the maximum displacement of an oscillator and the yield displacement of the oscillator. Results are presented for median values of D / D_y at each period.
- Results are also given for the likelihood that D / D_y exceeds certain threshold values. Values of 2, 3.5, and 6 were chosen, as these represent ductility limits for various performance levels proposed by WSDOT for bridges in Western Washington (Khaleghi 2019). Ductility limits of 2 and 3.5 apply to bridges on the lifeline routes, while ductility limits of 2 and 6 apply to bridges not on the lifeline. Ductility limits of 2 represent minimal expected post-earthquake damage with full bridge service, 3.5 represents moderate damage with limited service expected, and 6 represents significant damage with no expected service.
- For clarity, results are shown only for soil types C2 and D3, the stiffest and softest soils, respectively, that were considered in the parametric study.

Figures 7.6 through 7.9 show results for new and old bridges with mean strengths for the cities of Ocean Shores, Olympia, Port Angeles and Seattle. Results for all 10 cities and all four site classes can be found in Appendix B. Spectral accelerations for the four cities (shown in top plots for figure 7.6 to 7.9) show the effects of the sedimentary basin on the simulated M9 ground motions. In Olympia and Ocean Shores, two cities outside the sedimentary basin, the spectral accelerations peak at periods below 0.5 seconds, and decline for periods larger than 0.5 seconds. In contrast, Seattle and Port Angeles, two cities located on the basin, have small spectral acceleration peaks at low periods, but instead have ground motion amplification between periods

of approximately 1 and 2 seconds. These differences are attributable to the effects of the sedimentary basins.

The plots in the second row of figure 7.6-7.9 show normalized spectral accelerations, S_a W / F_y, for each city. Bridges in all four cities were assumed to have the same normalized base shear strength curves. In all four cities, normalized spectral accelerations are small at low periods (less than about 0.5 seconds). This occurs despite the fact that spectral accelerations peak at low periods, because bridges in the WSDOT lifeline database were found to have very high normalized base shear strengths at low periods. In Olympia and Ocean Shores, outside the sedimentary basin, this results in generally low values of normalized spectral acceleration, which peak at or below periods of 1 second. Seattle and Port Angeles, located on the basin, show normalized spectral accelerations peaking at periods between 1 and 2 seconds as a result of basin effects. Even though spectral accelerations in Seattle and Port Angeles are similar at 0.5 seconds and 1.5 seconds, the normalized spectral accelerations are much greater at periods around 1.5 seconds, because bridges in this period range are significantly weaker than those at lower periods. This combination of basin amplification effects and weaker bridges at longer periods results in substantially higher normalized spectral accelerations in cities with sedimentary basins.

The bottom four plots for each city in Figures 7.6-7.9 show various measures of the displacement ductility, D / D_y. In Seattle, located on a deep sedimentary basin, median values of D / D_y are generally small for low periods, owing to the high strength of the bridges in this period range. Particularly on the softer D3 soil type, median D / D_y values are significantly higher at periods around 1 - 1.5 seconds, with median D / D_y values as high as 5 for older bridges. Displacement ductility demands for new and old bridges are generally similar, although new bridges show slightly lower ductility demands, as expected. The limit state exceedance

graphs in Figure 7.6 show the probability that D / D_y will exceed certain threshold values. In Seattle, for both new and old bridges, there is a 90% probability that bridges with periods between 1 and 2 seconds will exceed ductility demands of 2 on D3 soils. For the stiffer C2 soils, there is an 80% probability that D / D_y exceeds 2 in that period range. Bridges with periods under 0.5 seconds are protected by their relatively high strengths, and show virtually no probability of exceeding any of the threshold ductility demands.

Ocean Shores, representing coastal cities without a sedimentary basin, has very high spectral accelerations at low periods. As a result, low period bridges show higher ductility demands in Ocean Shores than in cities farther from the coast. Up to half of bridges on C2 soils exceed ductility demands of 2 for periods below 1 second. For periods below 0.3 seconds, bridges on D3 soils show lower ductility demands than C2 soils, while at higher periods, the trend is reversed. For both new and old bridges, 40 - 50% of bridges on D3 soils with periods around 1 second exceed D / D_y of 3.5, and up to 25% exceed ductility demands of 6. Bridges on C2 soils are unlikely to exceed D / D_y of 6 at any period, while up to 25% exceed D / D_y of 3.5 across periods less than 2 seconds for new and old bridges.

Olympia, representing inland cities not located on a sedimentary basin, shows relatively low levels of damage for both new and old bridges at all period ranges. Bridges with periods around 0.5 seconds located on D3 soils show some light damage (40 - 50% exceeding D / D_y of 2 for new and old), but all other soils and period ranges show low levels of damage.

Port Angeles, located on a shallow sedimentary basin, shows displacement ductility demands similar to Seattle. The vast majority of bridges on soft soils at periods around 1 second will exceed ductility demands of 2, with up to half of these bridges exceeding ductility demands

of 6 for both new and old bridges. Bridges at very high or low periods fare significantly better than those in period ranges where the ground motion is amplified due to basin effects.

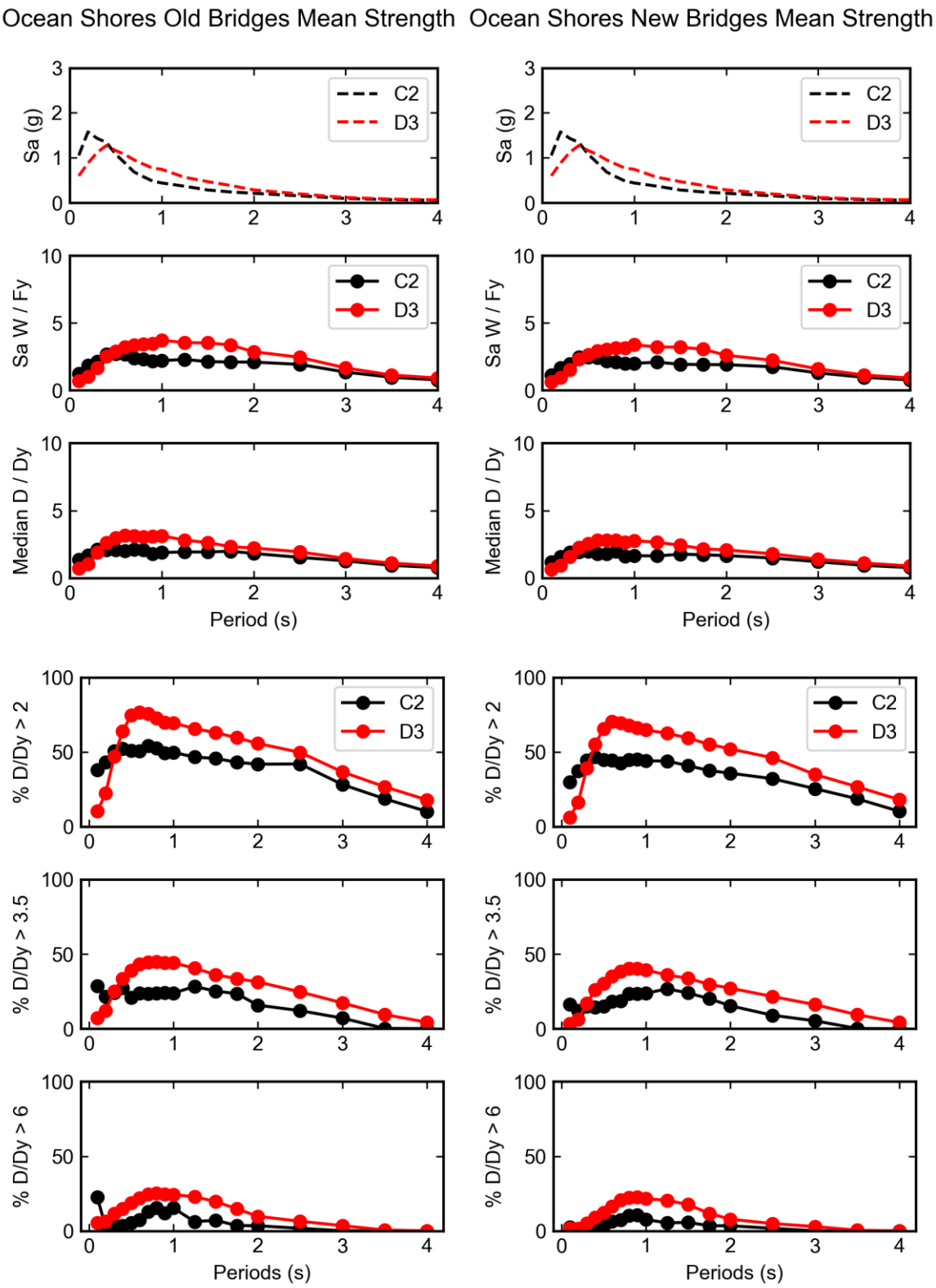

Figure 7.6. Normalized spectral accelerations, median displacement ductility demands, and likelihood of exceeding various ductility limit states for mean strength bridges (Ocean Shores)

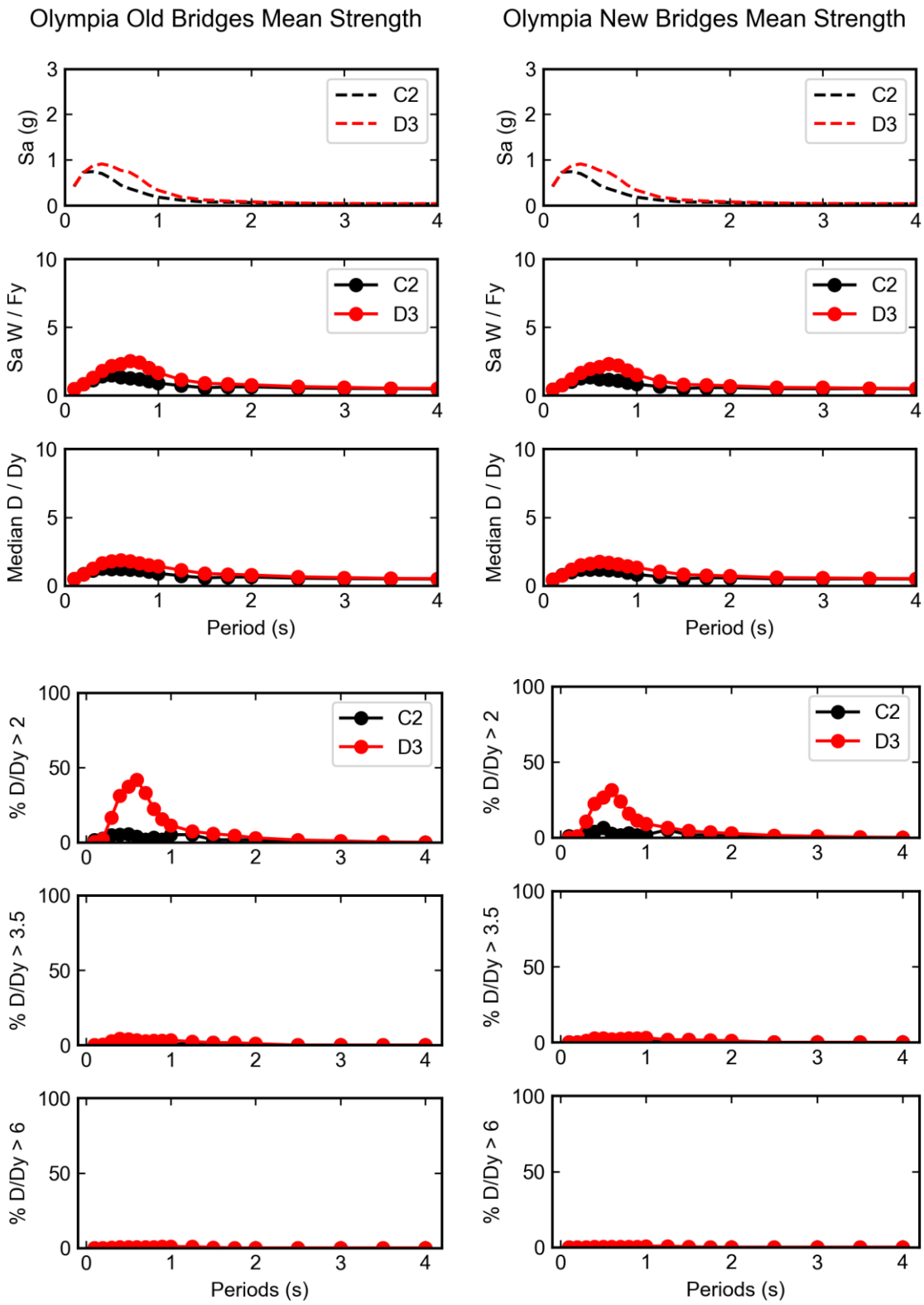

Figure 7.7. Normalized spectral accelerations, median displacement ductility demands, and likelihood of exceeding various ductility limit states for mean strength bridges (Olympia)

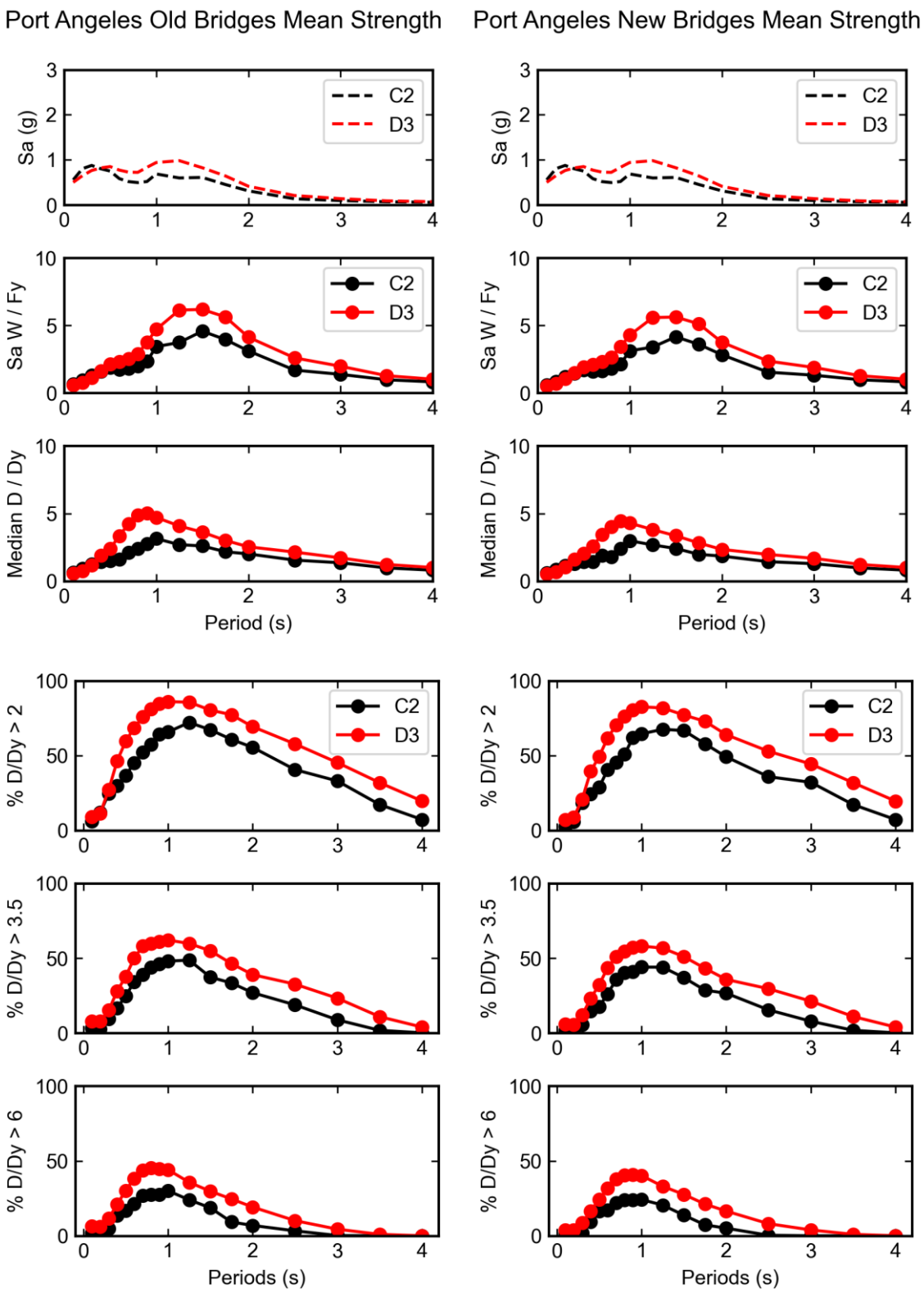

Figure 7.8. Normalized spectral accelerations, median displacement ductility demands, and likelihood of exceeding various ductility limit states for mean strength bridges (Port Angeles)

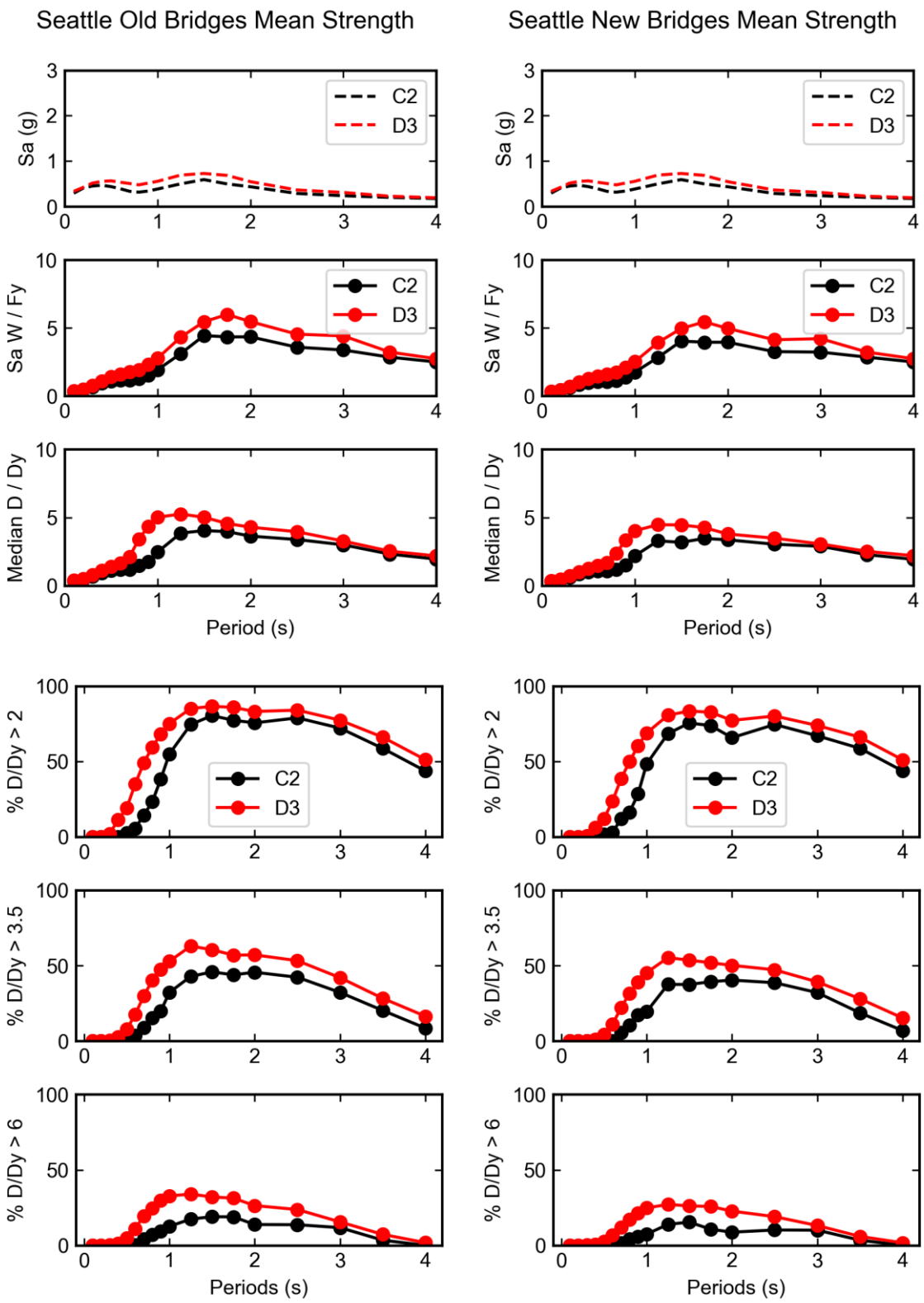

Figure 7.9. Normalized spectral accelerations, median displacement ductility demands, and likelihood of exceeding various ductility limit states for mean strength bridges (Seattle).

7.7 SPECTRAL ACCELERATIONS AND DUCTILITY DEMANDS FOR REDUCED STRENGTH

Figure 7.10 shows equivalent plots for the Seattle for bridges with strengths one standard deviation below the mean (denoted as “reduced strength”). The trends with location, period, and soil type are all similar to those for mean strength bridges. Reduced strength bridges in Seattle almost uniformly exceed ductility demands of 2 for bridges with periods above 1 second. Results for all cities and soil types for reduced strength bridges can be found in Appendix B.

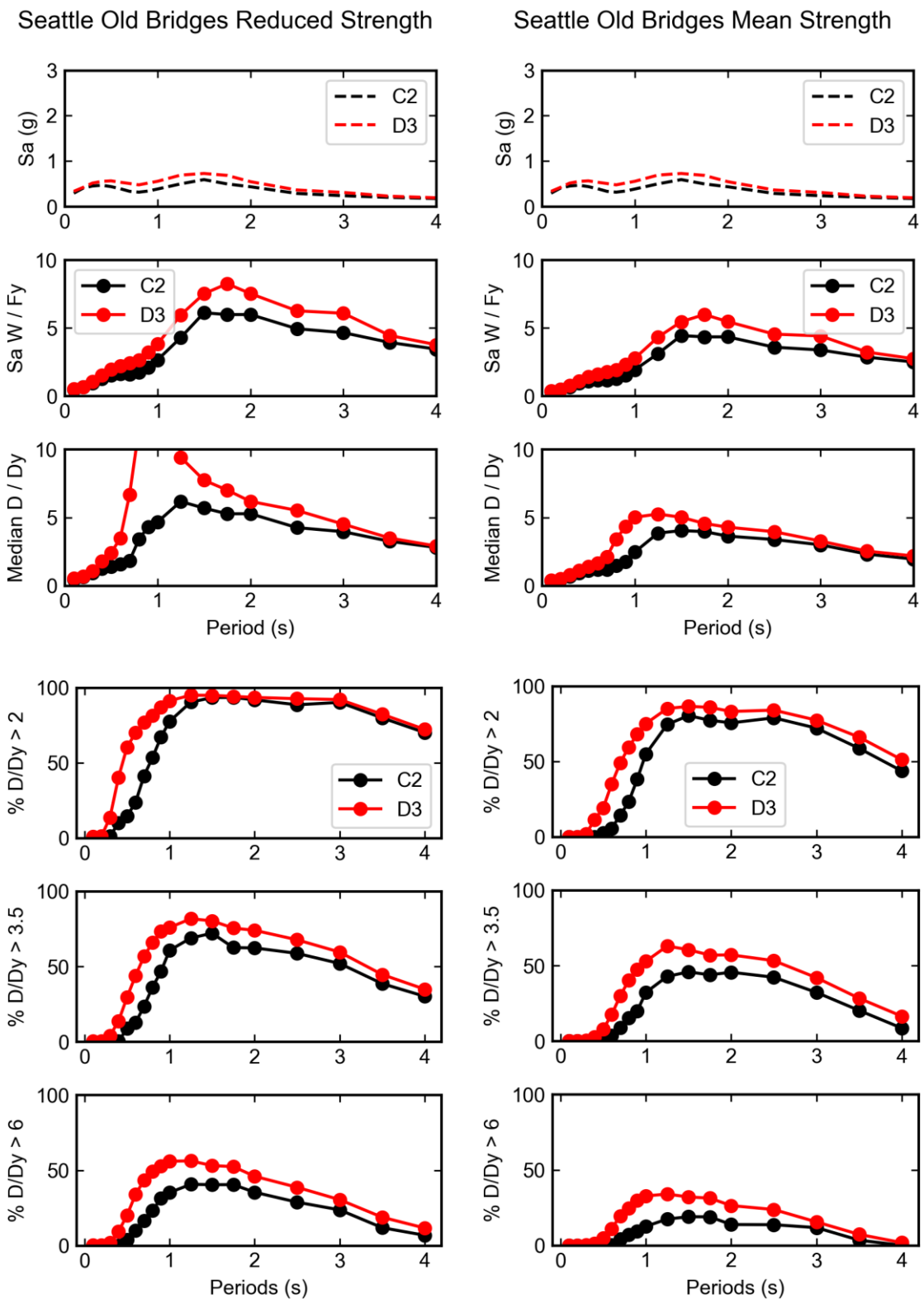

Figure 7.10. Comparison of spectral accelerations, median displacement ductility demands, and likelihood of exceeding ductility limit states for mean and reduced strength bridges

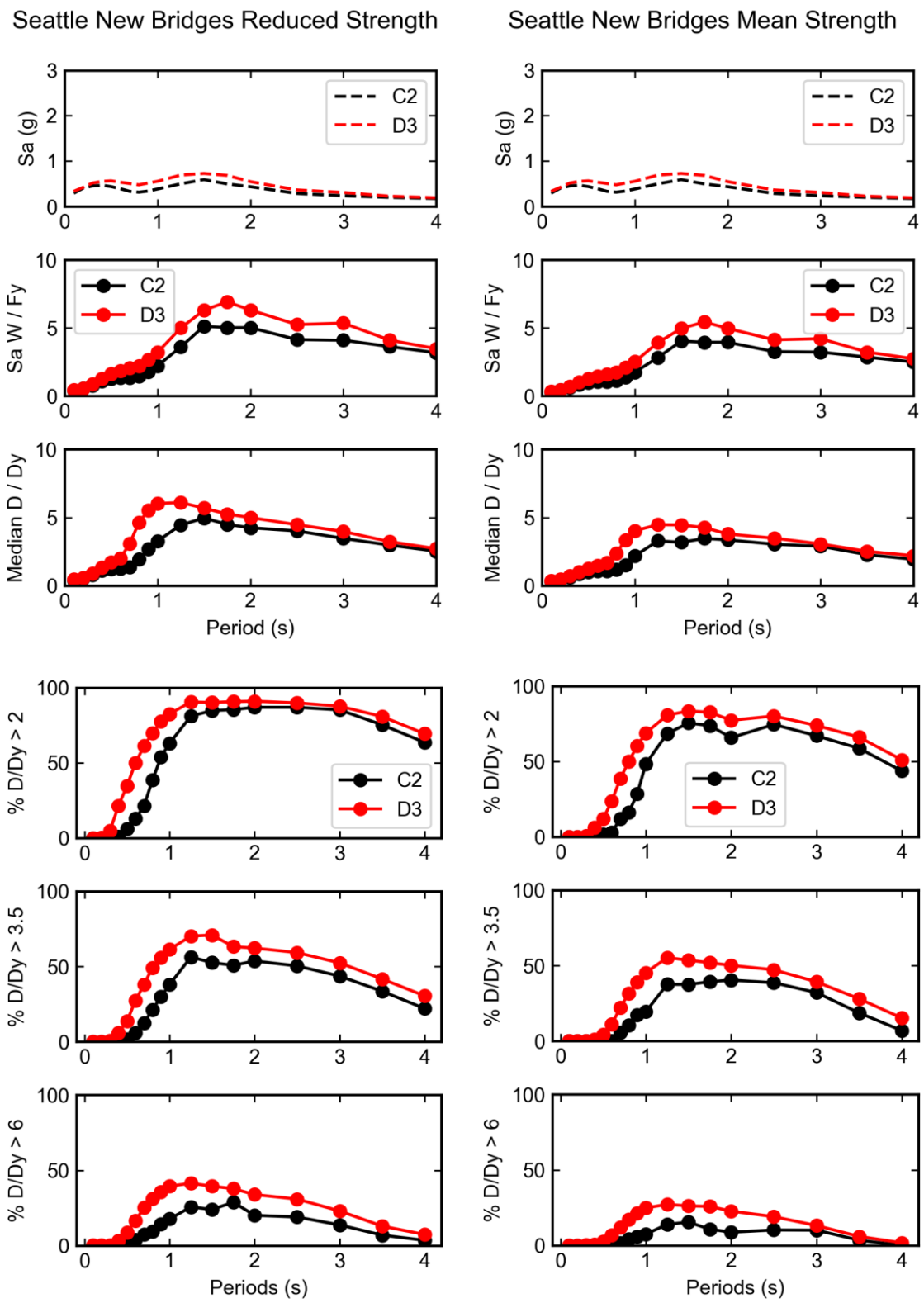

Figure 7.10. Comparison of spectral accelerations, median displacement ductility demands, and likelihood of exceeding ductility limit states for mean and reduced strength bridges (continued)

Figures 7.6 and 7.7 help demonstrate the importance of location, soil conditions, and basin effects on ground motions. Bridges in Olympia, a city outside the basin, are relatively undamaged by the simulated M9 motions. In Seattle and Port Angeles, located on a deep and shallow basin, respectively, the simulated M9 motions are amplified between periods of 1 and 2 seconds, and result in much more widespread damage in this period range. Ocean Shores, not on a basin but located on the Pacific coast close to the fault, has relatively strong ground motions especially at low periods, and shows a moderate amount of damage across a range of periods. In general, softer soils result in higher levels of ductility demand except at very low periods, while new bridges show only slightly lower ductility demands than older bridges. Bridges with strengths one standard deviation below the mean were significantly more likely to exceed the given ductility thresholds across all periods and soil types.

7.8 SPALLING AND BAR BUCKLING

The displacement demands described above can be used to produce estimates of the likelihood of various column damage states. Results are presented here for two damage states, concrete spalling and longitudinal bar buckling. These two damage states were chosen because spalling generally represents the first visible damage to a column that may require repairs, while bar buckling represents a more severe form of damage that may require long-term bridge closure and expensive repairs. For spalling, probabilities were calculated using fragility curves developed by Berry and Eberhard (2008). The fragility functions are lognormal cumulative probability functions with the median drift ratios causing spalling given as:

$$\text{Spalling: } \frac{\Delta_{sp,calc}}{L}(\%) = 1.6\left(1 - \frac{P}{A_g f_c'}\right)\left(1 + \frac{L}{10D}\right) \qquad \text{(Eq. 7-1)}$$

Similarly, fragility functions for bar buckling from Berry and Eberhard (2005) where the median drift ratio causing bar buckling is given by:

$$\text{Buckling: } \frac{\Delta_{bb,calc}}{L}(\%) = 3.25\left(1 + k_{e,bb}\rho_{eff}\frac{d_b}{D}\right)\left(1 - \frac{P}{A_g f_c'}\right)\left(1 + \frac{L}{10D}\right) \quad \text{(Eq. 7-2)}$$

K_{e_bb} was taken as 150, ρ_{eff} was taken as 0.0 for old bridges and 0.008 for new bridges, d_b/D was taken as 1/25, $P/A_g f'_c$ was taken as 0.05, and L and L/D were calculated using the relationships between column lengths and period discussed in Chapter 4.

Figures 7.11 and 7.12 show the probabilities of bar buckling and spalling for four cities. Complete results for all cities and soil classes are provided in Appendix C. The trends with location, period, and soil class are all very similar to the trends observed for ductility demand. In the basin cities of Seattle and Port Angeles, probability of spalling peaks at roughly 75% at periods of around 1 second for bridges located on D3 soils. In Ocean Shores, probability of

spalling peaks at roughly 60% for periods around 0.8 seconds, while in Olympia, spalling probability peaks at only 25% on D3 soils and is negligible for bridges on stiffer soils. Across all four cities, probability of bar buckling is lower than it is for spalling, with probability of bar buckling peaking at close to 50% in Seattle and Port Townsend, 30% in Ocean Shores, and essentially negligible in Olympia.

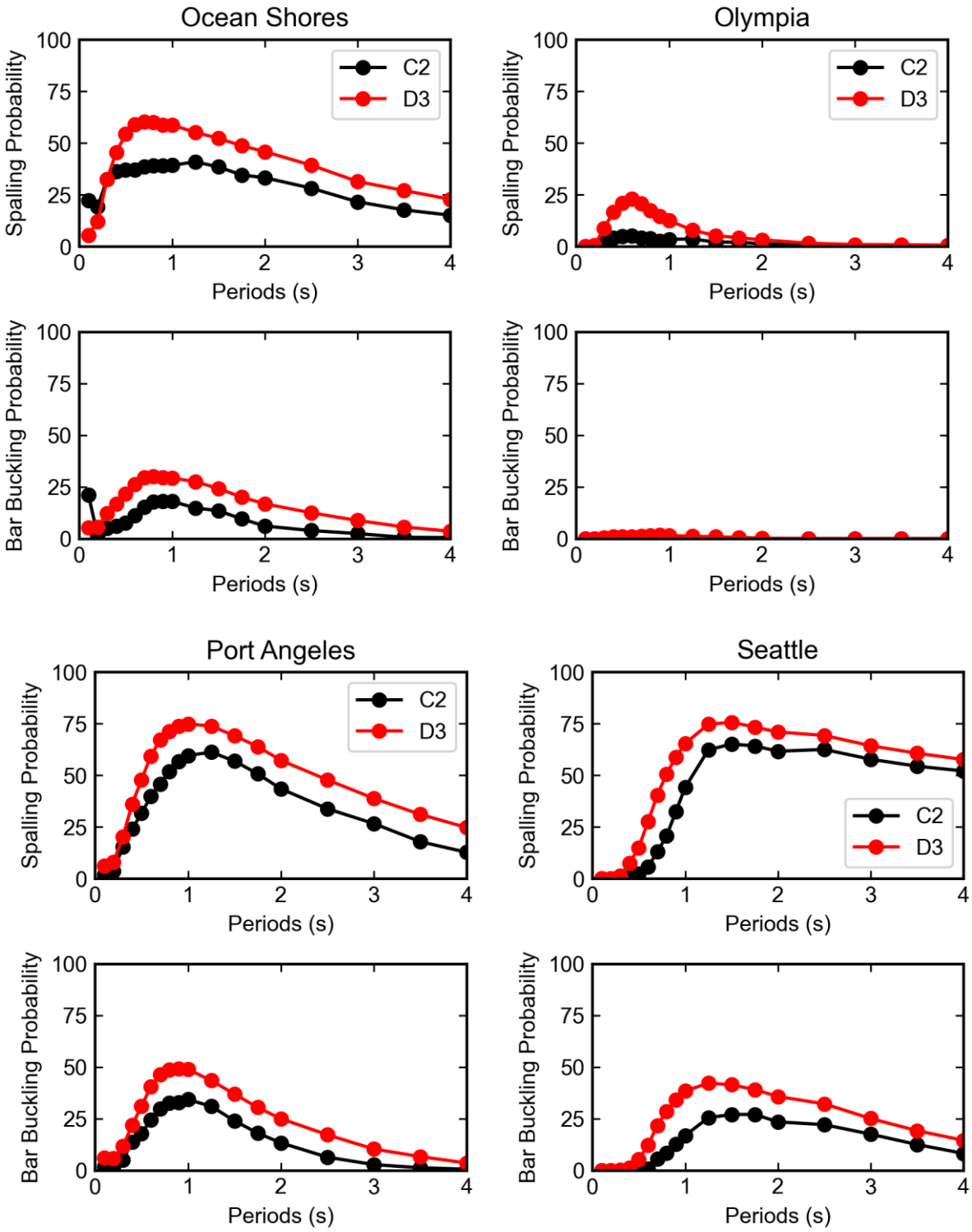

Figure 7.11. Probability of spalling and bar buckling for old bridges with mean strengths.

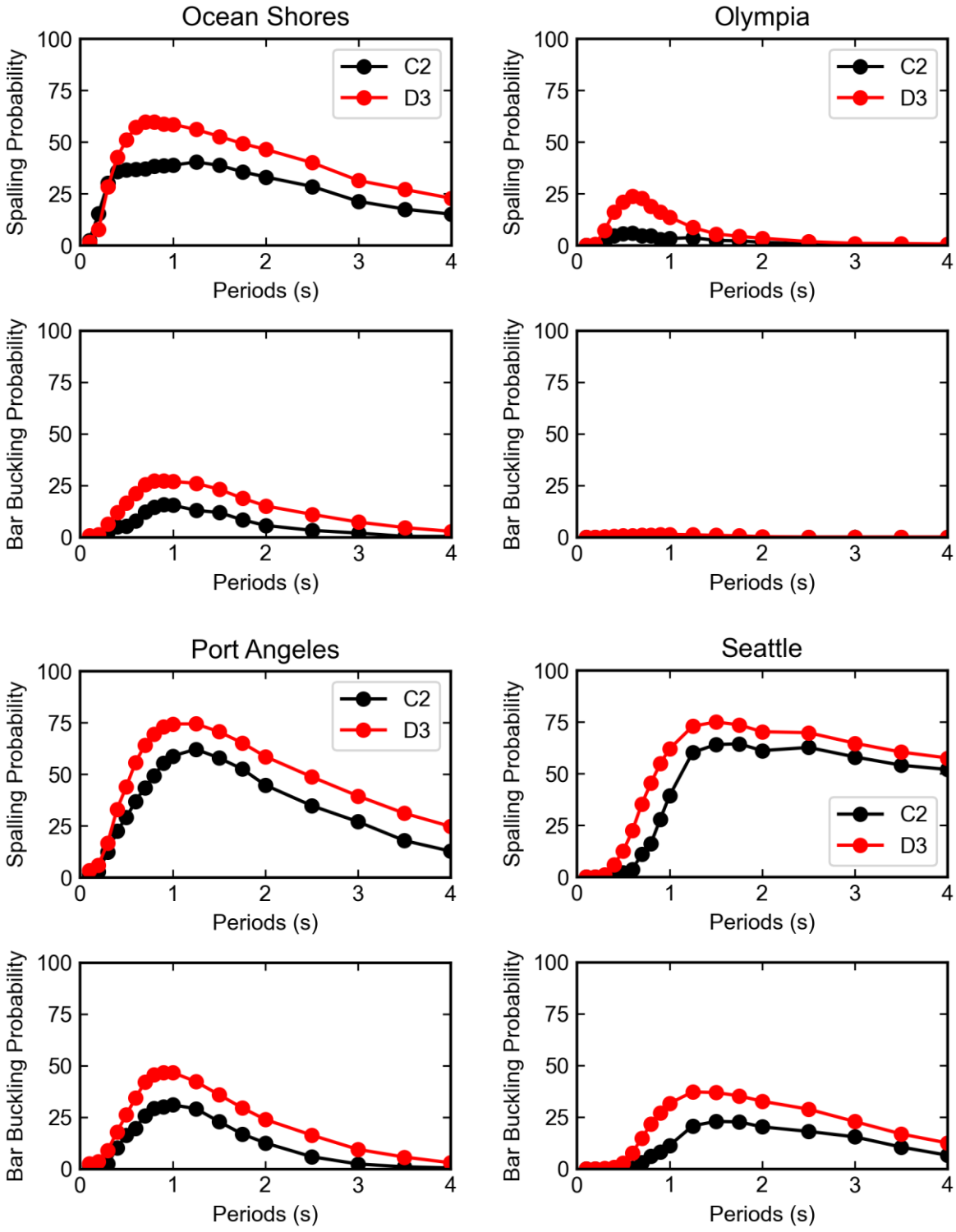

Figure 7.12. Probability of spalling and bar buckling for new bridges with mean strengths.

Chapter 8: Fragility Curves

This chapter discusses the development of fragility curves from the displacement ductility data reported in Chapter 7. Fragility is expressed in terms of likelihood of exceeding various ductility demands. In this chapter, fragility curves are developed as a function of both spectral acceleration, S_a, and effective spectral acceleration, $S_{a,eff}$, a measure of spectral acceleration which takes into account the spectral shape and duration of a ground motion (Marafi et al. 2016).

8.1 FRAGILITY AS A FUNCTION OF SPECTRAL ACCELERATION

From the ductility demand data in Chapter 7, fragility curves were developed for new and old bridges in each location. For a given location and bridge age, spectral accelerations and ductility demands were calculated for each of the soil-adjusted ground motions at every period considered in the parametric study, for both mean and reduced strength oscillators. The results of these analyses were then binned by spectral acceleration divided by the normalized base shear strength, F_y / W, and within each bin, the likelihood of exceeding ductility demands of 2, 3.5, 6, and 8 were calculated. For each ductility demand, a cumulative distribution function was calculated using maximum likelihood estimation.

Fragility curves based on spectral acceleration can be seen in Figure 8.1. Each fragility curve for a given location and age represents demands for all 30 ground motions, the baseline motions and the soil-adjusted motions for all 4 soil types, all 30 soil profiles within each soil type, for both mean and reduced strength bridges, across all periods, in both the x and y directions. Fragility curves for all locations, as well as equations for the fitted CDFs, can be found in Appendix D.

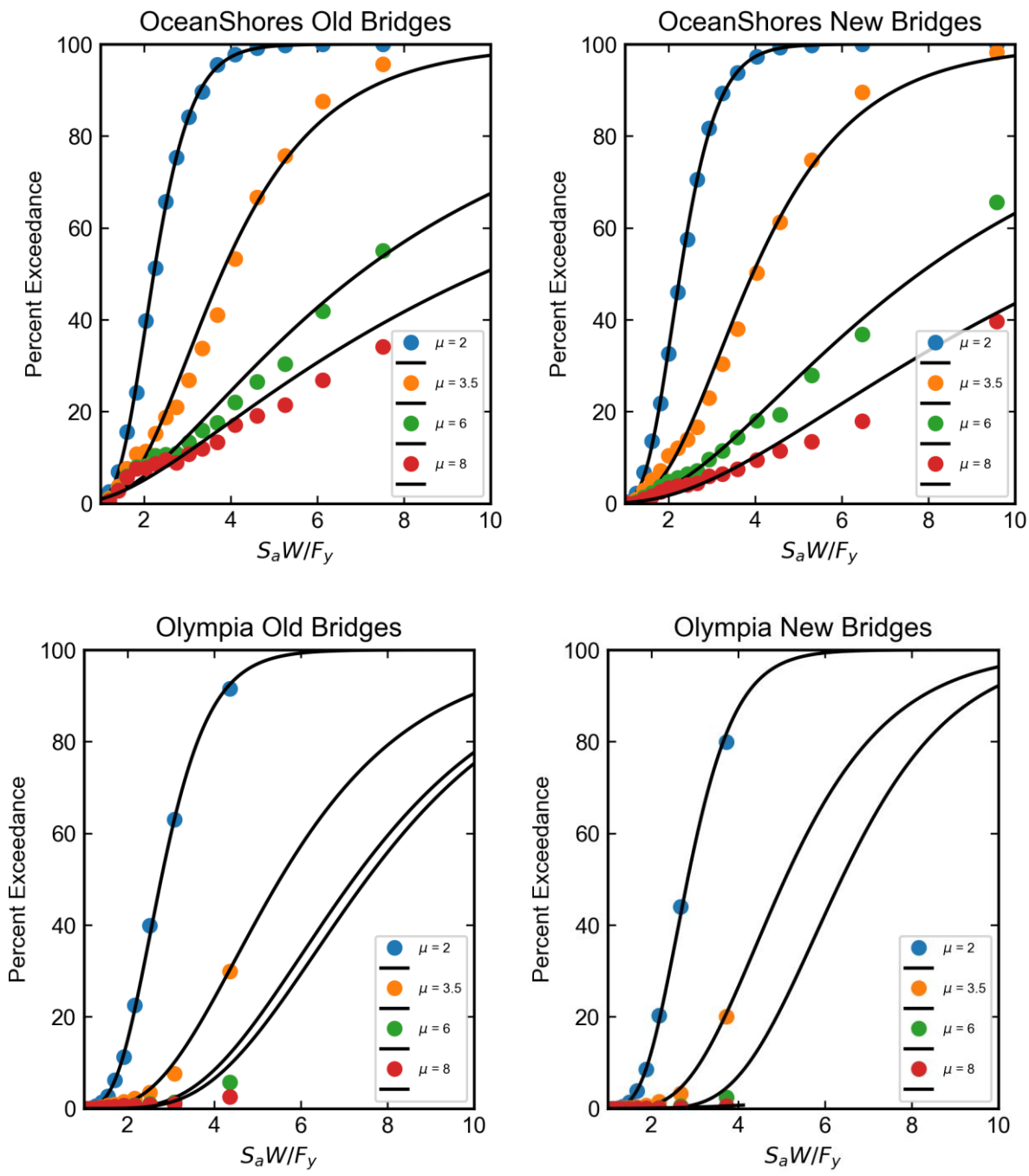

Figure 8.1. Fragility curves based on spectral acceleration.

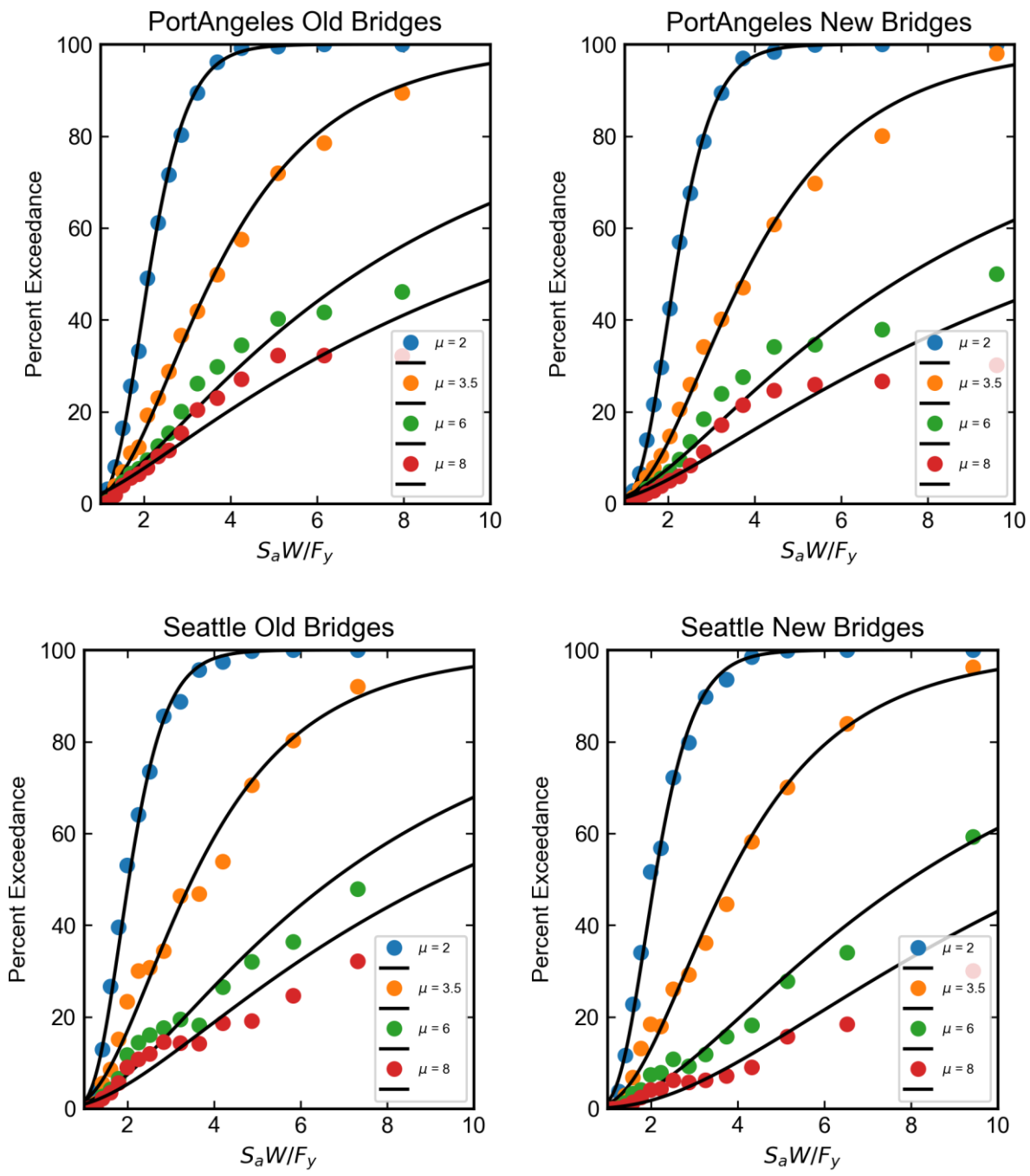

Figure 8.1. Fragility curves based on spectral acceleration (continued).

As expected from the discussion in Chapter 7, the fragilities for new and old bridges are similar at each location, with older bridges having slightly higher probabilities of exceeding each ductility threshold for a given S_aW / F_y value. Particularly for the higher ductility thresholds, the fragility curves are relatively flat and the data show moderate scatter from the fitted cumulative distribution functions. For a ductility threshold of 2, 50% exceedance is reached at a normalized spectral acceleration of between 2 and 3 across all four locations for both new and old bridges. At normalized spectral accelerations above 4, nearly all bridges exceed ductility demands of 2. For a ductility threshold of 8, 50% exceedance is not reached until normalized spectral accelerations ranging from 7 to more than 10.

In addition, it can be seen that the fragility curves for different locations vary significantly, in part because of the effects of different spectral shapes at each of the locations. Olympia, outside the basin and far from the fault, has lower probabilities of exceeding all ductility thresholds. Sites inside the basin have higher probabilities of exceeding the ductility demands, as do sites closer to the fault such as Ocean Shores. The differing spectral shapes are influenced by basin effects and distance to the fault, resulting in spectral acceleration being a less than ideal measure for predicting bridge fragilities.

8.2 FRAGILITY AS A FUNCTION OF EFFECTIVE SPECTRAL ACCELERATION

Fragility curves were also calculated for each city using effective spectral acceleration, $S_{a,eff}$, a measure of ground motion intensity which takes into account spectral acceleration, ground motion duration, and spectral shape. $S_{a,eff}$ was calculated for each ground motion using the equations outlined in Marafi et al (2019) as:

$$S_{a,eff}(T_n) = S_a(T_n) \cdot \gamma_{dur} \cdot \gamma_{shape} \qquad \text{(eq. 8-1)}$$

$S_a(T_n)$ is the spectral acceleration at a given period, γ_{dur} is a factor related to the ground motion duration, and γ_{shape} is a factor related to the shape of the response spectrum for a given ground motion. The duration factor, γ_{dur}, is taken as:

$$\gamma_{dur} = (D_s / 12T_n)^{C1} \quad \text{(eq. 8-2)}$$

D_s is the significant duration of the ground motion computed at the 5% - 95% thresholds, and C1 is taken as 0.1 for collapse estimates and 0.0 for ductility demand estimates. The shape factor, γ_{shape} is taken as:

$$\gamma_{shape} = (SS_a(T_n, \alpha) / SS_{a,0})^{C2} \quad \text{(eq. 8-3)}$$

α is taken as $\mu^{0.5}$, where μ is the target level of ductility demand, $SS_{a,0}$ is taken as $\ln(\alpha) / (\alpha - 1)$, C2 is taken as $0.65 * (\mu - 1)^{0.5}$ with an upper limit of 1, and $SS_a(T_n, \alpha)$ is the spectral shape factor for a ground motion, computed as:

$$SS_a(T_n, \alpha) = \frac{\int_{T_n}^{\alpha T_n} S_a(T)dT}{S_a(T_n)(\alpha-1)T_n} \quad \text{(eq. 8-4)}$$

Taken together, these equations produce a measure of ground motion intensity, $S_{a,eff}$, which can more effectively predict ductility demands than S_a alone. Fragility curves using $S_{a,eff}$ were computed using an identical procedure to that described in Section 8.1, but using $S_{a,eff}$ in place of S_a. Figure 8.2 below shows fragility curves produced using $S_{a,eff}$ divided by the normalized base shear strength, F_y / W, for four selected cities for new and old bridges, at a variety of ductility demand limit states. For some ductility states, not enough data was available to fit a cumulative distribution function to the data; in these cases, the fitted CDF is omitted. Fragility curves for all locations, as well as equations for the fitted CDFs, can be found in Appendix D.

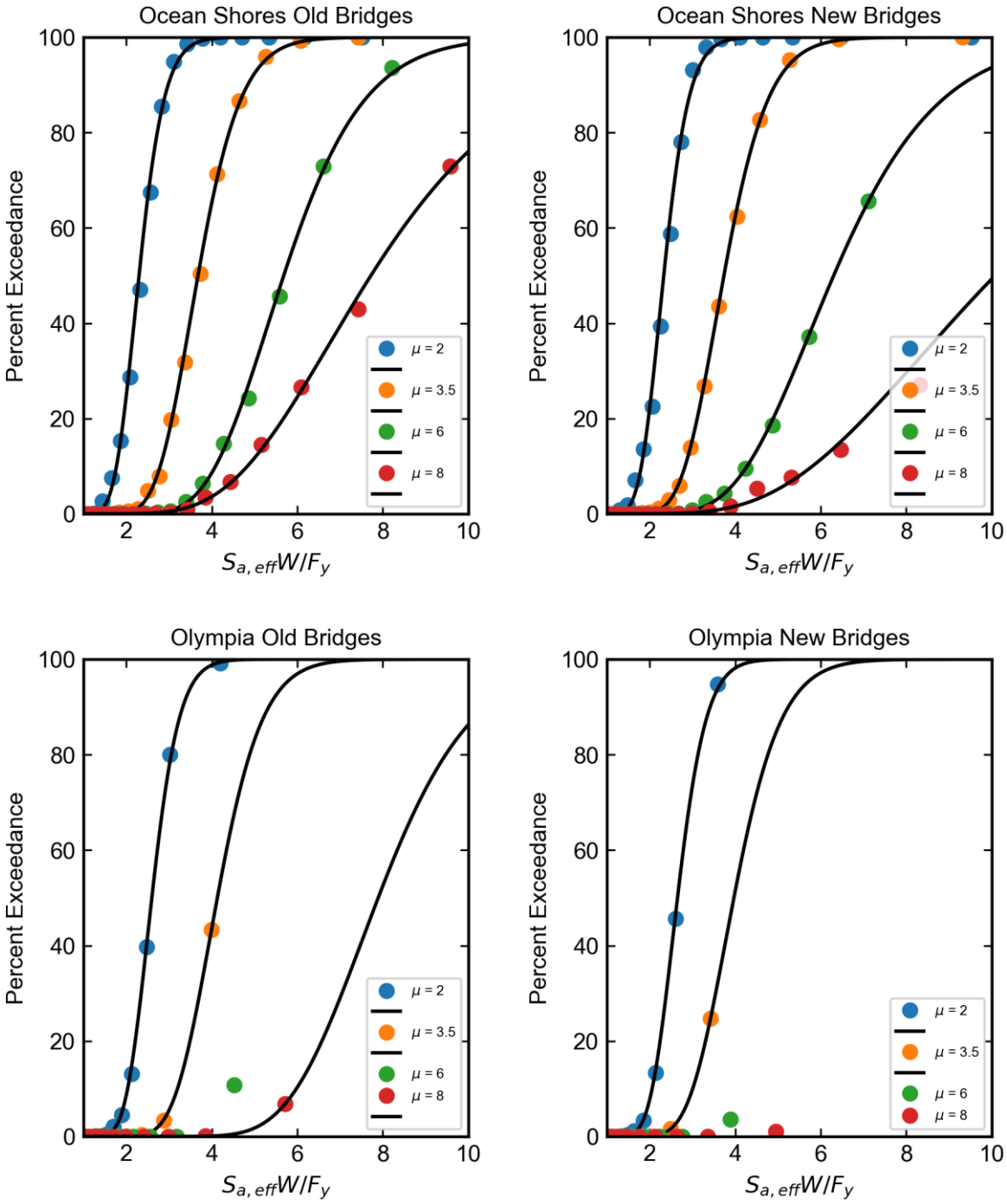

Figure 8.2. Fragility curves based on effective spectral acceleration.

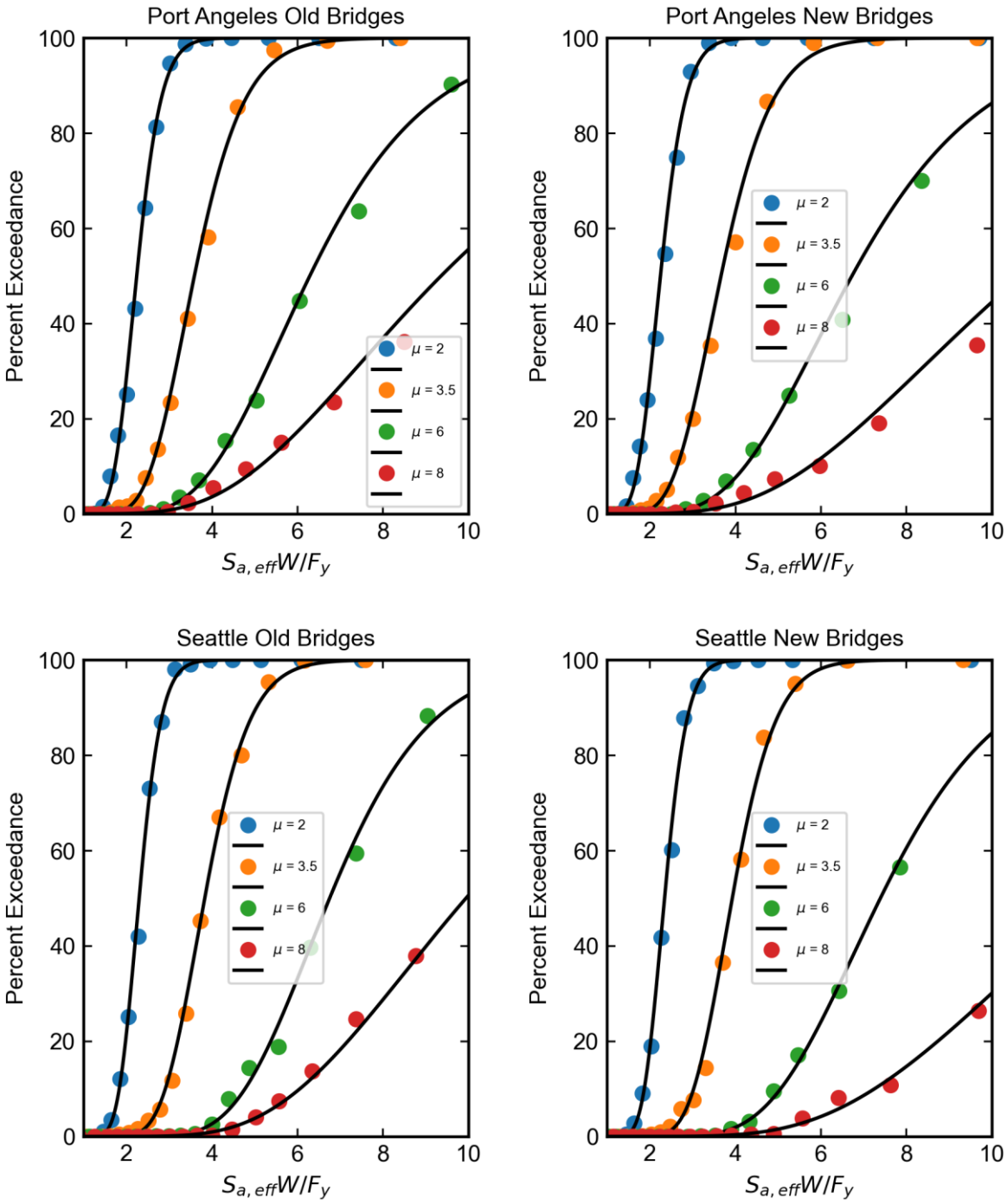

Figure 8.2. Fragility curves based on effective spectral acceleration (continued).

Similarly to the fragility curves based on spectral acceleration, the fragilities based on effective spectral acceleration are similar for new and old bridges, with older bridges showing slightly higher probabilities of exceeding each level of ductility demand. Across all four locations and for both new and old bridges, 50% exceedance is reached for a ductility threshold of 2 at a normalized effective spectral acceleration value of between 2 and 2.5, while for normalized $S_{a,eff}$ above 3.5, nearly all bridges will exceed ductility demands of 2 at all locations.

Several advantages of effective spectral acceleration are apparent when comparing Figures 8.1 and 8.2. First, the fragilities computed using effective spectral acceleration are relatively location-independent. Figure 8.3 shows comparisons between the fragility curves at a variety of locations for ductility demands of 2 and 3.5. Fragility curves are shown for all cities for which enough data was available to produce reliable curves. While the fitted cumulative distribution functions using S_a vary significantly between locations, the $S_{a,eff}$ CDFs show strong consistency among the 10 cities. The CDFs computed using effective spectral accelerations can therefore be used to evaluate fragility for any location. Additionally, the fitted CDFs produced using effective spectral acceleration are much steeper and show less scatter than those produced using spectral acceleration alone.

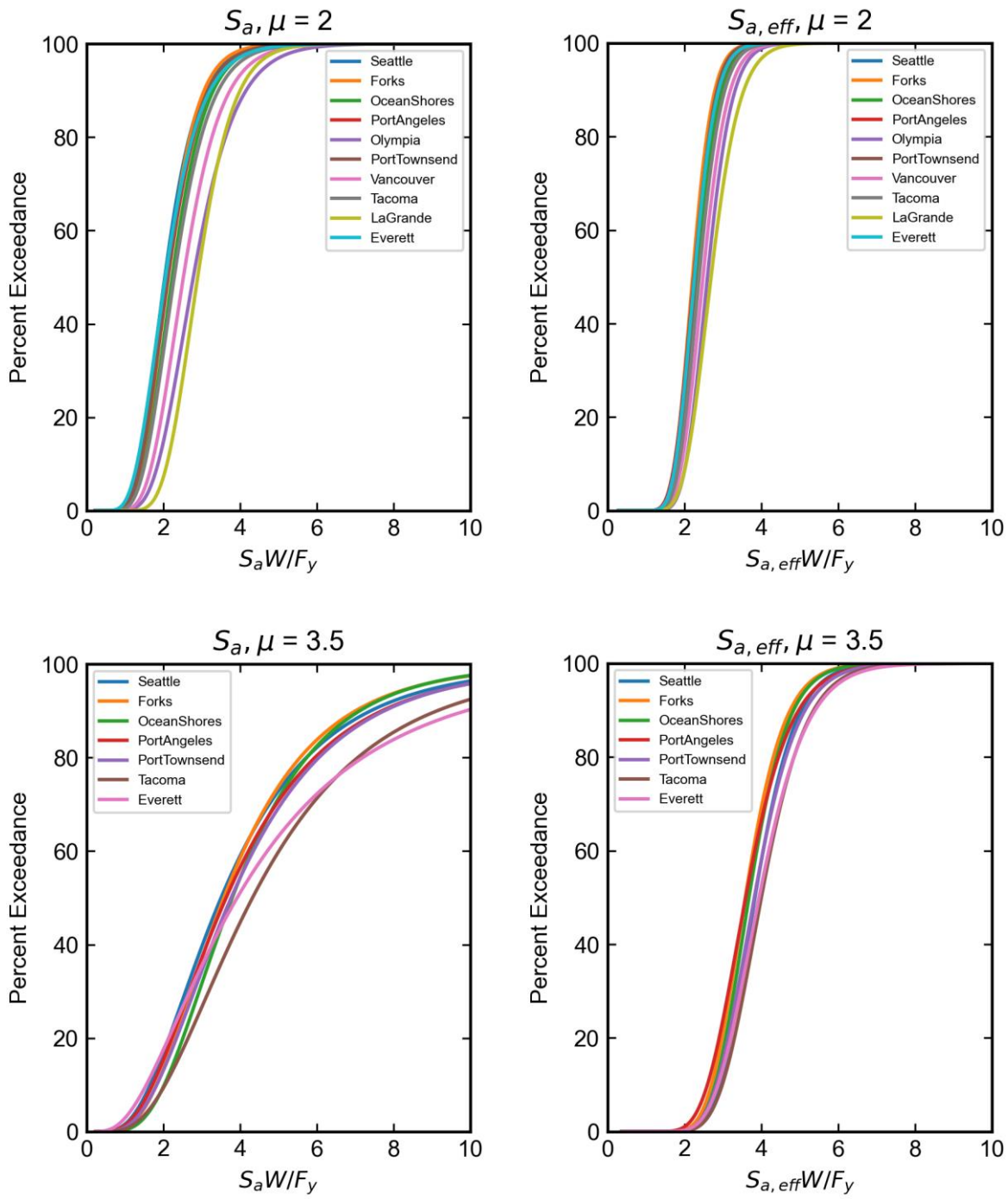

Figure 8.3. Comparison of fragilities calculated using S_a and $S_{a,eff}$ at all locations for which data was available for ductility demand thresholds of 2 and 3.5 for old bridges.

Because the computed fragility curves using $S_{a,eff}$ are location-independent, data from all 10 cities can be combined to produce a single set of fragility curves that are valid for any location across Western Washington. Figure 8.4 shows fragility curves computed using $S_{a,eff}$ data from all 10 cities for new and old bridges. Fragility curves were computed using the same procedure described in Section 8.1, but data from all 10 cities were combined to produce one set of fragility curves. Fragilities are shown for the same four ductility thresholds as in Figures 8.1 and 8.2. As with the city-specific fragilities, the combined fragilities are relatively similar for new and old bridges at lower ductility demands. For the larger ductility thresholds (D/Dy = 6 and 8), the old bridges are somewhat more likely to exceed the threshold than new bridges. This occurs because of the different ductility capacities assumed for new and old bridges (see Section 5.3 for detailed calibration of ductility capacities). It is important to note that shear and flexure-shear failures are not considered here, and that large ductility demands may result in such failures.

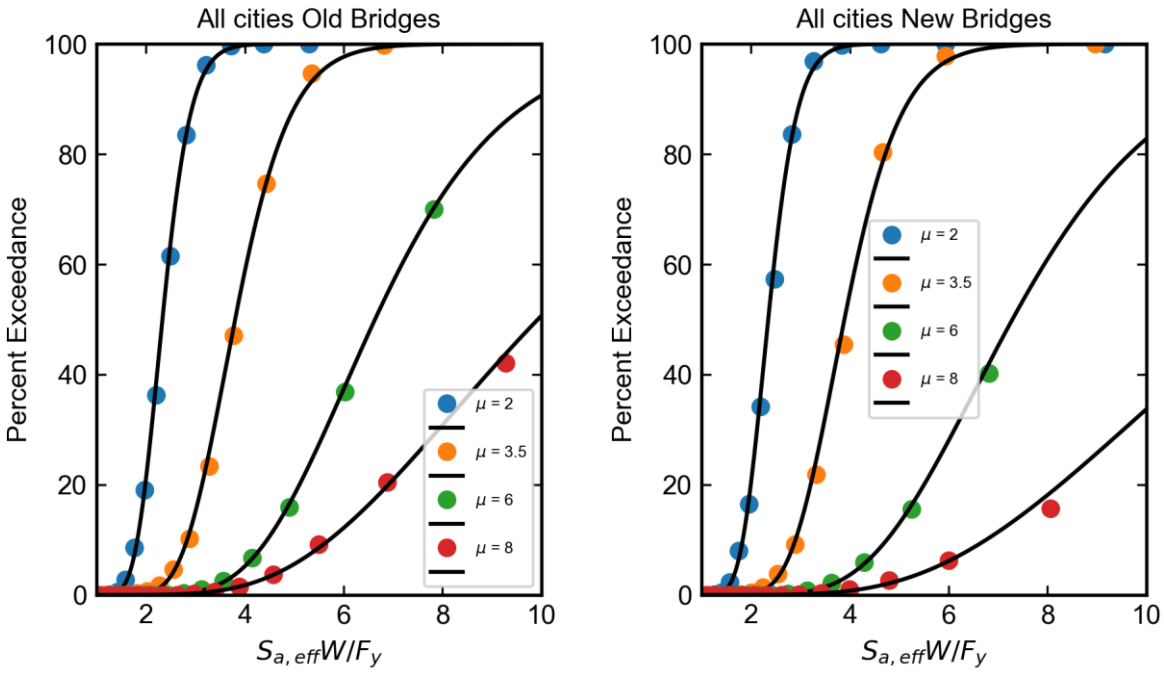

Figure 8.4. Fragility curves combining data for all 10 cities, using effective spectral acceleration.

Chapter 9: Conclusions

This research was conducted to estimate the impacts of an M9 earthquake on bridges in Western Washington State. The study built on the results of physics-based simulations of M9 earthquake (Frankel et al. 2018), the results of modeling of the effect of local site conditions (De Zamacona 2019), and a detailed database of WSDOT bridges along lifelines in the Puget Sound region.

Seattle and many of the surrounding cities on the Puget Sound are underlaid by deep sedimentary basins. Simulated M9 ground motions that take into account the effects of these subsurface sedimentary basins were found to have spectral accelerations that exceeded design spectral accelerations for bridges in Western Washington, which are currently calculated without taking into account basin effects.

9.1 RESEARCH APPROACH

The simulated, soil-adjusted M9 motions were used to conduct a parametric study of single-degree-of-freedom systems in order to analyze the impact of an M9 event on highway bridges in Washington. These SDOF models were subjected to soil-adjusted simulated M9 ground motions corresponding to 10 cities across Washington State. The 10 representative cities were divided into four categories: Coastal cities without a basin (Ocean Shores and Forks), inland cities without a basin (Olympia, Vancouver, and La Grande), inland cities with a shallow sedimentary basin (Port Townsend and Port Angeles), and inland cities with a deep basin (Seattle and Everett), and results were discussed for cities representing each category.

Chapters 3, 4, and 5 discuss the use of a WSDOT bridge database to calibrate the SDOF models to have properties representative of highway bridges in Western Washington. These

properties included strength, stiffness, backbone response and cyclic deterioration. Chapter 6 presents the full range of parameters that were varied. Detailed discussions of the impact of geographic location, bridge age, bridge strength and basin effects on the response of the SDOF bridge models were presented in Chapter 7 for selected cities and soil types (full results are available in Appendices B and C). Finally, fragility curves were developed for new and old bridges at each location using two measures of ground motion intensity: S_a and $S_{a,eff}$. The following details the conclusions from various sections of the work.

9.1 PROPERTIES OF WSDOT BRIDGES

The Washington State Department of Transportation compiled a database containing information on key parameters for 609 "lifeline" bridges in Western Washington. From the information in this database, estimates were made for the mass, stiffness, and strength of bridges supported by circular columns.

Bridges in the lifeline database were found to be significantly stronger than what would be expected from minimum design strengths, even after accounting for material overstrength (Figure 4.8). Additionally, it was found that a number of important differences existed between bridges built before 1976 and those built after (earthquake design codes for bridges changed significantly in Washington State in about 1976, following the 1971 San Fernando earthquake). Pre-1976 bridges, on average, had significantly lower transverse reinforcement ratios than newer bridges (Figure 3.6). Older bridges also had slightly lower and significantly more variable normalized base shear strengths than new bridges, reflecting the lack of stringent seismic design standards in older design codes (Figure 4.7).

9.2 MODEL CALIBRATION

From the column test data in the UW-PEER Structural Performance Database, it was found that column ductility capacity and cyclic strength and stiffness deterioration were both greatly affected by levels of transverse reinforcement. A material model, the Modified Ibarra-Medina-Krawinkler model (IMK), was calibrated in OpenSEES to match the cyclic force-displacement response of reinforced concrete columns. Parameters for the IMK model controlling ductility capacity and cyclic deterioration were calibrated to match the results of column tests, and simple relationships between these parameters and transverse reinforcement ratio were proposed (Figures 5.6 and 5.8). The results of this column calibration informed the properties of the SDOF oscillators used to conduct the parametric study.

9.3 RESULTS OF SDOF PARAMETRIC STUDY

The simulated M9 ground motions varied significantly among the 10 locations considered, as a result of both distance to the fault and the presence of sedimentary basins (Figure 2.2). Coastal cities without basins but located close to the fault showed high spectral accelerations (S_a) at low periods, and low S_a values at periods above 1 second. Inland cities located outside the basin had low spectral accelerations at all periods between 0 and 4 seconds. In inland cities located on deep or shallow sedimentary basins, the ground motions were amplified between periods of about 1 and 2 seconds, resulting in large spectral accelerations in this period range.

In cities located on deep sedimentary basins, like Seattle, bridges with periods between 1 and 3 seconds were highly likely to exceed ductility demands of 2, and up to 50% exceeded ductility demands of 3.5 for both new and old bridges. Inland cities on shallow sedimentary

basins showed similar levels of damage between periods of about 0.7 and 2 seconds. Coastal cities such as Ocean Shores had moderate levels of damage at periods between 0.5 and 1.5 seconds, with up to 75% exceeding ductility demands of 2. Inland cities without sedimentary basins were largely unaffected by the M9 motions, with only bridges on the softest soils (D3) between periods of 0.4 and 1.0 seconds exceeding ductility demands of 2 (Figures 7.6 – 7.10).

Using the ductility demand data, estimates were made for the probability of spalling and bar buckling of bridge columns (Figures 7.11 and 7.12). The trends for these damage states were similar to those for ductility demand. Inland cities on basins had up to a 75% probability of spalling, and up to 50% probability of bar buckling for bridges on D3 soils. Coastal cities had probabilities that were only slightly lower, peaking at 60% and 30% probabilities of spalling and bar buckling, respectively. Finally, inland cities not located on a sedimentary basin had low probabilities of spalling and negligible probabilities of bar buckling across all period ranges.

From the ductility demand data, fragility curves were constructed using both S_a and $S_{a,eff}$ for various levels of ductility demand (Figures 8.1 and 8.2). It was found that fragility curves produced using S_a showed significant regional variation, while those produced using $S_{a,eff}$ were highly consistent across the 10 locations (Figure 8.3). In addition, the fragility curves produced using $S_{a,eff}$ were much steeper and showed less scatter than those produced using spectral acceleration alone.

9.4 STUDY LIMITATIONS

The results of these analyses come with important caveats. Namely, the analyses conducted as part of this study:

- Neglected the resistance provided by abutments

- Did not consider the behavior of very soft soils (e.g., site classes E and F). The interaction between the site profiles with long periods might exacerbate the amplification of long-period components of motions observed in sedimentary basins.
- Neglected the likelihood of span unseating, under the assumption that previous WSDOT retrofit efforts have precluded this failure mode
- Neglected the likely correlation between ductility demand and performance levels for a given M9 event. In other words, some events might lead to much larger (or smaller) demands and damage than others, leading to much larger (or smaller) damage levels for a particular event.
- Most importantly, shear or foundation failures were not considered. Both of these failure modes might be critical in older bridges with low levels of transverse reinforcement.

9.5 FUTURE WORK

There are a number of opportunities to further the work presented in this report. The WSDOT lifeline bridge database did not contain information on bridge abutments, and contained only bridges located in and around the Seattle area. Modifying the response of the SDOF oscillators to account for the presence of abutments would help to create a more accurate representation of the behavior of highway bridges. More detailed bridge models, such as multiple-degree-of-freedom systems, could also be used to provide more accurate predictions of bridge response.

It is possible that bridges outside the Seattle area were designed to different strength levels. Future work could include the calculation of normalized base shear strengths for bridges outside the Seattle area using the procedures described in this report. This would help to more accurately reflect the bridge inventory in Western Washington.

In addition, soil liquefaction and shear or flexure-shear failure of bridge columns were not considered in this report. It is likely that both factors would contribute to collapse risk during an M9 earthquake. Evaluating these factors would provide a more comprehensive assessment of the total risk to Washington highway bridges from an M9 event.

Bibliography

AASHTO. 2017. LRFD Bridge Design Specifications. American Association of State Highway and Transportation Officials.

Ahdi, S.K, Stewart, J., Ancheta, T, Kwak, D., and Mitra, D. 2017. "Development of VS Profile Database and Proxy-based Models for VS30 Prediction in the Pacific Northwest Region of North America." Bulletin of the Seismological Society of America 107: 1781-1801.

Arthur Frankel, Erin Wirth, Nasser Marafi, John Vidale, and William Stephenson; Broadband Synthetic Seismograms for Magnitude 9 Earthquakes on the Cascadia Megathrust Based on 3D Simulations and Stochastic Synthetics, Part 1: Methodology and Overall Results. Bulletin of the Seismological Society of America 2018; 108 (5A): 2347–2369. doi: https://doi.org/10.1785/0120180034

Berry, Michael, and Eberhard, Marc, 2007. "Performance Modeling Strategies for Modern Reinforced Concrete Bridge Columns," PEER-2007/07, Pacific Earthquake Engineering Research Center, University of California, Berkeley.

Berry, Michael, and Eberhard, Marc. 2005. "Practical Performance Model for Bar Buckling." Journal of Structural Engineering.

Chandramohan, Reagan, Baker, Jack, and Deierlein, Gregory. 2019. "Quantifying the Influence of Ground Motion Duration on Structural Collapse Capacity Using Spectrally Equivalent Records". Earthquake Spectra, Vol. 32 Issue 2, 927-950.

De Zamacona Cervantes, Gloria, 2019. "Response of Idealized Structural Systems to Simulated M9 Cascadia Subduction Zone Earthquakes Considering Local Soil Conditions." Master's Thesis, University of Washington, Seattle.

Elwood, Kenneth, and Eberhard, Marc, 2009. "Effective Stiffness of Reinforced Concrete Columns," ACI Structural Journal/July-August 2009: 476-484.

Erin A. Wirth, Arthur D. Frankel, Nasser Marafi, John E. Vidale, and W. J. Stephenson; Broadband Synthetic Seismograms for Magnitude 9 Earthquakes on the Cascadia Megathrust Based on 3D Simulations and Stochastic Synthetics, Part 2: Rupture Parameters and Variability. Bulletin of the Seismological Society of America 2018; 108 (5A): 2370–2388. doi: https://doi.org/10.1785/0120180029

FEMA (Federal Emergency Management Agency). 1995. NEHRP Recommended Seismic Provisions for Seismic Regulations for New Buildings (FEMA 222A and 223A).

Frankel, Arthur, Wirth, Erin, Marafi, Nasser. 2018. "The M9 Project Ground Motions", in The M9 Project Ground Motions. DesignSafe-CI. https://doi.org/10.17603/DS2WM3W.

Haselton, Curt, Liel, Abbie, Lange, Sarah, and Deierlein, Gregory. 2008. "Beam-Column Element Model Calibrated for Predicting Flexural Response Leading to Global Collapse of RC Frame Buildings." PEER Report 2007/03.

Kaklamanos, J., Bradley, B. A., Thompson, E. M., and Baise, L. G. 2013. Critical parameters affecting bias and variability in site- response analyses using KiK- net downhole array data. *Bulletin of the Seismological Society of America*, *103*(3), 1733-1749.

Khaleghi, Bijan. 2019. Memo to All Design Section Staff. Washington State Department of Transportation Bridge and Structures Office.

Lignos, D.G. and Krawinkler, H. 2012. "Sidesway collapse of deteriorating structural systems under seismic excitations," Rep.No.TB 177, The John A. Blume Earthquake Engineering Research Center, Stanford University, Stanford, CA.

Mander, J. B.; Priestley, M. J. N.; and Park, R., 1988. "Theoretical Stress-Strain Model for Confined Concrete," Journal of Structural Engineering, V. 114, No. 8: 1804-1826.

Marafi, N.A., Eberhard, M.O., Berman, J.W., Wirth, E.A., and Frankel, A.D. (2017). "Effects of Deep Basins on Structural Collapse During Large Subduction Zone Earthquakes." Earthquake Spectra, 33(3), 963-997. https://doi.org/10.1193/071916EQS114M

Marafi, Nasser, Eberhard, Marc, Berman, Jeffrey, Wirth, Erin, and Frankel, Arthur. 2017. "Effects of Deep Basins on Structural Collapse during Large Subduction Earthquakes." Earthquake Spectra. 33(3), 963-997.

Marafi, Nasser, Makdisi, Andrew, Eberhard, Marc, and Berman, Jeffrey. 2020. "Performance of RC Core-Wall Buildings during Simulated M9 Cascadia Subduction Zone Earthquake Scenarios". Journal of Structural Engineering, Volume 146, Issue 2.

Marafi, Nasser, Berman, Jeff, and Eberhard, Marc, 2016. "Ductility-dependent intensity measure that accounts for ground-motion spectral shape and duration". Earthquake Engineering & Structural Dynamics 45, 653–672.

Marafi, Nasser, Eberhard, Marc, and Berman, Jeffrey. 2019. "Impacts of Simulated M9 Cascadia Subduction Zone Motions on Idealized Systems". Earthquake Spectra, Vol 35, Issue 3, 2019.

Pacific Northwest Seismic Network. "Cascadia Subduction Zone." https://pnsn.org/outreach/earthquakesources/csz (May 31, 2021)

Palmer, S., Magsin, S., Bilderback, E., Poelstra, J., Folger, D., and Niggemann, R. 2007. "Liquefaction Susceptibility and Site Class Maps of Washington State, By County." Washington Division of Geology and Earth Resources. Open File Report 2004-20. ftp://ww4.dnr.wa.gov/geology/pubs/ofr04-20/ (June 4, 2019).

United States Geological Survey. "Earthquakes, Landslides, and Tsunamis: Mapping Geohazards in the Cascadia Subduction Zone". https://www.usgs.gov/center-news/earthquakes-landslides-

and-tsunamis-mapping-geohazards-cascadia-subduction-zone?qt-news_science_products=1#qt-news_science_products. (May 31, 2021).

University of Washington-Pacific Earthquake Engineering Research Structural Performance Database. https://nisee.berkeley.edu/spd/. Accessed June 2020.

WSDOT. 2018. Bridge Design Manual (LRFD). Washington State Department of Transportation.

Appendix A: Response Spectra

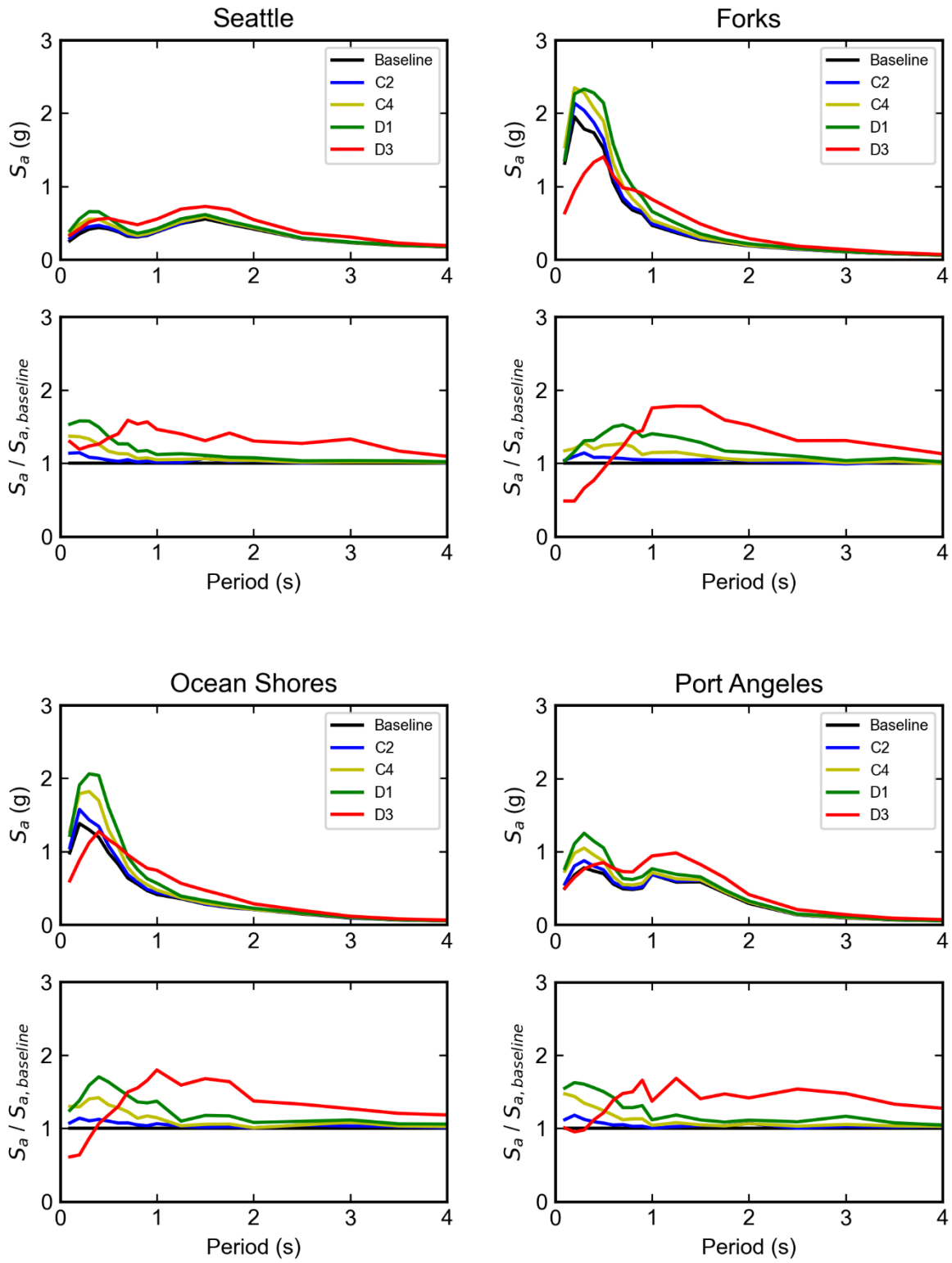
Seattle
Forks
Ocean Shores
Port Angeles
Baseline
C2
C4
D1
D3
S_a (g)
S_a / $S_{a,baseline}$
Period (s)

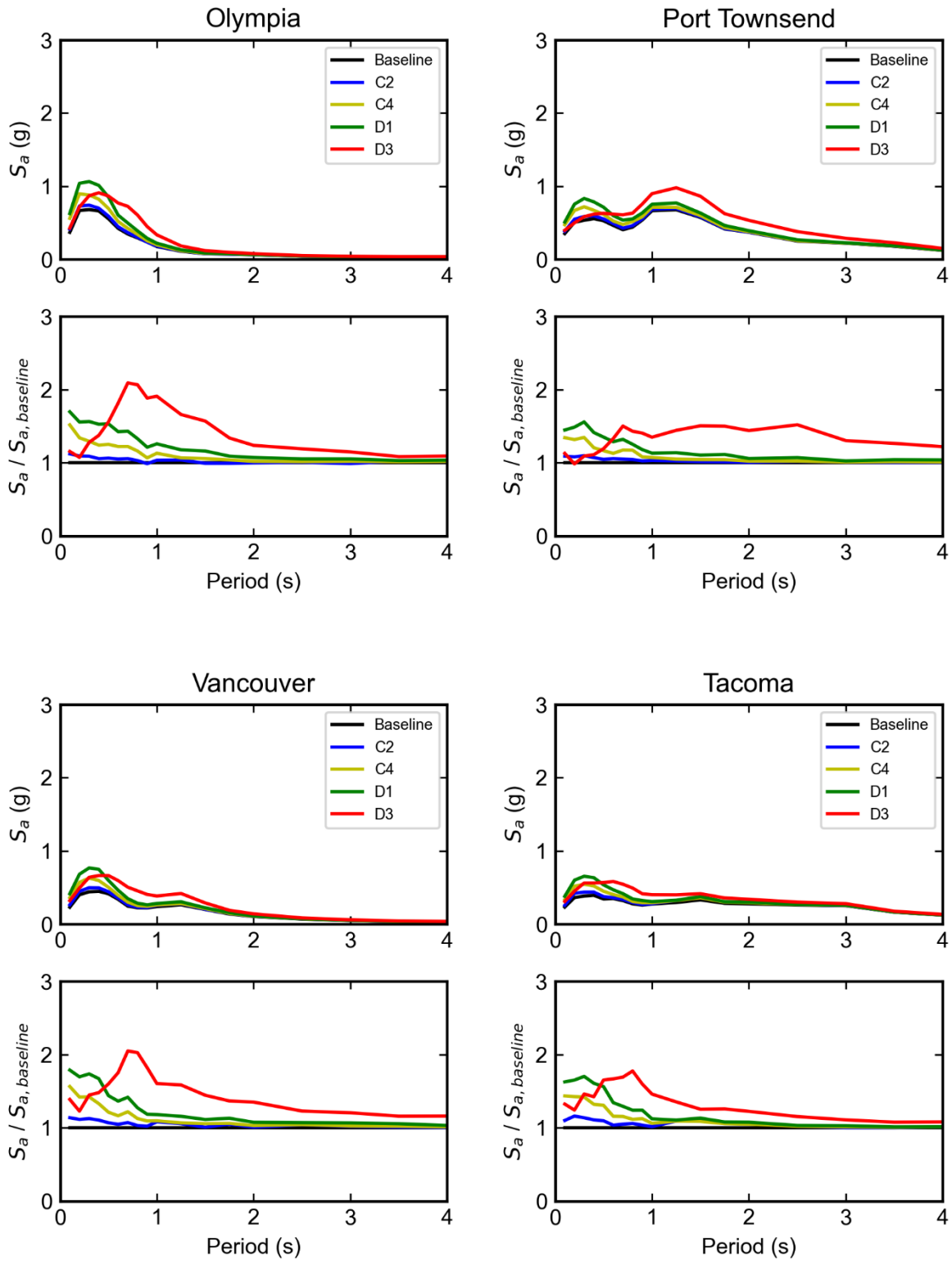
Olympia
Port Townsend
Vancouver
Tacoma
Baseline
C2
C4
D1
D3
S_a (g)
S_a / $S_{a,baseline}$
Period (s)

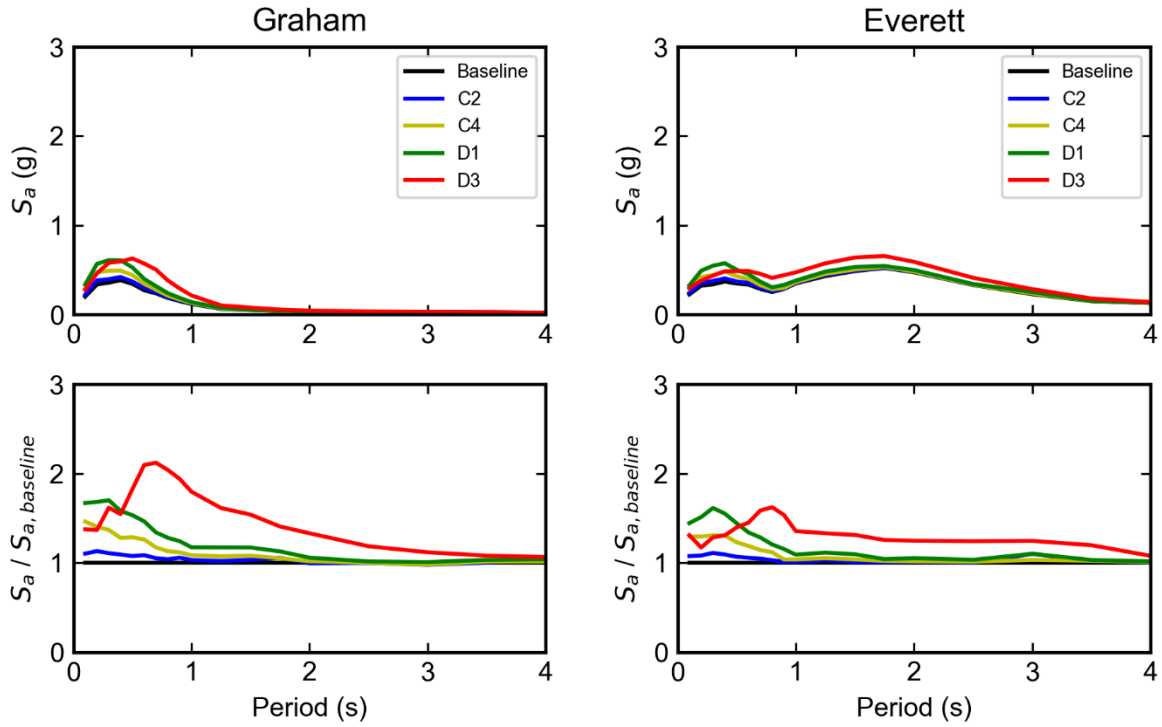
Graham
Everett
Baseline
C2
C4
D1
D3
S_a (g)
S_a / $S_{a,baseline}$
Period (s)

Appendix B: Ductility Demands

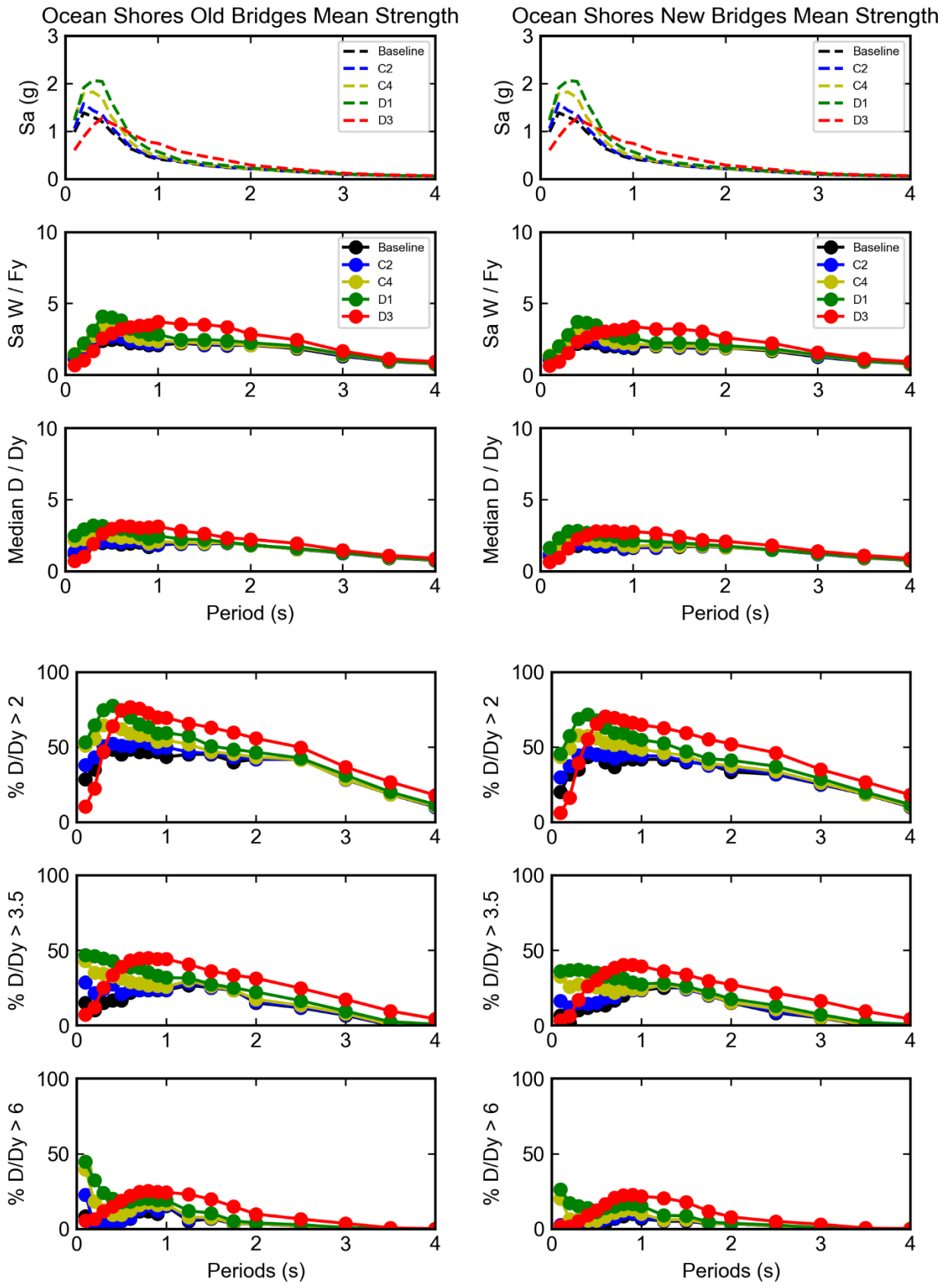
Ocean Shores Old Bridges Mean Strength
Ocean Shores New Bridges Mean Strength
Sa (g)
Sa W / Fy
Median D / Dy
% D/Dy > 2
% D/Dy > 3.5
% D/Dy > 6
Baseline
C2
C4
D1
D3
Period (s)
Periods (s)

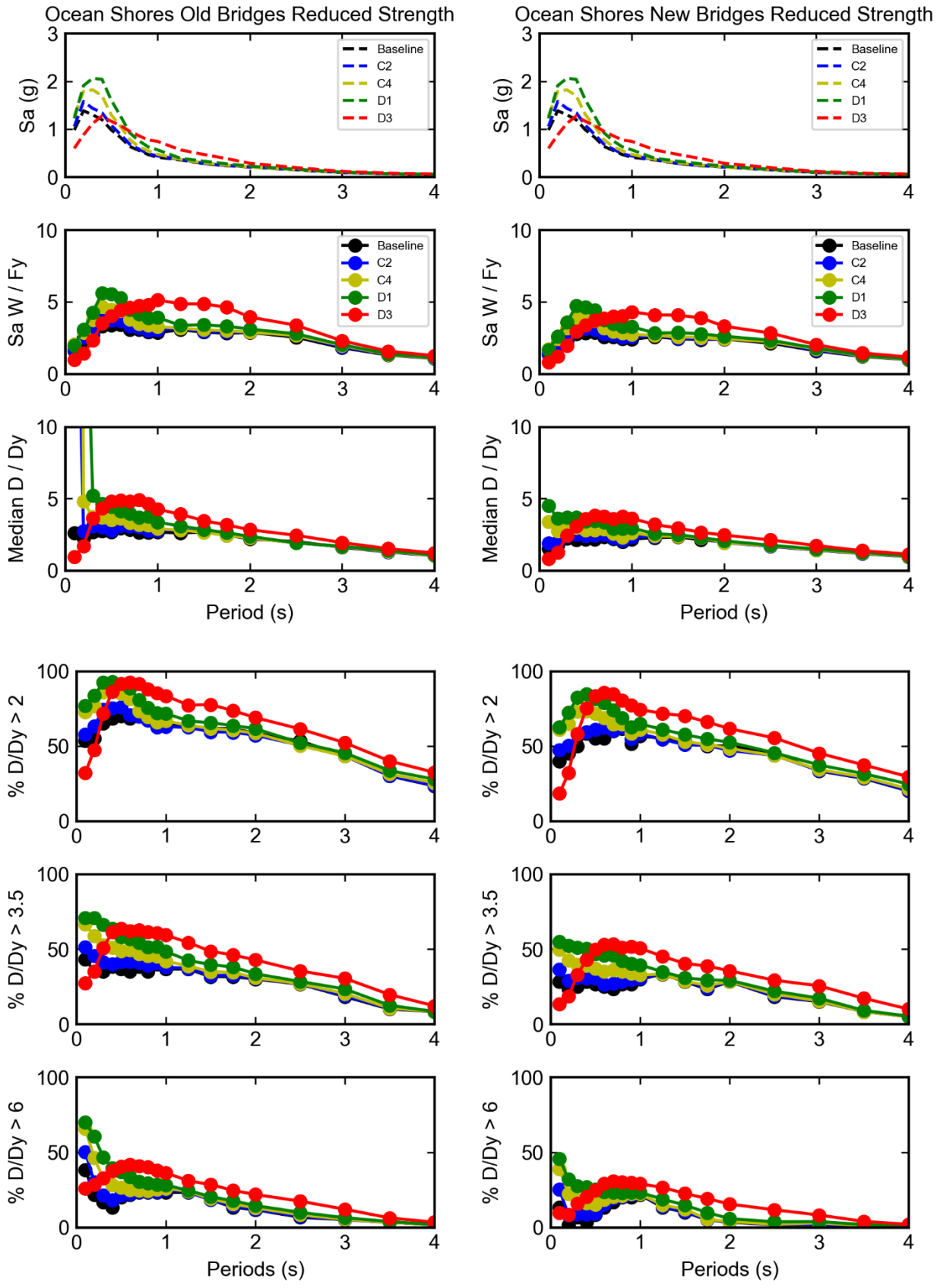
Ocean Shores Old Bridges Reduced Strength
Ocean Shores New Bridges Reduced Strength
Sa (g)
Sa W / Fy
Median D / Dy
% D/Dy > 2
% D/Dy > 3.5
% D/Dy > 6
Baseline
C2
C4
D1
D3
Period (s)
Periods (s)

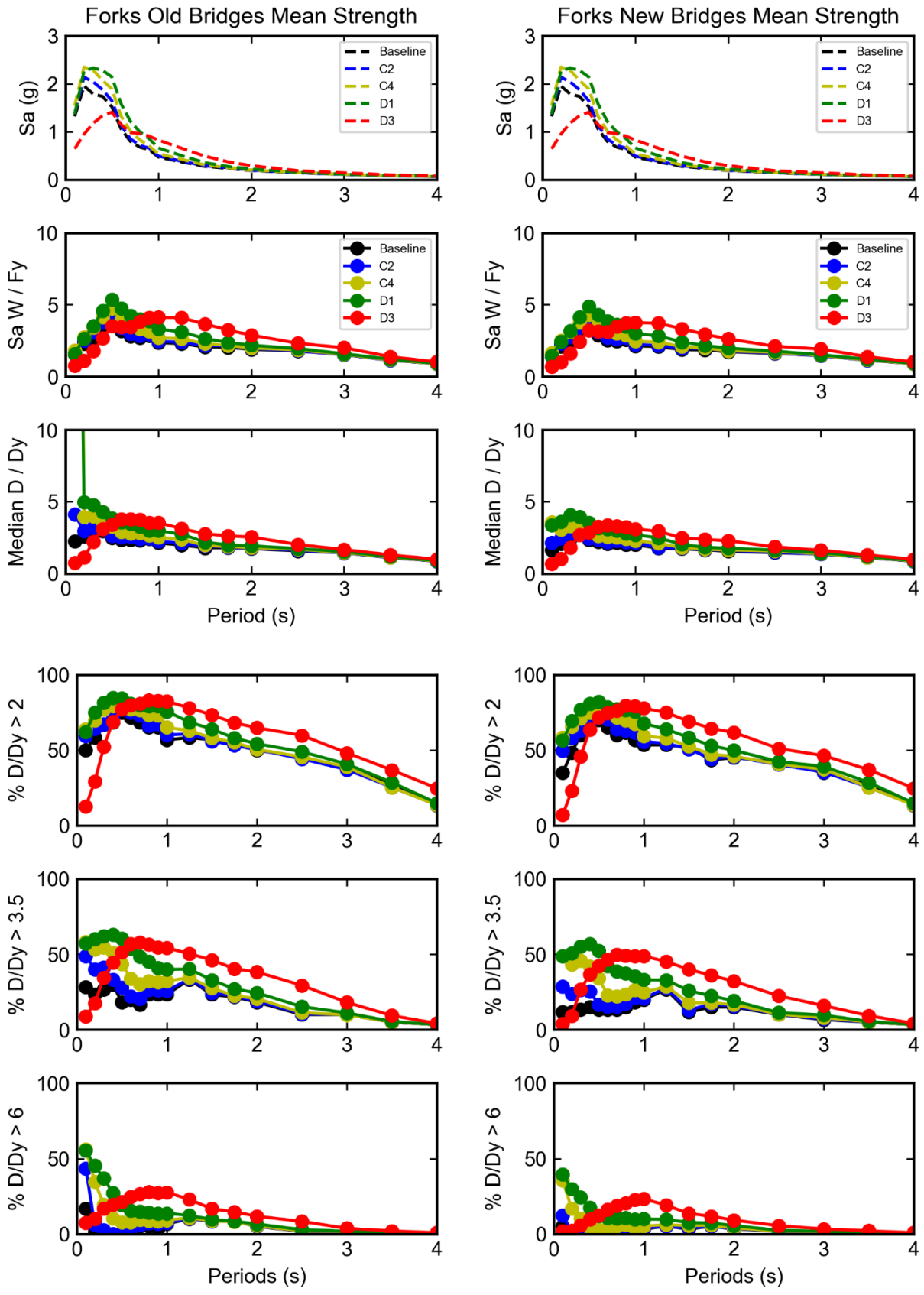
Forks Old Bridges Mean Strength
Forks New Bridges Mean Strength
Sa (g)
Sa W / Fy
Median D / Dy
% D/Dy > 2
% D/Dy > 3.5
% D/Dy > 6
Baseline
C2
C4
D1
D3
Period (s)
Periods (s)

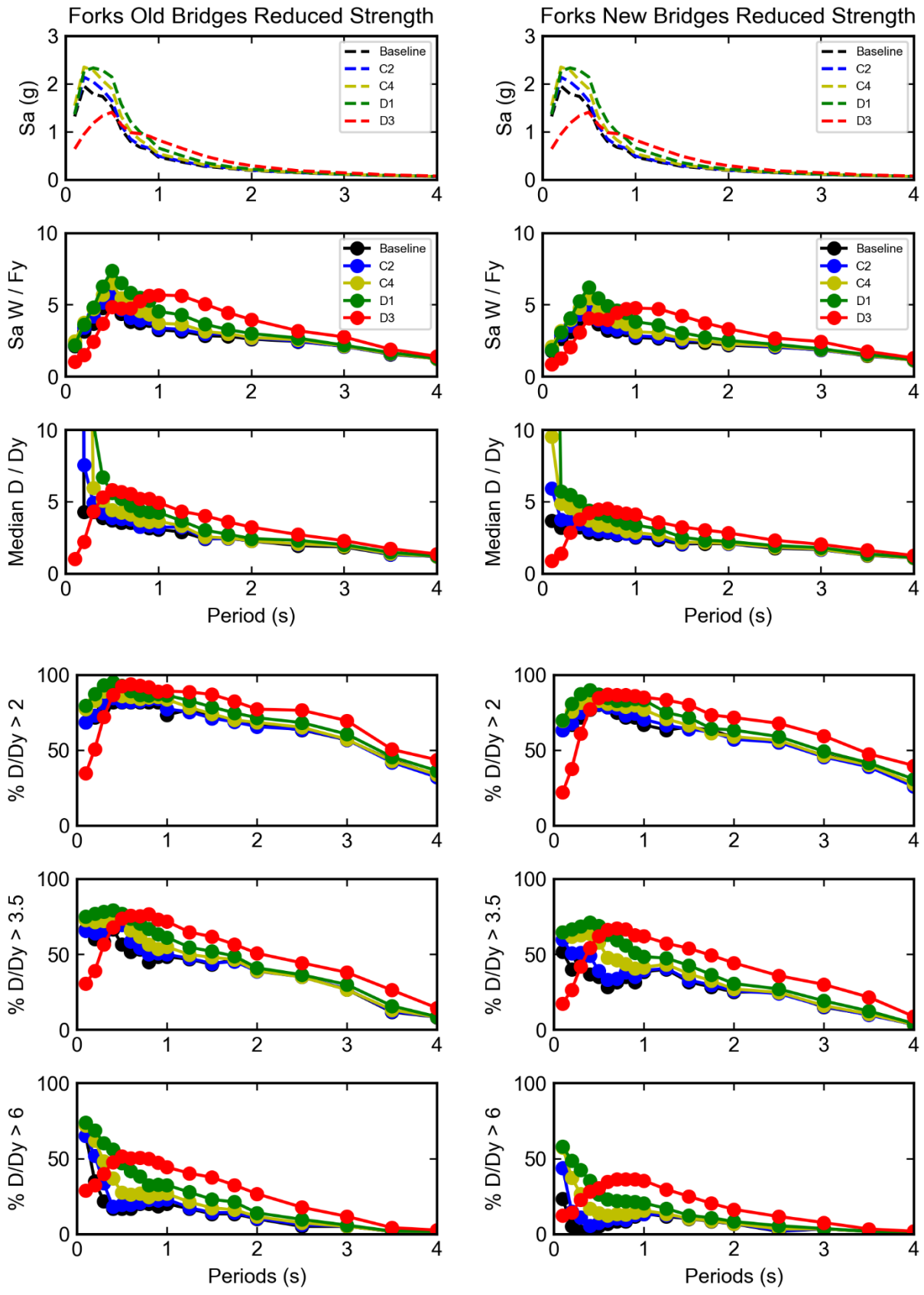
Forks Old Bridges Reduced Strength
Forks New Bridges Reduced Strength
Sa (g)
Sa W / Fy
Median D / Dy
% D/Dy > 2
% D/Dy > 3.5
% D/Dy > 6
Baseline
C2
C4
D1
D3
Period (s)
Periods (s)

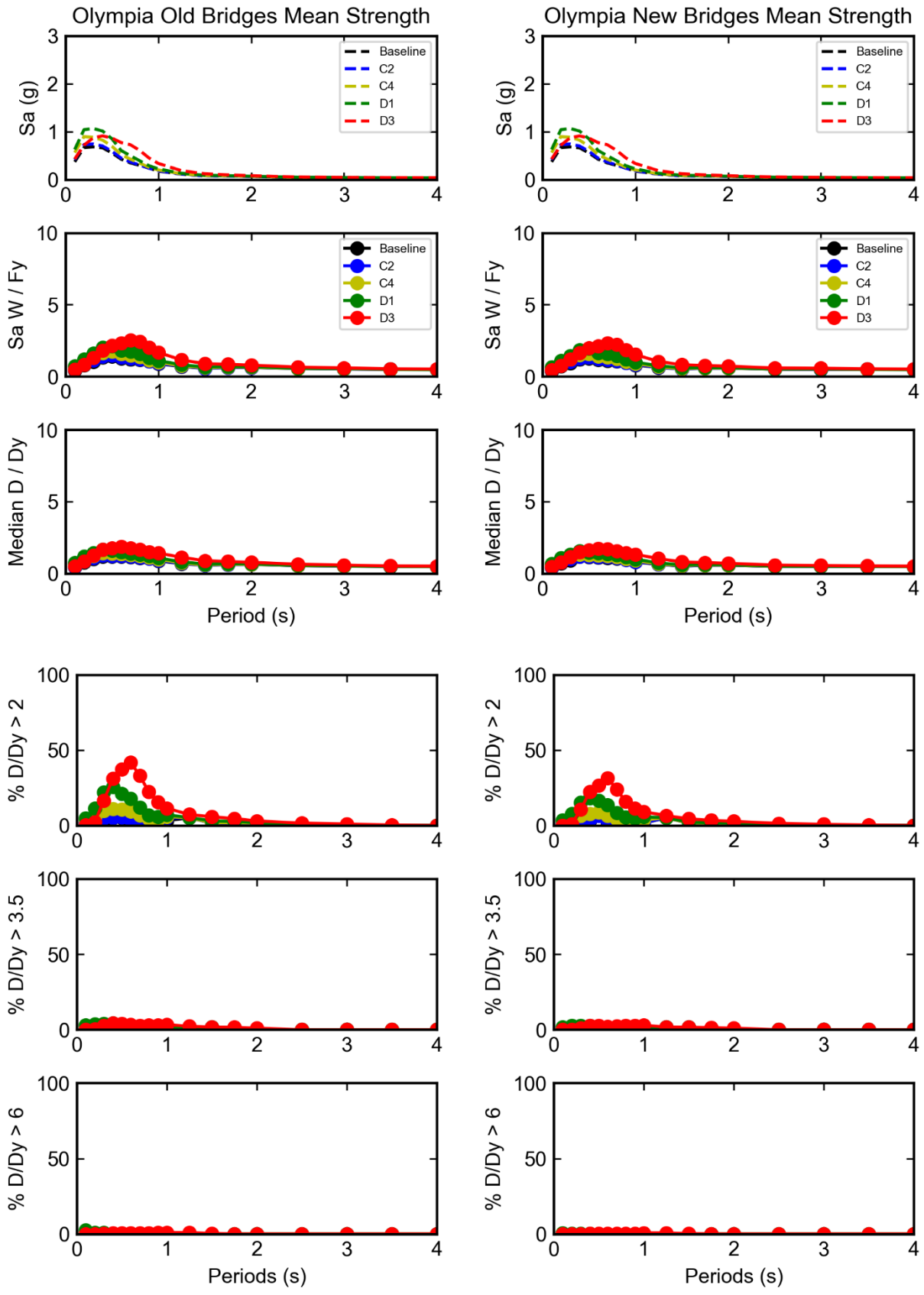
Olympia Old Bridges Mean Strength
Olympia New Bridges Mean Strength
Baseline
C2
C4
D1
D3
Sa (g)
Sa W / Fy
Median D / Dy
% D/Dy > 2
% D/Dy > 3.5
% D/Dy > 6
Period (s)
Periods (s)

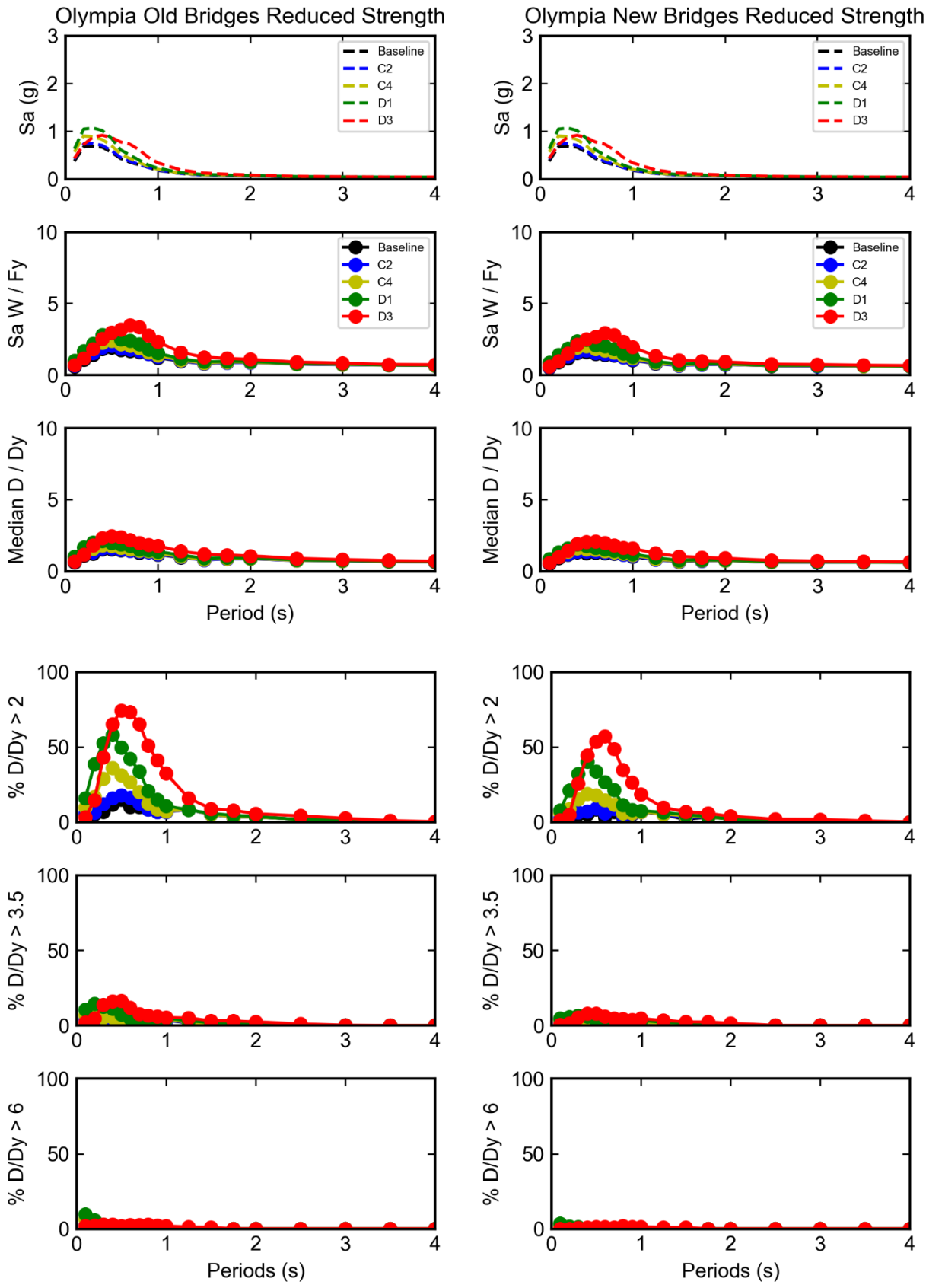
Olympia Old Bridges Reduced Strength
Olympia New Bridges Reduced Strength
Sa (g)
Sa W / Fy
Median D / Dy
% D/Dy > 2
% D/Dy > 3.5
% D/Dy > 6
Baseline
C2
C4
D1
D3
Period (s)
Periods (s)

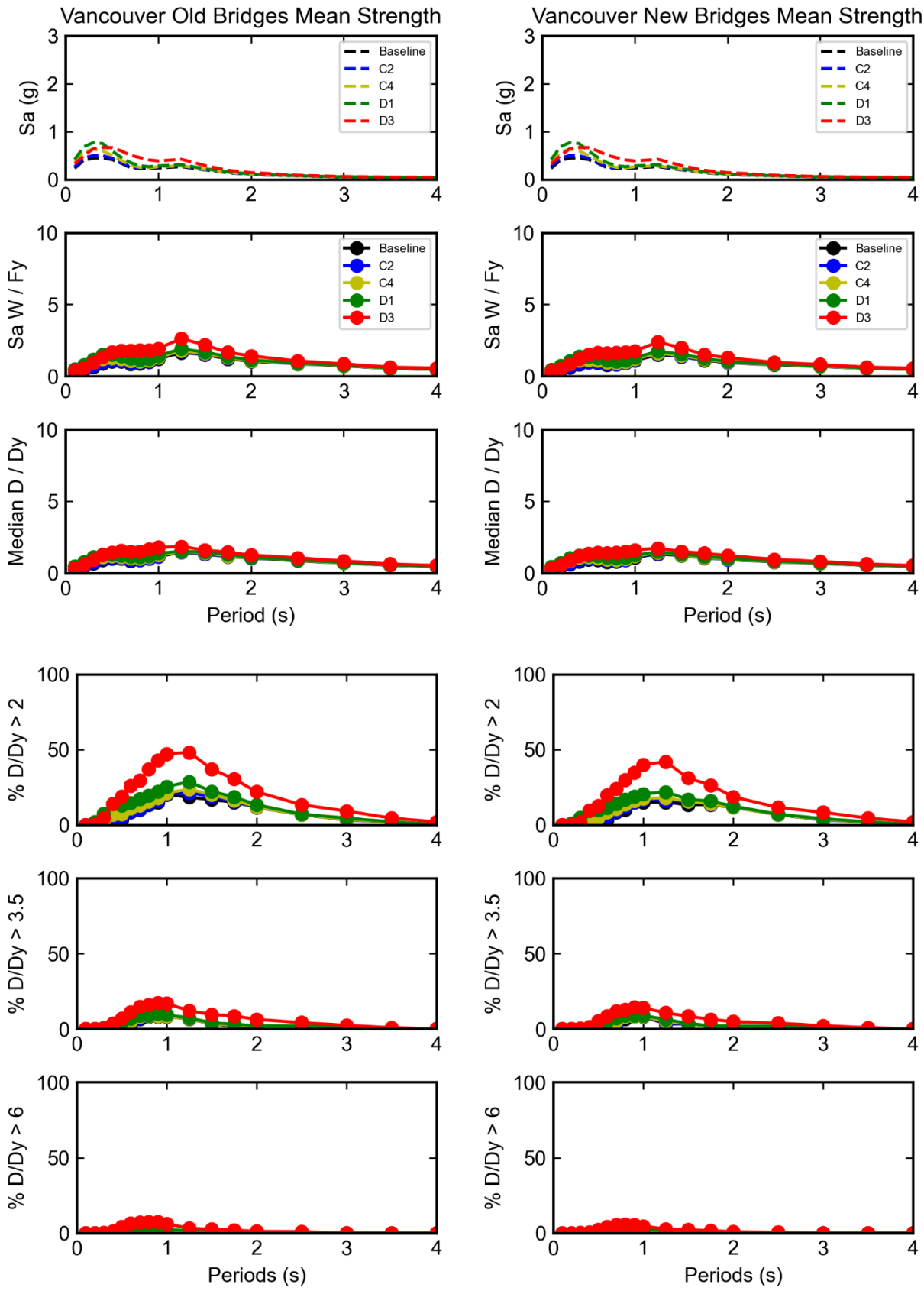
Vancouver Old Bridges Mean Strength
Vancouver New Bridges Mean Strength
Sa (g)
Sa W / Fy
Median D / Dy
% D/Dy > 2
% D/Dy > 3.5
% D/Dy > 6
Baseline
C2
C4
D1
D3
Period (s)
Periods (s)

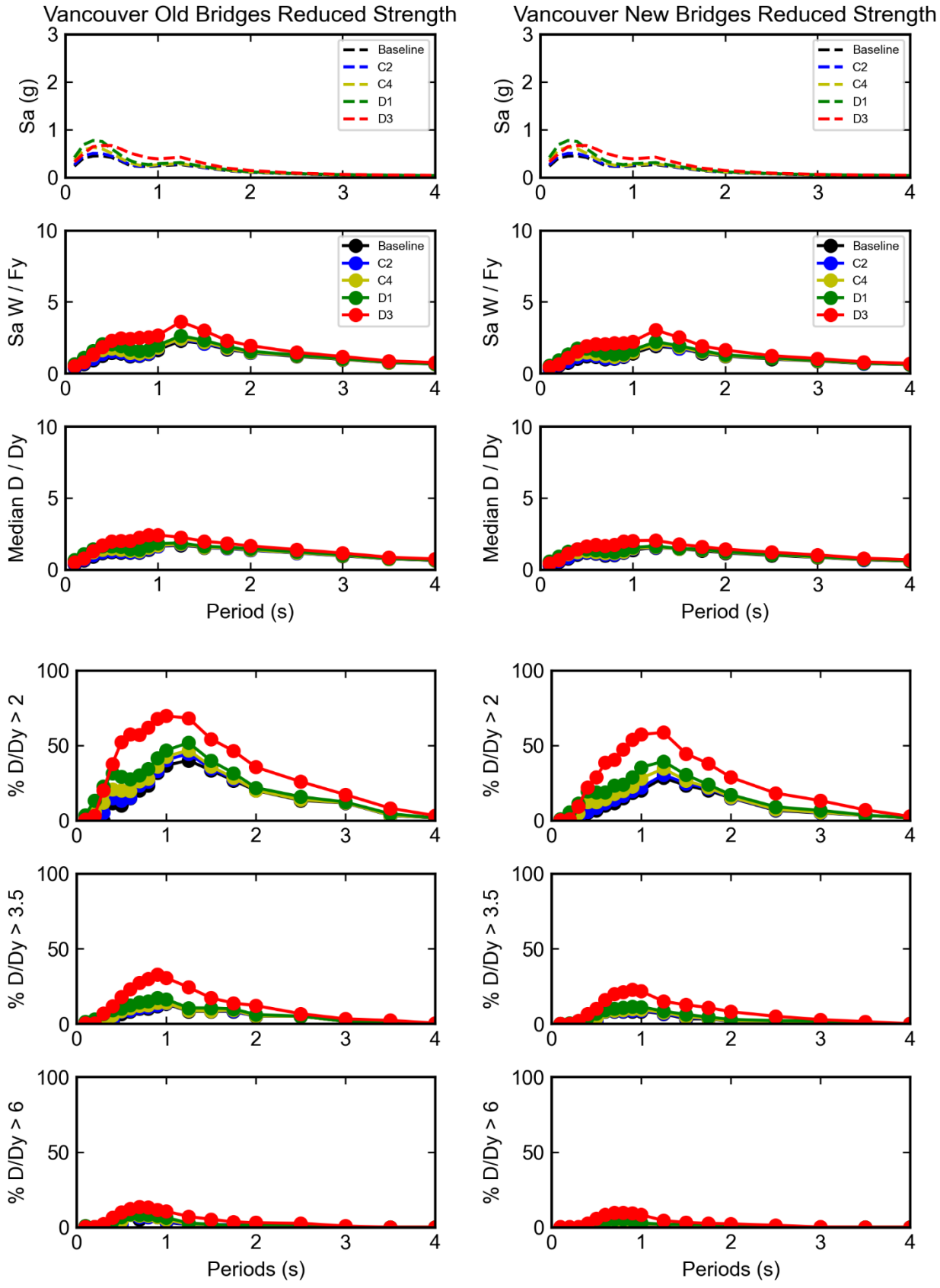
Vancouver Old Bridges Reduced Strength
Vancouver New Bridges Reduced Strength
Sa (g)
Sa W / Fy
Median D / Dy
% D/Dy > 2
% D/Dy > 3.5
% D/Dy > 6
Baseline
C2
C4
D1
D3
Period (s)
Periods (s)

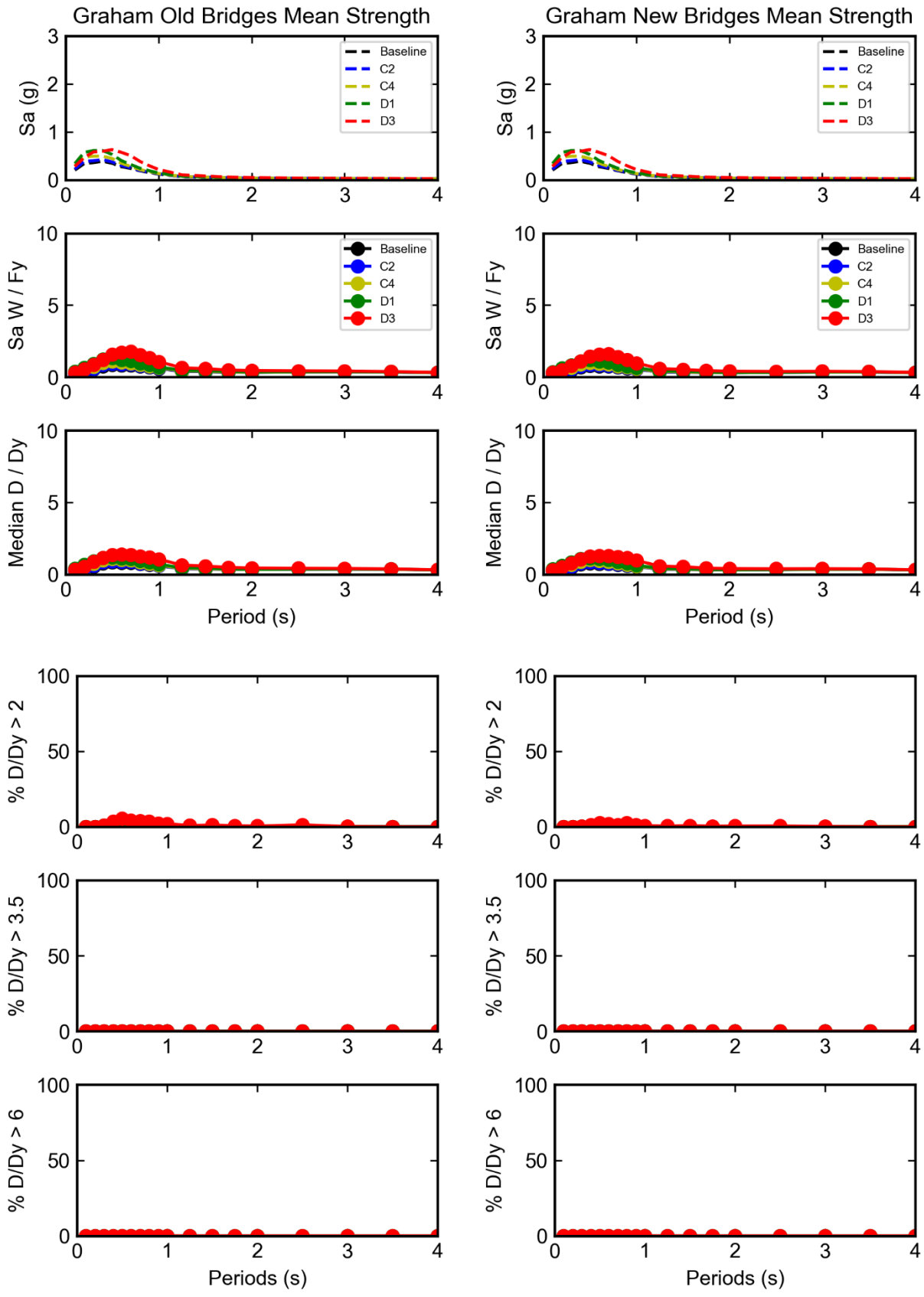
Graham Old Bridges Mean Strength
Graham New Bridges Mean Strength
Sa (g)
Sa W / Fy
Median D / Dy
% D/Dy > 2
% D/Dy > 3.5
% D/Dy > 6
Baseline
C2
C4
D1
D3
Period (s)
Periods (s)

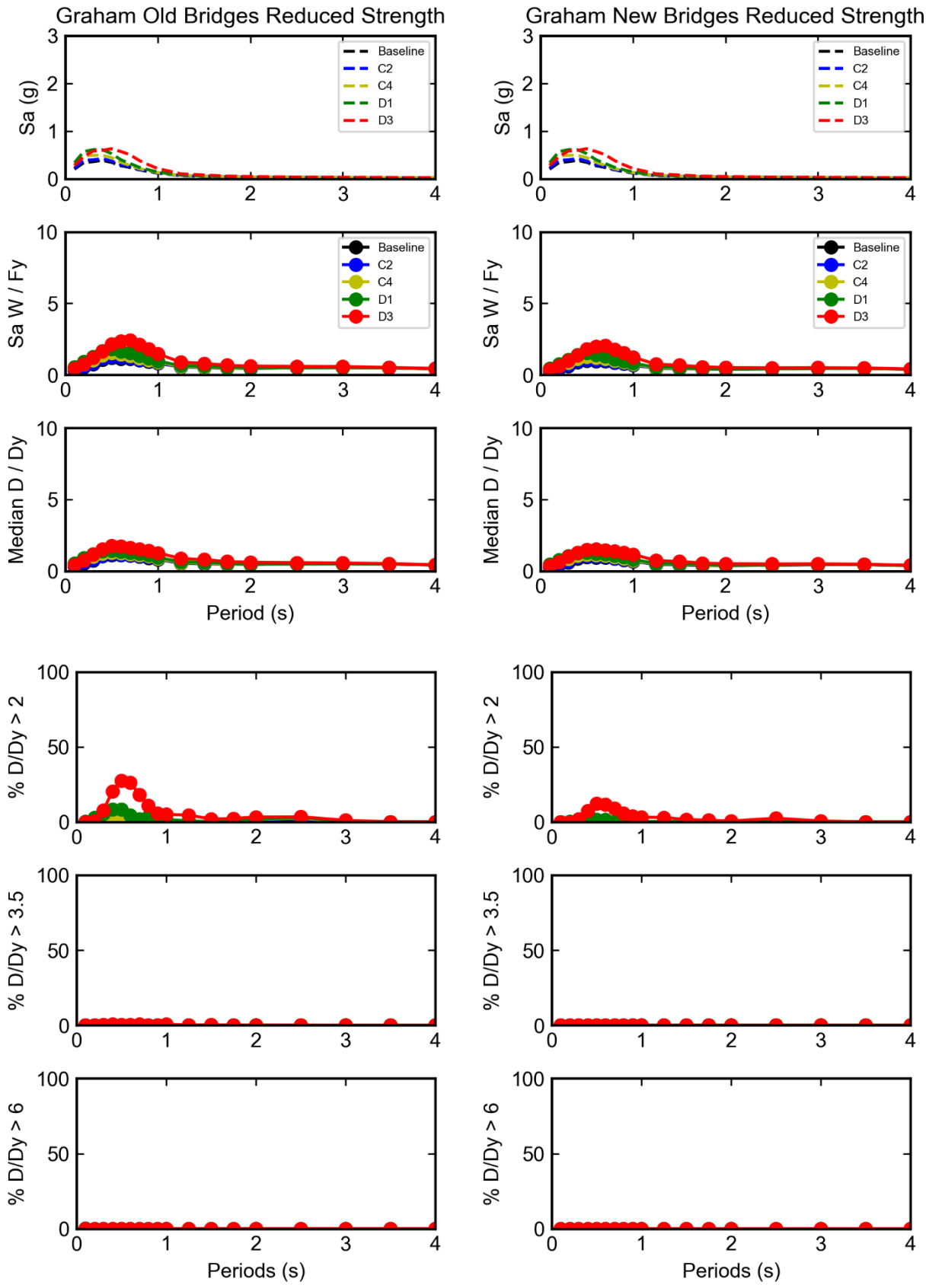
Graham Old Bridges Reduced Strength
Graham New Bridges Reduced Strength
Sa (g)
Sa W / Fy
Median D / Dy
% D/Dy > 2
% D/Dy > 3.5
% D/Dy > 6
Baseline
C2
C4
D1
D3
Period (s)
Periods (s)

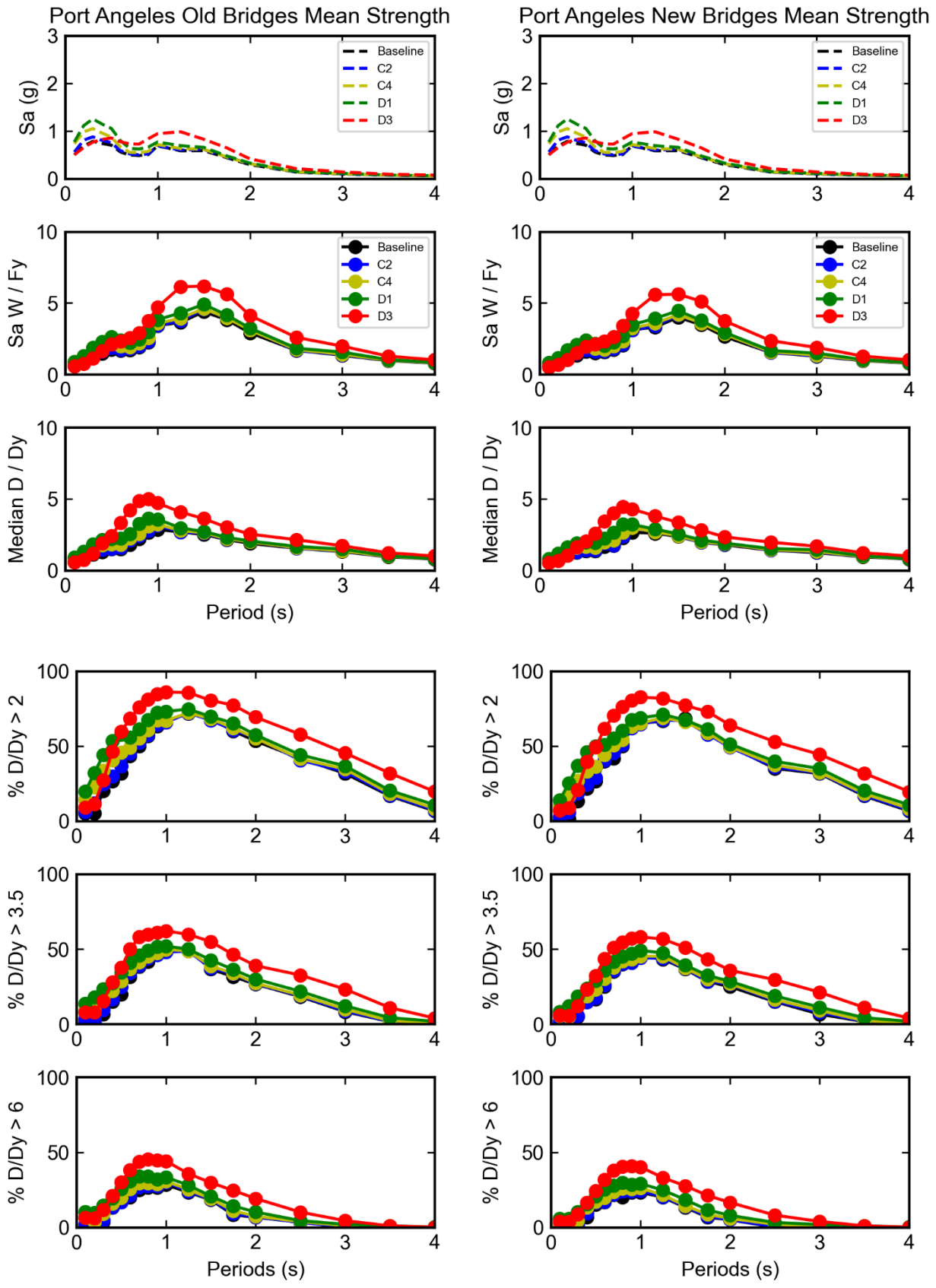
Port Angeles Old Bridges Mean Strength
Port Angeles New Bridges Mean Strength
Sa (g)
Sa W / Fy
Median D / Dy
% D/Dy > 2
% D/Dy > 3.5
% D/Dy > 6
Baseline
C2
C4
D1
D3
Period (s)
Periods (s)

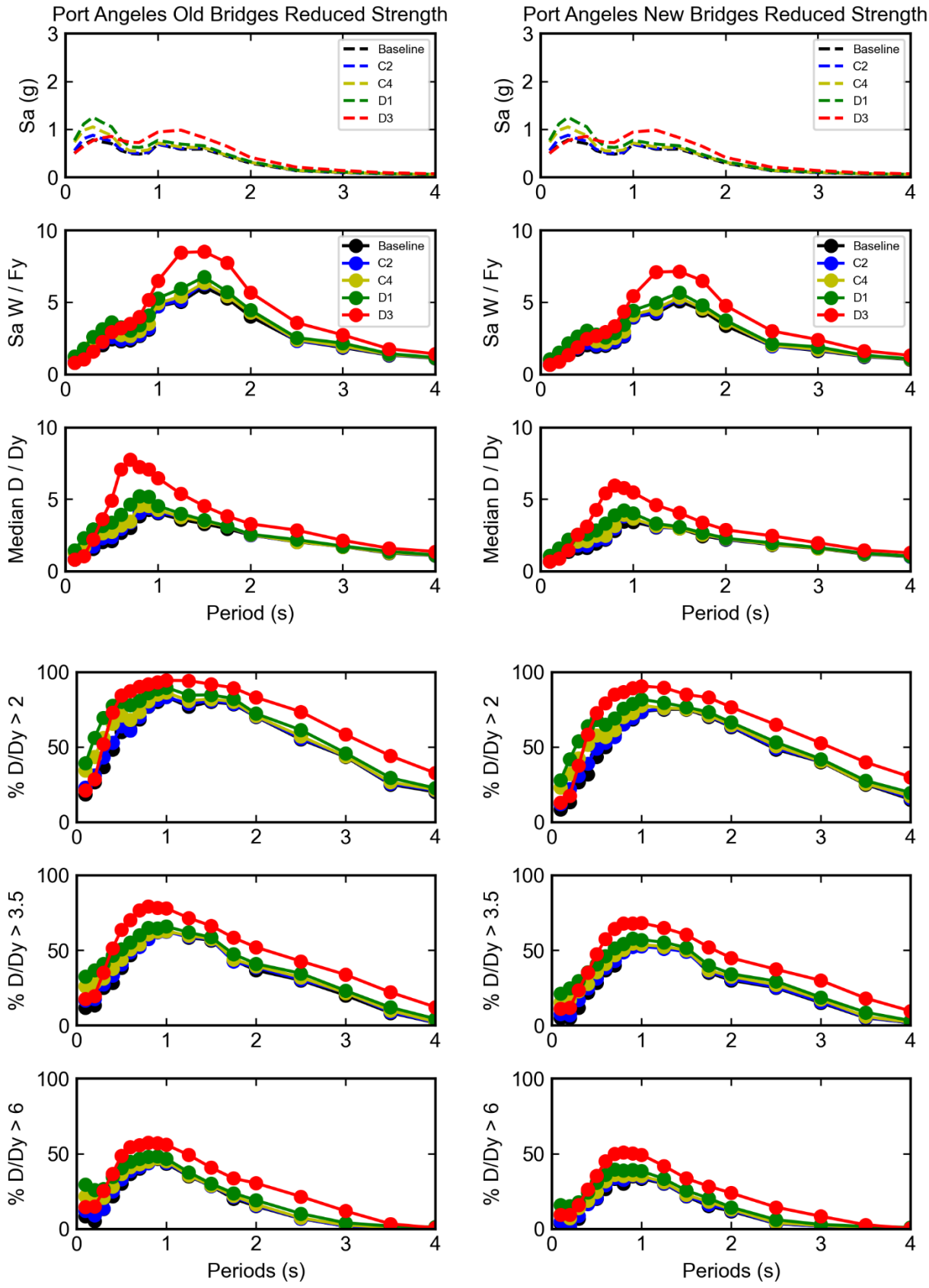
Port Angeles Old Bridges Reduced Strength
Port Angeles New Bridges Reduced Strength
Sa (g)
Sa W / Fy
Median D / Dy
% D/Dy > 2
% D/Dy > 3.5
% D/Dy > 6
Baseline
C2
C4
D1
D3
Period (s)
Periods (s)

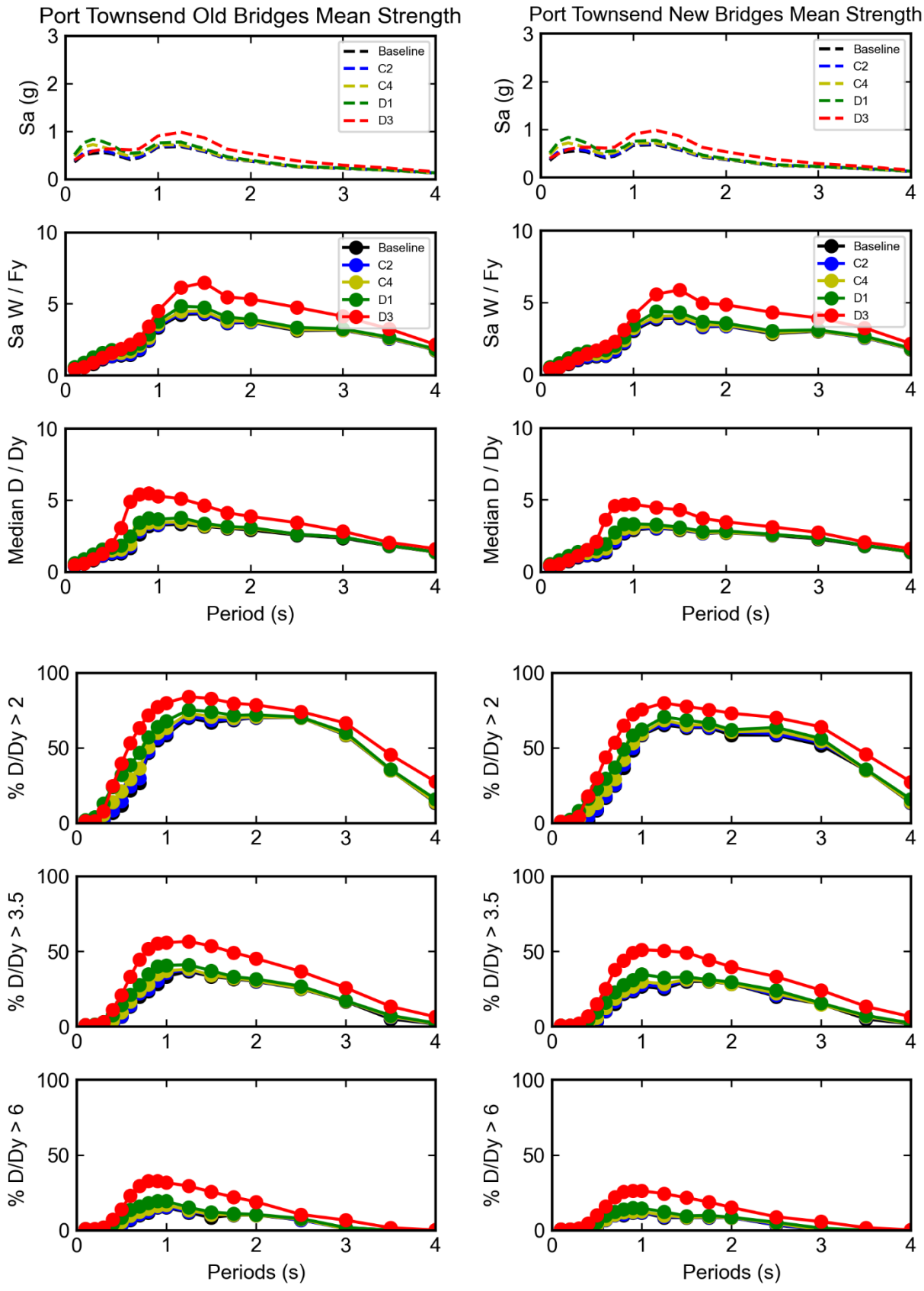
Port Townsend Old Bridges Mean Strength
Port Townsend New Bridges Mean Strength
Sa (g)
Sa W / Fy
Median D / Dy
% D/Dy > 2
% D/Dy > 3.5
% D/Dy > 6
Baseline
C2
C4
D1
D3
Period (s)
Periods (s)

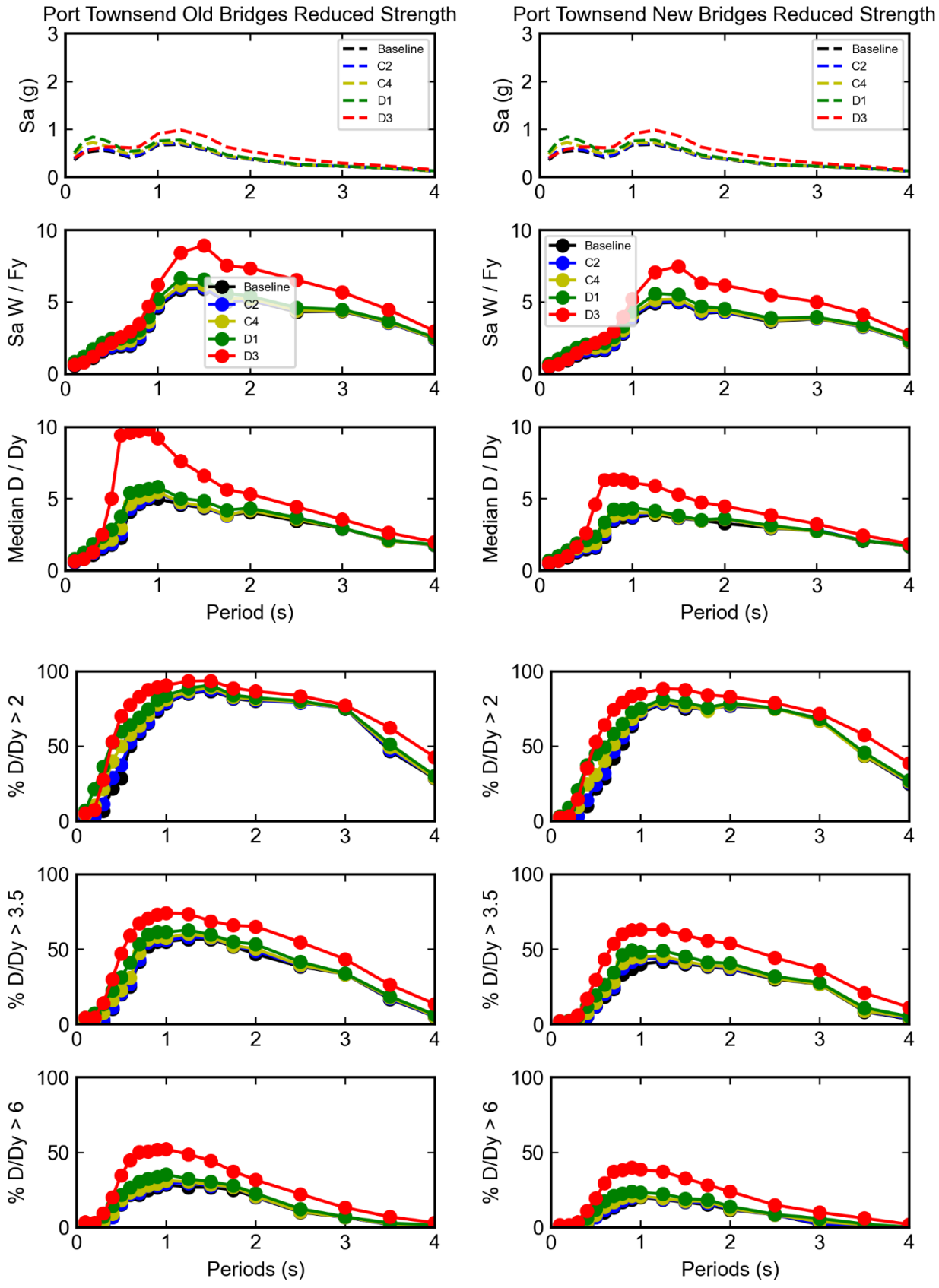
Port Townsend Old Bridges Reduced Strength
Port Townsend New Bridges Reduced Strength
Sa (g)
Sa W / Fy
Median D / Dy
% D/Dy > 2
% D/Dy > 3.5
% D/Dy > 6
Period (s)
Periods (s)
Baseline
C2
C4
D1
D3

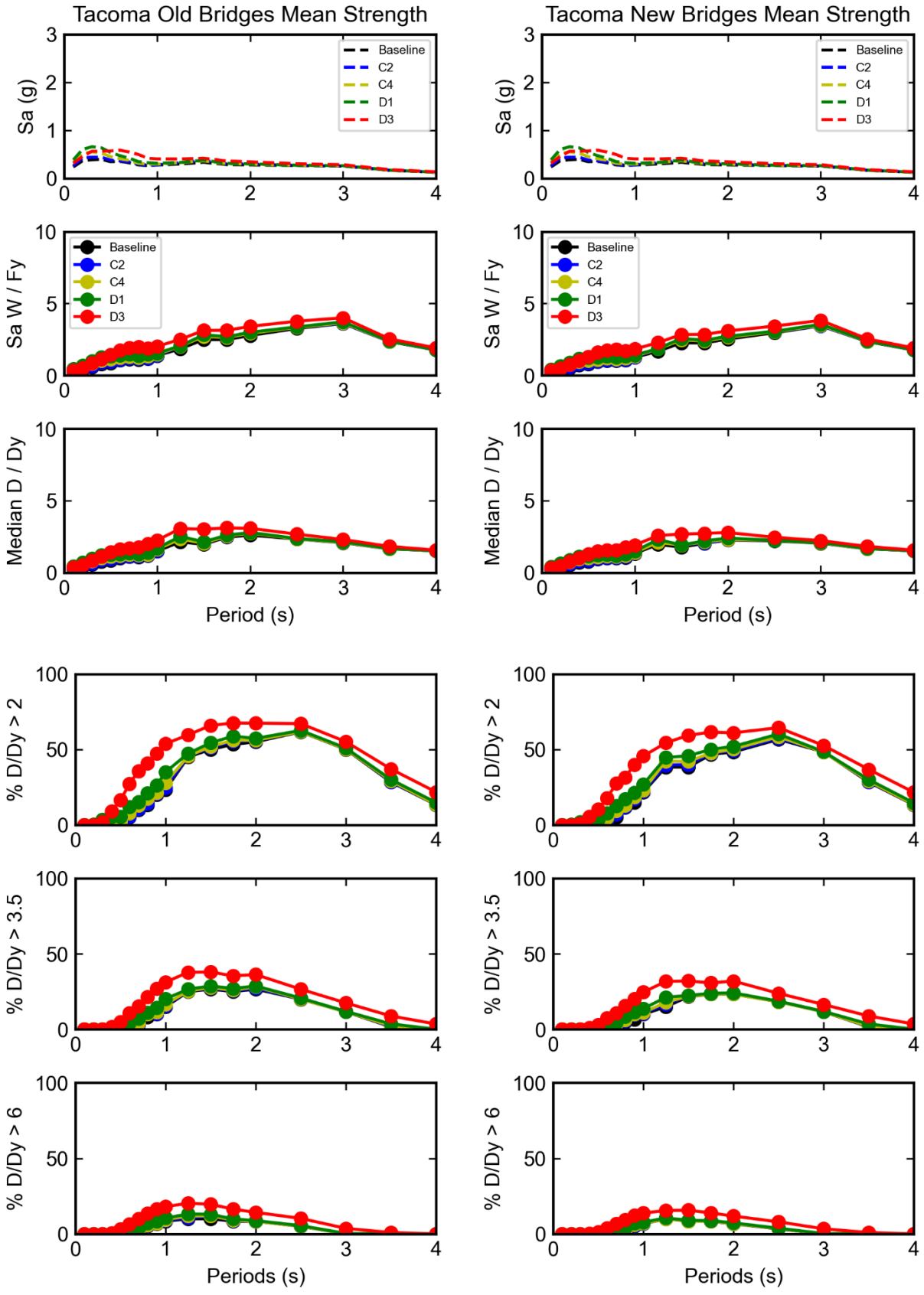
Tacoma Old Bridges Mean Strength
Tacoma New Bridges Mean Strength
Sa (g)
Sa W / Fy
Median D / Dy
% D/Dy > 2
% D/Dy > 3.5
% D/Dy > 6
Baseline
C2
C4
D1
D3
Period (s)
Periods (s)

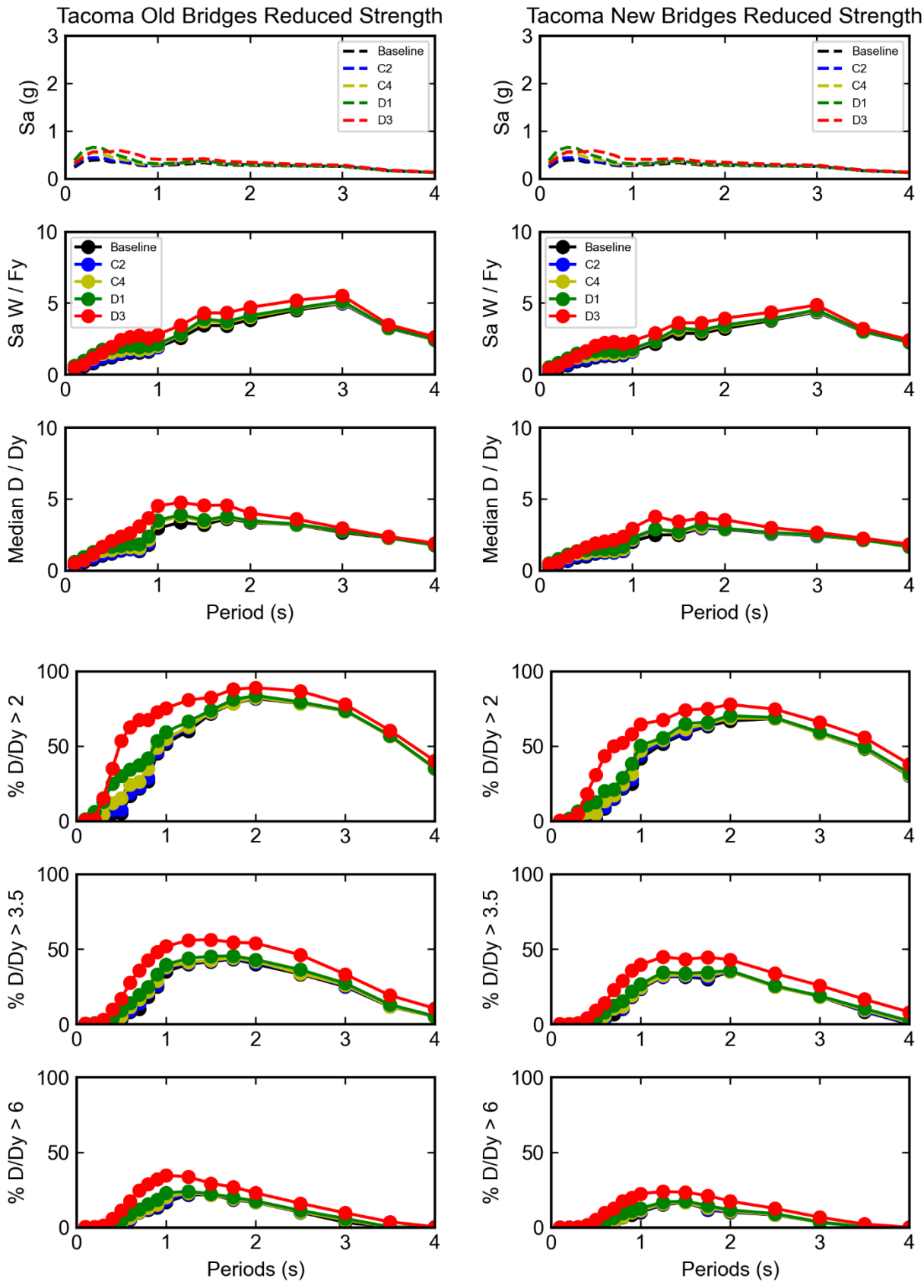
Tacoma Old Bridges Reduced Strength
Tacoma New Bridges Reduced Strength
Sa (g)
Sa W / Fy
Median D / Dy
% D/Dy > 2
% D/Dy > 3.5
% D/Dy > 6
Baseline
C2
C4
D1
D3
Period (s)
Periods (s)

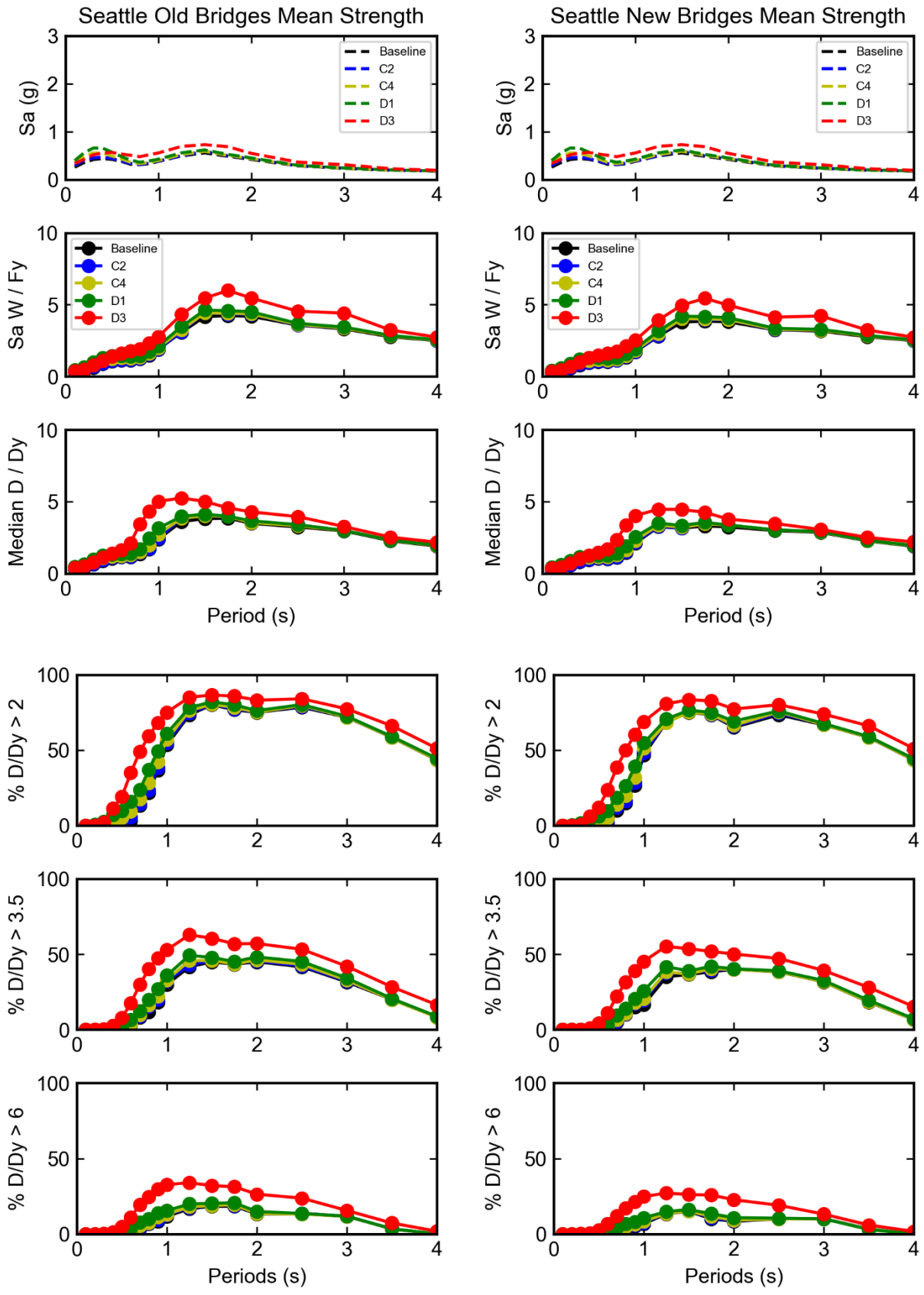
Seattle Old Bridges Mean Strength
Seattle New Bridges Mean Strength
Sa (g)
Sa W / Fy
Median D / Dy
% D/Dy > 2
% D/Dy > 3.5
% D/Dy > 6
Baseline
C2
C4
D1
D3
Period (s)
Periods (s)

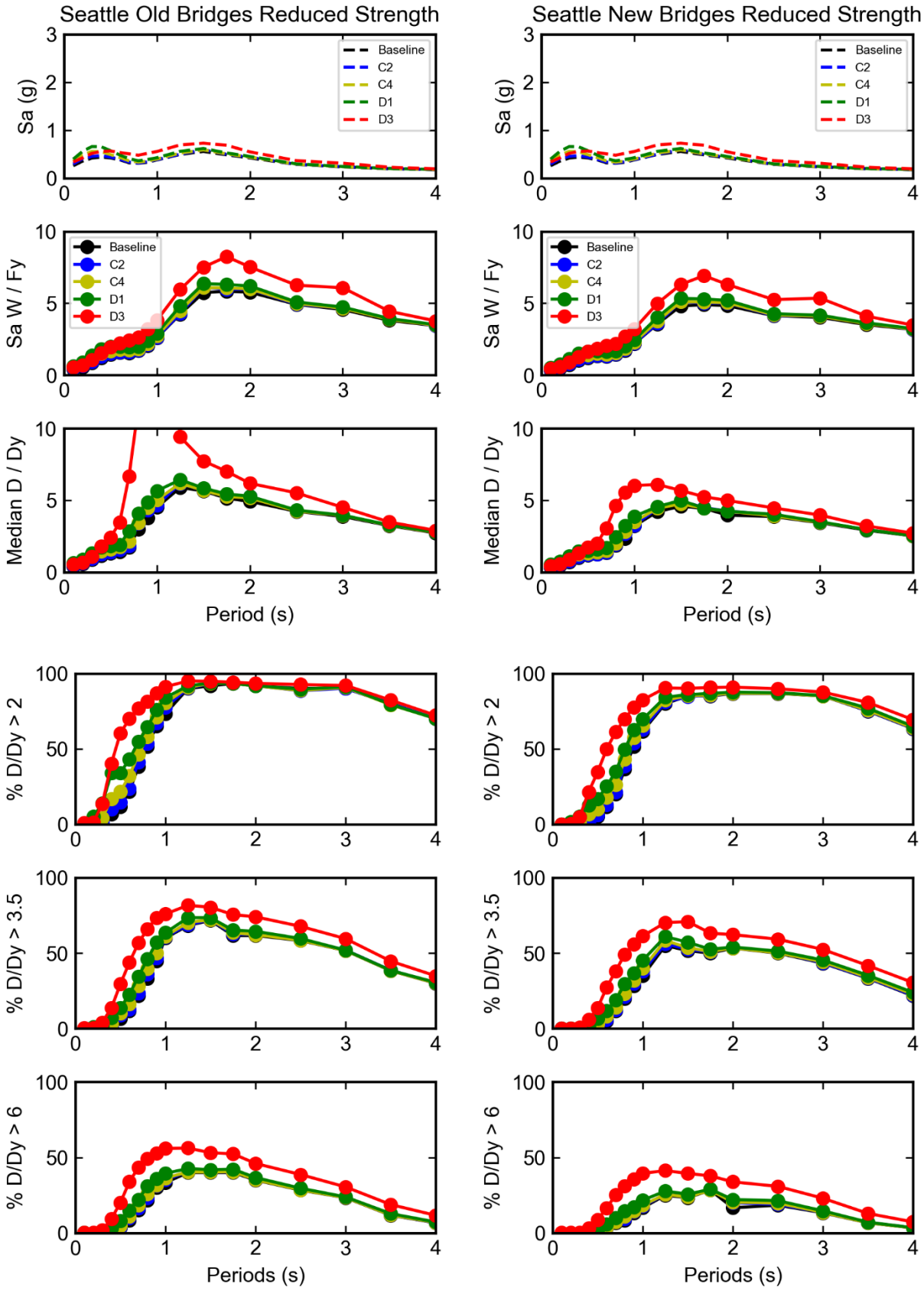
Seattle Old Bridges Reduced Strength
Seattle New Bridges Reduced Strength
Sa (g)
Sa W / Fy
Median D / Dy
% D/Dy > 2
% D/Dy > 3.5
% D/Dy > 6
Baseline
C2
C4
D1
D3
Period (s)
Periods (s)

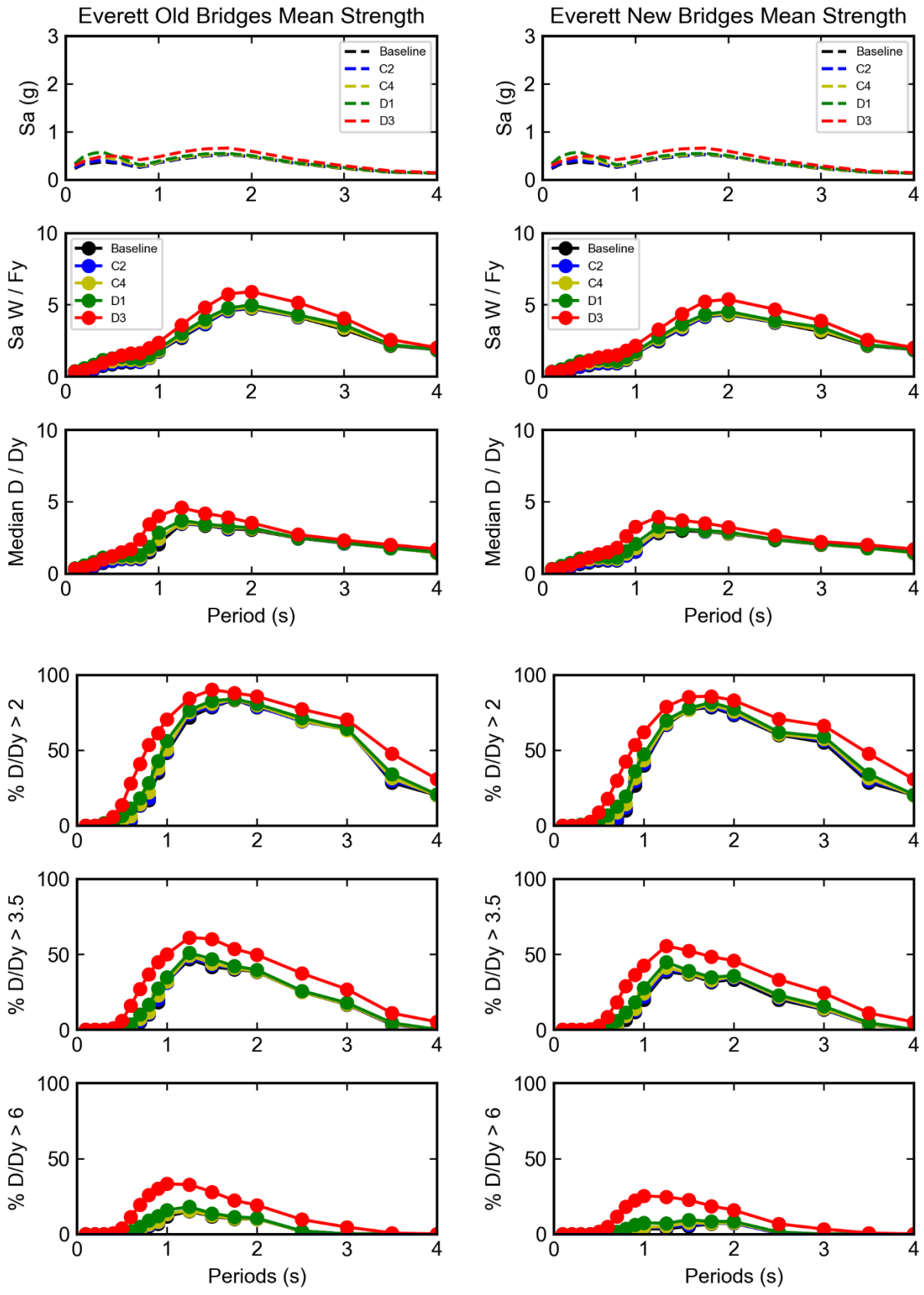
Everett Old Bridges Mean Strength
Everett New Bridges Mean Strength
Sa (g)
Sa W / Fy
Median D / Dy
% D/Dy > 2
% D/Dy > 3.5
% D/Dy > 6
Baseline
C2
C4
D1
D3
Period (s)
Periods (s)

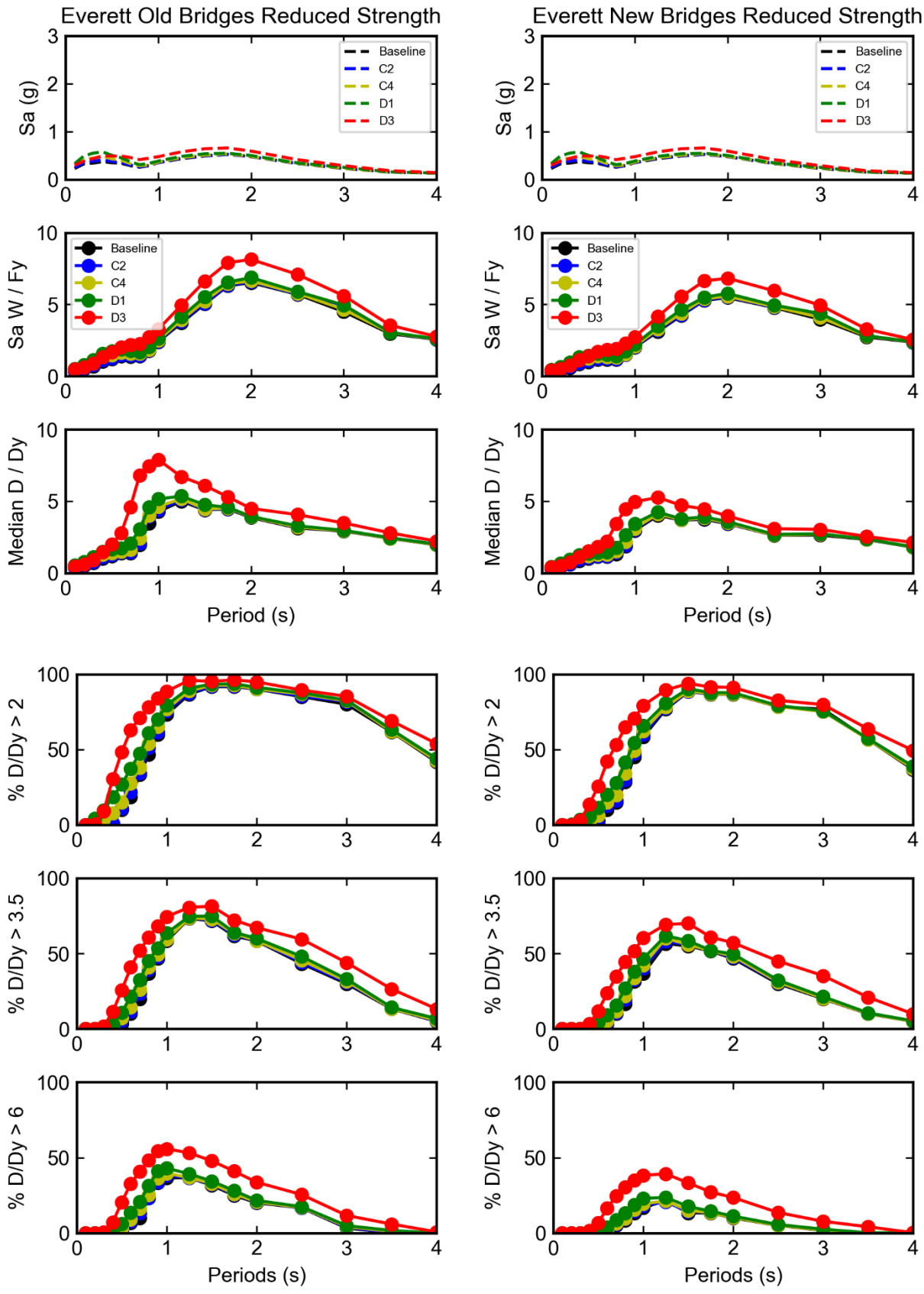
Everett Old Bridges Reduced Strength
Everett New Bridges Reduced Strength
Sa (g)
Sa W / Fy
Median D / Dy
% D/Dy > 2
% D/Dy > 3.5
% D/Dy > 6
Baseline
C2
C4
D1
D3
Period (s)
Periods (s)

Appendix C: Damage Probabilities

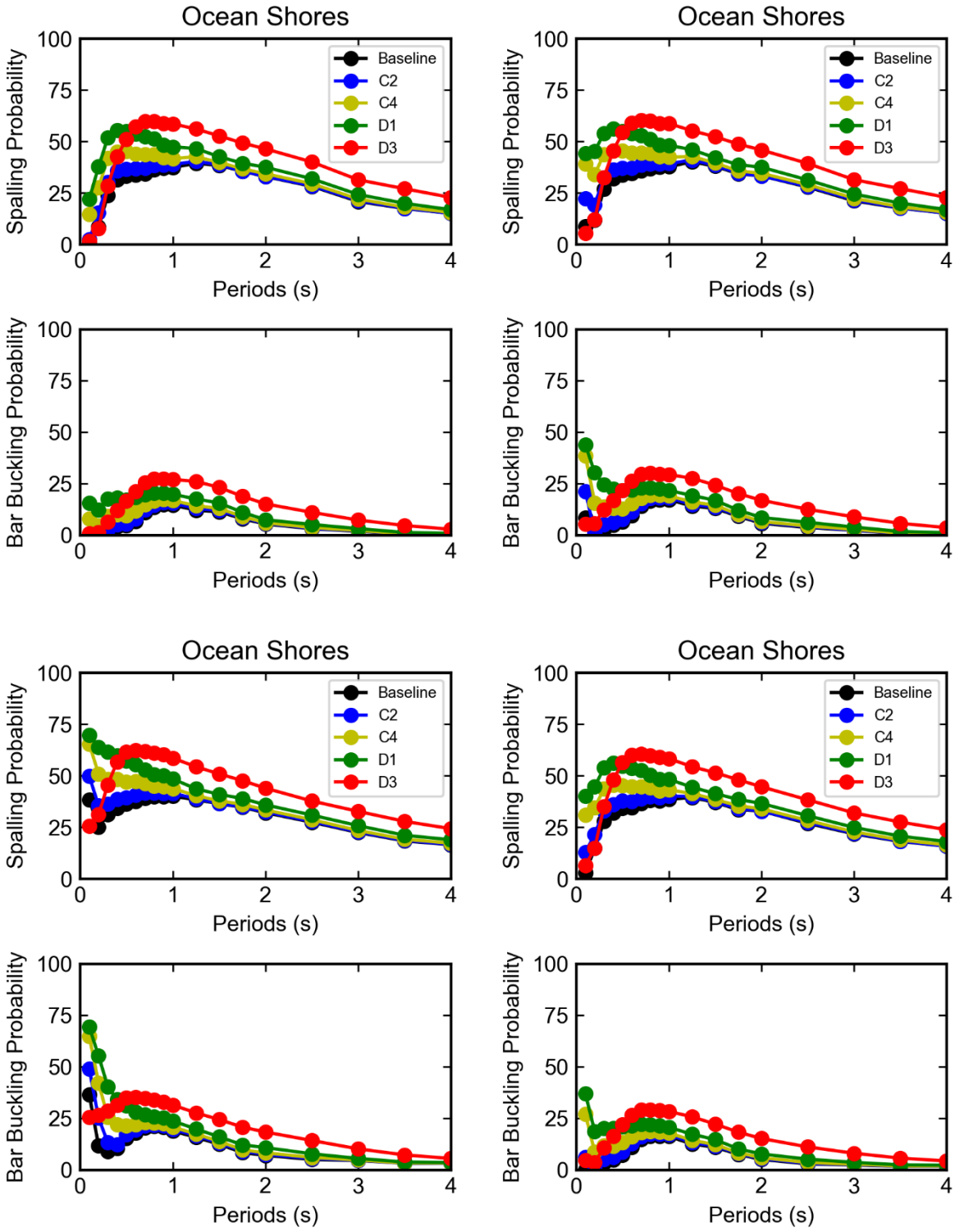

Figure C.1. Probability of spalling and bar buckling in Ocean Shores for old (left) and new (right) bridges, and for mean (top) and reduced (bottom) strength.

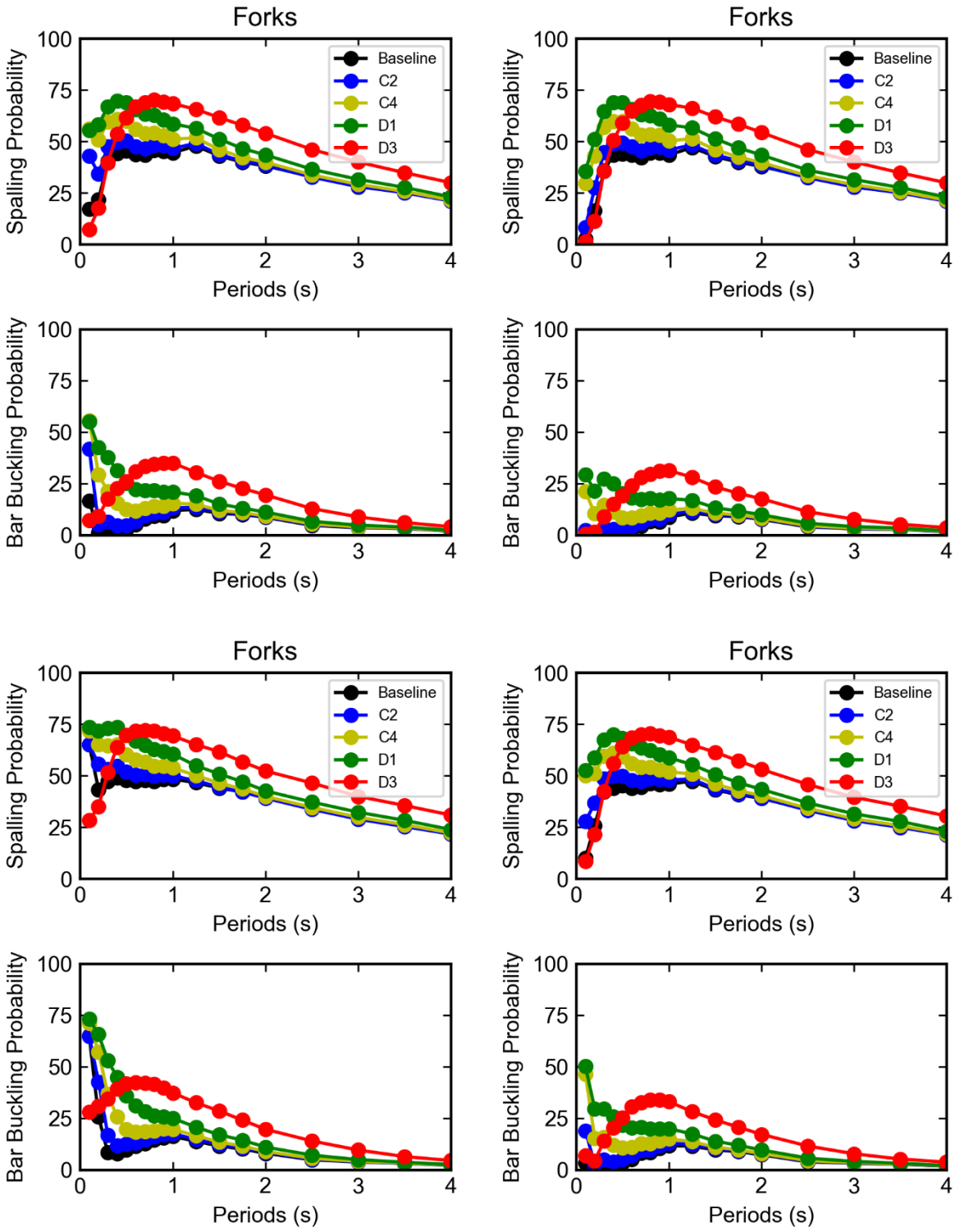

Figure C.2. Probability of spalling and bar buckling in Forks for old (left) and new (right) bridges, and for mean (top) and reduced (bottom) strength.

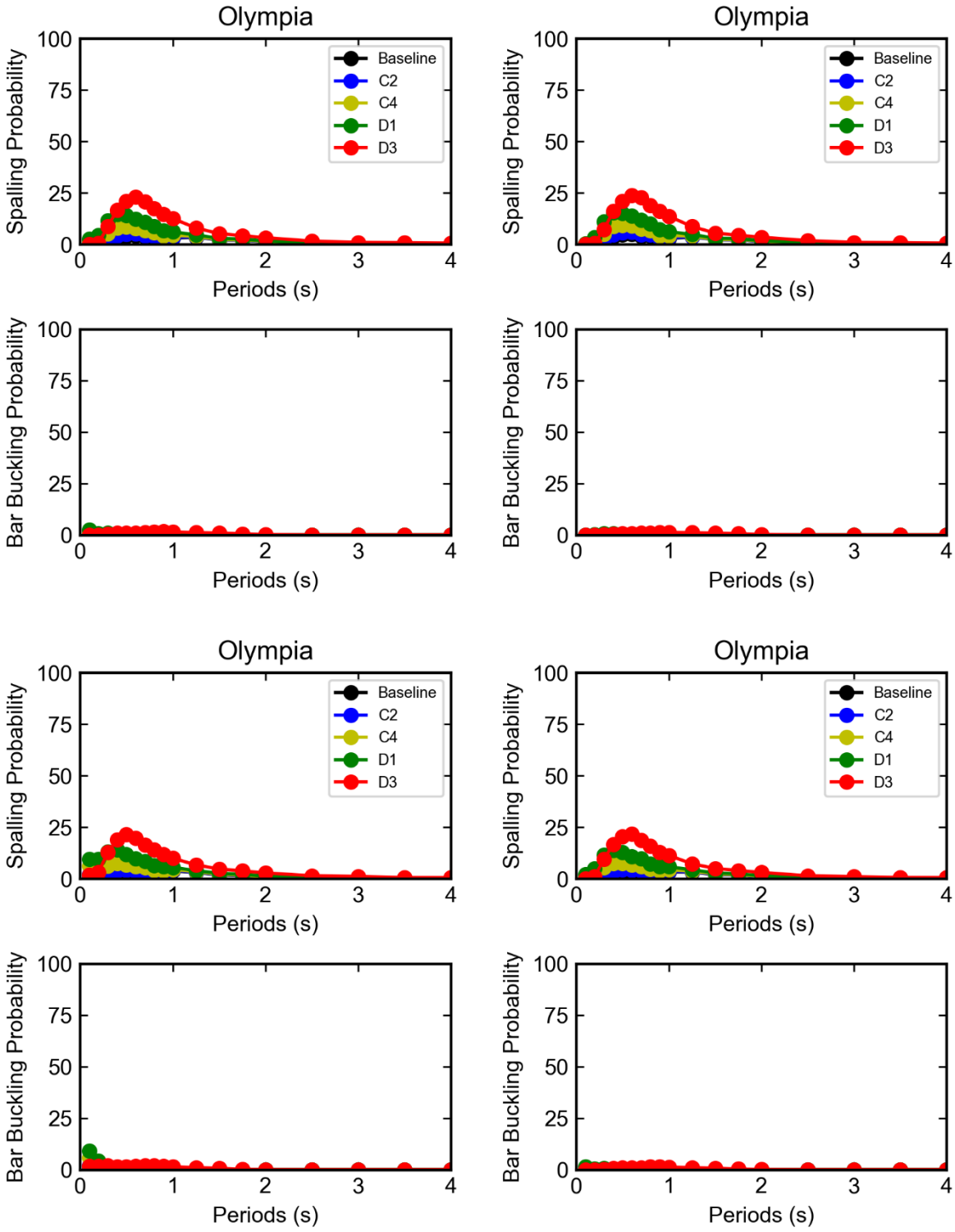

Figure C.3. Probability of spalling and bar buckling in Olympia for old (left) and new (right) bridges, and for mean (top) and reduced (bottom) strength.

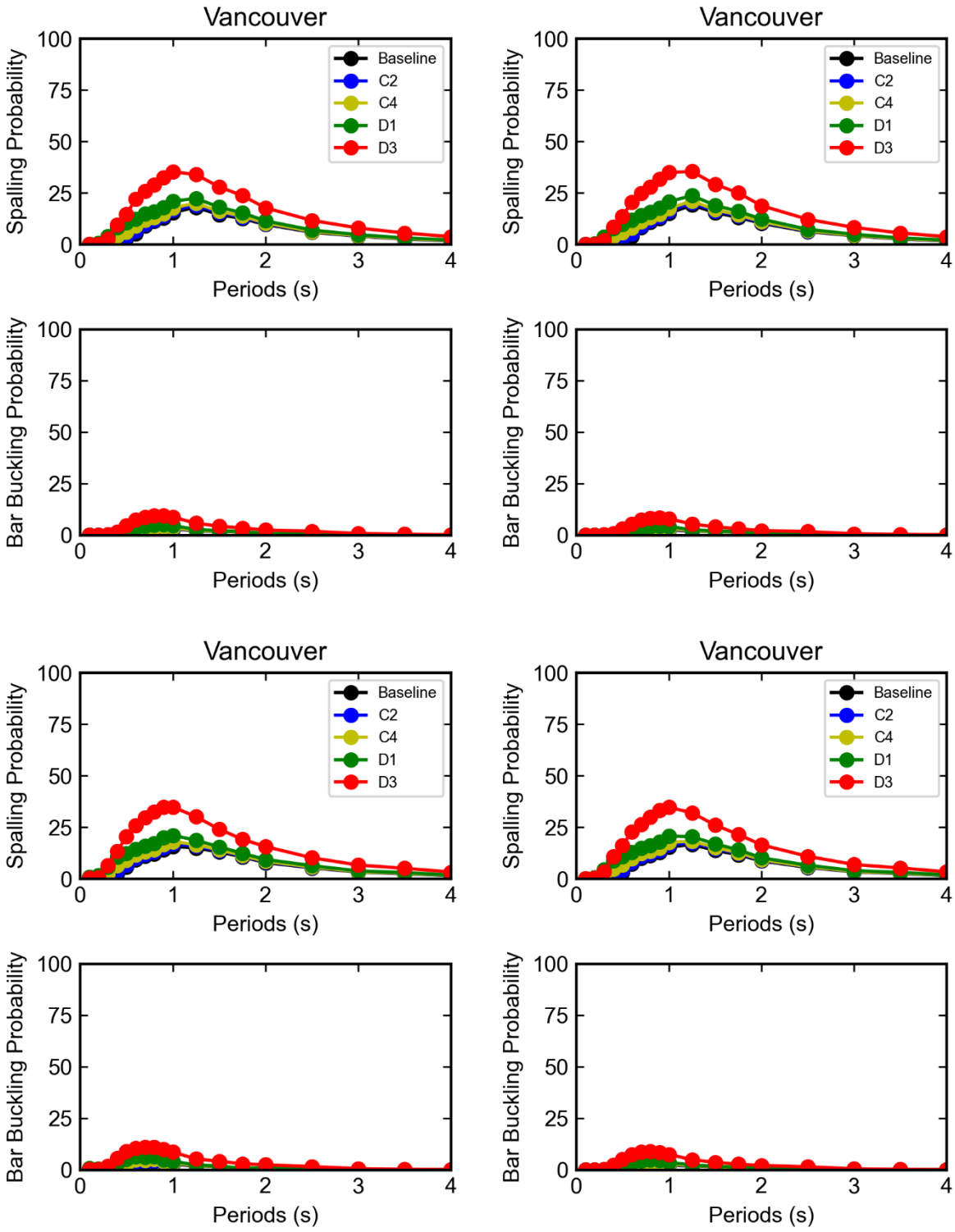

Figure C.4. Probability of spalling and bar buckling in Vancouver for old (left) and new (right) bridges, and for mean (top) and reduced (bottom) strength.

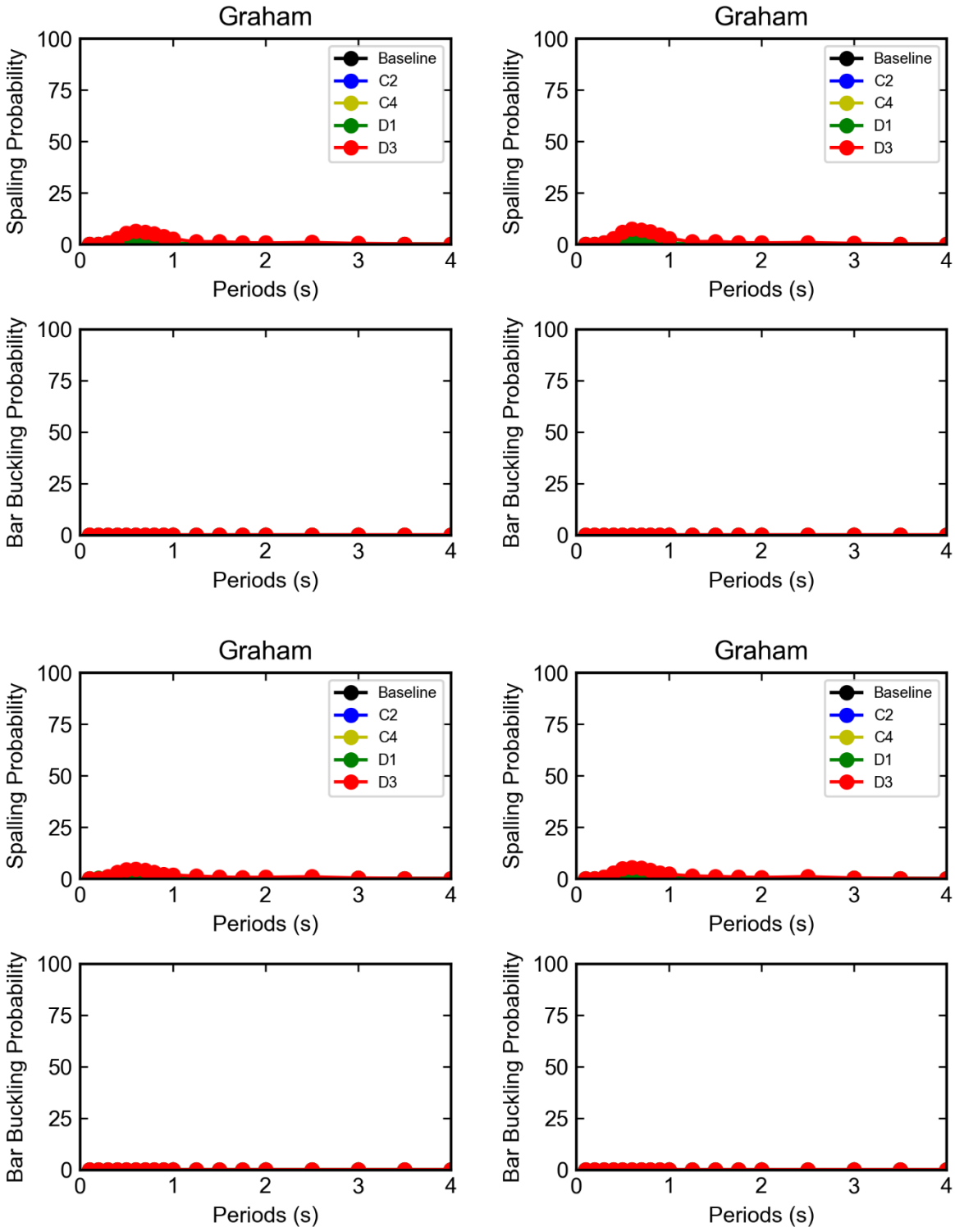

Figure C.5. Probability of spalling and bar buckling in Graham for old (left) and new (right) bridges, and for mean (top) and reduced (bottom) strength.

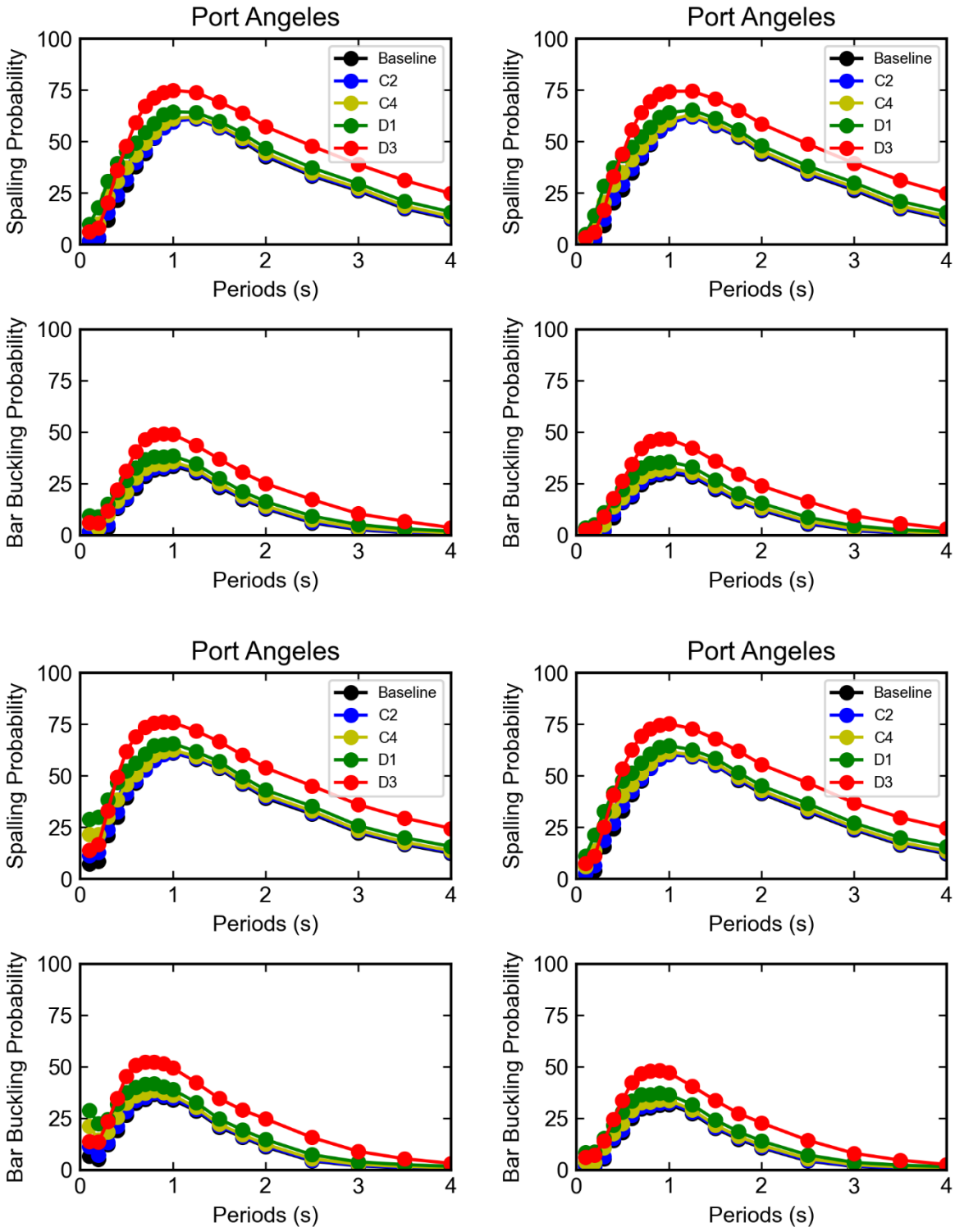

Figure C.6. Probability of spalling and bar buckling in Port Angeles for old (left) and new (right) bridges, and for mean (top) and reduced (bottom) strength.

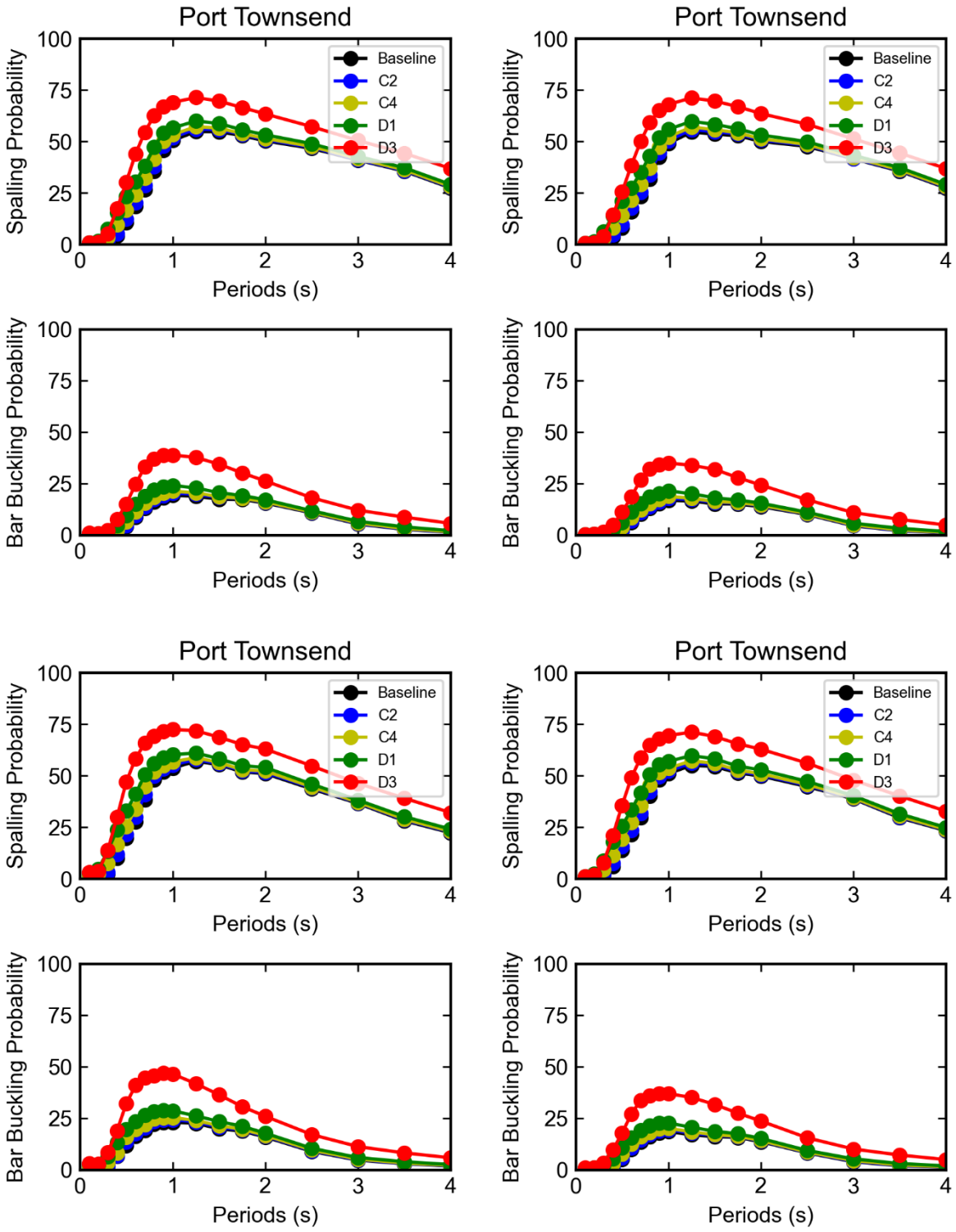

Figure C.7. Probability of spalling and bar buckling in Port Townsend for old (left) and new (right) bridges, and for mean (top) and reduced (bottom) strength.

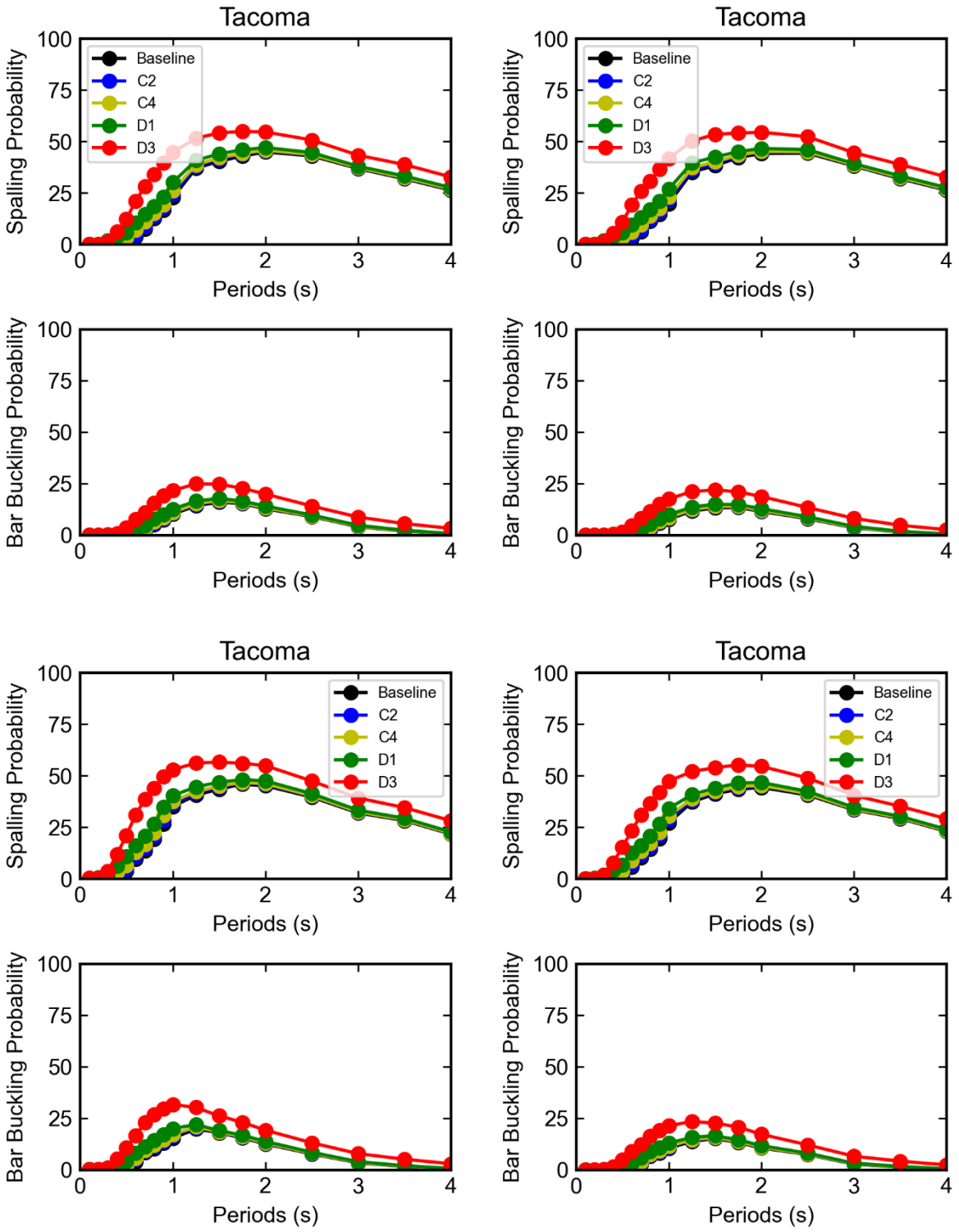

Figure C.8. Probability of spalling and bar buckling in Tacoma for old (left) and new (right) bridges, and for mean (top) and reduced (bottom) strength.

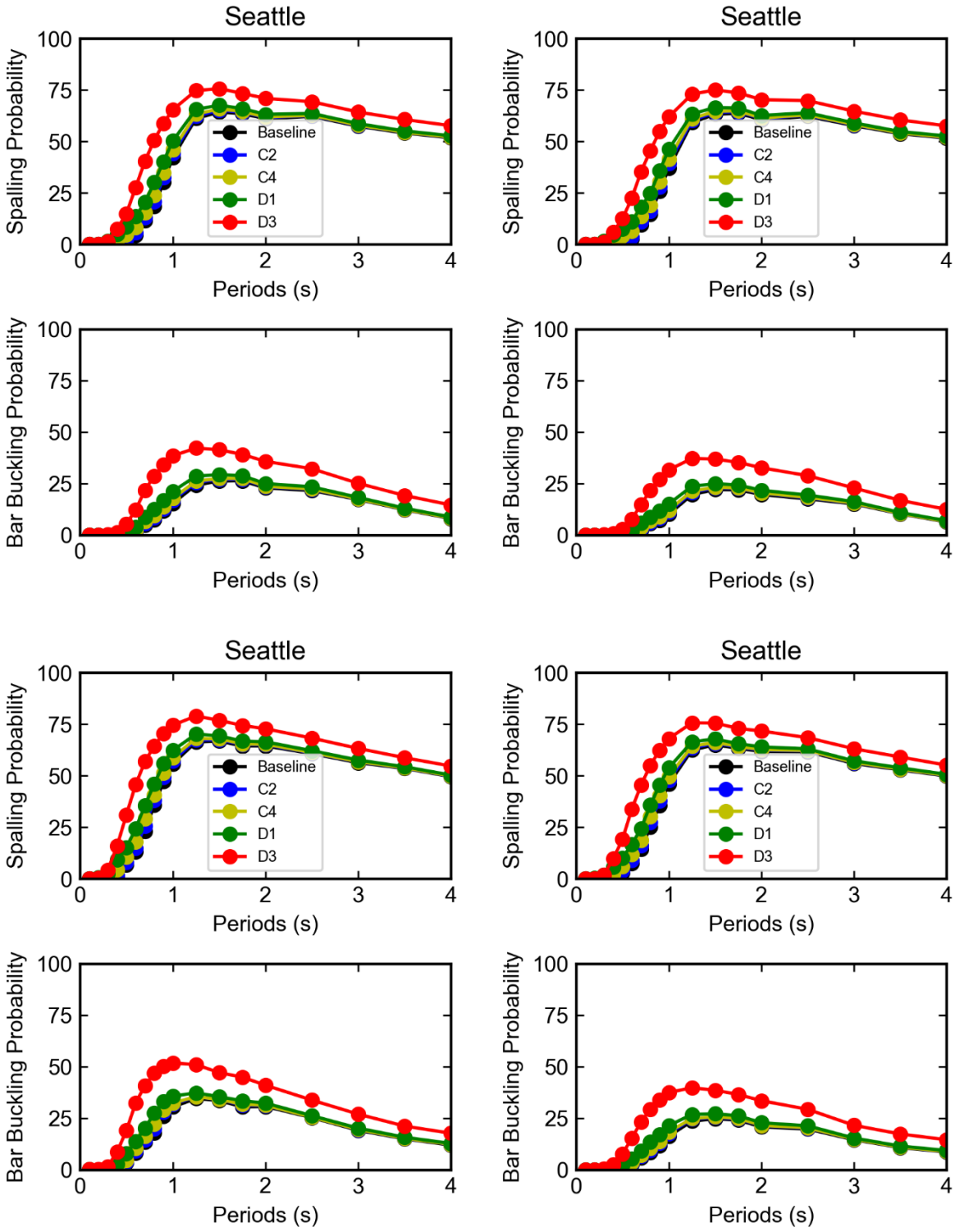

Figure C.9. Probability of spalling and bar buckling in Seattle for old (left) and new (right) bridges, and for mean (top) and reduced (bottom) strength.

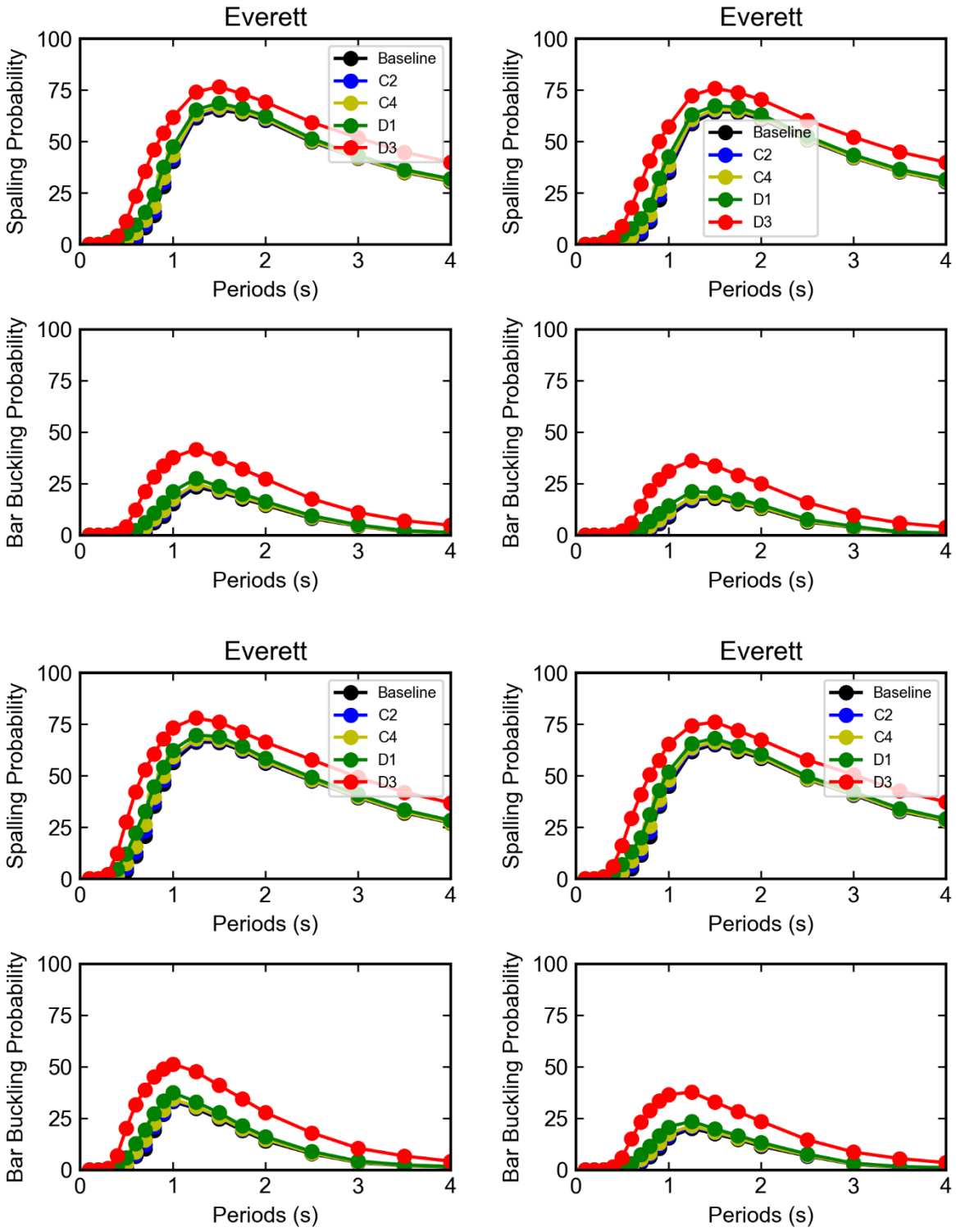

Figure C.10. Probability of spalling and bar buckling in Everett for old (left) and new (right) bridges, and for mean (top) and reduced (bottom) strength.

Appendix D: Fragility Curves

Table D.1: Spectral Acceleration: Parameters for Fragility Curves

		μ = 2		μ = 3.5		μ = 6		μ = 8	
City	**Age**	**Median**	**β**	**Median**	**β**	**Median**	**β**	**Median**	**β**
Seattle	Old	2.04	0.32	3.50	0.58	6.77	0.84	9.26	0.95
	New	2.09	0.33	3.78	0.57	7.98	0.80	11.58	0.83
Forks	Old	2.10	0.29	3.58	0.53	7.37	0.85	10.74	1.00
	New	2.12	0.29	3.85	0.53	8.61	0.79	12.47	0.83
Ocean Shores	Old	2.23	0.31	3.80	0.49	6.96	0.80	9.80	0.97
	New	2.27	0.29	3.95	0.47	7.79	0.74	11.45	0.83
Port Angeles	Old	2.12	0.32	3.64	0.59	6.92	0.93	10.40	1.15
	New	2.17	0.32	3.79	0.57	7.58	0.93	11.73	1.09
Olympia	Old	2.78	0.31	5.52	0.46	7.22	0.43	7.53	0.42
	New	2.84	0.30	5.08	0.38	6.39	0.32	49.95	1.02
Port Townsend	Old	2.11	0.32	3.77	0.56	7.63	0.84	10.81	0.96
	New	2.17	0.32	4.06	0.55	8.47	0.81	12.25	0.88
Vancouver	Old	2.52	0.31	5.01	0.53	8.75	0.66	10.87	0.65
	New	2.59	0.31	5.07	0.52	8.59	0.60	19.81	0.89
Tacoma	Old	2.28	0.32	4.32	0.58	7.99	0.77	10.03	0.81
	New	2.34	0.32	4.58	0.58	8.17	0.70	18.89	1.07
Graham	Old	2.89	0.25	7.17	0.42	Na	NA	Na	NA
	New	2.74	0.21	Na	NA	Na	NA	Na	NA
Everett	Old	2.05	0.35	3.92	0.72	9.22	1.08	13.65	1.15
	New	2.14	0.35	4.40	0.71	10.92	0.94	14.80	0.86

Table D.2: Effective Spectral Acceleration: Parameters for Fragility Curves

		μ = 2		μ = 3.5		μ = 6		μ = 8	
City	**Age**	**Median**	**β**	**Median**	**β**	**Median**	**β**	**Median**	**β**
Seattle	Old	2.30	0.18	3.83	0.21	6.76	0.27	9.95	0.39
	New	2.35	0.18	3.93	0.20	7.40	0.30	12.47	0.42
Forks	Old	2.21	0.18	3.58	0.22	5.90	0.27	8.13	0.34
	New	2.21	0.19	3.69	0.23	6.56	0.28	10.63	0.40
Ocean Shores	Old	2.30	0.20	3.68	0.21	5.68	0.26	7.72	0.37
	New	2.33	0.20	3.74	0.22	6.30	0.30	10.08	0.43
Port Angeles	Old	2.24	0.20	3.59	0.25	6.29	0.34	9.36	0.47
	New	2.25	0.21	3.67	0.26	6.73	0.36	10.70	0.48
Olympia	Old	2.60	0.19	4.13	0.20	NA	NA	7.89	0.22
	New	2.65	0.20	3.97	0.22	NA	NA	NA	NA
Port Townsend	Old	2.27	0.18	3.82	0.23	6.93	0.31	10.34	0.42
	New	2.31	0.19	3.93	0.22	7.39	0.31	12.11	0.43
Vancouver	Old	2.48	0.20	4.37	0.27	8.22	0.39	12.38	0.42
	New	2.52	0.21	4.55	0.28	8.86	0.41	12.75	0.38
Tacoma	Old	2.38	0.19	4.00	0.23	6.97	0.29	10.18	0.38
	New	2.41	0.20	4.04	0.21	7.18	0.30	11.69	0.40
Graham	Old	2.69	0.22	NA	NA	NA	NA	NA	NA
	New	2.58	0.20	NA	NA	NA	NA	NA	NA
Everett	Old	2.26	0.19	3.94	0.25	7.69	0.31	13.37	0.48
	New	2.31	0.19	4.15	0.24	8.94	0.33	17.51	0.45

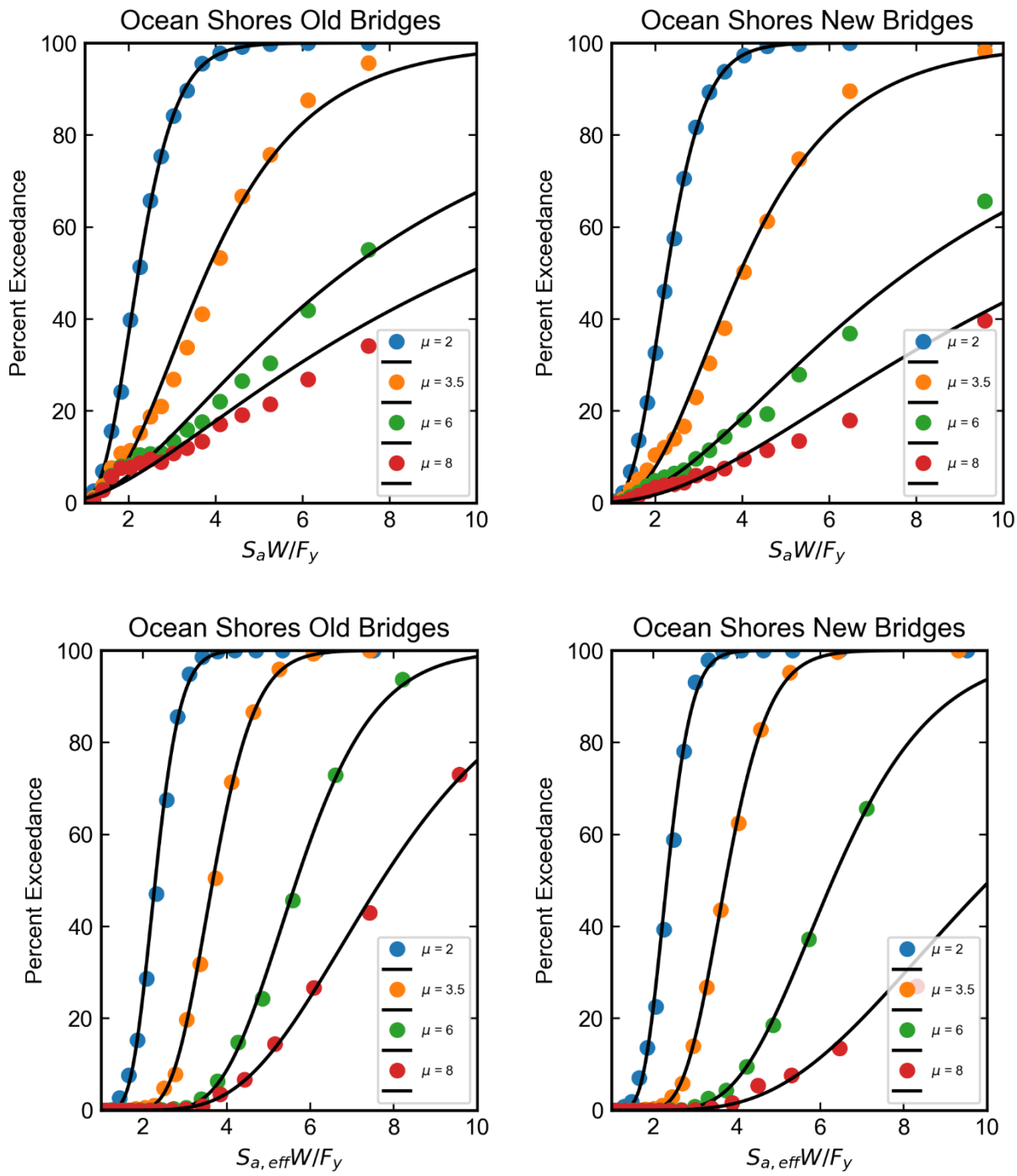

Figure D.1. Fragility Curves for Ocean Shores

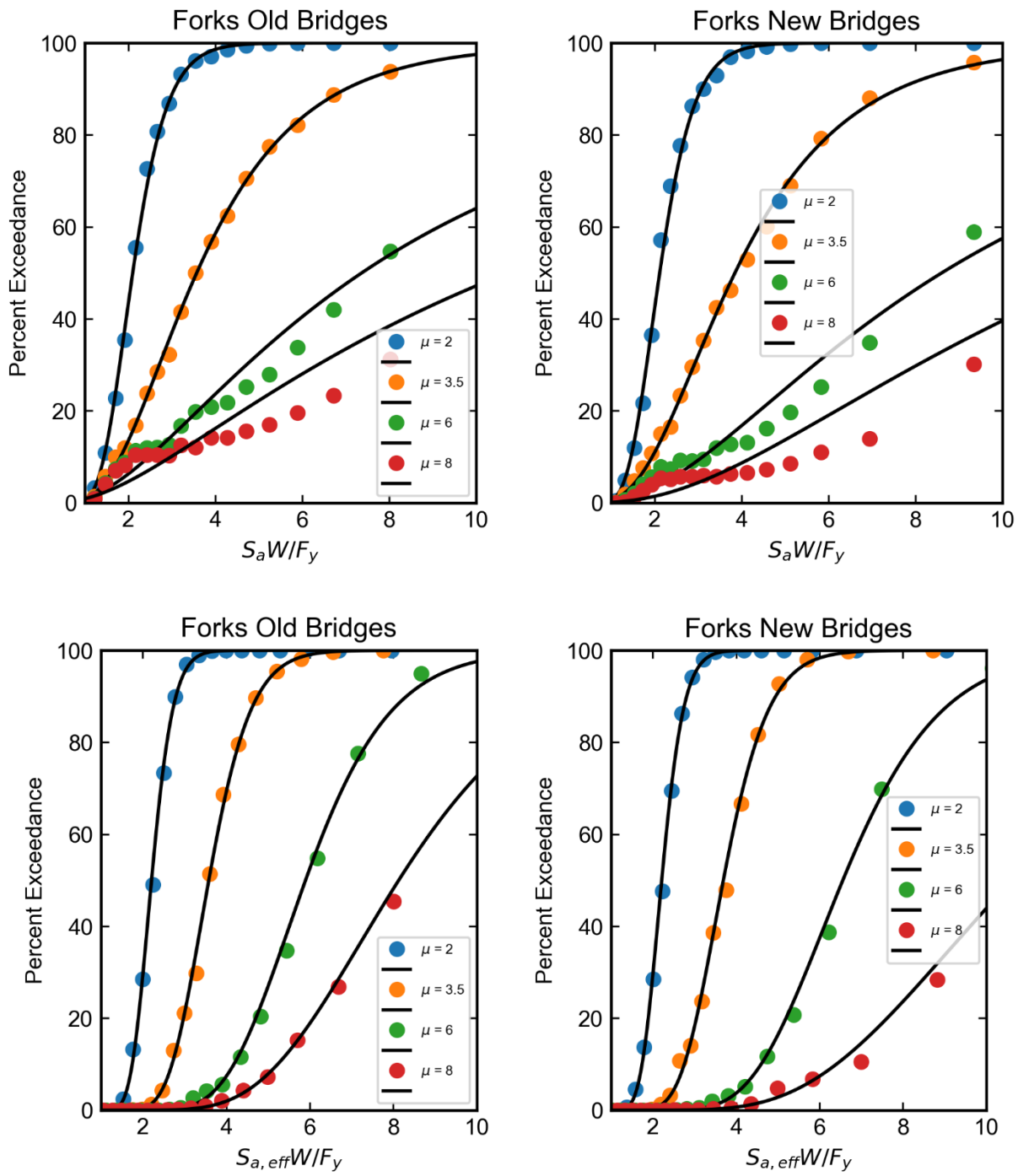

Figure D.2. Fragility Curves for Forks

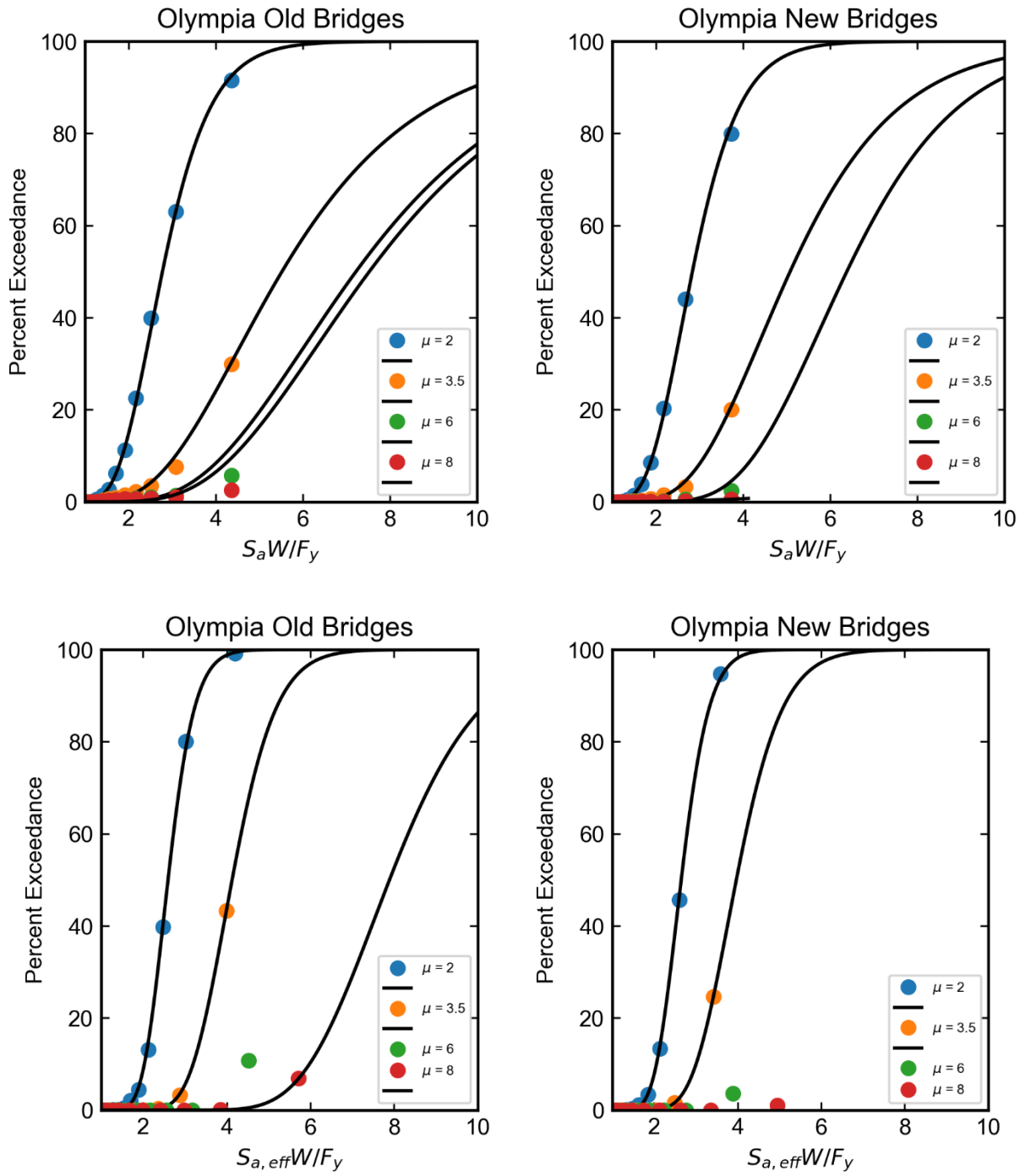

Figure D.3. Fragility Curves for Olympia

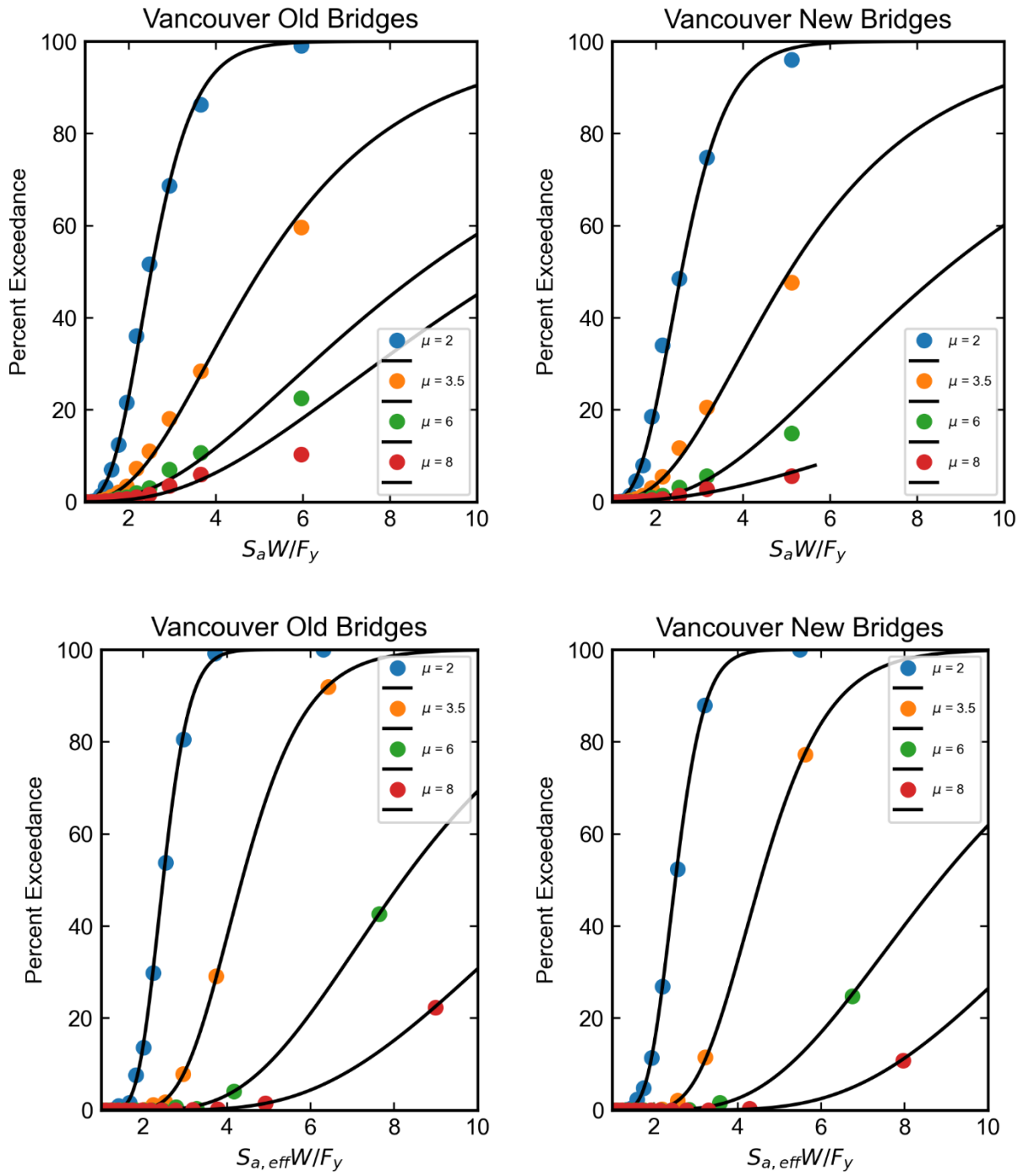

Figure D.4. Fragility Curves for Vancouver

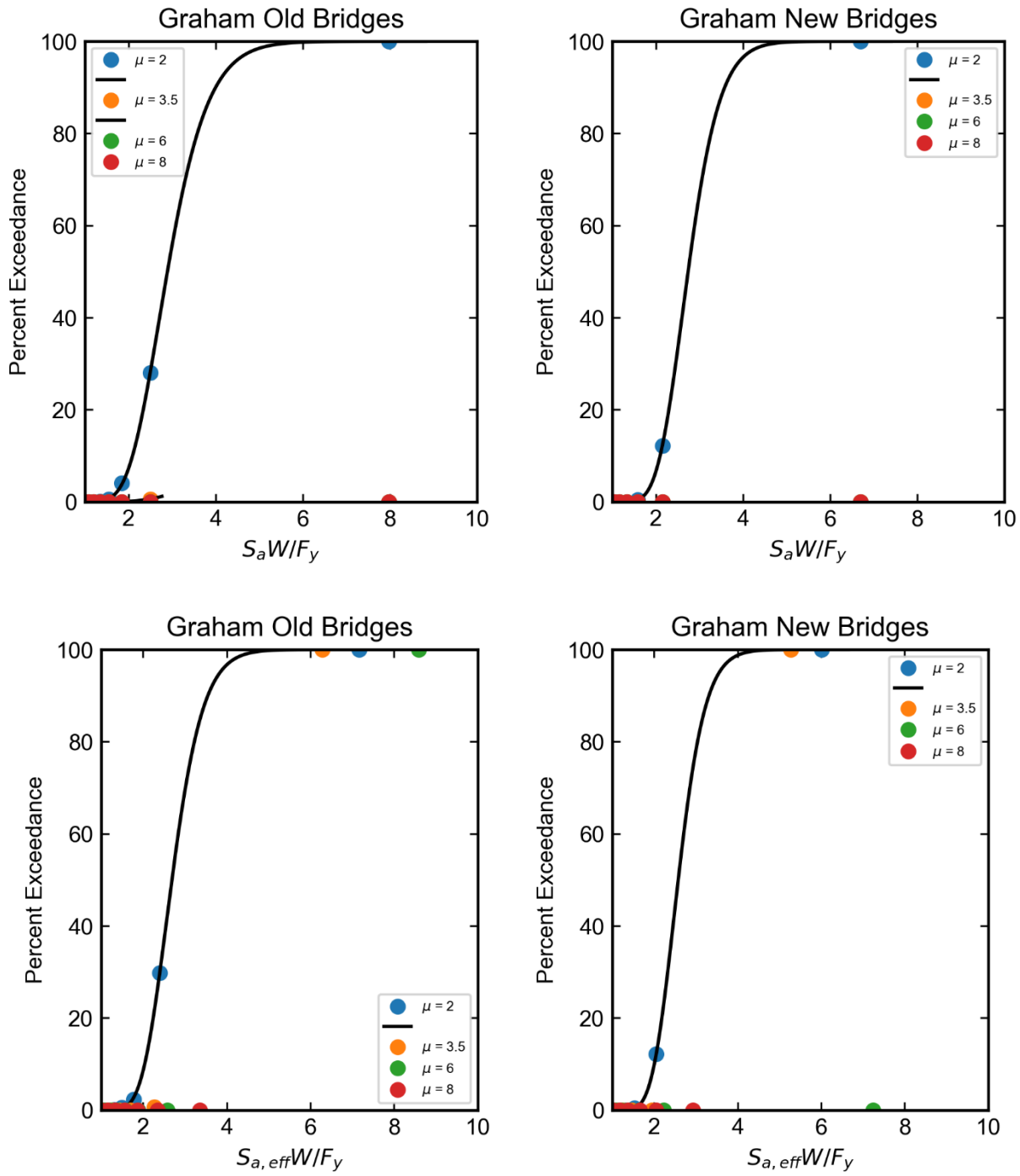

Figure D.5. Fragility Curves for Graham

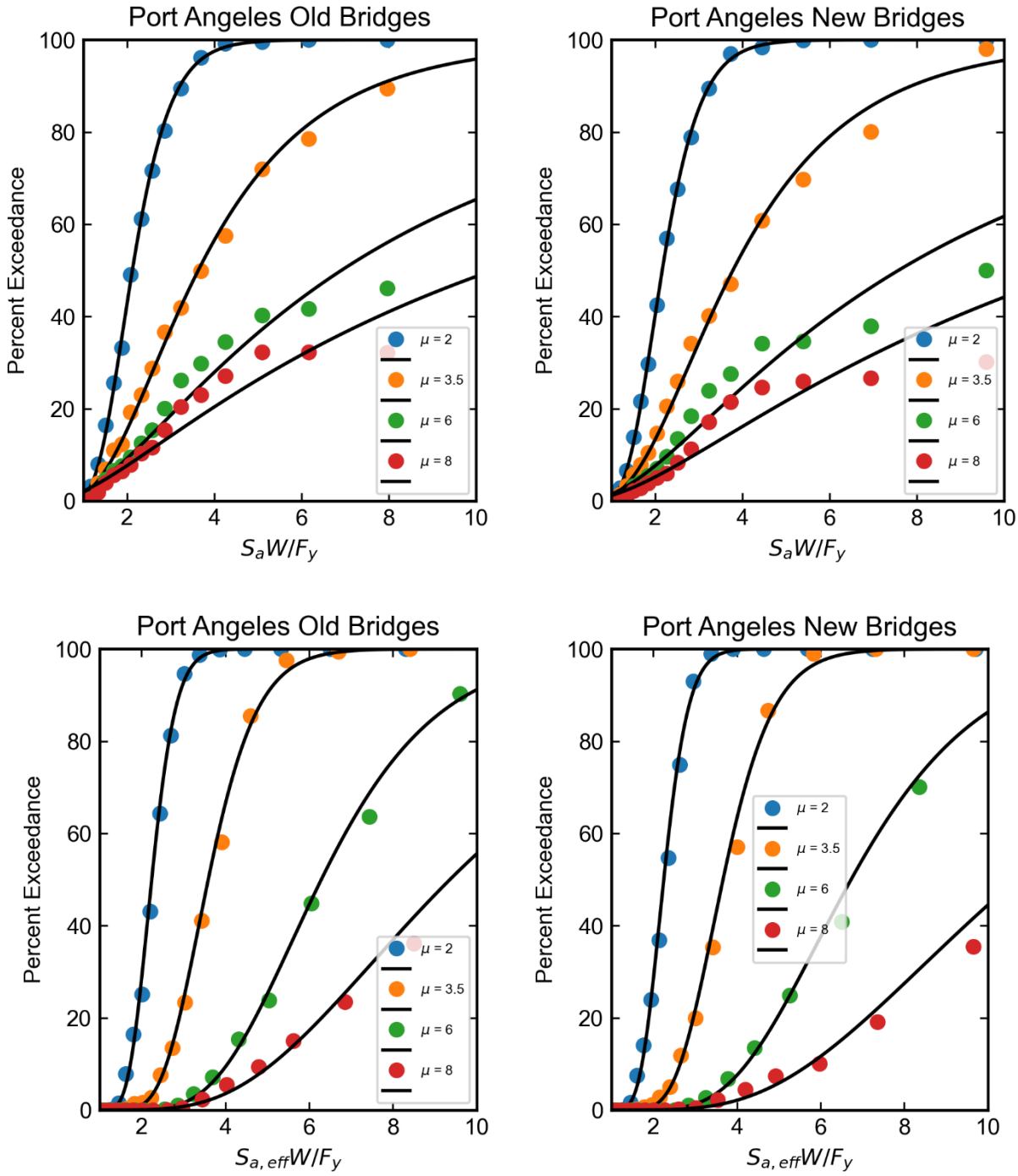

Figure D.6. Fragility Curves for Port Angeles

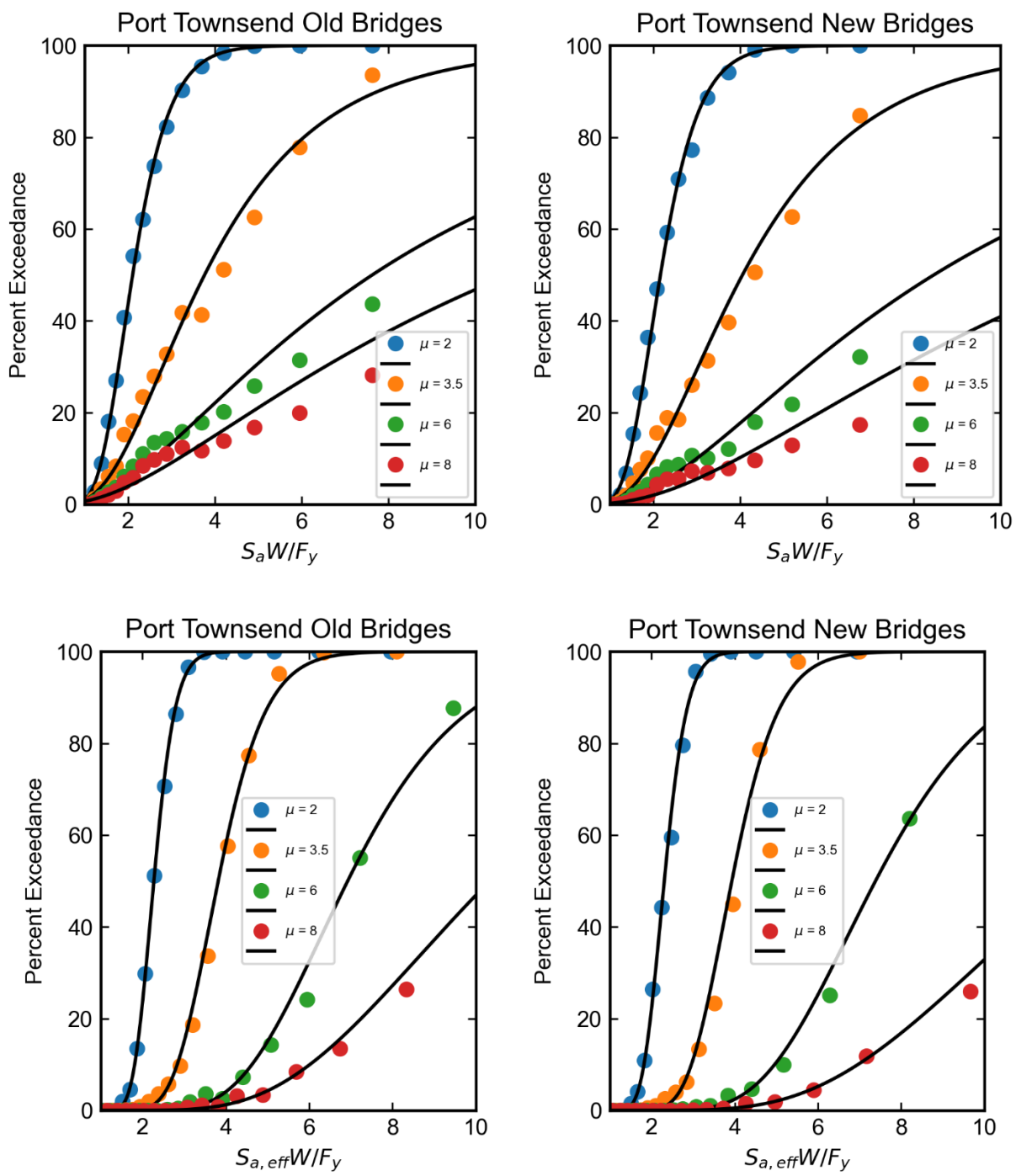

Figure D.7. Fragility Curves for Port Townsend

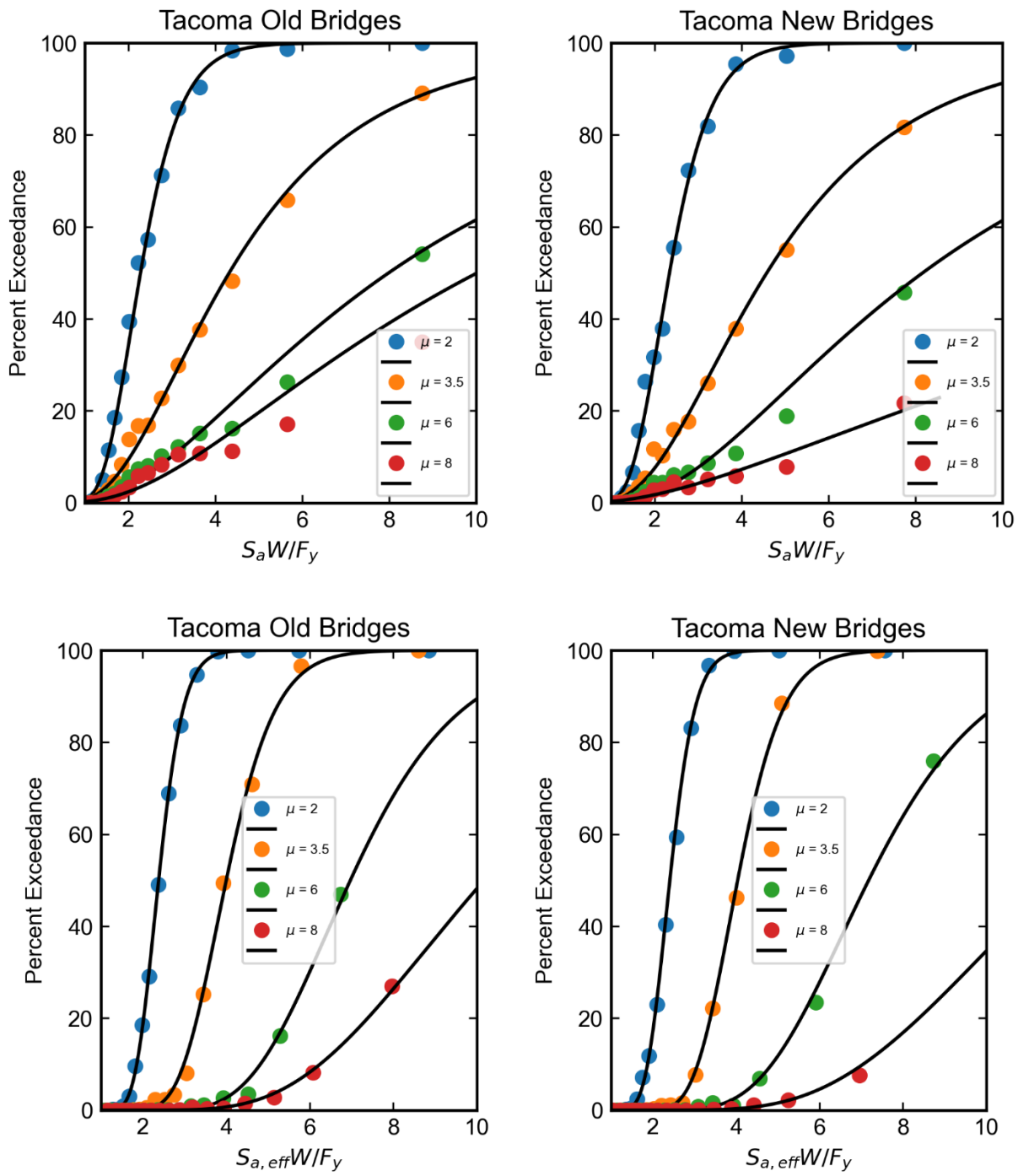

Figure D.8. Fragility Curves for Tacoma

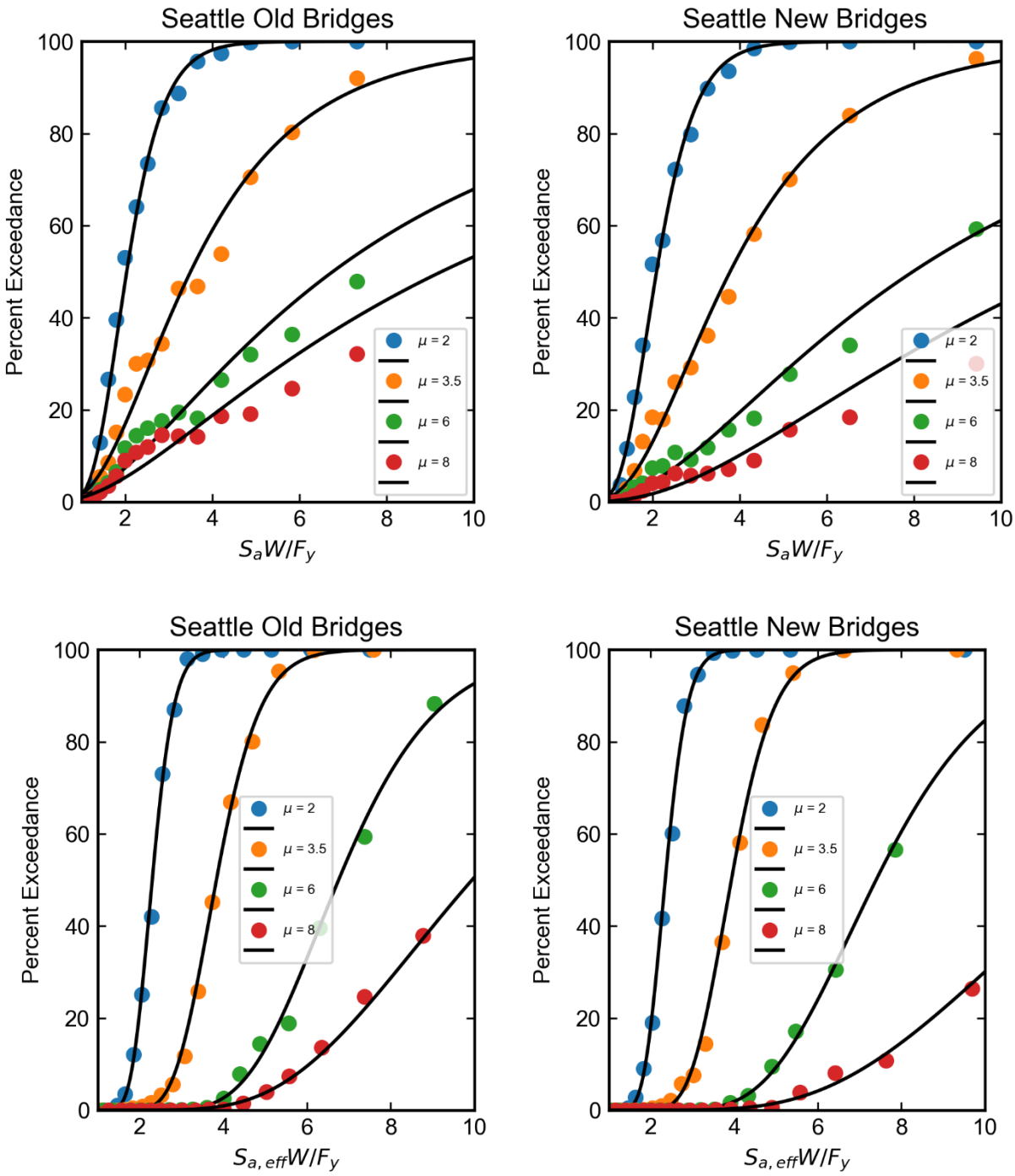

Figure D.9. Fragility Curves for Seattle

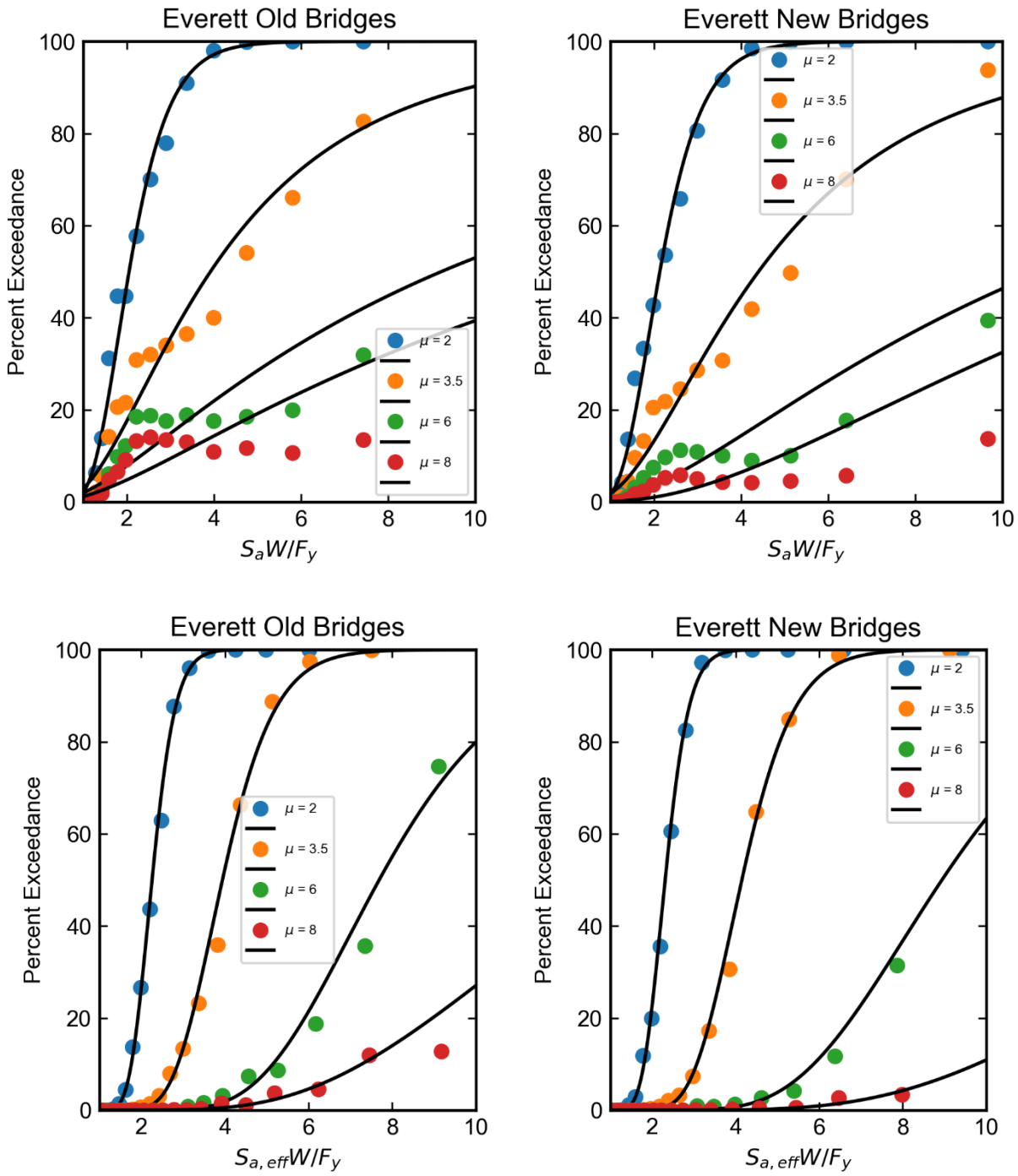

Figure D.10. Fragility Curves for Everett